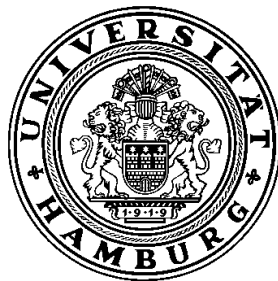


Quantum dissipative dynamics of electrons in tailored molecular systems and of excitons in biomolecular systems

Dissertation
zur Erlangung des Doktorgrades
des Fachbereichs Physik
der Universität Hamburg



vorgelegt von
Cesar Augusto Mujica Martinez
aus Valencia, Venezuela

September 2014

Gutachter der Dissertation:	Prof. Dr. M. Thorwart Prof. Dr. U. Kleinekathöfer
Gutachter der Disputation:	Prof. Dr. M. Thorwart Prof. Dr. C. Herrmann
Datum der Disputation:	26.09.2014
Vorsitzender des Prüfungsausschusses:	Prof. Dr. P. Schmelcher
Vorsitzender des Promotionsausschusses:	Prof. Dr. D. Pfannkuche
Leiter des Fachbereichs Physik:	Prof. Dr. P. Hauschildt
Dekan der MIN-Fakultät:	Prof. Dr. H. Graener

List of abbreviations

AM1	Austin Model 1
AO	atomic orbital
BChl	bacteriochlorophyll
DBV	15,16-dihydrobiliverdin
DQD	double quantum dot
EET	excitation energy transfer
EHM	extended Hückel method
FLN	fluorescence line-narrowing
FMO	Fenna-Matthews-Olson
HOMO	highest occupied molecular orbital
LUMO	lowest unoccupied molecular orbital
<i>l</i> -PPP	ladder-type poly-(<i>p</i> -phenylene)
MO	molecular orbital
PDA	poly-diacetylene
PE545	phycoerythrin 545 complex
PEB	phycoerythrobilin
PES	potential energy surface
PPP	poly-(<i>p</i> -phenylene)
QD	quantum dot
QUAPI	quasi-adiabatic propagator path integral
RC	reaction center
TLS	two-level system

Abstract

In this work, the quantum dissipative dynamics of electrons in tailored molecular systems and of excitons in biomolecular light-harvesting complexes is determined by using the numerically exact quasi-adiabatic propagator path integral scheme.

In the first part of the thesis, molecular double quantum dots are designed by using π -conjugated multi-block copolymers of poly-diacetylene (PDA) and ladder-type poly-(*p*-phenylene) (*l*-PPP). A charge qubit results when doping the molecule single negatively forming a polymeric radical anion. By systematically modifying the length of the oligomers, it is possible to restrict the number of confined electronic states to only two. They are described in terms of the spin-boson model, in which the molecular vibrations are formalized as the bosonic bath. The parameters characterizing the system and the vibrational bath are extracted from electronic structure calculations. At room temperature, coherent oscillations in the population difference are found, with values for the coherence times spreading over about two orders of magnitude. Non-Markovian effects contribute to sustain coherences. Controlled transitions between the basis states of the charge qubit, analogous to single qubit gates, are achieved by means of an external field. These systems constitute then a novel implementation for quantum computation hardware able, in principle, to operate at room temperature.

In the second part, the excitation energy transfer dynamics of the chlorophyll-containing Fenna-Matthews-Olson (FMO) complex in the green sulfur bacteria *Chlorobium tepidum* is evaluated. The aim is to elucidate the origin of the sustained excitonic coherence found experimentally and its significance in the speed and efficiency of the energy transfer dynamics. In this case, the bath is given by the vi-

brational pigment-protein-solvent environment, which contains localized vibrational modes. The results indicate that the experimental findings cannot be explained by only considering environmental equilibrium fluctuations, but by explicitly considering the nonequilibrium dynamics of the localized vibrational modes. No evidence of non-Markovian effects is found in the exciton dynamics of the FMO complex. Simultaneous sustained coherence and faster energy transfer is found depending on which molecular site the vibrational modes couples to. However, sustained coherence is not functionally necessary for the speed-up of the energy transfer, and consequently, for the increased transfer efficiency, which constitutes a very general mechanism elucidated in this work.

An overdamped excitonic dynamics, that exhibits a Markovian behavior, is found in the third part of this work for the bilin-containing phycoerythrin 545 (PE545) complex of the cryptophyte algae *Rhodomonas* CS24.

Kurzfassung

In dieser Arbeit wird die dissipative Quantendynamik von Elektronen in maßgeschneiderten molekularen Systemen und von Exzitonen in biomolekularen Lichtsammelkomplexen mit Hilfe der numerisch exakten quasi-adiabatischen Pfadintegral-Propagatorfunktion bestimmt.

Im ersten Teil der Arbeit werden molekulare Doppel-Quantenpunkte aus Polydiacetylen (PDA) und Leiterpolymere vom Poly(para-phenylen)-Typ (*l*-PPP) π -konjugierten Multi-Block-Kopolymeren betrachtet. Eine n-Dotierung des Moleküls mit einem Einzelektron bildet ein polymeres Radikal-Anion, welches ein Ladungsqubit darstellt. Durch systematische Modifizierung der Länge der Oligomere ist es möglich, die Anzahl der lokalisierten elektronischen Zustände auf nur zwei zu beschränken. Sie werden durch das Spin-Boson-Modell beschrieben, in dem die Molekülschwingungen formal als bosonisches Bad auftreten. Die Parameter des Systems und des Schwingungsbads werden aus Berechnungen der elektronischen Struktur entnommen. Bei Raumtemperatur werden kohärente Oszillationen in der Populationsdifferenz gefunden, bei denen sich die Werte für die Kohärenzzeiten über etwa zwei Größenordnungen ausbreiten. Nicht-Markovsche-Effekte tragen dazu bei, die kohärenten Oszillationen zu erhalten. Kontrollierte Übergänge zwischen den Grundzuständen des Ladungsqubits werden durch ein externes Feld erreicht, die ähnlich zu denen eines einzelnen Qubit-Gatters sind. Diese Systeme bilden dann eine neue Implementierung für Quantencomputer-Hardware, welche im Prinzip in der Lage ist, bei Raumtemperatur arbeiten.

Im zweiten Teil, wird die Exzitonenenergietransfer-Dynamik des chlorophyllhaltigen Fenna-Matthews-Olson-Komplex (FMO) der Grünen Schwefelbakterien *Chloro-*

bium tepidum ausgewertet. Ziel ist es, den Ursprung der experimentell gefundenen anhaltenden exzitonischen Kohärenz und sein Einfluss auf die Geschwindigkeit und die Effizienz der Energieübertragungsdynamik aufzuklären. In diesem Fall wird das Bad durch die Schwingungen der Pigment-Protein-Lösungsumgebung gegeben, welches lokalisierte Schwingungsmoden enthält. Die Ergebnisse zeigen, dass die experimentellen Befunde nicht durch die Berücksichtigung der Gleichgewichtsfluktuationen der Umgebung erklärt werden, sondern durch die explizite Berücksichtigung der Nichtgleichgewichtsdynamik der lokalisierten Schwingungsmoden. Es wurde kein Nachweis von Nicht-Markovschen-Effekten in der Exzitonendynamik des FMO-Komplex gefunden. Abhängig davon welches Chromophor an die Schwingungsmoden koppelt, werden gleichzeitig anhaltende Kohärenz und schnellerer Energietransfer gesehen. Trotzdem zeigen die Ergebnisse, dass die anhaltende Kohärenz für die Beschleunigung der Energieübertragung und somit für die erhöhte Übertragungsleistung funktionell nicht notwendig ist. Dies folgt einem sehr allgemeinen Mechanismus, der in dieser Arbeit erläutert wird.

Im dritten Teil dieser Arbeit wird eine übergedämpfte exzitonische Dynamik für den Bilin-haltige Phycoerythrin-545-Komplex (PE545) der Cryptophyceen Algen *Rhodomonas* CS24 gefunden, der ein Markov-Verhalten zeigt.

Contents

1	Introduction	1
2	Dynamics of open quantum systems	5
2.1	Path integral propagator	6
2.2	The method of the quasi-adiabatic propagator path integral	8
2.2.1	Path integral formulation	11
2.2.2	Extended QUAPI scheme	17
2.3	Quantification of non-Markovian effects	18
I	Tailored molecular systems: π-conjugated copolymers	23
3	Organic π-conjugated block copolymers	25
4	Design of organic π-conjugated molecular charge qubits	31
4.1	Electronic structure	31
4.2	Vibrational states	33
4.3	Modeling of molecular charge qubits	35
4.3.1	Fluctuational spectrum of molecular charge qubits	36
4.3.2	Electron–vibration coupling strength	37
5	Dynamics of π-conjugated molecular charge qubits	41
5.1	Dynamics of undriven molecular charge qubits	42

5.1.1	Non-Markovian effects in molecular charge qubits	46
5.2	Dynamics of driven molecular charge qubits	49
5.3	Concluding remarks	55
II	Biomolecular systems: The FMO complex	59
6	Light-harvesting systems and the FMO complex	61
7	Modeling the FMO complex	71
7.1	FMO Model	71
7.1.1	Experimental determination of the spectral density function	73
7.2	Spectral density of Adolphs and Renger	75
7.3	Spectral density of Kreisbeck and Kramer	79
7.4	Spectral density of Aghtar <i>et al.</i>	80
7.5	Discussion	82
8	Dynamics in presence of equilibrium vibrations	85
8.1	Population dynamics in the Adolphs-Renger model	87
8.2	Population dynamics in the Kreisbeck-Kramer model	93
8.3	Population dynamics in the Aghtar <i>et al.</i> model	96
8.4	Concluding remarks	99
9	Dynamics in presence of non-equilibrium vibrations	101
9.1	Effect of intermediate-frequency vibrational modes	103
9.1.1	EET dynamics in the intermediate coupling regime	104
9.1.2	EET dynamics in the strong coupling regime	111
9.1.3	EET dynamics including an equilibrium vibrational mode	115
9.2	Effect of low-frequency vibrational modes	116
9.2.1	Dynamics in presence of the 36 cm ⁻¹ vibrational mode	116
9.2.2	Dynamics in presence of the 70 cm ⁻¹ vibrational mode	121
9.3	Concluding remarks	124
10	Quantification of non-Markovian effects in the exciton dynamics	127
10.1	Non-Markovian effects in presence of equilibrium vibrations	128
10.1.1	Non-Markovianity in the Adolphs-Renger model	128
10.1.2	Non-Markovianity in the Kreisbeck-Kramer model	130
10.1.3	Non-Markovianity in the Aghtar <i>et al.</i> model	130
10.2	Non-Markovian effects in presence of non-equilibrium vibrations	132
10.2.1	Non-Markovianity in presence of the 180 cm ⁻¹ mode	133

10.2.2	Non-Markovianity in presence of the 36 and 70 cm^{-1} modes	134
10.3	Concluding remarks	135
III	Biomolecular systems: The PE545 complex	137
11	The PE545 complex	139
11.1	PE545 Model	142
12	Dynamics of the PE545 complex	145
12.1	Concluding remarks	147
13	Summary	149
Appendix		153
A	Spin in electronic structure methods	153
B	About geometry optimizations and vibrational analysis	155
B1	Geometry optimizations	155
B2	Vibrational analysis	158
C	The extended Hückel method	161
D	MOs of the Δ_N molecular heterostructures	163
E	$J(\omega)$ and $L(t)$ of the Δ_N molecular heterostructures	169
F	Dissipative dynamics of the Δ_4 system	181
Bibliography		187

Introduction

Quantum systems are not isolated but interact with their surroundings. The former are usually described by a few relevant dynamical variables, but the latter is, in general, difficult to characterize microscopically due to the large number of degrees of freedom involved. This results in the “macroscopic bath” exerting a fluctuating force on the system causing fluctuations of its degrees of freedom. The interaction between the system and the environment leads to entanglement between their degrees of freedom. The result is an irreversible energy transfer from the system to the environment until equilibrium is established, i.e., dissipation and decoherence. By this, coherent superpositions of quantum states are destroyed. Thus, the environment acts as a continuous measuring apparatus leading to an incessant destruction of the phase correlations due to the collapse of the wavefunction [1].

The destructive environmental influence on the coherent superpositions is of prime importance for quantum computation, which demands a high degree of control over the quantum states. The main challenge in actually building a quantum computer is to maintain the simultaneous abilities to control quantum systems, to measure them, and to preserve their isolation from uncontrolled parts of their environment [2]. This requires that the basic units of quantum information, i.e., the qubits, have some robust *physical representation*, in which they retain their quantum properties, but also that they can be made to evolve as desired [3]. Quantum computation is based on transformation of quantum states. Their evolution proceeds via the Schrödinger equation, where time-dependent terms mediate physical

interactions that depend on the materials used to represent the qubits [4]. In spite of the different sources of decoherence in the different qubit representations (e.g., in terms of spins, charge, or photons), their performance can be compared in terms of the quotient between the time for which the system remains quantum-mechanically coherent and the time it takes to perform elementary unitary transformations involving at least two qubits, since they are both determined by the strength of coupling of the system to the environment [3]. For solid-state implementations, this quotient can be increased by rigorous control over material properties. For example, both SiGe and AlGaAs exhibit a high sensitivity to charge fluctuation noise, some of which can be minimized by proper device layer engineering [4].

On the other hand, excitation energy transfer between chromophores in photosynthetic biomolecules is limited by the environmental fluctuations generated by vibrational modes of the molecular pigments, the surrounding protein, and the polar solvent. In general, these systems exhibit high transfer efficiencies, even at room temperature, in spite of the noisy environment. Optimal photosynthetic capabilities are determined by the specific chromophore type, as well as their numbers and their arrangement.

Throughout this work, it is assumed that the properties of the microscopic system of interest can be probed experimentally (e.g., via spectroscopic techniques), while the environment is of interest only to the extent that it affects the dynamics of the system [5]. The system-bath model provides a realistic description of the effects of condensed-phase environments on the observable dynamics of the system, where the environment is modelled by a large number of harmonic degrees of freedom (e.g., phonons). A typical example is an impurity in a crystalline solid, where a harmonic bath emerges naturally from the small-amplitude lattice vibrations [6]. On the other hand, if the medium is characterized by a large-amplitude floppy motion, as in the case of the electron transfer in solution or in a (bio-)molecular host, the donor and acceptor potential surfaces are expected to be very anharmonic functions of the atomic displacements. However, the process of electron transfer is governed by the collective motion of the large number of environmental coordinates. In these cases, within the regime of validity of the linear response theory, effective modes with a Gaussian response can be obtained, such that the dynamics induced by the actual multidimensional anharmonic medium is equivalent to that of an effective harmonic bath with an appropriate spectral density [5, 6].

In a system-bath approach, the environmental influence on the system dynamics is given by the spectral density function, which is the coupling-weighted density of states of the phonon bath [1]. It determines the temporal correlation properties of the fluctuations via the bath autocorrelation function. Finite-size environments

(e.g., isolated small organic molecules) are characterized by a highly structured spectral density, which is mainly composed of δ -peaks at particular frequencies associated with specific molecular vibrations. On the other hand, broad unstructured spectral densities are characteristic of macroscopic host media like solids, liquids, or large biological molecules. In order for system relaxation transitions to occur via first-order processes, the spectral function must have a significant weight at the characteristic frequencies of the quantum system, otherwise, transitions can take place only via multiphonon processes, which are, in general, somewhat weaker [5, 7].

In this work, the dissipative quantum dynamics of three molecular systems is evaluated. All of them are described by a system-bath model. In Part I, it is proposed the use of molecular heterostructures based on organic π -conjugated block copolymers to implement charge qubits. A bottom-up approach is followed. This allows one to chemically engineer the electronic and vibrational structure of the designed molecules, which depend not only on the type but also on the number of oligomers employed. By this, it is possible to restrict the set of accessible electronic states to only two, as required for a qubit. Most importantly, these molecular systems allow one to tailor the environmental degrees of freedom influencing the dynamics of the charge qubit, as compared, for example, to other condensed matter implementations. Because of the molecular nature of these systems, discrete peaks in the spectral density result. The influence of these peaks on the qubit coherence times can be then quantitatively evaluated by treating the molecules in terms of an electronic system and a vibrational bath. The vibrational and electronic structures are determined by using quantum chemistry calculations, as indicated in Appendices B and C, respectively. The two-dimensional electronic Hilbert space can be represented as a “particle” of spin 1/2 in contact with a bosonic environment, known as the spin-boson model [1, 8]. This generic model has been used to describe, for example, the motion of defects in crystalline solids, the tunneling of light particles in metals, and some chemical reactions involving electron or proton transfer processes [1, 8]. The two-level system is the simplest system showing constructive and destructive quantum interference effects [1, 8, 9, 10], and several other non-trivial effects like coherent destruction of tunneling [11] or quantum phase transitions [12]. Results in Part I present the design of a molecular two-level system exhibiting coherent dynamics determined by a tailored environment. Thus, the resulting systems constitute a novel implementation of quantum hardware, where the charge degree of freedom in molecular architectures is exploited. Other approaches using molecules to implement qubits have been proposed. These include, apart from nuclear spins [13], soliton states in the middle of the gap of polyacetylene single chains [14], electronic spins in coordination magnetic molecules [15, 16, 17], vibrational states in

polyatomic molecules [18, 19], and rovibronic states in diatomic molecules [20]. One intrinsic advantage of molecular systems is their scalability since it is possible to build macroscopic arrays of identical molecules.

In contrast to the molecular systems presented in Part I, which are designed “from scratch” to exhibit sustained coherent dynamics, Parts II and III evaluate the excitation energy transfer dynamics of biomolecular light-harvesting complexes. Transfer in these biomolecular systems occurs at room temperature, in which rather short-lived quantum effects, if any, are expected due to the noisy and hot environment. Remarkably, signatures of nontrivial quantum effects, in the form of excitonic coherences lasting several hundreds of fs, at cryogenic and even at room temperature have been experimentally found in different complexes [21]. These results have led to the hypothesis that the transfer of energy occurs by a coherent superposition of excited electronic states, which leads to a transfer efficiency higher than would be possible by diffusive, incoherent excitation energy transfer. In order to elucidate the role played by quantum coherence in the speed and efficiency of the energy transfer dynamics of these systems, it is assumed that the system consists of the electronic degrees of freedom within the single excitation subspace of the pigments involved in the energy transfer. Thermal fluctuations on the excitation transfer dynamics are induced by the vibrational pigment-protein-solvent environment. The corresponding fluctuational spectrum can be determined from experimental results or from molecular dynamics simulations. In any case, it exhibits discrete peaks. Their influence is determined by evaluating whether a breakdown of the Franck-Condon (or, equivalently, the Born-Oppenheimer) approximation occurs, i.e., by evaluating the exciton dynamics in presence of equilibrium and nonequilibrium vibrational modes. A mechanism explaining the transfer efficiency is identified for the system evaluated in Part II. It relies in underdamped vibrational modes and depends only weakly on the life time of the coherent oscillations in the overall dynamics. This mechanism is, however, of general character and can be used, for example, for optimizing artificial light-harvesting systems as well.

Each part of this work is composed of the following chapters: an initial introductory chapter presenting the physical system, the next chapter is devoted to the theoretical modeling of the corresponding system, in which the system and bath parameters are extracted either from electronic structure calculations (as in Part I) or from experimental results (as in Parts II and III), and used to determine the explicit quantum dissipative dynamics in the subsequent chapter(s). The main results obtained in this work are summarized in chapter 13.

Dynamics of open quantum systems

This chapter describes the numerical method used to calculate the quantum dynamics of the different systems evaluated in this work. The path integral formalism is introduced in Sec. 2.1, which is used to derive the propagator for an isolated system. When this system is in contact with a harmonic bath, as in Sec. 2.2, the full system-bath propagator can be partitioned by using an adiabatic reference, which, within the path integral formulation, allows one to integrate out the harmonic degrees of freedom of the bath, leaving the propagator for the system coordinate as the only one that requires to be numerically generated [22, 23]. The result is a modified path integral expression involving one-dimensional propagators that describe the exact dynamics of the system along the adiabatic path, as well as a (nonlocal-in-time) influence functional that incorporates multidimensional nonadiabatic corrections [22]. The nonlocal interactions in the influence functional are of finite range in time if the bath is characterized by a broad spectrum. This can be explored in an “unfolding” procedure which yields an iterative scheme, known as the tensor multiplication scheme, for evaluating the path integral for arbitrary time intervals [22]. The derivation does not involve any kind of approximations related with the strength of the system-bath coupling as in Förster or in Redfield theories, and therefore, all non-Markovian effects are included exactly. A recently proposed non-Markovianity measure based on the physical features of the system-bath interaction is presented in Sec. 2.3.

2.1 Path integral propagator

The postulates of quantum mechanics [24] establish that all the information about a particular quantum system is contained in its wave function $|\psi(t)\rangle$, and its time evolution is determined by the Schrödinger equation $\partial_t|\psi(t)\rangle = -(i/\hbar)H|\psi(t)\rangle$, with H being the full system Hamiltonian. An analytical solution, however, can be obtained for a few systems only, and a numerical solution should be found instead. Because of the delocalized nature of quantum mechanics, the storing effort necessary for a wavefunction represented on a basis set grows exponentially with the number of interacting degrees of freedom, which limits the size of the systems possible to treat. Formally, the state of the system at any time t can be written as $|\psi(t)\rangle = U(t,0)|\psi(0)\rangle$, with $U(t,0)$ being the propagator between the initial time $t = 0$ and the final time t . For a time-dependent Hamiltonian $H(t)$, the propagator is given by $U(t,0) = \mathcal{T} \exp \left\{ -(i/\hbar) \int_0^t dt' H(t') \right\}$, with \mathcal{T} being the time ordering operator. In the case of the Hamiltonian being time-independent, the propagator simplifies to $U(t,0) = \exp(-iHt/\hbar)$.

Alternatively, one can use Feynman's path integral formulation of time-dependent quantum mechanics, which is based on the Lagrange formalism of classical mechanics with the action as the central concept [25, 26]. In this approach, instead of finding the eigenfunctions of the Hamiltonian, one now has to evaluate a functional integral which directly yields the propagator required to determine the dynamics of the quantum system [25]. More precisely, in position representation, the amplitude to get from a point x_0 to the point x_f in time t is expressed in the path integral formulation as a sum of contributions from all conceivable paths that connect these points [26]. The contribution of each path $x(t)$ is proportional to a phase given by the action functional $S[x(t)]$ along that path as [6]

$$\langle x_f | e^{-iHt/\hbar} | x_0 \rangle = \int \mathcal{D}x_t e^{-iS[x(t)]/\hbar}, \quad (2.1.1)$$

where the integration is carried out for all paths $x(t)$ that satisfy the boundary conditions $x(0) = x_0$ and $x(t) = x_f$, and the action is defined as $S[x(t)] = \int_0^t dt' L(t')$, with $L = T - V$ being the Lagrangian function. The time-dependent Schrödinger equation can be recovered by using Eq. (2.1.1) and the superposition principle for the evolution of a wavefunction, which probes the equivalence of both formulations [26, 27].

For a particle of mass m with kinetic energy operator $T = p^2/2m$ and potential energy $V(x)$, the resulting action is

$$S[x] = \int_0^t dt' \left(\frac{m}{2} \dot{x}^2 - V(x) \right). \quad (2.1.2)$$

The discretized path integral representation of the propagator in Eq. (2.1.1) is obtained by dividing the total time t into N time slices of length δt as $t = N\delta t = N(t_k - t_{k-1})$, such that $e^{-iHt/\hbar} = \prod_{k=1}^N e^{-iH(t_k - t_{k-1})/\hbar}$, and using the completeness of the position eigenstates $\int dx_k |x_k\rangle\langle x_k| = 1$. The resulting discretized propagator is

$$\langle x_f | e^{-iHt/\hbar} | x_0 \rangle = \prod_{k=1}^N \int dx_k \langle x_k | e^{-iH(t_k - t_{k-1})/\hbar} | x_{k-1} \rangle, \quad (2.1.3)$$

which is exact for any value of N with $x_N = x_f$. Because each x_k is associated with a particular time t_k , the set $\{x_k\}$ defines a specific path composed of straight line segments [22]. By partitioning the Hamiltonian into kinetic and potential energy terms, a symmetric splitting of the short-time propagator in Eq. (2.1.3) is obtained as

$$e^{-iH\delta t/\hbar} \approx e^{-iV\delta t/2\hbar} e^{-iT\delta t/\hbar} e^{-iV\delta t/2\hbar}, \quad (2.1.4)$$

which is exact in the limit $\delta t \rightarrow 0$, but introduces an error of the order $[V, [T, V]]\delta t^3$ [22, 28]. Since the potential is diagonal in the position representation, the resulting short-time propagator is

$$\begin{aligned} \langle x_k | e^{-iH(t_k - t_{k-1})/\hbar} | x_{k-1} \rangle &\approx \langle x_k | e^{-iT(t_k - t_{k-1})/\hbar} | x_{k-1} \rangle \\ &\times \exp \left\{ \frac{-i(t_k - t_{k-1})}{2\hbar} [V(x_k) + V(x_{k-1})] \right\}. \end{aligned} \quad (2.1.5)$$

The eigenfunctions of the kinetic energy operator $T = p^2/2m$ correspond to those of a free particle, i.e., plane waves of the form $\psi_p(x) = (2\pi\hbar)^{-1/2} e^{ipx/\hbar}$. By using the identity $\int_{-\infty}^{\infty} dx e^{-(ax^2 + 2bx)} = (\pi/a)^{1/2} e^{b^2/a}$ in Eq. (2.1.5), the kinetic term can be evaluated exactly, giving

$$\langle x_k | e^{-iT\delta t/\hbar} | x_{k-1} \rangle = \left(\frac{m}{2\pi i \hbar \delta t} \right)^{1/2} \exp \left\{ \frac{i}{\hbar} \frac{m}{2\delta t} (x_k - x_{k-1})^2 \right\}. \quad (2.1.6)$$

An explicit form of the discretized propagator in Eq. (2.1.3) is then obtained as

$$\begin{aligned} \langle x_f | e^{-iHt/\hbar} | x_0 \rangle &\approx \prod_{k=1}^N \int dx_k \left(\frac{m}{2\pi i \hbar (t_k - t_{k-1})} \right)^{1/2} \\ &\times \exp \left\{ \frac{i}{\hbar} \sum_{k=1}^N (t_k - t_{k-1}) \left[\frac{m}{2} \left(\frac{x_k - x_{k-1}}{t_k - t_{k-1}} \right)^2 - \frac{1}{2} [V(x_k) + V(x_{k-1})] \right] \right\}, \end{aligned} \quad (2.1.7)$$

with the equality being valid in the limit $t_k - t_{k-1} \rightarrow 0$, and therefore, numerical evaluation requires a large number of integration variables for time lengths of interest. The exponent of the propagator in Eq. (2.1.7) contains the trapezoid rule discretization of the action in Eq. (2.1.2), which requires minimal storage. However,

the entire volume of integration must be evaluated because all paths $\{x_k\}$ enter with the same weight. This fact, together with the rapidly oscillating integrand, which leads to an enormous phase cancellation, results in the failure of sampling Monte Carlo schemes. Furthermore, observe that in the propagator of Eq. (2.1.7) the potential value is adjusted at each discrete time as $[V(x_k) + V(x_{k-1})]/2$, which requires many time steps δt in order to reproduce the actual potential. This indicates the necessity of using a physically motivated reference in the discretization of the path integral instead of the simple factorization of the time-evolution operator into potential and kinetic energy parts used in Eq. (2.1.4) [5, 6, 22, 23].

2.2 The method of the quasi-adiabatic propagator path integral

The propagator in Eq. (2.1.7) is valid for an isolated system, however, real quantum systems interact with their environment. In particular, processes occurring in the condensed phase are modulated by the interaction of the quantum system of interest with the collective vibrations of its surrounding host [5]. This situation can be described by a generic system-bath Hamiltonian in the form

$$H = \frac{p_x^2}{2m} + V(x) + \sum_j \left[\frac{p_j^2}{2m_j} + \frac{m_j \omega_j^2}{2} \left(q_j - \frac{c_j x}{m_j \omega_j^2} \right)^2 \right], \quad (2.2.1)$$

which represents a “reaction coordinate” x describing the system of interest coupled to a large number of harmonic “bath” degrees of freedom that mimic the effects of the environment [22]. It is assumed a bilinear coupling with coupling constants c_j between the system of mass m and the bath described by harmonic oscillators of masses m_j with coordinate and momentum operators q_j and p_j and oscillator frequencies ω_j . Equation (2.2.1) includes quadratic counterterms in x in order to renormalize the potential such that important potential features, like the barrier height, do not depend on the system-bath coupling strength [5, 6, 22, 23]. This is clear when considering the minimum of the Hamiltonian in Eq. (2.2.1) with respect to the coordinates of the system and environment [25]. From the requirement

$$\frac{\partial H}{\partial q_j} = m_j \omega_j^2 q_j - c_j x = 0, \quad (2.2.2)$$

it is obtained that

$$q_j = \frac{c_j}{m_j \omega_j^2} x. \quad (2.2.3)$$

This is used to determine the minimum of the Hamiltonian with respect to the system coordinate, which results in

$$\frac{\partial H}{\partial x} = \frac{\partial V}{\partial x} - c_j q_j + \frac{c_j}{m_j \omega_j^2} x^2 = \frac{\partial V}{\partial x}, \quad (2.2.4)$$

i.e., the counterterms in Eq. (2.2.1) ensure that the minimum is determined by the bare potential $V(x)$.

From the Hamiltonian in Eq. (2.2.1), it is possible to derive an effective description of the system alone by eliminating the environmental degrees of freedom. Two approaches can be followed. In the first one, a generalized quantum master equation for the reduced density matrix of the system of interest can be obtained by working in the Schrödinger picture. Alternatively, one can use the Heisenberg picture to obtain a generalized Langevin equation for the relevant set of operators of the small system [1]. The resulting quantum Langevin equation has the form [1, 25, 28]

$$m\ddot{x}(t) + m \int dt' \chi(t-t') \dot{x}(t') + \partial_x V = \xi(t) - m\chi(t)x(0), \quad (2.2.5)$$

which is an equation of motion for the position operator of the system $x(t)$ with memory-friction $\chi(t)$ and random force $\xi(t)$, with the last term in the right-hand-side arising from the counterterms in Eq. (2.2.1). The explicit form of the damping kernel $\chi(t)$ is given by

$$\chi(t) = \frac{1}{m} \sum_j \frac{c_j^2}{m_j \omega_j^2} \cos(\omega_j t), \quad (2.2.6)$$

while the time-dependent operator-valued fluctuating force has the form

$$\xi(t) = \sum_j c_j \left[q_j(0) \cos(\omega_j t) + \frac{p_j(0)}{m_j \omega_j} \sin(\omega_j t) \right]. \quad (2.2.7)$$

The mean value of the stochastic force with respect to the harmonic bath $H_B = \sum_j [p_j^2/2m_j + m_j \omega_j^2 q_j^2/2]$ vanishes, i.e., $\langle \xi(t) \rangle_B = 0$, meanwhile the temporal correlation properties of the fluctuations are given by the bath autocorrelation function

$$\langle \xi(t) \xi(0) \rangle_B = \sum_j \frac{\hbar c_j^2}{2m_j \omega_j} \left[\coth \left(\frac{\hbar \omega}{2k_B T} \right) \cos(\omega_j t) - i \sin(\omega_j t) \right]. \quad (2.2.8)$$

Within a reduced description for the system alone, all quantities characterizing the environment may be expressed in terms of the bath spectral density [1, 25]

$$J(\omega) = \frac{\pi}{2} \sum_j \frac{c_j^2}{m_j \omega_j} \delta(\omega - \omega_j), \quad (2.2.9)$$

i.e., instead of specifying all parameters c_j , m_j , and ω_j , it is enough to define the spectral density $J(\omega)$. It is a coupling constant weighted density of states that can be treated as a continuous function for macroscopic environments such that the sum over the discrete bath modes is replaced by a frequency integral. Using this allows one to express the damping kernel as

$$\chi(t) = \frac{2}{m} \int_0^\infty \frac{J(\omega)}{\pi\omega} \cos(\omega t) d\omega, \quad (2.2.10)$$

and the autocorrelation function as

$$\langle \xi(t)\xi(0) \rangle_B = \frac{\hbar}{\pi} \int_0^\infty d\omega J(\omega) \left[\coth\left(\frac{\hbar\omega}{2k_B T}\right) \cos(\omega t) - i \sin(\omega t) \right] = L(t). \quad (2.2.11)$$

Hence, the fluctuations are composed of harmonic modes with frequency ω at temperature T , and each mode contributes with a spectral weight given by $J(\omega)$, thus determining the relaxation and decoherence features of the quantum system of interest. In this picture, friction arises from the transfer of energy from the system to the large environment. This energy, once transferred, dissipates into the environment and is not given back within any physically relevant period of time, called the Poincaré recurrence time. For an environment composed of a huge number of bath oscillators, it is practically infinity [1].

In the Born-Markov approximation assumed in Redfield-type theories [29], the real part of $L(t)$ is replaced by a δ -function and the imaginary part is neglected, such that the fluctuations at a certain instant of time do not depend on their previous history and thus are uncorrelated over time. Then, the resulting time evolution becomes local in time, rendering the solution of the underlying equations of motion rather simple.

In the classical limit, $T \rightarrow \infty$ and $\hbar \rightarrow 0$, the real part of the autocorrelation function in Eq. (2.2.11) reduces to $L_R(t) = mk_B T \chi(t)$, while the imaginary part reduces to $L_I(t) = m\hbar\dot{\chi}(t)/2$ [25]. A purely Ohmic spectral density function of the form $J(\omega) = \alpha m\omega$, results in the damping kernel $\chi(t) = 2\alpha\delta(t)$, which renders Eq. (2.2.5) memory-free, i.e., a Markovian equation. This indicates that the Born-Markov approximation can be adequately applied in this specific situation. For many condensed matter systems, the typical situation [1] corresponds to a bath with a smooth structureless Ohmic spectral density $J(\omega) = \alpha\omega e^{-\omega/\omega_c}$ with a cutoff frequency ω_c , which is chosen to be the largest frequency scale in the problem. In the high temperature limit $T \rightarrow \infty$, $L_R(t)$ becomes a Lorentzian peak centered at $t = 0$ with height and width proportional to ω_c and ω_c^{-1} , respectively, and thus reducing to $\delta(t)$ in the limit $\omega_c \rightarrow \infty$ [23]. This implies that the environmental fluctuations evolve on the shortest time scale characterized by ω_c^{-1} , describing a fast

bath, where the memory effects are rather instantaneously lost or simply do not exist [30]. For any other finite temperature, $L(t)$ is comprised of multiple terms. They have the form of powers of Lorentzians resulting from a Taylor expansion of the $\coth(\hbar\omega/2k_B T)$, with their sum being a sharp peak around $t = 0$, but broader than the one in the $T \rightarrow \infty$ case [23]. This indicates that the bath correlations have a finite range if the environment has a smooth continuous spectrum, which results from phase cancellation among the infinite number of different frequency modes [5, 22, 23].

In contrast to the structureless Ohmic environments typical from extended bulk condensed matter systems, non-Ohmic and highly structured environmental spectral densities arise in finite size systems, such as, for instance, molecular systems. The peaks in $J(\omega)$ characterize distinct molecular vibrational modes at particular frequencies. One can include such sharp molecular modes in the environmental spectral density via δ -peaks at the mode frequencies. The consequence for the correlation properties is immediately clear by considering a single vibrational mode at frequency $\Omega > 0$ such that $J_\Omega(\omega) \propto \delta(\omega - \Omega)$. For temperatures $k_B T \ll \hbar\Omega$, pertinent oscillatory correlations are generated according to $L(t) \propto e^{-i\Omega t}$, which follows from Eq. (2.2.11). If a finite linewidth γ is associated to this vibrational mode, the oscillatory correlations decay exponentially with time according to $L(t) \propto e^{-i\Omega t - \gamma t}$ [31]. When these vibrational lifetimes are of the order of the system time scale, all bath-induced memory effects live on a comparable time scale and a Markovian approximation no longer can be made a priori for such a highly structured environmental spectrum [31]. The fluctuational spectrum of actual molecules is highly structured with many prominent vibrational peaks which induce a complicated pattern of several vibrational oscillatory correlations with long lifetime, and therefore, the Markovian approximation is even more questionable.

The description of a system given by the quantum Langevin equation [Eq. (2.2.5)] is exact for harmonic systems, but deteriorates for nearly harmonic ones, being unreliable when the anharmonicity of the potential is of crucial importance like, for instance, in quantum tunneling [1]. A more general description is given by the path integral formulation, where all relevant environmental effects are contained in an influence functional that depends on the bath spectral properties and on the temperature.

2.2.1 Path integral formulation

An alternative way to specify the state of a system is in terms of the density matrix $\hat{\rho}(t) = |\psi(t)\rangle\langle\psi(t)| = U(t, 0)|\psi(0)\rangle\langle\psi(0)|U^\dagger(t, 0) = U(t, 0)\hat{\rho}(0)U^\dagger(t, 0)$.

The dynamics of the quantum system of interest within the bipartite system-bath is described in terms of the time evolution of the reduced density matrix $\rho(t)$ which is obtained after tracing out the bath degrees of freedom. In position representation, $\rho(t)$ is then given by

$$\rho(t) = \text{tr}_B \langle x | e^{-iHt/\hbar} \hat{\rho}(0) e^{iHt/\hbar} | x' \rangle, \quad (2.2.12)$$

where H is the full system-plus-bath Hamiltonian in Eq. (2.2.1) and $\hat{\rho}(0)$ is the density operator of the entire system-plus-bath at initial time $t = 0$. In order to specify $\hat{\rho}(0)$, the system and bath are assumed to be initially decoupled and initial correlations between them are neglected. Alternatively, it can be thought as if the interaction between the system and bath is switched on at $t = 0$. This results in a factorized initial state of the form $\hat{\rho}(0) = \rho(0) \otimes \rho_B$, where $\rho(0)$ is the density operator of the system at initial time $t = 0$, and $\rho_B = Z_B^{-1} \exp(-H_B/k_B T)$ is the canonical equilibrium distribution of the bath at temperature T , with $Z_B = \text{tr} \exp(-H_B/k_B T)$ being the partition function of the bath.

A physically motivated reference to discretize the time-evolution operator in Eq. (2.2.12) is obtained by partitioning the full system-plus-bath Hamiltonian in Eq. (2.2.1) into an adiabatic reference given by

$$H_0 = \frac{p_x^2}{2m} + V(x), \quad (2.2.13)$$

and a bath of harmonic oscillators given by

$$H_{\text{env}} = H - H_0 = \sum_j \left[\frac{p_j^2}{2m_j} + \frac{m_j \omega_j^2}{2} \left(q_j - \frac{c_j x}{m_j \omega_j^2} \right)^2 \right] = \sum_j H_j. \quad (2.2.14)$$

The adiabatic reference H_0 includes the potential along the adiabatic path given by $q_j = c_j x / m_j \omega_j^2$ [Eq. (2.2.3)], which is the one-dimensional path that minimizes the total potential energy at each fixed value of the system coordinate as shown in Eq. (2.2.4). Meanwhile, the harmonic potential of each bath oscillator in Eq. (2.2.14) is centered at the point of minimum energy for each value of the system coordinate, i.e., their equilibrium positions are adiabatically displaced along the system coordinate [22, 23].

The total propagation time t is divided into N time slices of length δt such that $t_k = k\delta t$. It is assumed a symmetric splitting of the time evolution operator based on the adiabatic partitioning of the system-bath Hamiltonian, such that $e^{-iH\delta t/\hbar} \approx e^{-iH_{\text{env}}\delta t/2\hbar} e^{-iH_0\delta t/\hbar} e^{-iH_{\text{env}}\delta t/2\hbar}$. This splitting introduces an error of the order $[H_{\text{env}}, [H_0, H_{\text{env}}]]\delta t^3$ that vanishes if $\delta t \rightarrow 0$. The resulting short-time quasi-

adiabatic propagator in position representation is given by

$$\begin{aligned} \langle x_k \mathbf{q}_k | e^{-iH\delta t/\hbar} | x_{k-1} \mathbf{q}_{k-1} \rangle &\approx \langle x_k | e^{-iH_0\delta t/\hbar} | x_{k-1} \rangle \\ &\times \prod_{j=1}^N \langle q_{j,k} | e^{-iH_j(x_k)\delta t/2\hbar} e^{-iH_j(x_{k-1})\delta t/2\hbar} | q_{j,k-1} \rangle. \end{aligned} \quad (2.2.15)$$

The propagator of the adiabatic reference is calculated by solving the Schrödinger equation numerically using, for example, the Runge-Kutta scheme with adaptive step-size control [32]. By using the factorized initial state of $\hat{\rho}(0)$, Eq. (2.2.12) can be explicitly written as the quasi-adiabatic propagator path integral (QUAPI)

$$\begin{aligned} \rho(x, x'; t) &= \int dx_0^+ \int dx_1^+ \cdots \int dx_{N-1}^+ \int dx_0^- \int dx_1^- \cdots \int dx_{N-1}^- \\ &\times \langle x_N^+ | e^{-iH_0\delta t/\hbar} | x_{N-1}^+ \rangle \cdots \langle x_1^+ | e^{-iH_0\delta t/\hbar} | x_0^+ \rangle \\ &\times \langle x_0^+ | \rho(0) | x_0^- \rangle \\ &\times \langle x_0^- | e^{iH_0\delta t/\hbar} | x_1^- \rangle \cdots \langle x_{N-1}^- | e^{iH_0\delta t/\hbar} | x_N^- \rangle \\ &\times \mathcal{I}(\{x_k^+, x_k^-\}; \delta t). \end{aligned} \quad (2.2.16)$$

\mathcal{I} is the discretized influence functional

$$\mathcal{I}(\{x_k^+, x_k^-\}; \delta t) = \exp \left\{ -\frac{1}{\hbar} \sum_{k=0}^N \sum_{k'=0}^k [x_k^+ - x_k^-] [\eta_{kk'} x_{k'}^+ - \eta_{kk'}^* x_{k'}^-] \right\}, \quad (2.2.17)$$

where $\{x_0^+, x_1^+, \dots, x_N^+ = x\}$ and $\{x_0^-, x_1^-, \dots, x_N^- = x'\}$ denote discretizations of the forward and backward paths. These consist of constant segments $x^\pm(t) = x_k^\pm$ within the time interval $t_k - \delta t/2 < t < t_k + \delta t/2$. The superscript $*$ denotes the complex conjugate. The coefficients $\eta_{kk'}$ depend only on the difference $\Delta k = k - k'$ if $k, k' \neq 0, N$, i.e., on the time difference $t_k - t_{k'}$. Their explicit form can be found in Refs. [22, 23, 28]. The role of the influence functional $\mathcal{I}(x_k^+, x_k^-)$ in the quasi-adiabatic propagator path integral [Eq. (2.2.16)] is to include multidimensional nonadiabatic corrections to the exact dynamics along the adiabatic paths x_k^\pm , which results in a non-Markovian dynamics [22].

The influence functional in Eq. (2.2.17) is the discretized form of the general expression [33]

$$\begin{aligned} \mathcal{I}(x_k^+, x_k^-) &= \\ &\exp \left\{ -\frac{1}{\hbar} \int_0^t dt' \int_0^{t'} dt'' [x^+(t') - x^-(t')] [L(t' - t'')x^+(t'') - L^*(t' - t'')x^-(t'')] \right\} \\ &\times \exp \left\{ -\frac{i}{2\hbar} \int_0^t dt' \sum_j \frac{c_j}{m_j \omega_j^2} [x^+(t')^2 - x^-(t')^2] \right\}. \end{aligned} \quad (2.2.18)$$

It results from using the general path-integral expression in Eq. (2.1.1) to calculate $\rho(t)$ in Eq. (2.2.12) by partitioning the full system-plus-bath Hamiltonian in Eq. (2.2.1) into H_0 and H_{env} and performing the path-integral over the bath coordinates. $\mathcal{I}(x_k^+, x_k^-)$ in Eq. (2.2.18) is a functional of the system coordinates x^+ and x^- only, with $L(t)$ being the bath autocorrelation function in Eq. (2.2.11). The sum in the last term of Eq. (2.2.18) can be transformed into a continuous integral, which allows one to define an integral kernel in the continuous limit as [34, 35]

$$\eta(t) = L(t) + i\delta(t)\frac{2}{\pi} \int_0^\infty \frac{J(\omega)}{\omega} d\omega. \quad (2.2.19)$$

The influence functional can then be written as

$$\mathcal{I}(x_k^+, x_k^-) = \exp \left\{ -\frac{1}{\hbar} \int_0^t dt' \int_0^{t'} dt'' [x^+(t') - x^-(t')] [\eta(t' - t'')x^+(t'') - \eta^*(t' - t'')x^-(t'')] \right\}, \quad (2.2.20)$$

which is directly comparable with the discretized form in Eq. (2.2.17).

The structure of $\mathcal{I}(x_k^+, x_k^-)$ indicates interactions between path integral variables that may be separated by many time steps [6]. This non-local character of the temporal interactions arises from the η coefficients, which are essentially discretized versions of the bath autocorrelation function $L(t)$ as seen from Eq. (2.2.19). However, since the bath correlations have a finite range if the environment is described by a smooth continuous spectrum at finite temperature [see discussion following Eq. (2.2.11)], the nonlocality of the influence functional spans only finite intervals and the resulting dynamics is non-Markovian though of finite memory, i.e., the magnitude of the coefficients $\eta_{kk'}$ decreases as $|k - k'|$ increases. This feature arises from destructive phase interference due to the large number of environmental degrees of freedom, resulting in disruption of quantum phase coherence and in loss of memory of initial conditions after sufficiently long time. The path integral in Eq. (2.2.16) can then be broken into multiple integrals of finite dimension [22, 23]. This is done by neglecting in Eq. (2.2.17) those $\eta_{kk'}$ for which $|k - k'|$ is greater than a certain value K , which defines the memory time $\tau = K\delta t$ as the time range over which the bath autocorrelation function given in Eq. (2.2.11) is significantly different from zero, and therefore, $L(t)$ is approximated as zero for $t > \tau$. The approximated influence functional then reads [28]

$$\mathcal{I}(\{x_k^+, x_k^-\}; \delta t) \approx \prod_{k=0}^N \prod_{k'=0}^{\min\{N, K\}} \exp \left\{ -\frac{1}{\hbar} [x_k^+ - x_k^-] [\eta_{kk'} x_{k'}^+ - \eta_{kk'}^* x_{k'}^-] \right\}. \quad (2.2.21)$$

By inserting this truncated influence functional in Eq. (2.2.16) and reordering the integrals, the so-called *tensor multiplication scheme* is obtained, which involves

products of multi-dimensional arrays in analogy with matrix-vector multiplication schemes. It reads

$$\rho(x, x'; t) = A_N(\{x_k^\pm\}; t) \exp \left\{ -\frac{1}{\hbar} [x_N^+ - x_N^-] [\eta_{NN} x_N^+ - \eta_{NN}^* x_N^-] \right\}, \quad (2.2.22)$$

where the reduced density tensor A_k is calculated iteratively as

$$\begin{aligned} A_{k+1}(x_{k+1}^\pm, \dots, x_{k+K}^\pm; (k+1)\delta t) &= \int dx_k^\pm \Lambda_k(x_k^\pm, \dots, x_{k+K}^\pm) \\ &\times A_k(x_k^\pm, \dots, x_{k+K-1}^\pm; k\delta t), \end{aligned} \quad (2.2.23)$$

by propagating through a time increment δt with the propagator tensor Λ_k

$$\begin{aligned} \Lambda_k(x_k^\pm, \dots, x_{k+K}^\pm) &= \langle x_{k+1}^+ | e^{-iH_0\delta t/\hbar} | x_k^+ \rangle \langle x_k^- | e^{iH_0\delta t/\hbar} | x_{k+1}^- \rangle \\ &\times \prod_{k'=0}^K \exp \left\{ -\frac{1}{\hbar} [x_k^+ - x_k^-] [\eta_{kk'} x_{k'}^+ - \eta_{kk'}^* x_{k'}^-] \right\}, \end{aligned} \quad (2.2.24)$$

and with the initial condition

$$A_0(x_0^\pm, \dots, x_{K-1}^\pm; 0) = \langle x_0^+ | \rho(0) | x_0^- \rangle. \quad (2.2.25)$$

Observe that the rank of the tensors A_k and Λ_k is primarily related to the number of time steps K necessary to span the memory of the influence functional. The tensor multiplication scheme consists then in the multiplication of an augmented rank- K reduced density tensor A_k by a rank- $2K$ propagator tensor Λ_k .

In order to implement this scheme, storage requirements should be considered, which depend on the rank and on the dimension of the involved tensors, in particular, the propagator tensor. Its dimension is determined by the number of quadrature points required for each integration in the path integral in Eq. (2.2.24) and therefore, an efficient system-specific integration grid is required. Such a quadrature, is constructed from the eigenstates $|\phi\rangle$ of the adiabatically renormalized system Hamiltonian H_0 in Eq. (2.2.13). Because systems at finite temperatures are considered, it is enough to consider the M lowest energy eigenstates, such that the system dynamics occurs within this M -dimensional Hilbert sub-space. The basis set for the integration grid is obtained by performing a unitary transformation on the basis $\{\phi_i\}$ of the M lowest energy eigenstates of H_0 as

$$|u_i\rangle = \sum_{i'=1}^M R_{ii'} |\phi_{i'}\rangle, \quad (2.2.26)$$

where $R_{ii'}$ is the orthogonal transformation matrix and by requiring that the system position operator x be diagonal such that

$$\langle u_i | x | u_{i'} \rangle = s_i \delta_{ii'}. \quad (2.2.27)$$

The states $\{u_i\}$ form the so-called discrete variable representation (DVR) and the eigenvalues $\{s_i, \dots, s_M\}$ form the DVR integration grid. These DVR-states are localized in position space at the eigenvalues s_i of the position operator. Using the DVR-basis the completeness relation for the system coordinate now reads [23]

$$\int_{-\infty}^{\infty} dx_k^{\pm} |x_k^{\pm}\rangle \langle x_k^{\pm}| \rightarrow \sum_{i_k^{\pm}=1}^M |u_{i_k^{\pm}}\rangle \langle u_{i_k^{\pm}}|. \quad (2.2.28)$$

This allows one to express the tensor multiplication scheme in the DVR-basis as

$$\rho(s, s'; t) = A_N^{\text{DVR}} \left(\left\{ s_{i_k^{\pm}} \right\}; t \right) \exp \left\{ -\frac{1}{\hbar} \left[s_{i_N^+} - s_{i_N^-} \right] \left[\eta_{NN} s_{i_N^+} - \eta_{NN}^* s_{i_N^-} \right] \right\}. \quad (2.2.29)$$

The reduced density tensor is

$$\begin{aligned} A_{k+1}^{\text{DVR}}(s_{i_{k+1}^{\pm}}, \dots, s_{i_{k+K}^{\pm}}; (k+1)\delta t) &= \sum_{i_k^{\pm}=1}^M \Lambda_k^{\text{DVR}}(s_{i_k^{\pm}}, \dots, s_{i_{k+K}^{\pm}}) \\ &\times A_k^{\text{DVR}}(s_{i_k^{\pm}}, \dots, s_{i_{k+K-1}^{\pm}}; k\delta t), \end{aligned} \quad (2.2.30)$$

the propagator tensor is given by

$$\begin{aligned} \Lambda_k^{\text{DVR}}(s_{i_k^{\pm}}, \dots, s_{i_{k+K}^{\pm}}) &= \langle u_{i_{k+1}^+} | e^{-iH_0\delta t/\hbar} | u_{i_k^+} \rangle \langle u_{i_k^-} | e^{iH_0\delta t/\hbar} | u_{i_{k+1}^-} \rangle \\ &\times \prod_{k'=0}^K \exp \left\{ -\frac{1}{\hbar} \left[s_{i_k^+} - s_{i_k^-} \right] \left[\eta_{kk'} s_{i_{k'}^+} - \eta_{kk'}^* s_{i_{k'}^-} \right] \right\}, \end{aligned} \quad (2.2.31)$$

and the initial condition is

$$A_0^{\text{DVR}}(i_0^{\pm}, \dots, i_{K-1}^{\pm}; 0) = \langle u_{i_0^+} | \rho(0) | u_{i_0^-} \rangle. \quad (2.2.32)$$

Within the discrete variable representation, the tensor multiplication scheme can be interpreted as the multiplication of the vector A_k of dimension M^{2K} by the matrix Λ_k of dimension M^{2K+2} .

The implementation of the iterative scheme in Eqs. (2.2.29)-(2.2.32) requires to consider three parameters: (i) the finite step δt in the symmetric Trotter splitting of the short-time propagator [Eq. (2.2.15)]. It should be as small as possible in order to reduce the introduced Trotter error that is of the order of δt^3 . (ii) Moreover, the number of time steps K required to span the width of the bath autocorrelation function $L(t)$ in Eq. (2.2.11) should be as large as possible in order to make the memory time τ large and therefore include all non-local correlations in Eq. (2.2.21). In spite the opposite requirements for both parameters, it is normally possible to

find an optimal parameter combination where the quantities of interest are least sensitive to the variation of δt , known as the principle of minimal sensitivity [36]. The Trotter error and the error due to the finite memory are extrapolated to zero in a systematic way [35]. (iii) Finally, the M -dimensional Hilbert sub-space where the system dynamics takes place together with K determines the size of the reduced density and propagator tensors. In the low temperature limit, only a few energy eigenstates are populated and therefore M is small. However, the non-local correlations of the bath are longer-lived and K should be large. In the opposite high temperature limit, more eigenstates are populated, requiring larger M , but the bath correlations decay faster and therefore K can be smaller. This dependence is particularly important in spatially continuous systems. It has been shown that they can be described reasonably well by taking only a few basis states and a finite memory length into account [35]. For the finite-size systems evaluated in this work, a fixed parameter of $M = 2, 7$, and 8 is used in Parts I, II, and III, respectively. Results in Chap. 9 require the use of larger M values.

2.2.2 Extended QUAPI scheme

The influence functional in Eq. (2.2.17) contains the entire influence of a *single* bath coupled via the operator x to the quantum system of interest [Eq. (2.2.1)]. Certain physical systems however, like biological molecules, contain chromophores separated by several Å, embedded in different local environments and therefore under the influence of different baths. In such a case an extended QUAPI scheme has been developed to include multiple baths [37].

The effect caused by the environmental fluctuations will depend on whether they act locally or in a correlated manner. If multiple *independent baths*, H_B^α , couple to system operators x_α , they will simply result in a product of influence functionals, since each bath acts separately. Thus, the total influence functional assumes the form

$$\mathcal{I}(\{x_{k,\alpha}^+, x_{k,\alpha}^-\}; \delta t) = \exp \left\{ -\frac{1}{\hbar} \sum_{\alpha} \sum_{k=0}^N \sum_{k'=0}^k [x_{k,\alpha}^+ - x_{k,\alpha}^-] \left[\eta_{kk'}^{(\alpha\alpha)} x_{k',\alpha}^+ - \eta_{kk'}^{*(\alpha\alpha)} x_{k',\alpha}^- \right] \right\}, \quad (2.2.33)$$

where the additional superscripts in the coefficients $\eta_{kk'}^{(\alpha\alpha)}$ indicate that the autocorrelation function of the particular baths will, in general, differ from each other. On the other hand, if the fluctuations caused by several different baths are no longer independent, *spatial correlations* can be taken into account by generalizing Eq. (2.2.33)

as

$$\mathcal{I}(\{x_{k,\alpha}^+, x_{k,\beta}^-\}; \delta t) = \exp \left\{ -\frac{1}{\hbar} \sum_{\alpha,\beta} \sum_{k=0}^N \sum_{k'=0}^k [x_{k,\alpha}^+ - x_{k,\alpha}^-] \left[\eta_{kk'}^{(\alpha\beta)} x_{k',\beta}^+ - \eta_{kk'}^{*(\alpha\beta)} x_{k',\beta}^- \right] \right\}, \quad (2.2.34)$$

where $\eta_{kk'}^{(\alpha\beta)}$ indicates correlations of the fluctuations acting at operators x_α and x_β .

The tensor multiplication scheme can still be obtained for the multiple baths situation though the explicit expressions are more involved.

In summary, the iterative QUAPI scheme is a deterministic summation of the path integral that provides numerically exact results for the long time dynamics of quantum systems in dissipative environments. It rests on the intrinsic properties of the dissipative influence functional without making any ad hoc assumptions, and therefore including all non-Markovian (non-local) effects exactly, allowing one to treat nearly arbitrary spectral functions at finite temperatures. The quantum dynamics of many diverse open quantum systems has been obtained by using this scheme in its original version [30, 31, 34, 35, 38, 39, 40, 41, 42] and in its extended version [37, 43, 44, 45].

2.3 Quantification of non-Markovian effects

The iterative QUAPI scheme, presented in the last section, is numerically exact in the sense that all non-Markovian effects (within the time span τ) are included, but for the same reason, the practical implementation demands large computational resources in order to deal with the M^{2K+2} -dimensional arrays. It is then useful to quantify the importance of such non-Markovian effects in the system dynamics. If they are important, numerically exact methods are absolutely necessary. The reason being that even at very weak coupling, multiphonon processes dominate the decoherence dynamics in the presence of non-Markovian effects. This is not captured by lowest-order perturbative treatments, such as Redfield or Lindblad approaches [7]. However, if non-Markovian effects are not relevant, the Markovian approximation can be applied in order to obtain a Markovian quantum master equation to describe the system dynamics, which is much cheaper to implement computationally. In this section, a non-Markovianity measure based on the physical features of the interaction between the system and its environment is presented.

In an open quantum system, the evolution of any two initial states $\rho_{1,2}(0)$ is given by a family of trace-preserving and completely positive quantum dynamical maps $\Phi(t, 0)$ such that $\rho_{1,2}(t) = \Phi(t, 0)\rho_{1,2}(0)$. These two quantum states can be

distinguished in terms of the trace distance, which provides a metric in the space of physical states [46]. The dynamical change of the distinguishability of the states of an open quantum system can be interpreted in terms of information exchange between the system and its environment [46]. In a Markovian process, there is an infinitesimally small correlation time between the system and environment dynamics, which leads to a monotonic flow of information from the system to the environment. However, in a non-Markovian process the long lived correlations may generate a backflow of information from the environment to the system and memory effects can then occur. In order to quantify the degree of non-Markovianity during the quantum evolution, several non-Markovianity measurements have been recently proposed [47, 48, 49] based on different mathematical and physical concepts. For example, the non-Markovianity measure in Ref. [47] is rooted in the mathematical property of the dynamical map that generates the quantum time evolution, i.e., the deviation from divisibility of the trace-preserving completely positive map characteristic of a Markovian process. Similarly, the non-Markovianity measure in Ref. [48] is based on time snapshots of the dynamical map. On the other hand, the non-Markovianity measure in Ref. [49] is based on the physical features of the system-bath interaction in terms of information backflow from the environment to the system, which has been experimentally measured [50, 51]. This last measure is therefore used to quantify non-Markovian effects during the dynamics of the different systems studied in this work.

More precisely, the measure in Ref. [47] quantifies the dynamics of entanglement of a maximally entangled state between the open system (in contact with the environment) and an isomorphic auxiliary system (shielded from the environment). If there is no knowledge of the dynamics, the non-Markovianity can be measured as a departure of the entanglement (between the open and the auxiliary systems by using any entanglement quantifier, see Ref. [52] for a review) from a monotonically decaying behavior expected due to the decrease of quantum correlations in a Markovian process. On the other hand, if there is a complete knowledge about the dynamics, the non-Markovianity is given by the departure of the trace-preserving map from the divisibility property for a Markovian evolution given by $\Phi(t, 0) = \Phi(t, t')\Phi(t', 0)$ for all $t \geq t' \geq 0$. In contrast, the non-Markovianity measure in Ref. [49] quantifies the reversed flow of information from the environment back to the system. In general, these measures yield different results [53, 54, 55, 56, 57]. However, any process that is non-Markovian according to Ref. [49], is also non-Markovian according to Ref. [47], while the converse is not always true. The reason for this is that the conditions for information backflow are much more rigorous than those for indivisibility. Consequently, information backflow causes the indivisibility of the dynamics,

but the reverse is not always true [55, 56, 57].

The information exchange between the system and its environment can be quantified through the dynamics of the trace distance between a pair of quantum states ρ_1 and ρ_2 of the open system. This is defined as [3]

$$D(\rho_1, \rho_2) = \frac{1}{2} \text{tr} |\rho_1 - \rho_2|, \quad (2.3.1)$$

where $|O| = \sqrt{O^\dagger O}$. The trace distance can be interpreted as a measure of the distinguishability of states ρ_1 and ρ_2 , satisfying $0 \leq D \leq 1$ [49]. For open quantum systems, the trace distance of the states $\rho_{1,2}(t)$ [evolving under the dynamical map $\Phi(t)$] is a monotonically decreasing function of time, i.e., $D(\Phi\rho_1, \Phi\rho_2) \leq D(\rho_1, \rho_2)$. This means that the distinguishability of any two states always decreases. In general, under a Markovian evolution, any two initial states become less and less distinguishable as time increases. This can be interpreted as an unidirectional flow of information from the system to the environment, which continuously reduces the possibility of distinguishing the given states [49].

If the rate of change of the trace distance is defined as

$$\sigma(t, \rho_{1,2}(0)) = \frac{d}{dt} D(\rho_1(t), \rho_2(t)), \quad (2.3.2)$$

which depends on the specific initial states $\rho_{1,2}(0)$, a Markovian evolution implies that $\sigma \leq 0$ for all quantum processes. Conversely, a process is said to be non-Markovian if it satisfies $\sigma > 0$. In the latter case, the distinguishability of the pair of states increases at certain times by a backflow of information from the environment to the system. The non-Markovianity measure [of the quantum process $\Phi(t)$] quantifies the total increase of the distinguishability over the whole time evolution, i.e., the *total* amount of information that flows from the environment back to the system as

$$\mathcal{N}(\Phi) = \max_{\rho_{1,2}(0)} \int_{\sigma > 0} \sigma(t, \rho_{1,2}(0)) dt. \quad (2.3.3)$$

Here, the time integration extends over all time intervals (a_i, b_i) in which $\sigma > 0$, and the maximum is taken over all pairs of initial states [49, 58]. Therefore, $\mathcal{N}(\Phi)$ represents a functional of the family of dynamical maps $\Phi(t)$ describing the physical process [59].

The non-Markovianity measure $\mathcal{N}(\Phi)$ has been used to quantify non-Markovian effects during the quantum evolution of driven systems [53], the spin-boson model [59], biomolecular dimers [60], molecular charge qubits [42], the full Fenna-Matthews-Olson complex [45], initially correlated system-bath models [61, 62], and others [63, 64, 65, 66, 67]. Very recently, $\mathcal{N}(\Phi)$ has been measured experimentally for the

polarization states of photons acting as system states, coupled to the photon frequency modes acting as environmental states. In this setup, the polarization and frequency degrees of freedom are coupled in a quartz plate in which different evolution times are realized by varying the thickness of the plate [50]. Non-Markovian dynamics has been induced by controlling the initial state of the environment [50] or by modifying the interaction between the system and the environment [51]. These results demonstrate that this particular measure provides an experimentally accessible observable which quantifies memory effects [46].

This measure requires only local control and measurements of the open quantum system, therefore, in order to quantify the non-Markovianity of the quantum evolution via Eq. (2.3.3), the explicit system dynamics is needed. This is given by the time evolution of the reduced density matrix $\rho(t)$ obtained after tracing out the bath degrees of freedom as indicated in Eq. (2.2.12), and, in this work, is calculated by using the iterative QUAPI scheme presented in the last section.

Using the non-Markovianity quantifier, Eq. (2.3.3), one can evaluate the existence of non-Markovian effects during the system evolution and also the degree of non-Markovianity, i.e., how strongly its dynamics deviates from a Markovian one. The maximization procedure over all pairs of initial states in Eq. (2.3.3) is important in order to quantify the degree of non-Markovianity. In this work, the existence of non-Markovian effects is evaluated, therefore, the maximization procedure is not carried out. Besides, it has been shown [54, 57] that often this maximization can be removed without influencing the sensibility of the measure in finite-dimensional physical systems, which usually can only be prepared in specific initial states. For example, localized states in a double quantum dot or particular chromophores of photosynthetic complexes. By using this argument and Eq. (2.3.2), it is possible to write the non-Markovianity measurement in the form

$$\mathcal{N} = \sum_i [D(\rho_1(b_i), \rho_2(b_i)) - D(\rho_1(a_i), \rho_2(a_i))], \quad (2.3.4)$$

with the sum running over all time intervals (a_i, b_i) during which the trace distance increases, thus integrating over all time spans of growing distinguishability. Following Ref. [54], these time intervals on which the trace distance increases can be called ‘non-Markovian intervals’.

Part I

Tailored molecular systems: π -conjugated copolymers

Organic π -conjugated block copolymers

Information is recognized as a physical quantity, with its representation and processing being governed by the laws of quantum mechanics [3, 68]. In order for information to be processed, it must be represented as a certain physical entity, which allows it to be transmitted from one place to another, to interact with other pieces of information and to be subjected to controlled operations. In a quantum computer, information is represented using the quantum states of a general entity called qubit [3], which is a quantum two level system (TLS) represented by a pair of orthonormal quantum states. Many microscopic systems can be used as qubits [2, 3, 4, 69], however, a successful realization of a quantum computing architecture requires that fundamental criteria, like scalability and long coherence time, be fulfilled [70]. Solid-state based nanostructures are highly promising candidates for the realization of quantum information processing devices, exhibiting a particularly high degree of scalability. Semiconductor systems, in particular, offer the possibility of integration with current technologies. Several degrees of freedom can be exploited in semiconductor nanostructures. Exciton-based qubits [71] allow optical control but are intrinsically limited by the lifetime of the exciton. Spin qubits [72, 73, 74] have long coherence times [75, 76], but information access is often difficult. Charge qubits [77, 78] allow easier coupling to electric fields but, for the same reason, suffer from rapid decoherence.

When growing semiconductor heterostructures, the properties of the charge carriers are controlled via band engineering [79, 80]. The design principles can be trans-

ferred to molecular systems to design molecular heterostructures with π -conjugated oligomers [81]. The discovery of metallic conduction in organic π -conjugated polymers under doping conditions [82, 83, 84, 85, 86], opened the way for the design and synthesis of organic systems with tailored electronic properties. In their undoped form, conjugated polymers are intrinsically semiconductors [87, 88, 89, 90] which uniquely combine the electronic properties of semiconductors with the typical properties of plastics as low cost, versatility of chemical synthesis, ease of processing and flexibility, allowing them to replace their inorganic counterparts in many applications [91, 92].

In conjugated polymers, π molecular orbitals (MOs) are formed from the overlap of pure p atomic orbital (AOs) perpendicular to the molecular plane belonging to adjacent carbon atoms (see Fig. 3.1). Hence, these MOs are delocalized along the molecular chain, and therefore the charge carriers exhibit great mobility and polarizability. In the limit of an infinite polymeric chain, the energies of the π -MOs cluster together in π -bands, which are responsible for the electronic and optical properties for these materials [90]. The band gap is calculated as the energy differ-

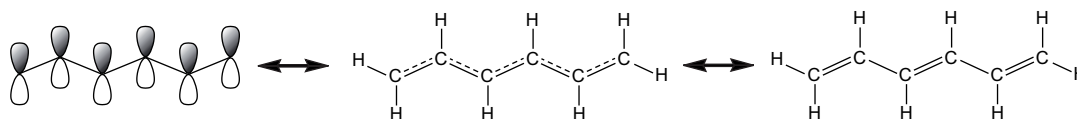


Figure 3.1: Schematic view of the formation of a π -MO in *trans*-polyacetylene.

ence between the top of the valence band and the bottom of the conduction band, which, in polymeric systems, are given by the energies of the highest occupied and lowest unoccupied MOs, respectively, i.e., the frontier MOs HOMO and LUMO, such that $E_{\text{gap}} = E_{\text{LUMO}} - E_{\text{HOMO}}$. In Fig. 3.2 are shown the frontier MOs and the molecular structure of the unit cell of different semiconducting π -conjugated polymers, where PA, PDA, PPP, *l*-PPP, *p*-saturated acene, Th, Py, and furan refer to *trans*-polyacetylene, poly-diacetylene, poly-(*p*-phenylene), ladder-type poly-(*p*-phenylene), poly-acene saturated in the *para*-positions, poly-thiophene, poly-pyrrol, and poly-furan, respectively. Observe that one-dimensional systems like PA or PDA have the smallest band gap. Meanwhile quasi-one-dimensional or ladder-type systems like PPP or *l*-PPP present a larger band gap due to the spreading of π -electron density in the perpendicular direction. On the other hand, heterocyclic systems (Th, Py, and furan) have larger band gaps due to the localization of π -electron density induced by the more electronegative heteroatom (S, N, and O, respectively). Insulator behavior is obtained when the π -electrons are localized by saturation, as it is the case in *p*-saturated acene. The E_{gap} value depends not only on the specific chemical

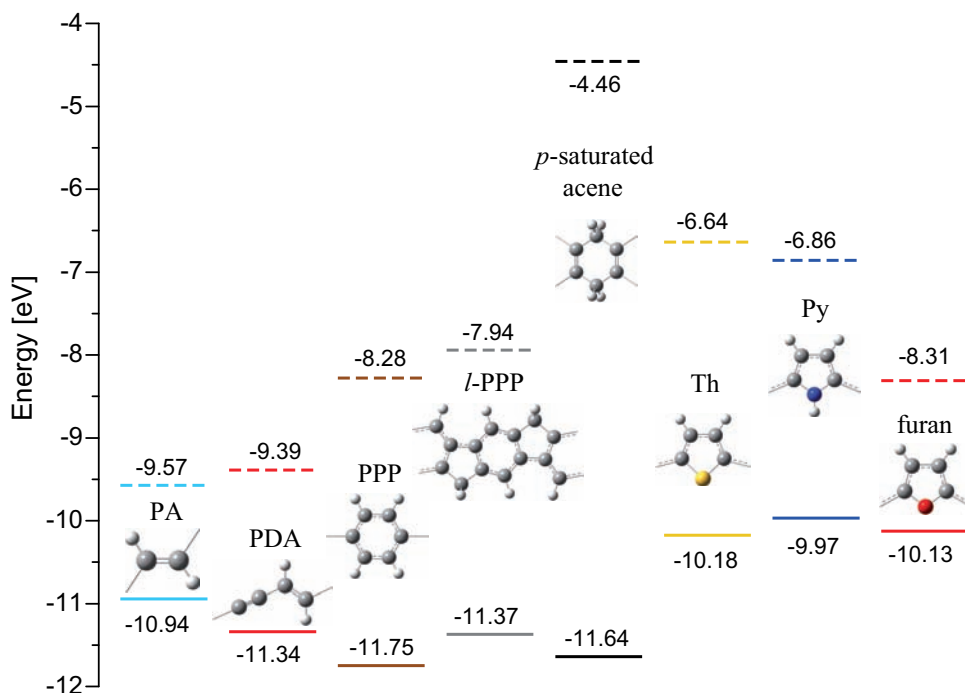


Figure 3.2: Alignment of the frontier MOs and molecular structure of the unit cell for different π -conjugated polymers. Solid lines: HOMOs, dashed lines: LUMOs. Gray, white, yellow, blue, and red spheres represent carbon, hydrogen, sulfur, nitrogen, and oxygen atoms, respectively. See text for details. MOs energies calculated with the extended Hückel method as specified in Appendix C.

structure of the system, but also on chemical substitution [93]. In fact, *l*-PPP can be thought as a chemically modified PPP with molecular cross-tie linkers in the form of methylene bridges between the ortho positions of adjacent phenyl rings, which does not modify substantially its electronic structure but avoids the twisting of the phenyl rings, leading to a stiff system [94].

The alignment of the frontier MOs in π -conjugated polymers shown in Fig. 3.2 suggests that it is possible to combine different oligomers to construct *molecular* heterostructures, in which, as in the case of inorganic superlattices, the charge carriers are confined in the growth direction of the heterostructure in a quantum well profile. The amount of quantized energy levels and their corresponding energy spacing depends on the length of the “well” and “barrier” regions [95]. An advantage of building heterostructures with π -conjugated oligomers is that the molecular energy scales involved are much larger than in their inorganic counterparts. Hence, temperature effects are negligible even at room temperature. In contrast, inorganic heterostructures require cryogenic temperatures due to the mesoscopic size.

Organic heterostructures do not suffer from interfacial stress since the heterojunction is a chemical carbon-carbon bond. They can be synthesized, for example, by “wet chemistry” methods [96, 97, 98], or using more refined strategies, like electrochemical polymerization [99, 100] or STM polymerization [101, 102]. This last technique gives long, highly regular, and well-separated polymer chains with a spatial precision on the order of 1 nm. Isolated micrometric PDA chains exhibit quantum spatial coherence limited only by the chain length [103]. Long coherence times (on the order of 250 fs) have been observed in poly[2-methoxy-5-(2'-ethyl-hexoxy)-1,4-phenylenevinylene] (MEH-PPV) chains in solution at room temperature [104, 105]. Here, electron-vibration coupling might play a role in preserving quantum coherences [106]. Moreover, individual ladder-type π -conjugated polymers [107] can be addressed spectroscopically and exhibit narrow spectral emission lines, weak interaction with the environment, and rather weak coupling to vibrational modes [108]. A molecular resonant-tunneling diode on the basis of a PDA/ZnPc/PDA molecular nanostructure (with ZnPc being a zinc phthalocyanine) has been suggested [109] which could operate in air at room temperature and carry negative charges. Furthermore, the spectral and electronic properties of π -conjugated copolymers have been shown to be remarkably resilient under structural variations [110]. They can carry Coulombically bound polaron pair spins which show surprisingly long phase coherence times up to several hundreds of nanoseconds at room temperature [111]. Moreover, they can be controlled by electrically detected spin echoes. Clear singlet-triplet spin Rabi oscillations have been reported as well [112].

In this part, molecular charge qubits from π -conjugated block copolymers are designed. In Chap. 4, the electronic energies are obtained from quantum chemical calculations and molecular double quantum dots (DQD) with energy splittings $\hbar\Delta > k_B T$ at room temperature are designed (Sec. 4.1). Furthermore, in Sec. 4.2 the vibrational spectrum is determined, i.e., the infrared (IR) active modes, which are believed to provide the dominant dephasing channel of the charge qubit. A tractable dynamical model is extracted in Sec. 4.3, where the fluctuational spectra and the coupling strength between the charge qubit and the IR fluctuations are determined. Varying the length of the oligomers allows one not only to engineer the electronic energies but also the fluctuation spectrum with the possibility to minimize dephasing. The dissipative dynamics in the presence of strongly non-Markovian IR fluctuations is calculated in Chap. 5 by means of the iterative QUAPI scheme presented in Sec. 2.2.1. A wide range of coherence times and quality factors at room temperature are found (Sec. 5.1). These molecular systems exhibit a strongly non-Markovian electronic dynamics as shown in Sec. 5.1.1 by using the non-Markovianity quantifier in Eq. (2.3.4). The population dynamics of the ex-

ternally driven systems presented in Sec. 5.2 can exhibit square-wave oscillations depending on the specific field parameters, allowing controlled transitions between the basis states of the charge qubit, analogous to single qubit gates.

Design of organic π -conjugated molecular charge qubits

4.1 Electronic structure

Type-I heterostructures [95, 113] of the form A/B/A generate a quantum well profile in the direction of growth, which in turn leads to a confinement of charge carriers in the B “well” region. In the case of molecular heterostructures, the carriers are confined in the three spatial directions, and therefore referred as quantum dots (QDs). Electrons within the conduction band or holes within the valence band can be confined by using several combinations of the π -conjugated polymers shown in Fig. 3.2. A charge qubit exploits the two possible locations of a single excess charge carrier (typically an electron, but a hole can be also used) in a DQD profile of the form A/B/A/B/A. The electron spin does not play a role. The two states are the lowest energy levels on each side of the DQD, with oscillations between the states caused by introducing a tunnel coupling $\hbar\Delta$ between the two states [114]. The same principle can be used to design organic molecular heterostructures from π -conjugated block copolymers such that two electronic states are spatially localized in separated regions of the molecule. Due to the relatively large offset of 1.45 eV in the conduction band, which offers an exceptional design versatility, the combination of *l*-PPP and PDA is chosen. A single unoccupied confined electronic state within the conduction band results from a molecular structure of *l*-PPP/PDA/*l*-PPP, thus

forming a QD. Two such QDs with a short barrier oligomer of *l*-PPP form the desired DQD. A charge qubit, with an excess electron localized in the left or right dot, is achieved by doping the molecule single negatively forming a polymeric radical anion. The resulting double well profile of the conduction band for a DQD structure *l*-PPP/PDA/*l*-PPP/PDA/*l*-PPP depicted in Fig. 4.1.

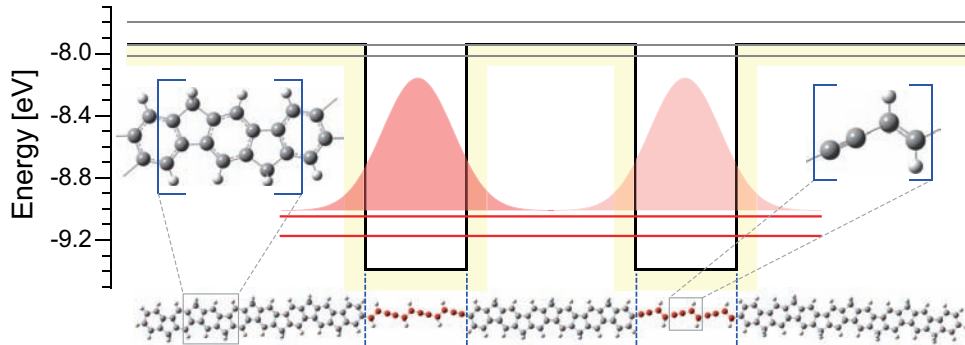


Figure 4.1: Molecular structure and potential energy profile for electrons within the conduction band for the symmetric DQD *l*-PPP₈/PDA₃/*l*-PPP₆/PDA₃/*l*-PPP₈. The two energy levels of the confined electronic states are indicated by the horizontal red lines. The wave functions are indicated schematically by the shaded red areas. Gray lines indicate delocalized states.

The electronic properties are determined by using a combination of the unrestricted¹ Austin model 1 (AM1) [115], as implemented in Ref. [116], for geometry optimizations (see Appendix B for details) with the extended Hückel method [117], as implemented in Ref. [118], for single-point electronic-structure calculations. The prefactor $\bar{K} = 2.43$ for the off-diagonal elements is used in extended Hückel calculations [81, 119] (see Appendix C for details).

A specific heterostructure is characterized by its energy splitting $\hbar\Delta$, which is the difference between the LUMO and LUMO+1 energy levels. These have been calculated after relaxation of the single negatively doped molecular structure. The energy splitting is controlled by the length of the PDA “well” oligomer and the center “barrier” oligomer *l*-PPP. Figure 4.2 shows $\hbar\Delta$ as a function of the well and barrier widths. The width of the lateral barriers is kept large enough to avoid edge effects in the confined energy levels due to the finite size of the molecule. As expected, a wider central *l*-PPP “barrier” reduces $\hbar\Delta$. Energy splittings on the order of hundreds of meV and thus from $\hbar\Delta \sim k_B T$ to $\hbar\Delta \gg k_B T$ at room temperature are found, which

¹The single excess electron in the doped molecule gives rise to an open shell system. See Appendix A for details.

reflects the design versatility for this particular combination of parent polymers.

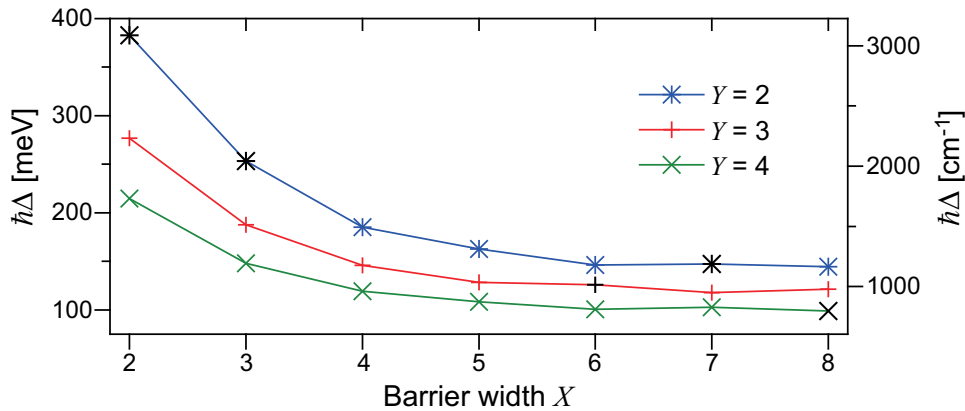


Figure 4.2: Splitting energy $\hbar\Delta = E_{\text{LUMO}+1} - E_{\text{LUMO}}$ as a function of the barrier X and well Y widths for the symmetric DQD $l\text{-PPP}_8/\text{PDA}_Y/l\text{-PPP}_X/\text{PDA}_Y/l\text{-PPP}_8$.

4.2 Vibrational states

Quantum information processing relies on long coherence times of the qubits. The charge qubit in the proposed setup will couple directly to electromagnetic fluctuations and thus also to the active IR vibrational excitations of the molecular structure. An example of the IR spectrum for the case $(X, Y) = (3, 2)$ calculated by the AM1 method² after including the molecular relaxation due to the single additional electron is shown in Fig. 4.3. All calculated frequencies have been multiplied by the scaling factor of 0.954 obtained from Ref. [120] (see Appendix B). The other cases yield similar spectra (see Appendix E). The modes in the IR spectrum can, roughly, be grouped according to their frequencies as: modes below and around 1000 cm^{-1} correspond to vibrations and rotations with twisting and wagging modes outside and scissoring and rocking modes inside the molecular plane. Meanwhile, stretching modes for aromatic and aliphatic carbon-carbon double bonds are observed around 1500 and 2200 cm^{-1} , respectively.

From the results in Fig. 4.3, it is evident that the splitting energy $\hbar\Delta$ covers the same range of energies as the IR modes. Engineering the molecular structure allows one to choose Δ in relation to the IR spectrum and thus to trim not only the electronic energy splitting of the charge qubit but also its damping behavior.

²The calculation of the vibrational frequencies must use the same method used to calculate the optimized geometry. See Appendix B for details.

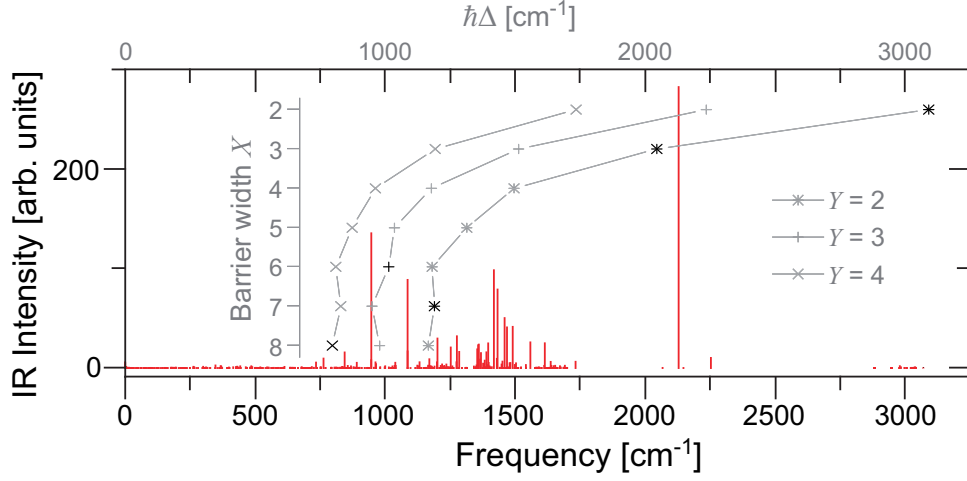


Figure 4.3: IR stick spectrum, shown as vertical red lines, of the molecular heterostructure l -PPP₈/PDA₂/ l -PPP₃/PDA₂/ l -PPP₈. The inset, in gray color, shows the results in Fig. 4.2.

Five molecular heterostructures are discussed, which have $N = 0, 1, 2, 3,$ and 4 main IR modes at energies below $\hbar\Delta_N$. These systems are marked in Figs. 4.2 and 4.3 by black symbols and their splitting energies are summarized in Table 4.1. The electronic transition energy of the chosen systems is always out of resonance with a vibrational transition and therefore, no pseudo-Jahn-Teller effect is expected [121].

N	(X, Y)	$\hbar\Delta_N$				Size [\AA]
		[meV]	[cm ⁻¹]	[fs]		
0	(8, 4)	98.8	797.0	6.66	137.6	
1	(6, 3)	125.7	1014.1	5.24	119.5	
2	(7, 2)	147.4	1188.8	4.47	113.7	
3	(3, 2)	253.3	2043.1	2.60	97.2	
4	(2, 2)	382.7	3086.9	1.72	93.0	

Table 4.1: Splitting energy $\hbar\Delta$ of the molecular heterostructure l -PPP₈/PDA _{Y} / l -PPP _{X} /PDA _{Y} / l -PPP₈ whose electronic dynamics is determined by $\hbar\Delta_N$ and influenced by N main vibrational bands. The size of the molecular systems refers to the total length of the molecule.

The first MOs within the conduction band of the Δ_N systems in Table 4.1 are shown in Appendix D. Figures D1-D5 show that only the energetic levels LUMO and LUMO+1 are localized, as indicated by the higher electron density in the PDA

“well” oligomer, meanwhile the levels LUMO+2 and LUMO+3 are mainly delocalized on the *l*-PPP “barrier” oligomer.

4.3 Modeling of molecular charge qubits

In order to calculate the dynamics of the charge qubit, its coupling to the IR active modes is treated within an open quantum system approach [1]. This results in the total Hamiltonian

$$H = H_S + H_B + H_{SB}, \quad (4.3.1)$$

where H_S is the system Hamiltonian, H_B is the bath Hamiltonian and H_{SB} is the system-bath coupling.

The electronic degrees of freedom are restricted to the two states $\{|L\rangle, |R\rangle\}$ forming the charge qubit, i.e., the localized states LUMO and LUMO+1 (spin effects are neglected). These two states are described by the quantum two-level Hamiltonian [8]

$$H_S = \frac{\hbar}{2} (\epsilon(t)\sigma_z - \Delta\sigma_x). \quad (4.3.2)$$

The term $\epsilon(t) = \epsilon_0 + \varepsilon(t)$ accounts for possible asymmetries. External electric fields couple to the charge position σ_z causing a time-dependent asymmetry $\varepsilon(t)$. Small static biases ϵ_0 may also arise due to the lacking point symmetry of the molecular structure. This results from electrostatic repulsion between hydrogen atoms across the heterojunction formed by the vinyl end of the PDA unit cell and the aromatic ring of the *l*-PPP unit cell, which breaks the planarity of the whole molecular heterostructure. This is evidenced in Figs. D1-D5 of Appendix D, where ϵ_0 increases with decreasing N in the Δ_N systems, then localizing the LUMO and LUMO+1 levels. In the following, this possibility is neglected for simplicity by setting $\epsilon_0 = 0$, since only small quantitative changes in the dynamical properties are expected.

In small molecules, like Betaine dye molecules, the intramolecular vibrational motions can have much greater effects on the total electronic coherence loss than environmental solvent molecules [122]. This is expected to be even more valid in large molecules, like the heterostructures in Table 4.1. Here, the vibrational modes of the whole polymeric molecule are formalized as the bosonic bath. Thus, the main source of decoherence would come from electron–vibration coupling effects. Within the harmonic approximation [29, 123], the vibrational modes are written as a bath of independent harmonic oscillators bilinearly coupled to the charge of the qubit,

resulting in

$$H_B + H_{SB} = \sum_i \hbar\omega_i a_i^\dagger a_i + \frac{\hbar}{2}\sigma_z \sum_i g_i (a_i + a_i^\dagger), \quad (4.3.3)$$

with bosonic creation and annihilation operators a_i^\dagger and a_i , oscillator frequency ω_i , and coupling constants g_i . The bath degrees of freedom are finally integrated out and the influence on the qubit dynamics is fully characterized by the spectral density $J(\omega) = (\pi/2) \sum_i g_i^2 \delta(\omega - \omega_i)$.

4.3.1 Fluctuational spectrum of molecular charge qubits

Using the AM1 method, a structured IR spectrum $\kappa(\omega) = \sum_i I_i \delta(\omega - \omega_i)$ with frequencies ω_i and intensities I_i is obtained (see Fig. 4.3). IR modes couple to the charge of the qubit in the same way as to external electric fields ($\propto \sigma_z$) and it is accordingly assumed that $J(\omega) = \kappa(\omega)$ and therefore, $I_i \equiv (\pi/2)g_i^2$.

Each peak in the IR spectrum is modeled by a Lorentzian [124] with width γ_i of the form $L_i(\omega) = \gamma_i / [(\omega - \omega_i)^2 + \gamma_i^2]$. Lorentzian profiles are typical for homogeneously broadened bands [125], and have been found in the structurally related poly-(*p*-phenylene-vinylene) polymer [126]. The widths are generated by the coupling of the IR modes to environmental charge fluctuations (from a solvent or substrate) which also generate an Ohmic background spectrum; thus, $J(\omega) \propto \omega$ for small frequencies.

In order to maintain the structure of $\kappa(\omega)$ but allow an Ohmic background, $I_i/\omega_i = \eta_i \gamma_i$ is set. It is also assumed an equal width for all peaks, i.e., $\gamma_i = \gamma$. Thus, the parameter γ determines also the overall coupling strength between the qubit and the IR modes through $\gamma_i = (\pi/2)(g_i^2/\omega_i \eta_i)$. Normalizing the spectrum with respect to the most intense mode i_{\max} gives $\eta_i = (I_i/I_{i_{\max}})(\omega_{i_{\max}}/\omega_i)$, with the corresponding $\eta_{i_{\max}} = 1$. This leads to the spectral function

$$J(\omega) = \omega \sum_i \frac{\eta_i \gamma^2}{(\omega - \omega_i)^2 + \gamma^2} = \gamma \omega \sum_i \eta_i L_i(\omega). \quad (4.3.4)$$

In order to get a tractable analytical expression for the spectral density, only IR modes with an intensity $I_i \geq 0.01 I_{i_{\max}}$ are included. Modes with lower intensities are not resolved within the Ohmic background. The final extracted spectral densities for all Δ_N systems in Table 4.1 are given in Appendix E. There, the resulting autocorrelation function in Eq. (2.2.11) is also shown for all systems. The case $N = 3$ is shown in Fig. 4.4. When plotting the spectral density as a function of the scaled frequency ω/Δ_N as in Appendix E, it is clear that the Δ_N systems have $N = 0, 1, 2, 3$, and 4 main IR modes at energies below $\hbar\Delta_N$. As expected, the

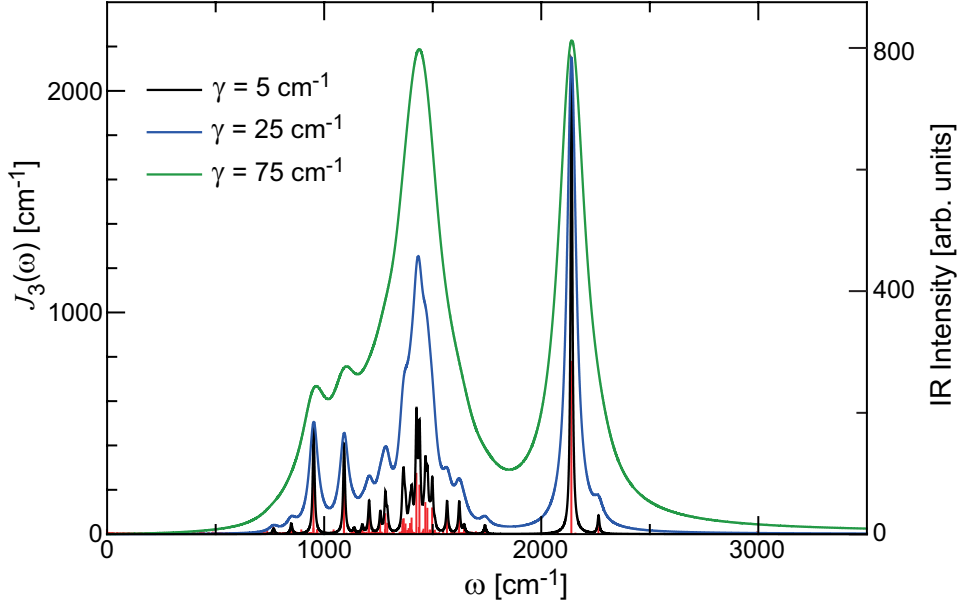


Figure 4.4: Spectral density in Eq. (4.3.4) for the system Δ_3 . The IR spectrum in Fig. 4.3 (shown as vertical red lines) is included for comparison. The solid black, blue, and green lines correspond to the widths $\gamma = 5, 25,$ and 75 cm^{-1} , respectively.

resulting correlations are longer-lived for a larger number of peaks at frequencies $\omega_i < \Delta_N$ as shown in Appendix E.

4.3.2 Electron–vibration coupling strength

As mentioned before, the overall coupling strength between the qubit and the vibrational modes is determined by γ via $\gamma_i = (\pi/2)(g_i^2/\omega_i\eta_i)$. Here, this is calculated by redetermining the energy splittings while the nuclear coordinates are displaced according to the mode with maximal intensity in the IR spectrum, for which $\eta_{i_{\max}} = 1$ (see Appendix E). It is assumed that this mode has a maximal electronic coupling strength. Consequently, a maximal shift of the energy splitting is expected when the nuclear coordinates are displaced. For a vibrational mode with frequency (i.e., eigenvalue) ω_i , the displacement coordinates are given by the eigenvectors associated to that mode. They are obtained by using the AM1 method (see Appendix B).

A molecular system with an energy splitting Δ_N ($\hbar \equiv 1$) has an IR mode with maximal intensity at frequency $\omega_{i_{\max}}$, i.e., the mode with $\eta_{i_{\max}} = 1$ in Appendix E. This mode has a force constant k as follows from the curvature at the potential minimum. The calculated nuclear displacement coordinates, \mathbf{r}_j , indicate that each atom is displaced in its normal mode direction by one unit of the oscillator length

(see Sec. B2). By summing over all atoms i , a potential energy $E_{\text{pot}} = (1/2)k \sum_i \mathbf{r}_i^2$ due to the nuclear displacement is introduced. This displaced nuclear configuration is then used to recalculate the electronic states, yielding an energy splitting $E^{(dis)}$. Typically, displacements generate an energy difference ϵ_0 for the electron in one of the two wells (i.e., a static bias) rather than modifying the tunnel coupling between the two wells. The energy splitting for an according two-level system is then $E^{(dis)} = \sqrt{\Delta_N^2 + \epsilon_0^2}$, whereas in equilibrium $E^{(equil)} = \Delta_N$. The difference between the two is then $\delta E = E^{(dis)} - E^{(equil)}$.

The displacements introduced correspond to the $E_{\text{pot}}/\omega_{i_{\text{max}}} = v$ -th excited state of the considered mode leading to $\epsilon_0 \simeq \sqrt{(\delta E)^2 + \Delta_N^2} - \Delta_N$. In turn, a single excitation of this mode corresponds to displacements smaller by a factor \sqrt{v} . It is assumed that the electronic qubit states couple bilinearly to vibrations, i.e., $\propto (1/2)\sigma_z g_j (a_j + a_j^\dagger)$ in Eq. (4.3.3). Hence, all nuclei are maximally displaced relative to a single excitation in the mode $\omega_{i_{\text{max}}}$. This results in an energy difference ϵ_0/\sqrt{v} which is identified with the coupling constant $g_{i_{\text{max}}}$.

This result can be directly replaced in $\gamma_i = (\pi/2)(g_i^2/\omega_i\eta_i)$, for which $\eta_{i_{\text{max}}} = 1$ due to the fact that only the IR mode with maximal intensity is considered. Thus,

$$\gamma_{i_{\text{max}}} = \frac{\pi g_{i_{\text{max}}}^2}{2 \omega_{i_{\text{max}}}}. \quad (4.3.5)$$

This indicates that the electron–vibration coupling constants g_i determine also the damping strength of the vibrational bath. This is given by the decay of the bath autocorrelation in Eq. (2.2.11), as shown in Appendix E.

Results for the systems with $N = 0, 1$, and 2 , obtained using the described methodology, are shown in Table 4.2. It is worth to note, however, that the coupling

System	k [eV/Å ²]	v -th excited state	$E^{(dis)}$ [cm ⁻¹]	ϵ_0 [cm ⁻¹]	$g_{i_{\text{max}}}$ [cm ⁻¹]	$\gamma_{i_{\text{max}}}$ [cm ⁻¹]
Δ_0	193.34	33rd	2325.27	926.61	161.30	20.14
Δ_1	204.81	34th	3196.35	1392.27	238.77	43.18
Δ_2	219.64	35th	5868.50	3639.54	615.19	278.28

Table 4.2: Electron–vibration coupling strength for the Δ_N systems with $N = 0, 1$, and 2 .

strength obtained for the system Δ_2 is quite large. This might be a consequence of the several modes at energies around $\hbar\Delta_2$ (see Table E3 and Fig. E5), which already results in a system with strong coupling to vibrational modes and will then exhibit strong damping (see results in Sec. 5.1). Due to their smaller molecular

size, displacing the atoms from their equilibrium position according to the most intense mode, as before, in the systems with $N = 3$ and 4 induces a very strong electronic rearrangement, which gives $E^{(dis)} < E^{(equil)}$, resulting in very small γ values. This is physically meaningless due to the fact that a smaller molecule will have a stronger electron–vibration coupling, which is consistent with the results in Table 4.2 for the largest systems. It is important to note that more elaborate ways to calculate the electronic level widths for different environments are available [127, 128]. The structural deformation due to the pseudo-Jahn-Teller effect [121] is negligible since $\gamma_{i_{\max}} \ll \Delta_N$ for all calculated systems, in contrast to the cases where a strong coherent electron–vibrational coupling leads to qualitative modifications of the electron dynamics [129, 130].

Dynamics of π -conjugated molecular charge qubits

In this chapter, the real-time dynamics of the different molecular charge qubits in Table 4.1 is investigated in terms of the time-dependent population difference

$$P(t) = \langle \sigma_z \rangle_t = \text{tr} [\rho(t) \sigma_z] \quad (5.0.1)$$

of the left and right wells. The reduced density matrix $\rho(t)$ is calculated by means of the iterative QUAPI scheme presented in Sec. 2.2.1. An initial preparation $\rho(0) = |L\rangle\langle L|$ in the left well is assumed. For all cases, $\hbar\Delta_N > k_B T$ at room temperature and thermal effects are negligible for the following considerations. All results reported below are for $T = 300$ K.

The long-lived oscillatory correlations of the Δ_4 system resulting from the large number of peaks at frequencies $\omega_i < \Delta_4$ lead to very long memory times $\tau = K\delta t$ in the autocorrelation function (see Fig. E10 in Appendix E). This makes difficult to find an optimal parameter combination of K and δt , and therefore, no results are shown for the Δ_4 system in this chapter. However, results obtained by choosing a compromise between a large enough memory time (given by a large K) and a small enough Trotter error (given by a small δt step) are presented in Appendix F for comparison purposes.

5.1 Dynamics of undriven molecular charge qubits

Here, it is assumed that $\epsilon(t) = 0$ in Eq. (4.3.2). The resulting dynamics is shown in Fig. 5.1 for all cases with $N = 0-3$. Because, in general, the strength of the electron–vibration coupling increases by decreasing the size of a molecule, coupling strengths

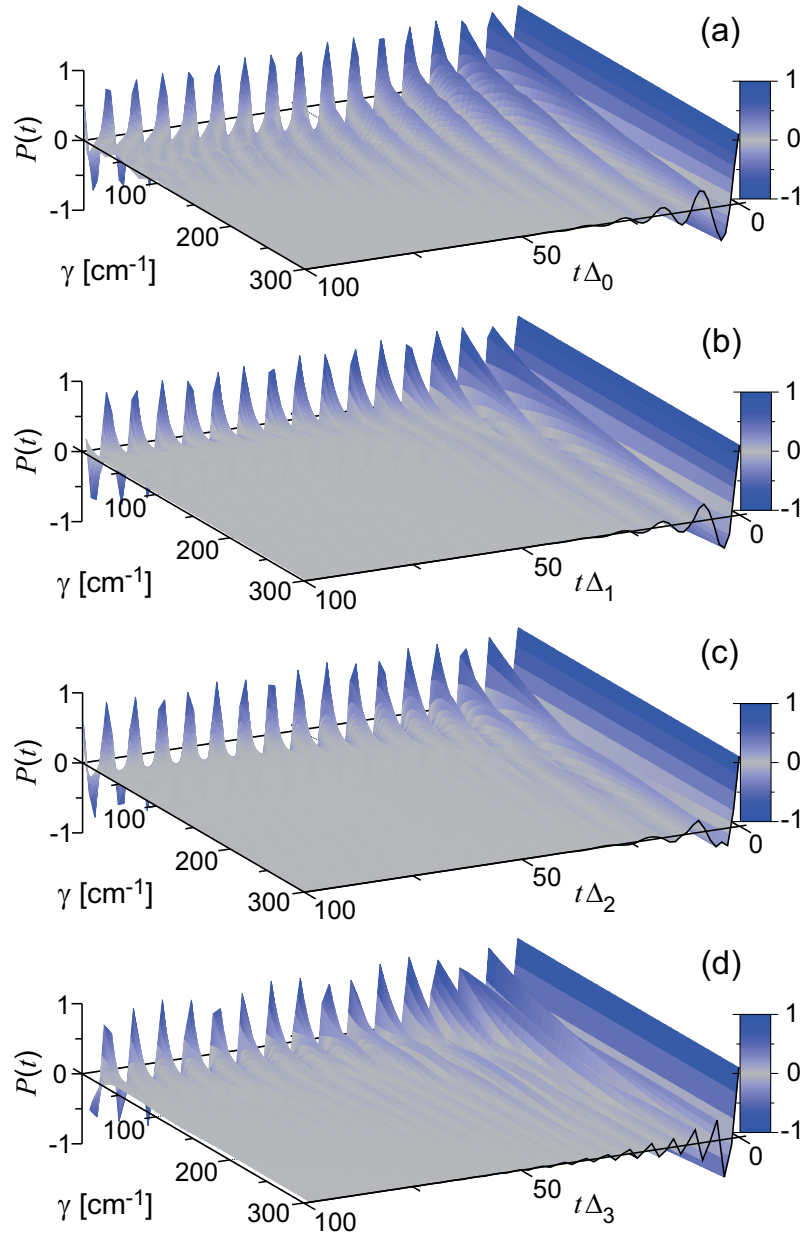


Figure 5.1: Time-dependent population difference $P(t)$ as a function of the damping strength γ for the heterostructures Δ_N with $N = 0-3$ (a)-(d).

up to 300 cm^{-1} have been investigated. Coherent oscillations of the population difference are found. Figure 5.2 compares the dynamics of all systems when the electron–vibration coupling is fixed at $\gamma = 250 \text{ cm}^{-1}$. The corresponding dynamics of the Δ_4 system is shown in Fig. F1.

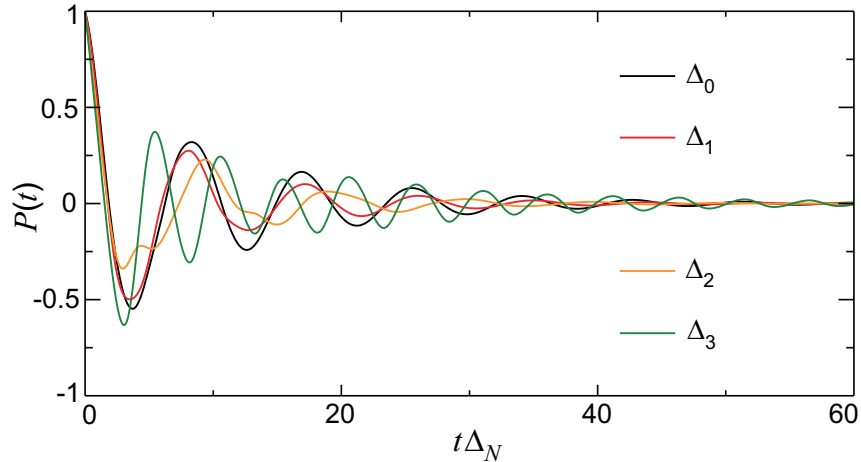


Figure 5.2: Time-dependent population difference $P(t)$ for a fixed value $\gamma = 250 \text{ cm}^{-1}$ of the electron–vibration coupling for the heterostructures Δ_N with $N = 0-3$.

By a fit of the population difference to the expression $P(t) = e^{-\Gamma t} \cos(\omega t)$, it is possible to extract the coherence time $T_{1,N} = \Gamma^{-1}$ and the quality factor $Q_N = \omega/\Gamma = T_{1,N}/\Delta_N$. The latter gives the number of operations that can be implemented in a physical qubit within the decoherence time [131]. The resulting values for $T_{1,N}$ and for Q_N as a function of the damping strength γ for all molecular systems Δ_N are shown in Fig. 5.3. Coherence times and quality factors for particular γ values are given in Table 5.1. It is found that the coherence times and, consequently, the quality factors decrease with increasing coupling. This can be understood when considering the autocorrelation function in Eq. (2.2.11) of the vibrational bath (see Appendix E): in the limit of small γ values, the autocorrelation function is slowly damped, and a long-lasting coherent decay of $P(t)$ is observed. In the opposite limit of large γ values, the bath-induced memory effects are quickly lost and therefore, $P(t)$ decays faster. Within the investigated γ values, it always holds that $\Delta_N \gg \gamma$, which explains the absence of a completely incoherent decay of $P(t)$ in Fig. 5.1. It is important to note that $\hbar\Delta_N$ is not in resonance with any vibrational mode in any of the five cases, which (together with the lacking point symmetry) excludes possible strong pseudo-Jahn-Teller effects [121]. Put differently, no significant polaron formation occurs. In such a case, a breakdown of the Franck-Condon (or, equivalently, the Born-Oppenheimer) approximation is expected. Due to the large number of peaks

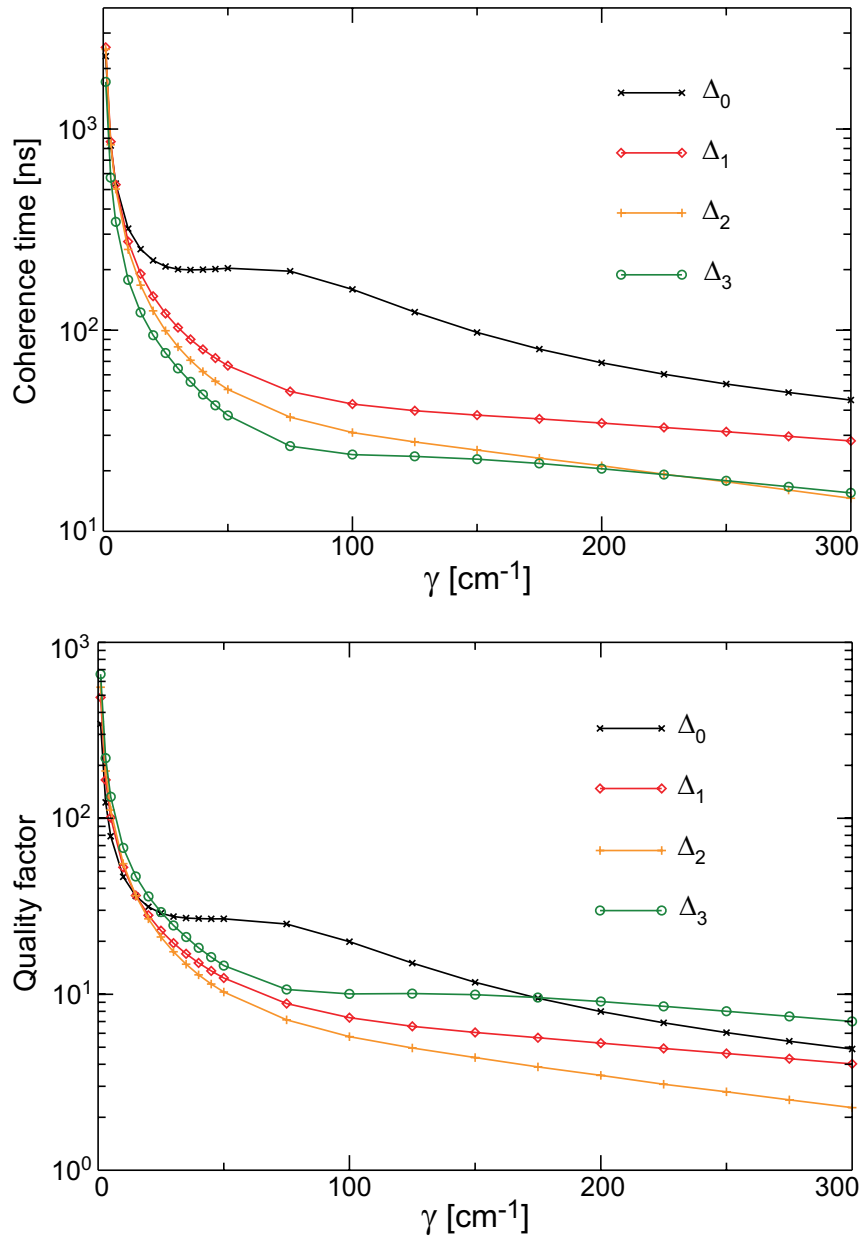


Figure 5.3: Coherence times $T_{1,N}$ (top) and quality factors Q_N (bottom) as a function of the damping strength γ for the heterostructures Δ_N with $N = 0-3$.

around 1500 cm^{-1} , a significant spectral overlap occurs in all heterostructures (see Appendix E). This leads to an effective broad single mode with a large spectral weight. This is the reason for the system Δ_2 , in particular, to exhibit the smallest quality factors. On the contrary, this effective mode has a negligible influence on the dynamics of the Δ_4 system resulting in quality factors an order of magnitude

System	γ				
	5 cm ⁻¹	20 cm ⁻¹	45 cm ⁻¹	100 cm ⁻¹	250 cm ⁻¹
Δ_0	535.394 (79)	222.275 (31)	201.258 (27)	159.552 (20)	53.986 (6)
Δ_1	528.736 (101)	147.498 (28)	72.650 (14)	42.911 (7)	31.258 (5)
Δ_2	503.075 (111)	124.848 (27)	55.739 (11)	30.982 (6)	17.641 (3)
Δ_3	345.562 (133)	94.453 (36)	42.308 (16)	24.068 (10)	17.846 (8)

Table 5.1: Coherence times $T_{1,N}$ (in ns) and quality factors Q_N (in parentheses) for all heterostructures with $N = 0-3$ for specific γ values as indicated.

larger (see Appendix F).

Notice that for small γ values, the quality factors increase for larger N , i.e., when the dynamics is influenced by N main vibrational bands below $\hbar\Delta_N$. The situation, however, is more complicated when increasing the damping strength γ . In the intermediate regime of γ values, the system Δ_0 exhibits the largest quality factors, with a maximum around 100 cm⁻¹. For this particular system, the energy difference between the electronic transition (given by Δ_0) and the first vibrational peak (see Table E1) is 98 cm⁻¹. A width γ of the vibrational transition close to this value will bring the electronic and vibrational transitions into resonance and therefore, sustained coherence is expected. This results in large coherence times and quality factors as observed in Fig. 5.3. A similar argument is valid for the systems Δ_1 and Δ_3 . In these cases, the corresponding energy differences are 89 cm⁻¹ for Δ_1 (taken with respect to the first vibrational peak at lower energy as compared to $\hbar\Delta_1$, see Table E2), and 96 cm⁻¹ for Δ_3 (taken with respect to the next vibrational peak at higher energy, see Table E4). For these two cases, however, no maximum in the quality factors is observed. The reason for this is the large spectral weight at the electronic transition, $J(\Delta_N)$, resulting from the overlap of the vibrational peaks around $\hbar\Delta_N$ (at larger energies for both cases, see Figs. E3 and E7).

Thus, it is possible to conclude that the design of the molecular heterostructures allows to *chemically* engineer the coherence times over very broad time scales for such molecular quantum devices. Similar chemical engineering was shown for molecular spin systems [132], where the electron spin phase memory time was extended by changing the substituent chemical groups in the molecular structure.

5.1.1 Non-Markovian effects in molecular charge qubits

With increasing Δ_N , the relevant vibrational IR bands shift from $\omega_j > \Delta_0$ to $\omega_j < \Delta_4$ (see Figs. E1, E3, E5, E7, and E9 in Appendix E). The peaks at frequencies $\omega_j < \Delta_N$ with width γ induce strong non-Markovian behavior [31] by introducing several oscillatory correlations of the form $e^{-i\omega_j t - \gamma t}$ in the bath autocorrelation function [see discussion following Eq. (2.2.11) and Figs. E2, E4, E6, E8, and E10 in Appendix E]. In order to quantify the non-Markovian effects in the dynamics of molecular charge qubits, the non-Markovianity quantifier in Eq. (2.3.4) is used. Here, the initial states $\rho_{1/2}(0)$ correspond to the additional charge being predominantly in the left or right dot.

Figure 5.4 shows the evolution of the trace distance $D(\rho_1, \rho_2)$ in Eq. (2.3.1) for increasing γ in all molecular charge qubits in Table 4.1 with $N = 0-3$. As was discussed in Sec. 2.3, in open quantum systems, the evolution due to the dynamical map $\Phi(t)$ leads to a decay of the trace distance with time. This is observed in Fig. 5.4. A comparison of all cases is shown in Fig. 5.5 when $\gamma = 250 \text{ cm}^{-1}$. It can be compared with the evolution of $P(t)$ presented in Fig. 5.2. It is found that the Δ_0 system exhibits the largest number of non-Markovian intervals, i.e., the time intervals on which the trace distance increases. They are smeared out for larger N . The corresponding results for the Δ_4 system are shown in Fig. F3.

Any growth of the trace distance is a signature for non-Markovian behavior and leads to a lower bound for the non-Markovianity measure \mathcal{N} [58]. As mentioned, the latter is obtained by integrating over all time spans on which the trace distance increases [see Eq. (2.3.4)]. Figure 5.6 shows the resulting \mathcal{N} as a function of γ . It is found that all systems exhibit non-Markovian effects. In these molecular systems, vibrational peaks at energies lower than $\hbar\Delta_N$ help to sustain coherent oscillations of the population difference by a non-Markovian flow of information from the vibrational degrees of freedom back to the electronic degrees of freedom, eventually leading to a prolonged quantum coherent dynamics. The decay of \mathcal{N} at large γ values occurs in the regime where the bath autocorrelation function decays faster. Then, the bath loses its memory more quickly and therefore, non-Markovian effects are less relevant. Notice that a maximum in \mathcal{N} exist around 100 cm^{-1} for the systems Δ_0 , Δ_1 , and Δ_3 . This can be attributed to near resonant electronic and vibrational transitions as discussed before. The large \mathcal{N} for the system Δ_0 explains the large coherence times obtained for this system.

These results show that non-Markovian behavior can be exploited as a resource of quantum coherence. Coherent dynamics is sustained longer by a coherent exchange of energy between the electronic and vibrational degrees of freedom leading

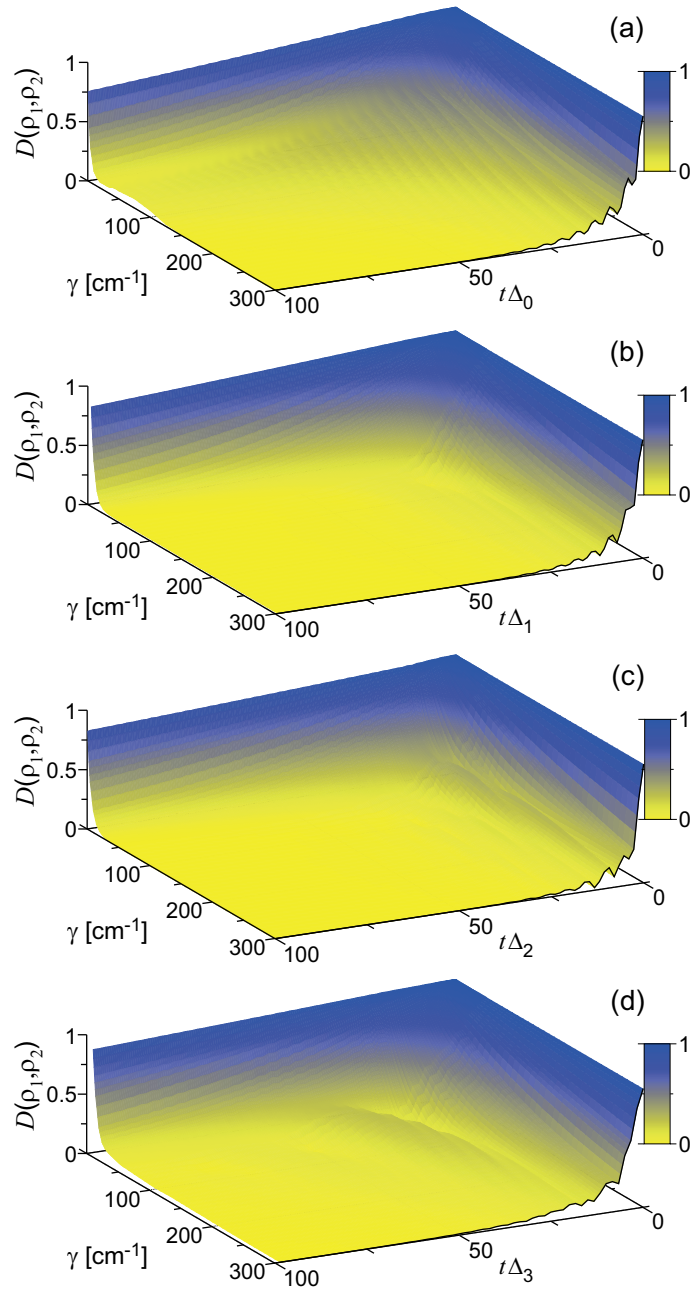


Figure 5.4: Time-dependent trace distance $D(\rho_1, \rho_2)$ in Eq. (2.3.1) as a function of the damping strength γ for the heterostructures Δ_N with $N = 0-3$ (a)-(d).

to a *dynamical storage of coherence* in vibrations. They typically have much longer coherence times as compared to electronic degrees of freedom. Memory effects can also arise from the rearrangement of the nuclear positions induced by the oscillating electronic charge. It changes the electronic distribution in the molecule, in analogy

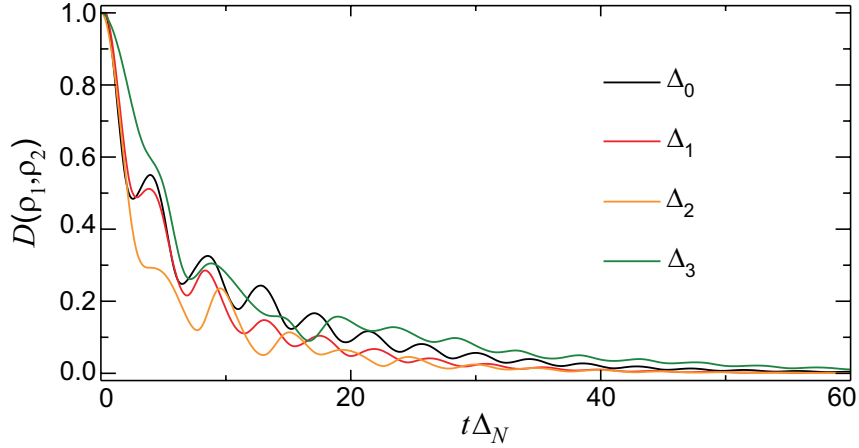


Figure 5.5: Time-dependent trace distance $D(\rho_1, \rho_2)$ at fixed $\gamma = 250 \text{ cm}^{-1}$ for the heterostructures Δ_N with $N = 0-3$.

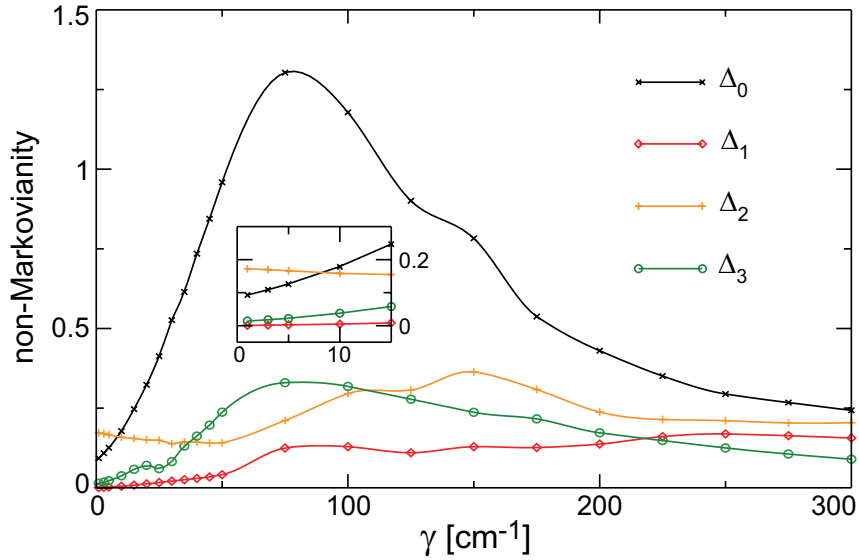


Figure 5.6: Non-Markovianity \mathcal{N} [see Eq. (2.3.4)] as a function of the damping strength γ for the heterostructures Δ_N with $N = 0-3$. Inset: zoom to the small γ region.

with the Stokes shift. Although this effect is expected in all systems due to the lack of point symmetry, it is more pronounced in the system Δ_0 , since it is the largest molecule (see Table 4.1).

It is then possible to conclude that the chemically engineered coherence times are the result of engineering the non-Markovian vibrational environment. This in-

fluences the electronic dynamics and constitutes a chemical approach to reservoir engineering techniques [133].

5.2 Dynamics of driven molecular charge qubits

The dynamics of the undriven charge qubits presented in the last section gives the intrinsic coherence times and elucidates the role played by non-Markovian effects. However, from the point of view of quantum processing of information, it is desirable to control the dynamics of the oscillating electronic charge, for example, to prepare an initial state or to implement specific quantum gates. This control can be achieved by the use of electric fields, similar to the methodology used in inorganic systems. In molecules, however, electric fields generate a sizeable Stark shift of the electronic levels, which, depending of the strength of the field, can couple the MO levels to the continuum. This may cause ionization or can even destroy the molecule. An alternative is the use of electromagnetic radiation. Laser pulses can be used to control the electronic dynamics of molecular systems [134, 135, 136]. These pulses demand a high degree of control both in amplitude and phase [137]. Nevertheless, they can be designed [138] and implemented experimentally [139].

The LUMO–LUMO+1 transition of the systems in Table 4.1 fall within the IR-active region, and therefore, it is easily addressable with THz lasers [140]. Arbitrary pulse shaping has been demonstrated in this spectral region [141, 142], which opens the possibility to implement control schemes [143]. Therefore, it is worth to investigate the conditions under which the dynamics of the molecular charge qubits can be controlled.

Here, it is assumed that the system is driven by a time-dependent external field of the form $\epsilon(t) = A \cos(\Omega t)$ in Eq. (4.3.2). This models a continuous wave laser with driving strength A and driving frequency Ω , which can be considered as the simplest control scheme possible. Particularly interesting is how the field parameters A and Ω influence the quantum coherent dynamics of the systems.

In the limit of a weak laser field, an initial decay of the population difference is observed, after which only stationary oscillations due to the external driving field survive as shown in Fig. 5.7 for the Δ_1 system. Similar behavior is observed in all other systems. Stronger electron–vibration coupling leads to a faster decay of $P(t)$ and the stationary state is reached more quickly, as found also in the undriven situation (compare with Fig. 5.1). Note that due to the small laser amplitude, the behavior of the trace distance does not differ considerably from the undriven case (compare with Fig. 5.4). The resulting dynamics of all systems under the same weak field parameters is shown in Fig. 5.8 when the electron–vibration coupling

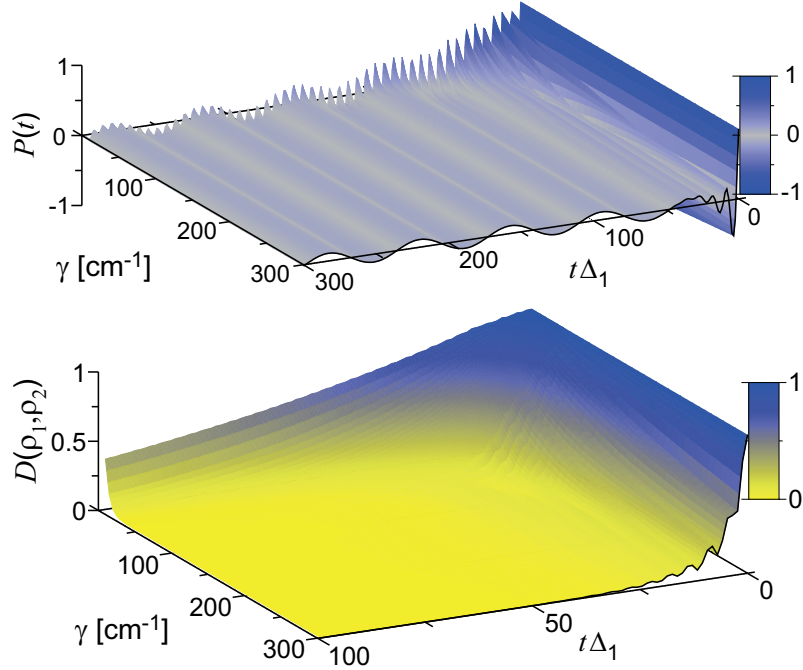


Figure 5.7: Time-dependent population difference $P(t)$ (top) and trace distance $D(\rho_1, \rho_2)$ (bottom) as a function of the damping strength γ for the Δ_1 system with field parameters $A = 0.1\Delta_1$ and $\Omega = 0.1\Delta_1$.

is fixed at $\gamma = 200 \text{ cm}^{-1}$. Figure F5 shows the corresponding results for the Δ_4 system. In all systems, initial superimposed oscillations due to coherent tunneling are observed before the system reaches its stationary state.

An increase in the driving strength A changes the form of the forced oscillations in the stationary limit as shown in Fig. 5.9 for the Δ_2 system. The observed stationary state plateaus in $P(t)$ appear as a result of population trapping due to the large quasistatic bias of the system dynamics generated by the large driving amplitude, as depicted in Fig. 5.10. Square-wave oscillations in $P(t)$ due to population trapping can be attained for all Δ_N systems by the combination of large amplitude with slow driving frequency, as illustrated in Fig. 5.11. Results are presented in Fig. F6 for the Δ_4 system in the regime where square-wave oscillations in $P(t)$ are obtained. Following Ref. [144], the results in Fig. 5.11 are given for a driving strength $\mu A/\hbar\Delta_N = 10$, where μ is the dipole moment generated by moving the excess electron between the left and right dots. Considering the size of the particular Δ_N molecule, these values correspond to an electric field strength of 18.7×10^7 , 31.8×10^7 , 38.0×10^7 , and $114.1 \times 10^7 \text{ V/m}$, and a driving frequency of 2.4, 3.0, 3.6, and 6.1 THz for the systems $N = 0, 1, 2$, and 3, respectively. All of

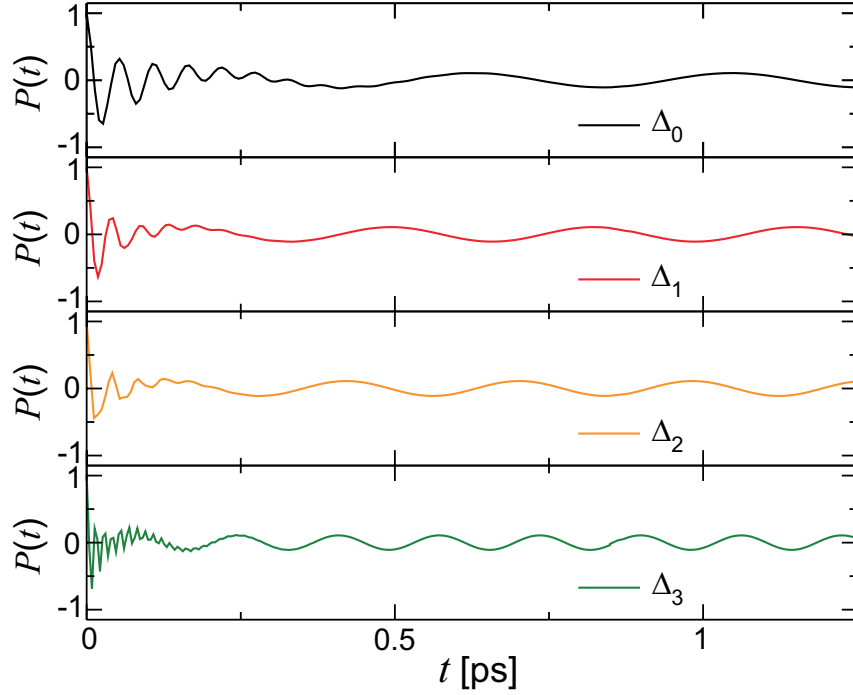


Figure 5.8: Time-dependent population difference $P(t)$ at fixed $\gamma = 200 \text{ cm}^{-1}$ for the heterostructures Δ_N with $N = 0-3$ and field parameters $A = 0.1\Delta_N$ and $\Omega = 0.1\Delta_N$.

these values are achievable, for example, with quantum cascade lasers, which are continuous-wave THz sources [140]. The corresponding field intensity $I = c\epsilon_0|A|^2$ is 9.3, 26.8, 38.3, and 346 GW/cm^2 for $N = 0 \rightarrow 3$, respectively. Competing processes such as bond breaking or ionization occur above a certain intensity threshold, which is typically between 1 and 10 TW/cm^2 for molecules [145]. The calculated values are below the intensity threshold.

Population trapping, under a slow driving frequency, has been shown theoretically in the case of two-level systems [30, 146], three-level ladder systems [147], and, experimentally, in frequency-modulated excitations of two isolated Rydberg Stark states of a potassium atom [148]. In general, population trapping requires, besides a slow driving frequency, a strong driving field and also strong coupling. A strong but slow field leads to maximum bias of the system at the extrema of the driving field, with self-trapping resulting from the much faster dynamics of the undriven system, and therefore, a square-wave profile of $P(t)$ results. The population jumps occur when the field sweeps the system through the resonance (see Fig. 5.10). Increasing the driving frequency leads to shorter-lived population trapping, and therefore, $P(t)$ does not exhibit square-wave oscillations in the stationary limit anymore, as

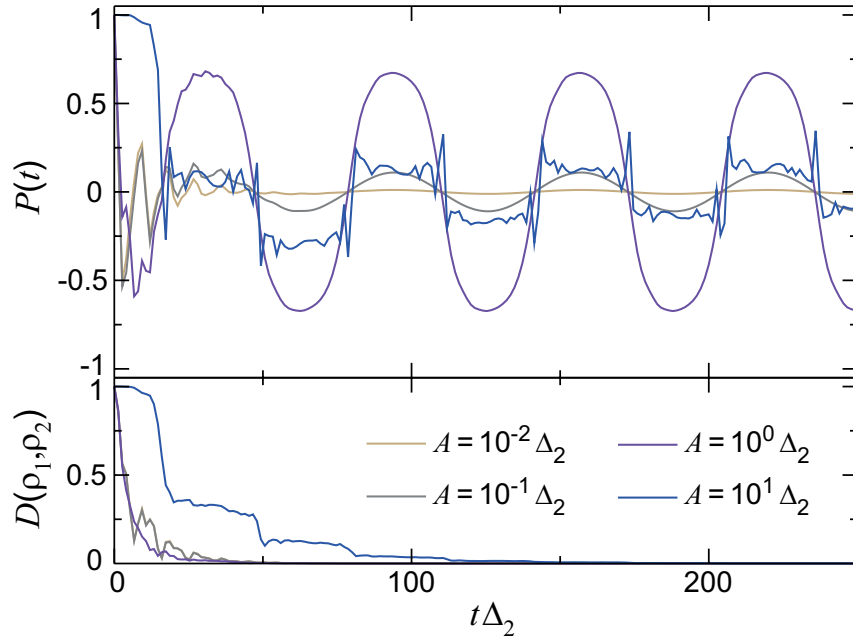


Figure 5.9: Evolution of $P(t)$ (top) and $D(\rho_1, \rho_2)$ (bottom) as a function of the driving strength A for the Δ_2 system at fixed $\gamma = 150 \text{ cm}^{-1}$ and driving frequency $\Omega = 0.1\Delta_2$.

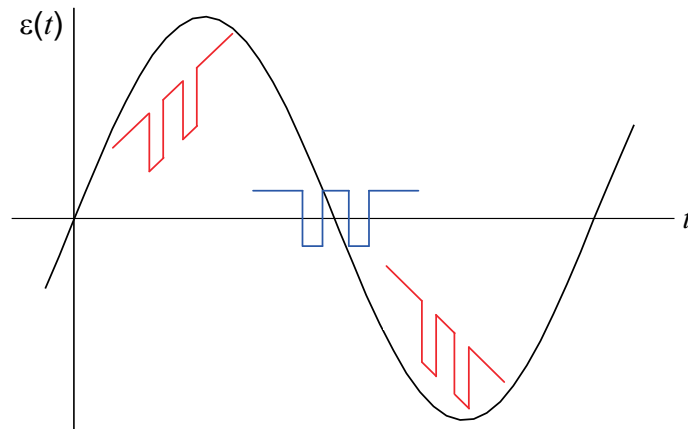


Figure 5.10: Schematic view of the laser-induced bias in a DQD: red diagrams indicate the maximally biased system at the extremes of the laser field, meanwhile the blue diagram indicates the system being swept through the resonance.

illustrated in Fig. 5.12 for the Δ_2 system.

In all molecular systems, the observed square-wave oscillations of $P(t)$ survive for several ps, which implies that it is possible to control externally the population

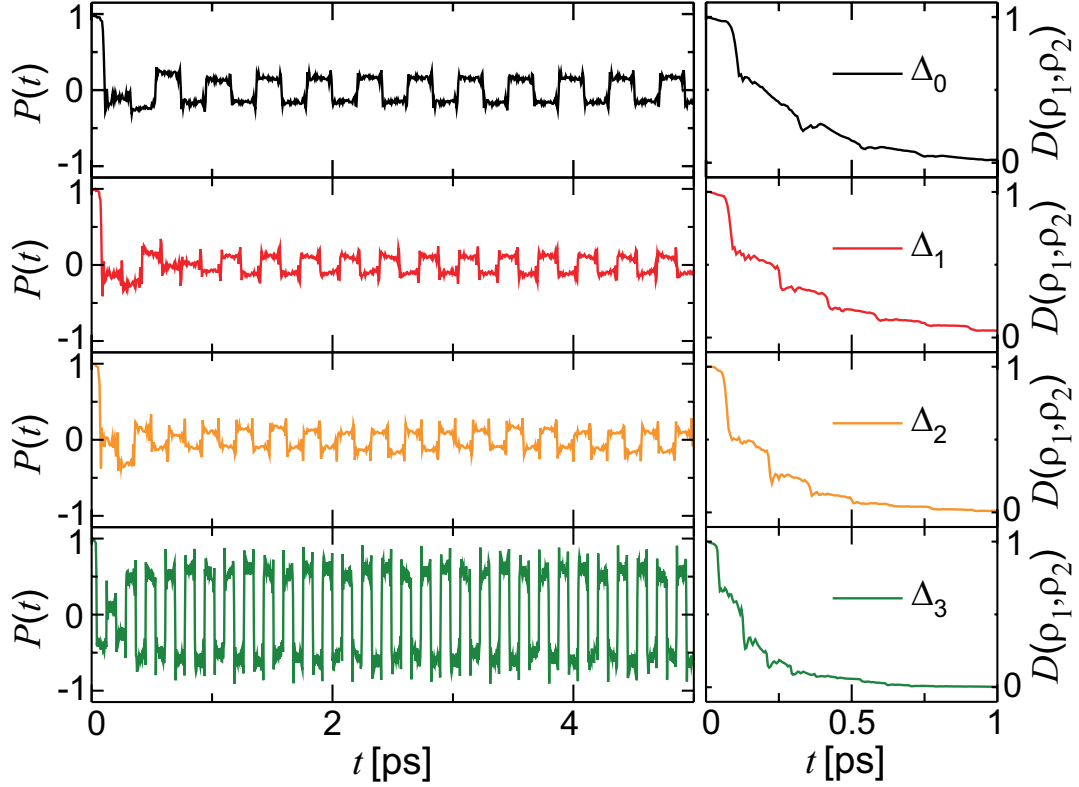


Figure 5.11: Evolution of $P(t)$ (left) and $D(\rho_1, \rho_2)$ (right) for the heterostructures Δ_N with $N = 0-3$ for a fixed value $\gamma = 100 \text{ cm}^{-1}$ of the electron–vibration coupling and with field parameters $A = 10\Delta_N$ and $\Omega = 0.1\Delta_N$.

of the left/right dot in the DQD, allowing controlled transitions between the basis states of the charge qubit. Thus, single qubit gates become possible.

It is interesting to note that the field parameters leading to population trapping, also generate a slower decay in the trace distance as compared to the case of weak driving (see Fig. 5.9 bottom). As a consequence of the population trapping, the decay of the trace distance occurs in a step-like way, with the decrease of a single step when the system is swept through the resonance. The steps are more clearly defined at larger electron–vibration coupling as shown in Fig. 5.13 for the Δ_1 systems. Here, the decay of the trace distance at $\gamma = 100 \text{ cm}^{-1}$ (thin black line) is compared with the decay for $\gamma = 300 \text{ cm}^{-1}$ (thick black line). Even under strong driving conditions, increasing the driving frequency, however, removes the step-like decay of the trace distance (see Fig. 5.12 bottom).

The resulting non-Markovianity measure \mathcal{N} is shown in Fig. 5.14 as a function of γ for increasing driving strength A . It is found that \mathcal{N} behaves in a similar way

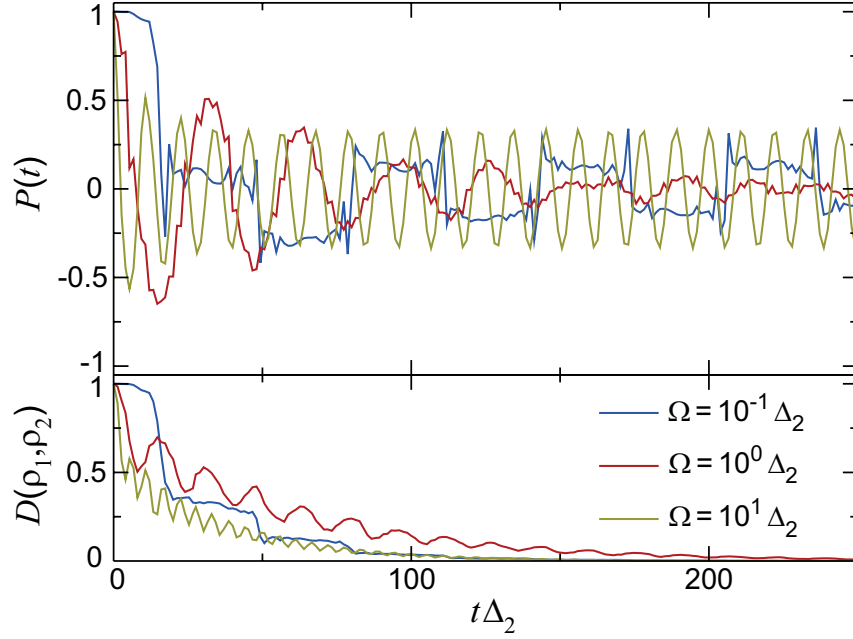


Figure 5.12: Evolution of $P(t)$ (top) and $D(\rho_1, \rho_2)$ (bottom) as a function of the driving frequency Ω for the Δ_2 system at fixed $\gamma = 150 \text{ cm}^{-1}$ and driving amplitude $A = 10\Delta_2$.

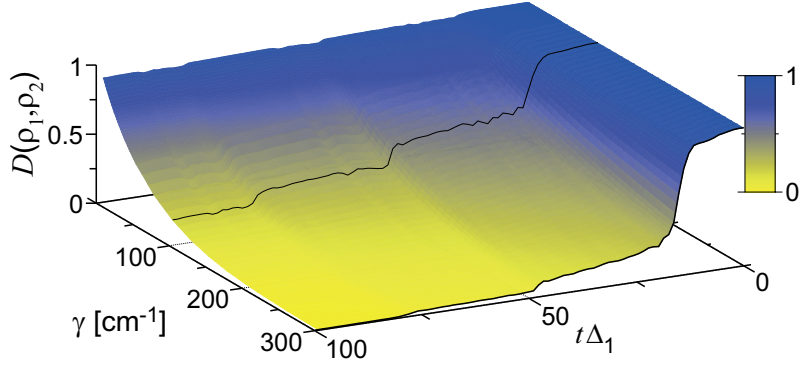


Figure 5.13: Time-dependent trace distance $D(\rho_1, \rho_2)$ as a function of the damping strength γ for the system Δ_1 with field parameters $A = 10\Delta_1$ and $\Omega = 0.1\Delta_1$.

as in the undriven case for both values of Ω (compare with Fig. 5.6). Notice that for the combination of driving parameters that maximize square-wave oscillations of $P(t)$ in the stationary limit, the non-Markovianity measure increases for larger N .

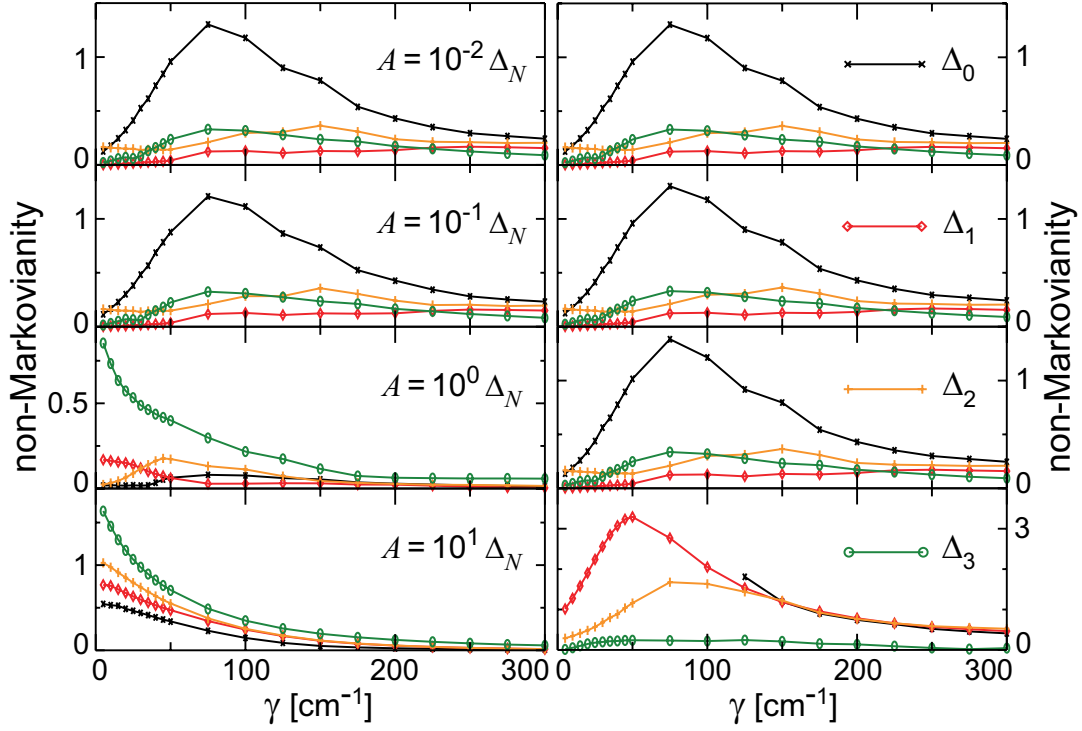


Figure 5.14: Non-Markovianity \mathcal{N} [see Eq. (2.3.4)] as a function of the damping strength γ for different values of the driving strength A for all heterostructures Δ_N with $N = 0-3$ at fixed driving frequencies $\Omega = 0.1\Delta_N$ (left) and $\Omega = 10\Delta_N$ (right).

5.3 Concluding remarks

Quantum computation requires a robust representation of quantum information, the ability to perform a universal family of unitary transformations, the ability to prepare a specific initial state, and the ability to reliably measure the output result [3, 70].

The designed molecular charge qubits based on ladder-type poly-(*p*-phenylene) and polydiacetylene π -conjugated heterostructures can serve as the basic elements of a quantum information processor. It can, in principle, operate at room temperature. This design can be realized by single π -conjugated molecular heterostructures spanned between a substrate and the tip of an atomic force microscope. This also allows one to address the qubit with minimal environmental influence. The scalability that these molecular systems offer allows the design of complex heterostructures for the implementation of control schemes for quantum computation [149].

By tuning the length of the *l*-PPP and PDA oligomers, the tunneling coupling as well as the dephasing properties can be *chemically* engineered (see Fig. 4.3). Long

coherence times can be obtained resulting in quality factors up to 10^2 (see Fig. 5.3 and Table 5.1). The highest quality factors are obtained in the limit of weak environmental damping. Localized molecular vibrational modes at energies below $\hbar\Delta_N$ induce strong non-Markovian effects which contribute to sustain quantum coherence by non-Markovian flow of information from the vibrational degrees of freedom back to the electronic degrees of freedom (see Figs. 5.4 and 5.6). Then, tuning the length of the *l*-PPP and PDA oligomers determines the non-Markovian vibrational environment that influences the electronic dynamics. This constitutes a chemical approach to reservoir engineering techniques [133] and shows that non-Markovian behavior can be exploited as a resource of quantum coherence.

By means of an external laser field, it is possible to control the transitions between the left/right states of the charge qubit (see Fig. 5.11). Optimal field conditions involve the combination of a strong driving amplitude A and a slow driving frequency Ω . This leads to population trapping with square-wave oscillations of the population difference in the stationary limit. These controlled transitions between the basis states of the charge qubit are essentially single qubit gates. The read-out of the charge qubit state can be done by using spectroscopic techniques, for example, transient absorption of a negatively charged exciton, known as a trion [150].

The quantum circuit model of quantum computation requires two-qubit gates, like the controlled-NOT gate, which together with single-qubit gates form a universal set of quantum logic gates. It means that any unitary operation on n qubits may be implemented exactly by composing single-qubit and controlled-NOT gates [3]. Two-qubit gates can be implemented in the macrocyclic system depicted in Fig. 5.15. In this case, two Δ_4 molecular charge qubits are held together by means of

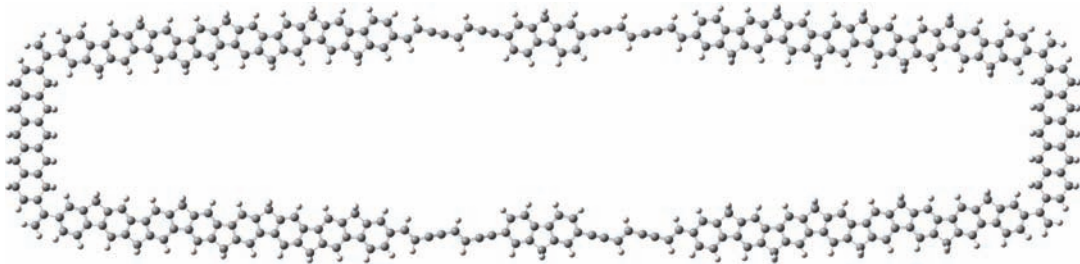


Figure 5.15: Molecular architecture where two Δ_4 systems are connected through a short oligomer of *p*-saturated acene.

a short oligomer of poly-acene saturated in the *para*-positions (see Fig. 3.2), which makes the whole system stiff. Similar architectures have been synthesized with PPP oligomers as molecular clamps [110, 151]. The length of the *p*-saturated acene

clamp controls the strength of the Coulomb interaction between the electrons in the different qubits. Single-qubit addressing in this macrocycle is possible because the separation between the qubits, is in general larger than 1 nm.

A more efficient control of the dynamics of the oscillating electronic charge can be achieved by means of quantum optimal control theory [138]. This requires to find the shape of a laser pulse that, for example, minimizes the time required to carry out a specific transition between the basis states of the charge qubit. Usually, this optimization is subject to physical constraints specific to the particular system, like for example, requiring that the fluence of the laser field be as small as possible in order to avoid competing processes [145]. This strategy has been applied to the implementation of quantum gates in molecules with vibrational qubits [18, 19].

The designed molecular charge qubits assume an excess electron (within the conduction band) localized in the left or right dot, which is achieved by doping the molecule single negatively. Then, a polymeric radical anion is formed. However, any charge carrier can be used, for example, a missing electron (within the valence band), or equivalently, a hole localized in the left or right dot. This is achieved by doping the molecule single positively such that a radical cation is formed. The combination of Th and *l*-PPP oligomers results in a type II-staggered heterostructure as shown in Fig. 5.16. Such a design offers an energy offset of 1.2 eV in the valence band, thus allowing the design of molecular charge qubits with positive doping. These systems

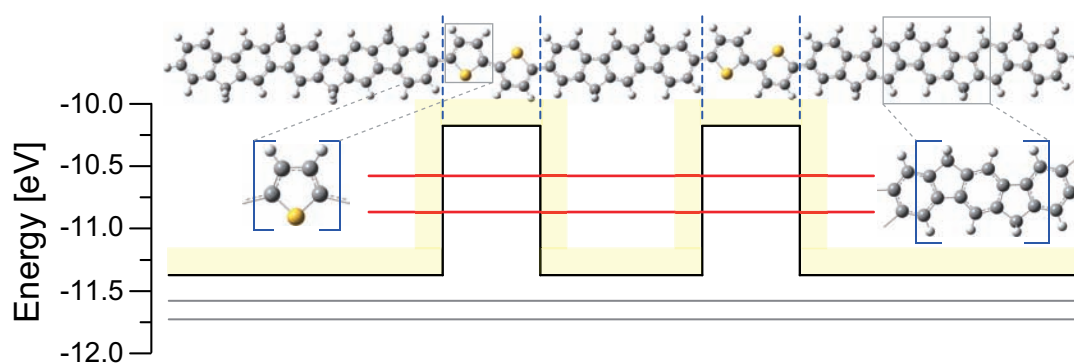


Figure 5.16: Molecular structure and potential energy profile for holes within the valence band for the symmetric DQD $l\text{-PPP}_5/\text{Th}_2/l\text{-PPP}_3/\text{Th}_2/l\text{-PPP}_5$. The two energy levels of the confined hole states are indicated by the horizontal red lines.

can be modelled as in Sec. 4.3. However, a different dynamics is expected due to the S atom in the Th oligomer, which results in a different profile of the IR spectra, and therefore, a different damping behavior.

Only intramolecular vibrational degrees of freedom have been considered to pro-

vide the dominant dephasing channel of the charge qubit. More elaborated models can elucidate the role of a possible substrate or a solvent.

Instead of using the proposed systems as quantum hardware, one can also envisage their use as a very sensitive charge meter. This role is currently fulfilled by single-electron transistors and by quantum point contacts. In the latter, the conductance through the quantum point contact channel is very sensitive to the electrostatic environment. This has been used to detect single-electron tunneling between a quantum dot and a reservoir in real-time [152]. For the proposed molecular systems, it is expected that their charge dynamics be also sensitive to nearby individual charges.

The fabrication of the proposed systems requires a refined control during the process of growing the molecular heterostructure. However, it seems feasible by current technologies, in particular, by STM polymerization [102].

Part II

Biomolecular systems: The FMO complex

Light-harvesting systems and the FMO complex

The directed transport of excitation energy is at the heart of photosynthesis which is one of the most important biochemical processes on Earth. It is a typical nonequilibrium transfer process that funnels the energy provided by the solar photons down to usable chemical energy in photoactive living systems. Photosynthesis allows the living organisms to harvest an enormous amount of energy. For instance, from the 100 PW of solar energy that Earth receives annually, the energy captured by photosynthesis is of the order of 100 TW. This should be compared to roughly 15 TW of the worldwide human energy consumption per year [153, 154]. Along with the harvest of energy goes the production of about 105 petagrams of biomass per year, with about 46% of the photosynthesis happening in organisms in water, i.e., mainly in the ocean, while the remaining 54% is performed by systems on the shore [155].

The elucidation of the molecular mechanism of light harvesting is of particular importance not only to understand the basic principles behind the fine-tuned functionalities of the light capture and energy transfer on the molecular level, but also to engineering artificial light-harvesting systems. This requires to identify the key features of minimal functional units, obscured by the accumulated complexity during evolution [156]. For instance, green plants contain chloroplasts in their leaves which contain a stack of membranes whose molecular structure is highly nontrivial. On a length scale of nanometers, many different biomolecular clusters act in concert

to harvest the energy of a solar photon and to convert it into chemical energy which starts a complicated sequence of chemical reactions [157]. Of particular interest are the early steps of the photosynthetic chain of reaction, especially, the ultrafast processes when the excitation energy is intermittently stored in an exciton which forms a quasiparticle of a strongly bound electron-hole pair [158]. These initial steps happen in particular parts of the biomolecular structure which are denoted as antenna pigment-protein complexes. After the exciton is formed at a certain molecular site, it transfers its energy by a radiationless Coulomb dipole coupling to neighboring sites such that the energy eventually finds its way through a network of few molecular sites. Finally, the energy ends up in the reaction center (RC), which is the energy sink of the antenna complex and the place where an electron transfer is initiated [159].

Figure 6.1 illustrates the molecular structure and the absorption spectra of some light-harvesting antennae encountered in different photosynthetic organisms. The wide variety of antenna structures in nature are the result of the different survival conditions that the different photosynthetic organisms have faced during evolution. This results in different chromophore types (e.g., chlorophyll, bilins, and carotenoids), as well as differences in the number and in the arrangement of such chromophores, leading to optimal light-harvesting capabilities in particular regions of the visible and near-infrared spectrum [156], as illustrated in Fig. 6.1. Nevertheless, all antennae complexes are able to convert the photogenerated excitations to charge separation with very high efficiency [160].

A central role during the cascade of the excitation energy transfer is played by the fluctuations provided by the environment in which the biomolecule is hosted. The quantum dynamics of the exciton is subject to fluctuating electric fields at the exciton position. These fluctuations are created by a continuous distribution of fluctuating polarization modes generated by the surrounding protein and the polar solvent. The fluctuations are reminiscent of phonons in a crystal and their distribution is characterized by the spectral density introduced in Eq. (2.2.9). In extended bulk condensed matter systems, Ohmic environments are ubiquitous, but non-Ohmic and highly structured environmental spectral densities arise in finite size systems, such as, the polymeric molecular architectures presented in Part I (see Appendix E) and biological molecules. For biomolecular systems, the spectral density can be obtained from experimental data [161, 162], or from theoretical modeling of the dielectric functions, for instance, in the Onsager continuum model of solvation [163], or from numerical simulations, such as molecular dynamics calculations [164, 165]. In contrast to small organic molecules, like those in Part I of this work,

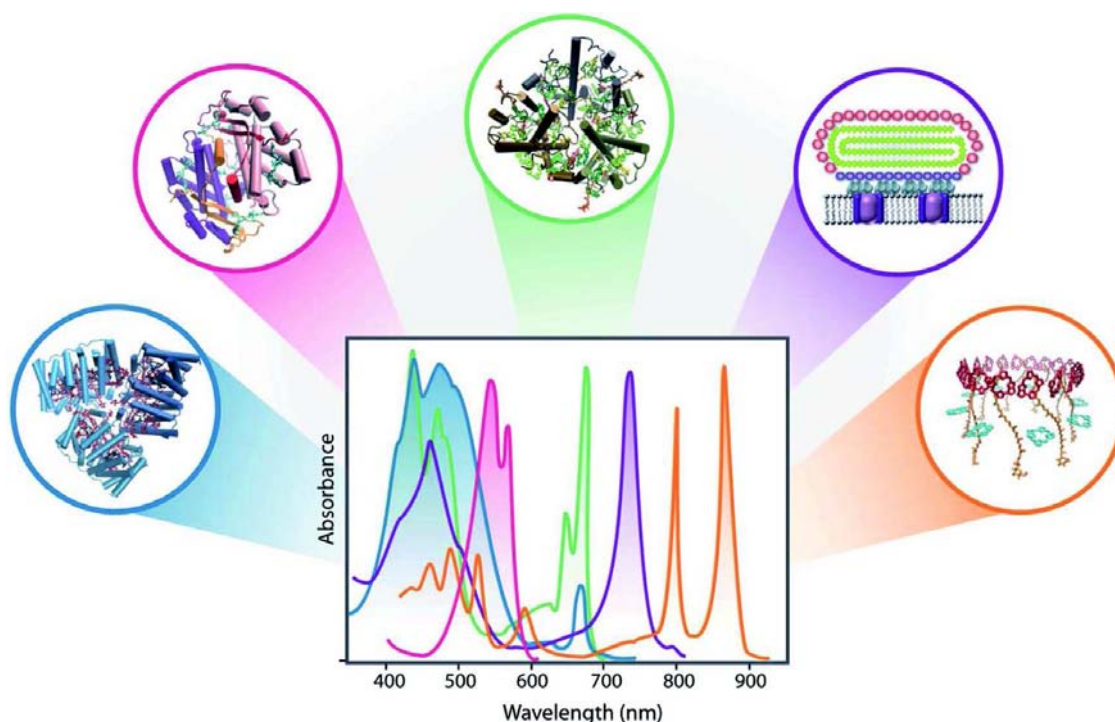


Figure 6.1: Molecular structures (with parent organisms in parentheses) and absorption spectra, shown from left to right in matching colours, of the light-harvesting antennae peridinin-chlorophyll-protein (of *Amphidinium carterae*), phycoerythrin 545 (of *Rhodomonas CS24*), light harvesting complex LHCII (of *Spinacia olearia*), chlorosome (of the green non-sulfur bacteria *Chloroflexus aurantiacus*), and light harvesting complex LH2 (of *Rhodospseudomonas acidophila*). Reproduced from Ref. [156] with permission from The Royal Society of Chemistry.

biological molecules typically weight several kDa¹. Because of their complexity, the determination of molecular properties by ab-initio or even semiempirical methods (as in Sec. 4.2) is out of the question and therefore, one has to rely on molecular dynamics calculations. There, the relevant part of the molecular system (e.g., the chromophores) are described by quantum mechanics, whereas the influence of the surrounding protein scaffold is normally well represented by classical molecular mechanics. A common feature of the pigment-protein-solvent environmental fluctuations of different light-harvesting systems is that the underlying spectral density function is highly structured with many prominent peaks, attributed to localized

¹The dalton (Da) or unified atomic mass unit (u) are alternative names (and symbols) for the same unit, equal to 1/12 times the mass of a free carbon 12 atom, at rest and in its ground state. In SI units it has a value of $1.66053886(28) \times 10^{-27}$ kg [166].

vibrational modes.

By nature, the transfer processes are quantum mechanical transfer processes. However, two limits have been used to describe the excitation energy transfer. (i) Förster theory, which applies to the regime where coupling between the chromophores and the environment dominates, and (ii) Redfield theory which assumes strong electronic coupling between the sites and allows for coherent oscillations of the populations at individual chromophore sites [160]. The first case, valid under strong environmental fluctuations, is a second-order perturbation theory with respect to the electronic coupling. It is based on the assumptions that the excitons are well localized quasiparticles and the transfer is a classical hopping-like dynamics along the molecular sites. The exciton population of each site is described by a classical probability (i.e., all coherences between sites are neglected) and quantum mechanics in this description enters only when the transfer rates are determined by Fermi's Golden Rule [167, 168]. The opposite limit of weak environmental fluctuations is described by Redfield theory, which is also a second-order perturbation theory but with respect to the electron-bath interaction. It assumes that the environment equilibrates infinitely fast after an electronic transition from the ground to the excited state (Markovian approximation). Hence, the transfer of excitation happens from equilibrium phonon states. The imaginary part in the autocorrelation function is also neglected (secular approximation). The resulting excitonic dynamics exhibits a coherent evolution of the exciton coherences oscillating with a frequency proportional to their energy difference, accompanied by dephasing of the coherences and relaxation of the excitons induced by the environment. Physically, this translates into coherent oscillations of the populations of the molecular sites, which is not captured by Förster-type mechanisms [160]. In many light-harvesting systems, however, the coupling strength of the electronic transitions to the environment is typically comparable in magnitude to the electronic coupling between chromophores, which results in an 'intermediate' coupling regime where all energy scales involved are similar. So, neither the electronic coupling (like in Förster theory) nor the excitation-bath coupling (like in Redfield theory) can be treated as a small perturbation. Furthermore, the typical time scale associated with equilibration of the pigment-protein-solvent environment in response to electronic excitation is often comparable with the time scale of excitation dynamics [160, 169].

Recently, two-dimensional electronic spectroscopy [170, 171, 172, 173] has provided additional insights into the excitation energy transfer dynamics of biologically active molecules [21, 156, 160, 174, 175, 176, 177]. In this technique, signal amplitudes are recorded as a two-dimensional map that correlates the energies of states that are photoexcited with those involved in radiating the signal after a wait-

ing time that is the same as the delay time variable in pump–probe experiments [156]. Of particular interest is the dynamical behavior of the off-diagonal signals (cross-peaks), which correspond to transitions with different excitation and emission frequencies. Cross-peaks at zero waiting time indicate an excitonic coupling via a common ground state. In turn, a growth of their amplitude as a function of the waiting time indicates energy transfer through a pathway revealed by their position in the spectrum [176]. Experimental results have shown long-lived oscillatory components in the ultrafast light-induced dynamics of electronic excitations in naturally occurring photosynthetic light-harvesting systems. They provide signatures of nontrivial quantum effects at cryogenic [178, 179, 180] and, surprisingly, also at room temperature [181, 182, 183, 184]. This has led to an increasing interest in elucidating the role played by quantum coherence for the energy transfer dynamics of these systems [7, 37, 40, 43, 185, 186, 187, 188, 189].

In order to explain these long-lasting coherences, several mechanisms have been proposed, e.g., a nonadiabatic vibrational–electronic mixing [185], vibrational coherences [186, 187], and vibronic excitons [188, 189]. In all cases, it is assumed that vibrational degrees of freedom are involved because they typically have much longer coherence times as compared to electronic ones. Besides, electronic transitions in molecular systems often couple strongly to vibrational modes whose frequencies match those of electronic energy gaps. Therefore, a significant amount of mixing between electronic and vibrational degrees of freedom can occur [160]. This is particularly relevant for the highly structured environmental fluctuations of light-harvesting systems [161, 162], where the many prominent vibrational peaks induce a complicated pattern of several oscillatory correlations with long life times. This requires then to consider the possible role played by the explicit nonequilibrium vibrational dynamics in the excitation energy transfer. An unambiguous interpretation of the spectral beatings observed in biological molecules is difficult due to their inherent complexity. Therefore, small molecular dimers have been synthesized to distinguish between electronic and vibronic coherences. The time traces of the off-diagonal features in the two-dimensional electronic spectra of halofluorescein heterodimers exhibit oscillatory behavior associated with coherent evolution at frequencies corresponding to the respective transition energy gaps. This is consistent with the presence of persistent electronic coherences [190]. On the other hand, the vibronic exciton model explains the underlying dynamical processes of bis-cyanine homodimers using the same experimental technique [191]. These results indicate then that the vibrational contribution to the oscillatory components depends on the molecular system in question.

One of the most extensively studied pigment-protein complexes is the Fenna-

Matthews-Olson (FMO) complex [192, 193] in the green sulfur bacteria (*Chlorobiaceae*). They are strictly anaerobic and depend on light, carbon dioxide and reduced inorganic sulfur compounds (mainly H_2S) or molecular hydrogen as electron donor for photosynthetic growth. Therefore, they occur where light reaches anoxic water layers or sediments that contain reduced sulfur compounds [194]. Its photosynthetic apparatus is illustrated in Fig. 6.2. The light-harvesting pigments in the green sulfur bacteria are bacteriochlorophylls (BChl) *c*, *d* and *e*, and chlorobactene and isorenieratene as the major carotenoids. These pigments are found in the chlorosomes that are the characteristic light-harvesting antenna complexes of green filamentous bacteria and green sulfur bacteria [195]. Each chlorosome contains thousands of BChl molecules and is energetically connected to 5-10 reaction centers. BChl *a* molecules are present in the portion of the chlorosome envelope facing the cytoplasmatic membrane (the so-called baseplate protein) that is in contact with the BChl *a*-containing FMO protein. It is a small water-soluble protein unique to the green sulfur bacteria and is responsible for passing the excitation energy from the chlorosome to the photosynthetic FeS-type RC, and thereby acting as a chemical wire. The RC is embedded in the cytoplasmatic membrane and receives the excitation energy via additional BChl *a* molecules (see Fig. 6.2) [194, 196]. Of the 15 known species of green sulfur bacteria, spectroscopic studies have focused mainly on the FMO complex of *Prosthecochloris aestuarii* (*P. aestuarii*) and *Chlorobium tepidum* (*Chl. tepidum*). The FMO proteins in these two species show a high degree of similarity, with the amino acid sequences being identical to one another within 77%, and the relative positions of each of the BChl *a* molecules matching almost perfectly [197]. For *Chl. tepidum*, in particular, its genome has been completely sequenced [198]. This has allowed to evaluate the spectral robustness of its FMO complex to genetically-induced structural modifications to the protein scaffold and to the chromophores [199].

The FMO protein is composed of three subunits related by a C_3 symmetry (see Fig. 6.3). Each subunit (365/366 amino acids) contains 8 BChl *a* molecules wrapped in a protein shell. It consists of 15 strands of a β -sheet folded in such a way that the strands at the front and the back of the shell are roughly perpendicular to each other with the shell opening oriented toward the center of the trimer (see Fig. 6.3 top), 6 short-length α -helices located at the open end of the shell connecting the separated β -strands, and a few regions of irregular conformation [195, 197]. The BChls are not covalently bound to the protein scaffold directly, but through the five-coordinate magnesium ion in the center of their tetrapyrrole ring. The distance between the pigments within a subunit range from 4 to 11 Å while the nearest neighbor in a different subunit is over 20 Å away [197]. This close proximity of the

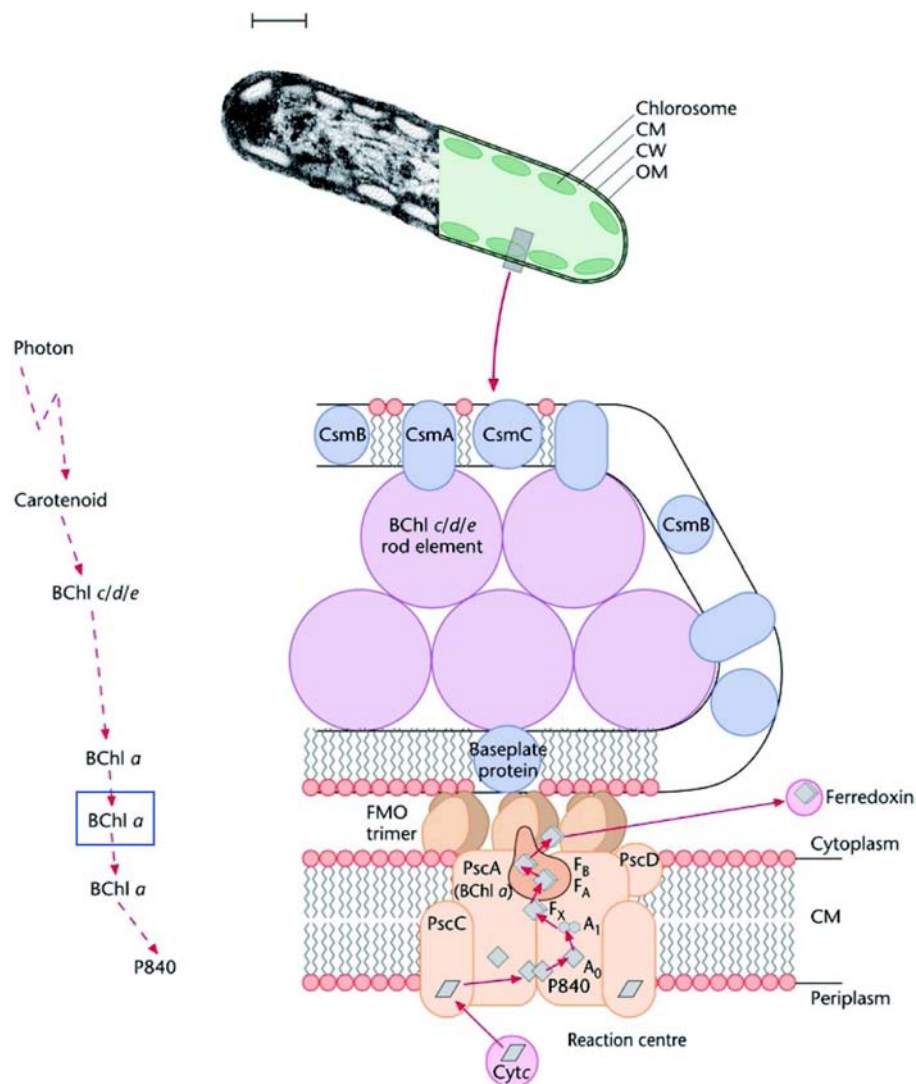


Figure 6.2: Photosynthetic apparatus of the green sulfur bacteria. Chlorosomes are visible as ovoid structures in transmission electron micrographs (bar scale $0.1 \mu\text{m}$) appressed to the inner side of the cytoplasmic membrane (CM). They are connected to the photosynthetic RC in the CM via the trimeric FMO proteins. Dashed arrows at the left indicate the transfer of excitation from the antenna carotenoids and BChls *c/d/e* in the chlorosomes toward P840 in the RC through BChl *a* molecules in the FMO complex (blue box). Reproduced from Ref. [194] with permission of John Wiley & Sons, Inc.

BChl *a* molecules leads to quite strong electronic coupling within a subunit. The recently resolved eighth pigment is located in a cleft at the surface of the subunit (see Fig. 6.3 right) and directed toward the chlorosome [193]. It acts as the linker

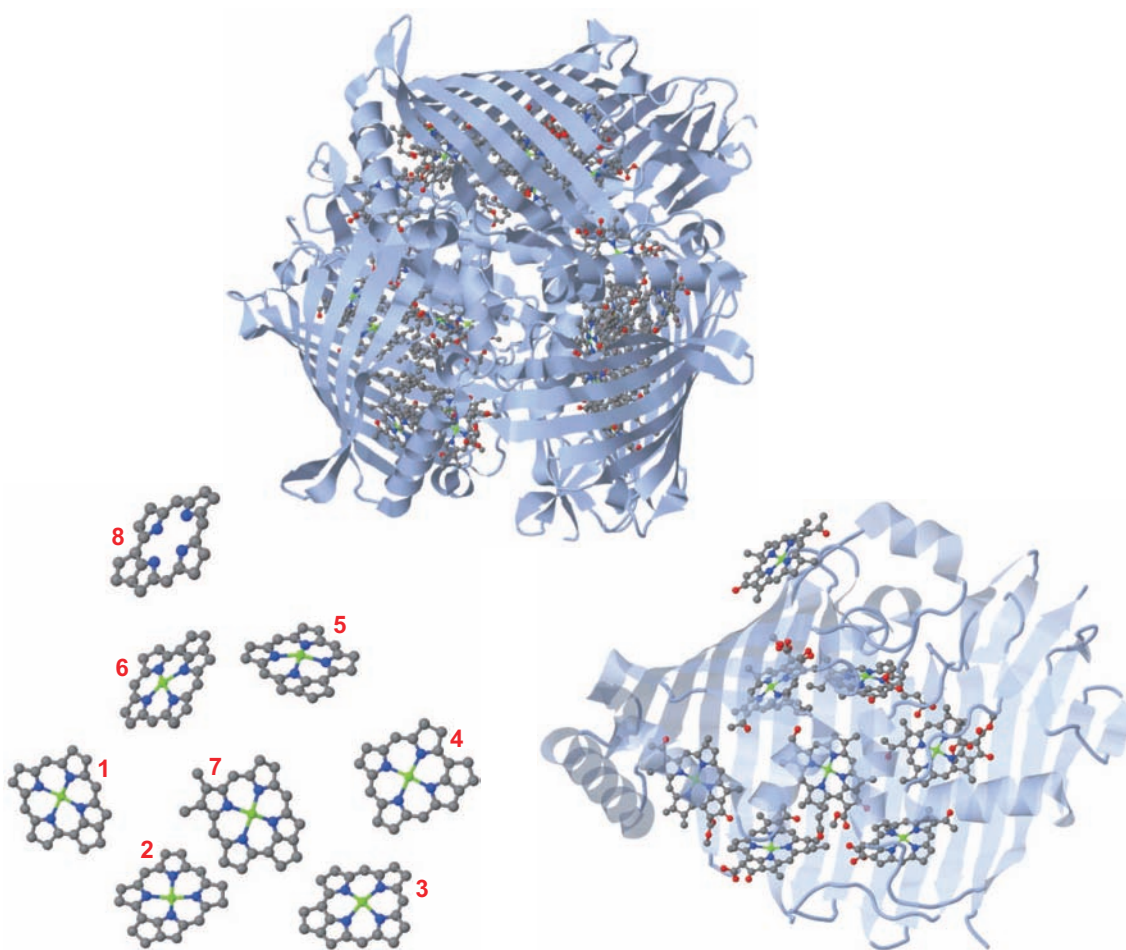


Figure 6.3: Molecular structure of the FMO complex in *Chl. tepidum*. Clockwise from top: trimer protein illustrating the C_3 symmetry; a single monomer subunit illustrating the location of the BChl 8 in a cleft at the surface of the protein shell; and BChls striped out of the protein envelope and of the side groups bound to the tetrapyrrole rings. Standard numeration is indicated by red numbers and the BChl 8 is shown without the central Mg ion. Images created with Jmol [200] from the Protein Data Bank file 3ENI [193].

pigment between the FMO protein and the baseplate protein. It is weakly coupled to the other BChls within the subunit [201] and thus irrelevant for the present investigation. Results in the following chapters are then shown for the remaining seven sites within a single subunit.

Two-dimensional optical spectra of the FMO complex in *Chl. tepidum* displayed beating oscillations in the signals associated to excitonic coherences lasting longer than 1 ps at 77 K [178, 179]. Even at room temperature, rather long-lasting os-

cillations for a few hundreds of fs were described [181]. Similar features were also found in a marine cryptophyte algae [182, 183] and in the light-harvesting complex 2 of the purple bacteria [184]. When electronic excitation of a molecule changes its equilibrium structure, excitation with a femtosecond pulse can generate a vibrational wavepacket that starts off at the equilibrium structure of the ground state and oscillates back and forth around the equilibrium structure of the excited electronic state [202]. However, electronic excitation of isolated chlorophylls does not change its equilibrium structure enough to generate vibrational wavepackets with sufficient vibrational amplitude to explain the observed oscillations due to the rigidity of the tetrapyrrole ring [202]. Therefore, they were assigned to long-lived *electronic* quantum coherence [179, 181]. This would imply that a coherent superposition of excited electronic states samples the most efficient route toward the RC much faster than would be possible by diffusive, incoherent excitation energy transfer [179, 191]. Alternative models, however, have been proposed to explain the observed long-lasting coherences [185, 187, 188, 189, 203]. These models take into account the presence of molecular vibrational modes, 30 of which have been identified experimentally in the FMO complex [162]. This implies that vibronic coupling acts as a significant mechanism to preserve electronic coherence [191].

Currently, there is not an unambiguous explanation about the nature of the long-lived oscillatory components observed in the two-dimensional optical spectra of photosynthetic light-harvesting systems. It has not been uniquely settled whether they are electronic coherences or vibrational coherences, or even a mixture of both. Even less clear is the role played by these long-lasting coherences in the excitation energy transfer dynamics, i.e., whether the energy transfer efficiency is increased by a coherence-assisted transport.

In this Part II of this work, the excitation energy transfer dynamics of the FMO complex is calculated by means of the iterative QUAPI scheme presented in Sec. 2.2.1. In Chap. 7, it is indicated how the FMO complex is modeled. Different environmental fluctuation spectral functions, extracted either from experimental data or from molecular dynamics simulations, are explicitly shown. All these spectral functions include localized vibrational modes. Two possibilities to capture these localized vibrations arise: (i) They can either be taken as part of the environment, or, (ii) their quantum dynamics can explicitly be followed as part of the system Hamiltonian. The difference between both is that in (i), the fluctuations are always assumed to be thermal, i.e., resulting from an equilibrated environment, while in (ii), the fluctuations are effectively non-thermal during the overall relaxation process. Both routes are followed below, with the resulting dynamics due to equilibrium vibrations presented in Chap. 8, while the dynamics due to nonequilibrium vibrations is pre-

sented in Chap. 9. It is shown that the observed long quantum coherence times of the electronic states cannot be explained by equilibrium fluctuations coming from a continuous frequency distribution of the fluctuating pigment-protein-solvent environment. Instead, the explicit nonequilibrium dynamics of the discrete vibrational modes of the molecular backbone may yield increased coherence times. Their effect, however, depends on which molecular site the vibration couples to. In the same way, it is shown that the presence of discrete vibrational states can also enhance the efficiency of the exciton transfer through the FMO complex. Finally, the non-Markovianity measure in Eq. (2.3.4) is used in Chap. 10 to quantify non-Markovian effects during the excitation energy transfer dynamics of the FMO complex in the presence of discrete vibrational modes. The results of this last chapter are useful to clarify the validity of a Markovian quantum master equation to describe the dynamics of the FMO complex which is commonly used in most theoretical works available in the literature, e.g., those in Refs. [188, 204, 205].

Modeling the FMO complex

7.1 FMO Model

Due to the strongly separated time scales of the exciton transfer (\sim ps) and the exciton recombination (\sim ns), the system Hamiltonian for the seven BChl sites within a single subunit of the FMO complex can be formulated within the single excitation subspace as $H_{\text{FMO}} = \sum_{j=1}^7 E_j |j\rangle\langle j| + \sum_{j \neq i} V_{ji} (|j\rangle\langle i| + |i\rangle\langle j|)$. This is also consistent with the weak sunlight intensity under physiological conditions due to the fact that under natural illumination conditions, antenna proteins are photoexcited at a rate that is low enough to guarantee that, at most, only a single excitation exists in an antenna at a given time [206]. The basis states $|j\rangle$ indicate that the j -th site is in its excited state and all other sites are in their ground states. E_j denotes the energy difference between the ground and first excited state of the j -th site and V_{ji} denotes the electronic coupling between sites j and i . Adolphs and Renger [207] have determined the relative shift in excitation energies of the seven sites from calculations of electrochromic shifts due to the charged amino acids of the protein and the different ligand types of the pigments and, independently, from a simultaneous fit of optical spectra (linear dichroism, circular dichroism, absorption, and the derivative of the absorption spectrum) with a genetic algorithm. The resulting Hamiltonian of the

FMO complex of *Chl. tepidum* in the site representation is

$$H_{\text{FMO}} = \begin{pmatrix} 240 & -87.7 & 5.5 & -5.9 & 6.7 & -13.7 & -9.9 \\ & 315 & 30.8 & 8.2 & 0.7 & 11.8 & 4.3 \\ & & 0 & -53.5 & -2.2 & -9.6 & 6.0 \\ & & & 130 & -70.7 & -17.0 & -63.3 \\ & & & & 285 & 81.1 & -1.3 \\ & & & & & 435 & 39.7 \\ & & & & & & 245 \end{pmatrix} \text{cm}^{-1}. \quad (7.1.1)$$

BChl 3 is the site with the lowest energy as revealed by simulations [197, 207]. Experimental results combining chemical labeling and mass spectrometry-based footprinting [208] indicate that this site interacts with the cytoplasmatic membrane, which embeds the reaction center. BChl 3 is then the exit site of the excitation energy in the FMO complex. Combined theoretical and experimental results [197, 208] have also revealed that BChls 1 and 6 are oriented toward the baseplate protein. Therefore, it is believed that these are the initially excited sites. Strictly speaking, because of its closest distance to the baseplate protein [193], and of the fact that it is most strongly coupled to BChls in the baseplate than to the other BChls within the subunit [201], BChl 8 is the initially excited site. Because it is also the blue-most site in the FMO complex (505 cm⁻¹ above the energy of BChl 3 [201]), it transfers its excitation energy to the other sites quickly, mainly to site 1 due to their mutual strong coupling and to site 6 due to their close spatial proximity (see Fig. 6.3 left). Consequently, the assumption that BChls 1 and 6 are the initially excited sites is justified.

The thermal fluctuations induced by the vibrational pigment-protein-solvent environment on the excitation transfer dynamics are described by employing a system-bath model [1, 29] in terms of the total Hamiltonian $H = H_{\text{FMO}} + H_{\text{SB}}$. It is explicitly written as

$$H = H_{\text{FMO}} + \sum_{j=1}^7 |j\rangle\langle j| \sum_k \kappa_k^{(j)} q_{j,k} + \sum_{j=1}^7 \frac{1}{2} \sum_k (p_{j,k}^2 + \omega_{j,k}^2 q_{j,k}^2), \quad (7.1.2)$$

with momenta $p_{j,k}$, displacements $q_{j,k}$, frequencies $\omega_{j,k}$, and couplings $\kappa_k^{(j)}$ of the environmental vibrations at site j . The fluctuations at different BChl sites are assumed to be identical in their characteristics, but spatially uncorrelated [43].

The spectral density function $J(\omega) = \sum_{j,k} \left(|\kappa_k^{(j)}|^2 / 2\omega_{j,k} \right) \delta(\omega - \omega_{j,k})$ fully characterizes the environmental influence on the system dynamics. It has a non-trivial structure with peaks associated to distinct molecular vibrational modes, 30 of which have been identified experimentally in the FMO complex by Wendling *et al.* [162] using temperature-dependent fluorescence line-narrowing measurements.

7.1.1 Experimental determination of the spectral density function

Spectroscopic studies of systems in the condensed phase are hindered by the spectral broadening introduced by the interaction of the electronic and nuclear degrees of freedom of the chromophore with those same degrees of freedom in the surrounding medium [209]. In general, the spectral broadening may have both static and dynamic contributions. In the Markovian picture, a single vibronic transition of a chromophore will have a Lorentzian width resulting from fast (homogeneous) pure dephasing and population decay, dressed with a Gaussian profile resulting from a slowly varying distribution of energy gaps (inhomogeneous broadening) [209]. The spectral density function $J(\omega)$, however, captures all the time scales and no distinctions between fast and slow processes are required.

The electrostatic interaction between the polar solvent and the chromophore is quantified in terms of the solvation energy. In general, the configuration of the surrounding solvent changes in response to a sudden change in the local charge distribution of the chromophore, e.g., a change in its electronic charge density following an optical transition, which results in relaxation of the solvation energy [210]. The driving force for this environmental change is the lowering of overall free energy that accompanies the buildup of solvent polarization [163]. The optical transition energy E_i between ground and excited states of the chromophore i in dilute solution is assumed to be composed of three contributions [211]: an average value for the whole ensemble $\langle E \rangle$, a dynamical part arising from fluctuations in the environment and the chromophore itself δV_i , and an offset from the mean transition energy ΔE_i . Then, $E_i = \langle E \rangle + \delta V_i + \Delta E_i$. Assuming that the fluctuations are similar for all members of the ensemble, it is possible to define a nonequilibrium solvation function, $S_{\text{solv}}(t)$, in terms of solvation energy differences as [163, 211]

$$S_{\text{solv}}(t) \equiv \frac{E_{\text{solv}}(t) - E_{\text{solv}}(\infty)}{E_{\text{solv}}(0) - E_{\text{solv}}(\infty)}. \quad (7.1.3)$$

Within the linear response approximation this becomes [163]

$$S_{\text{solv}}(t) = \frac{\langle \delta V(t) \rangle - \langle \delta V(\infty) \rangle}{\langle \delta V(0) \rangle - \langle \delta V(\infty) \rangle} = \frac{\langle \delta V(0) \delta V(t) \rangle}{\langle \delta V^2 \rangle} = C(t), \quad (7.1.4)$$

with $C(t)$ being the correlation function, which is related to the real part of the bath autocorrelation function in Eq. (2.2.11) as $C(t) = \text{Re } L(t)$ [212]. Because the solvation function $S_{\text{solv}}(t)$ is directly observable (e.g., by time-dependent fluorescence Stokes shift measurements), the spectral density function can be obtained by Fourier transform of the experimental data using Eq. (7.4.2).

Another alternative to obtain $J(\omega)$ is to use the properties of the solvent directly. These enter through the frequency and wave vector-dependent complex dielectric constant, $\varepsilon(\mathbf{k}, \omega) = \varepsilon'(\mathbf{k}, \omega) - i\varepsilon''(\mathbf{k}, \omega)$, with $\varepsilon'(\mathbf{k}, \omega)$ and $\varepsilon''(\mathbf{k}, \omega)$ representing the dispersive and dissipative couplings of the electric field to its electric displacement, respectively. The inverse Laplace transform of the solvation function, defined as $L_p^{-1}[S_{\text{solv}}(t)] \equiv \int_0^\infty dt e^{-i\omega t} S_{\text{solv}}(t)$, is a function of the susceptibility $\chi[\varepsilon(\mathbf{k}, \omega)]$, which is a function of the complex dielectric response, according to [210, 211]

$$L_p^{-1}[S_{\text{solv}}(t)] = \int_0^\infty d^3k \frac{\chi[\varepsilon(\mathbf{k}, 0)] - \chi[\varepsilon(\mathbf{k}, \omega)]}{i\omega (\chi[\varepsilon(\mathbf{k}, 0)] - \chi[\varepsilon(\mathbf{k}, \infty)])}. \quad (7.1.5)$$

Thus, if $\varepsilon(\mathbf{k}, \omega)$ is known through experiment (e.g., far-infrared absorption and microwave dielectric dispersion data) or theory (e.g., classical molecular dynamics simulations), the spectral density can be obtained directly. Explicit details are given in Refs. [210, 211]. Using a macroscopic model of solvation where the solvent is assumed to be a dielectric continuum, like in the simple dielectric continuum model, only the $\varepsilon(\mathbf{k} = 0, \omega)$ component is used, and therefore, the integration over phase space in Eq. (7.1.5) is not necessary. Microscopic details can be incorporated by treating the solvent as a hard sphere fluid, as in the dynamical mean spherical approximation [211]. Notice that the spectral density function defined in Eq. (2.2.9) is intrinsically temperature independent, but the experimentally determined spectral densities from solvation dynamics data are temperature-dependent because, for example, the dielectric constant change with temperature.

The spectral density function can also be determined by using spectral information as provided by temperature-dependent fluorescence line-narrowing (FLN) measurements. The use of the fluorescence spectrum rather than the absorption one is due to the fact that the static disorder in the absorption spectrum introduced by the protein and solvent environment overwhelms other details of that spectrum [216]. FLN measurements allow one to extract the one-phonon-vibration profile, which can be treated as a distribution of modes, including phonons and vibrations [213]. Specifically, it contains one-bulk-phonon (observed as the background) and one-vibration (observed as spikes at specific vibrational frequencies) contributions [162]. The extracted vibrational frequencies and their corresponding Franck-Condon factors for the excited to ground state transitions of the FMO complex are listed in Table 7.1. For one-vibration transitions, the Franck-Condon factor FC_i is equal to $S_i \exp(-S_i)$, with S_i being the Huang-Rhys factor. S_i characterizes the strength of the exciton-vibration coupling and is related to the displacement between the minimum energy positions of harmonic vibrational potentials associated with the ground and excited electronic states [29]. If $S_i < 0.1$, FC_i can be well approximated by S_i [162].

ω [cm ⁻¹]	FC factor	ω [cm ⁻¹]	FC factor	ω [cm ⁻¹]	FC factor
36	0.01	365	0.002	747	0.002
70	0.01	381	0.002	759	0.002
117	0.0055	479	0.001	768	0.004
173	0.008	541	0.001	777	0.0015
185	0.008	565	0.002	819	0.002
195	0.011	580	0.001	859	0.0025
237	0.005	635	0.003	896	0.002
260	0.0025	714	0.002	1158	0.004
284	0.005	723	0.003	1176	0.003
327	0.0015	730	0.001	1216	0.002

Table 7.1: Vibrational frequencies and Franck-Condon factors of the FMO complex determined from FLN measurements by Wendling *et al.* [162].

Different environmental spectral densities of the FMO complex result from different approaches. Aghtar *et al.* [165] (see Sec. 7.4) have obtained a spectral density from molecular dynamics simulations of the FMO complex in specific solvent environments. Adolphs and Renger [207] as well as Kreisbeck and Kramer [214, 215] extract a spectral density from the experimental results of Wendling *et al.* [162], but eventually obtain different functions. Adolphs and Renger (see Sec. 7.2) describe the phonon background based on data available for the B777-complexes [216] and add a single intramolecular vibrational mode in form of a δ -peak, which is believed to be the most relevant mode. In contrast, Kreisbeck and Kramer (see Sec. 7.3) are forced to parametrize the spectral density function as a sum of shifted Drude-Lorentz peaks, corresponding to the vibrational contribution of the one-phonon-vibration profile, due to the hierarchy equation of motion approach used to determine the dynamics.

7.2 Spectral density of Adolphs and Renger

Adolphs and Renger [207] give a closed expression for the spectral density based on two contributions: (i) a broad continuous low-frequency part $S_0 g_0(\omega)$, which originates in the phonon-like protein vibrations and contributes with the Huang-Rhys factor S_0 , and (ii) a single effective vibrational mode $S_H \delta(\omega - \omega_H)$ of the pigments with Huang-Rhys factor S_H . The total spectral density is written as

$$J(\omega) = \omega^2 S_0 g_0(\omega) + \omega^2 S_H \delta(\omega - \omega_H). \quad (7.2.1)$$

If one assumes that the local modulation of pigment transition energies by the

protein environment is a global quantity that does not differ much between the specific environment of the pigments [207], the low-frequency function $g_0(\omega)$ has the same form as the spectral density that was originally extracted from 1.6 K FLN spectra of B777-complexes measured at different excitation wavelengths [216]. These complexes consist of an α -helix and a BChl molecule, which makes them model systems for all larger complexes containing BChls, like the FMO complex. Roughly speaking, the FLN spectrum contains a resonant fluorescence band at the excitation wavelength and a vibrational sideband. At low temperature, the shape of the vibrational sideband is the same as the shape of the spectral density $g_0(\omega)$ [216]. In the case of the B777-complex, the shape of the sideband in the FLN spectrum excited in the low-energy wing of the absorption spectrum was used as a first guess for the spectral density. It was parametrized by the empirical functional form [216] $g_0(\omega) = \sum_{i=1,2} s_i k_i \omega^q e^{-(\omega/\omega_i)^p}$, with normalization factors s_i , ω_i , p , and q , k_i , and the overall Huang-Rhys factor given by $S = s_1 + s_2$. Excitation at higher energies leads to a broadening of the sideband, which can be used to estimate S , since its weight is determined by S [216]. The fit at the different excitation wavelengths gives the explicit form

$$g_0(\omega) = (6.105 \times 10^{-5}) \frac{\omega^3}{\omega_1^4} \exp \left[-\sqrt{\frac{\omega}{\omega_1}} \right] + (3.8156 \times 10^{-5}) \frac{\omega^3}{\omega_2^4} \exp \left[-\sqrt{\frac{\omega}{\omega_2}} \right],$$

with $\omega_1 = 0.575 \text{ cm}^{-1}$ and $\omega_2 = 2 \text{ cm}^{-1}$. The Huang-Rhys factor of the protein-pigment coupling was estimated to be $S_0 \sim 0.5$ and yields a satisfactory agreement with the experimental data.

In addition, Adolphs and Renger have included an effective single vibrational mode of the pigments at frequency $\omega_H = 180 \text{ cm}^{-1}$ with the Huang-Rhys factor $S_H = 0.22$ [207]. Wendling *et al.* [162], however, have identified up to 30 vibrational modes in their experimental data (see Table 7.1). Out of this, Adolphs and Renger constructed the effective Huang-Rhys factor S_H of a single vibrational mode at ω_H by including all high-frequency vibrational modes in the effective single mode. The value of $S_H = 0.22$ given by Adolphs and Renger appears to be somewhat large, which is due to the effective description [207]. In more detail, the effective mode at 180 cm^{-1} in fact consists of three strongly overlapping vibrational modes at 173, 185, and 195 cm^{-1} (bold numbers in Table 7.1). Following Wendling *et al.* [162], it is possible to combine the weight of these three modes to an effective Huang-Rhys factor of $S_H = 0.027$. Likewise, in a related work on the vibronic fine structure of the light-harvesting complex II of green plants [161], up to 48 vibrational modes were found with considerably smaller Huang-Rhys factors. Hence, for the single effective vibrational mode constructed by Adolphs and Renger [207], all spectral weight is

concentrated at this mode while, in a more detailed picture, the spectral weight is spread over many channels.

The Huang-Rhys factor S_H defines the coupling strength of a vibrational mode at frequency ω_H to the j -th excited site by $\kappa^{(j)} = \omega_H \sqrt{S_H}$. This is the coupling parameter in the Hamiltonian $H_{\text{exc-vib}} = \kappa^{(j)} |j\rangle \langle j| (a^\dagger + a)$ for the coupling of the excited site j to the vibrational mode with bosonic creation and annihilation operators a^\dagger and a . The Huang-Rhys factors $S_H = 0.22$ (from Adolphs and Renger [207]) and $S_H = 0.027$ (from Wendling *et al.* [162], bold numbers in Table 7.1), result in an exciton–vibrational mode coupling strengths of 84 and 30 cm^{-1} , respectively. Comparing these results to the site couplings of the FMO complex given in Eq. (7.1.1), these two values can be considered as being in the strong and intermediate coupling regime, respectively. Nevertheless, only small quantitative differences arise in the resulting dynamics for these two regimes (see Sec. 8.1 and Chap. 9).

Under realistic physiological conditions, the δ -peak in Eq. (7.2.1) should be broadened since the protein is embedded in water, which, as a polar solvent, gives rise to an additional weak Ohmic damping of the protein vibrations [43]. It is assumed that the broadening has a Lorentzian line shape with width γ in the form

$$\omega^2 S_H \delta(\omega - \omega_H) \rightarrow S_H \omega_H^2 \gamma \frac{\omega^2}{(\omega^2 - \omega_H^2)^2 + (\gamma\omega)^2}. \quad (7.2.2)$$

This specific form of the peak ensures that the Huang-Rhys factor S_H is kept constant when varying the width γ . The resulting spectral density function of Eq. (7.2.1) is shown in Fig. 7.1 for several widths γ .

The influence of vibrational modes on the system dynamics is relevant only when their energies are comparable to the energy difference between the exciton states [44]. The exciton states $|\Phi_r\rangle$ of the FMO complex are obtained by diagonalizing Eq. (7.1.1), such that $|\Phi_r\rangle = \sum_{j=1}^7 b_{r,j} |j\rangle$. The squares of the eigenvector elements of the seven exciton states $|b_{r,j}|^2$ are tabulated in Table 7.2 and schematically shown in Fig. 7.2. These results indicate that the lowest-energy exciton 1 is almost completely localized at BChl 3, which is in agreement with this site being the energy sink toward the reaction center. The excitons 3 and 6 are mainly localized on BChls 1 and 2, which are the most strongly coupled sites in the Adolphs-Renger FMO Hamiltonian [Eq. (7.1.1)]. In contrast, the excitons 5 and 7 are mainly localized on BChls 5 and 6. This is the second most strongly coupled BChl pair. From the results in Table 7.2, the energy difference between excitons 3 and 6 and between excitons 5 and 7 is 190.8 and 211.0 cm^{-1} , respectively. Due to the orientation of BChls 1 and 6, it is expected that these specific excitons play a relevant role on the excitation energy transfer dynamics, in particular, since their energy differences are close to that of the localized vibrational mode at 180 cm^{-1} .

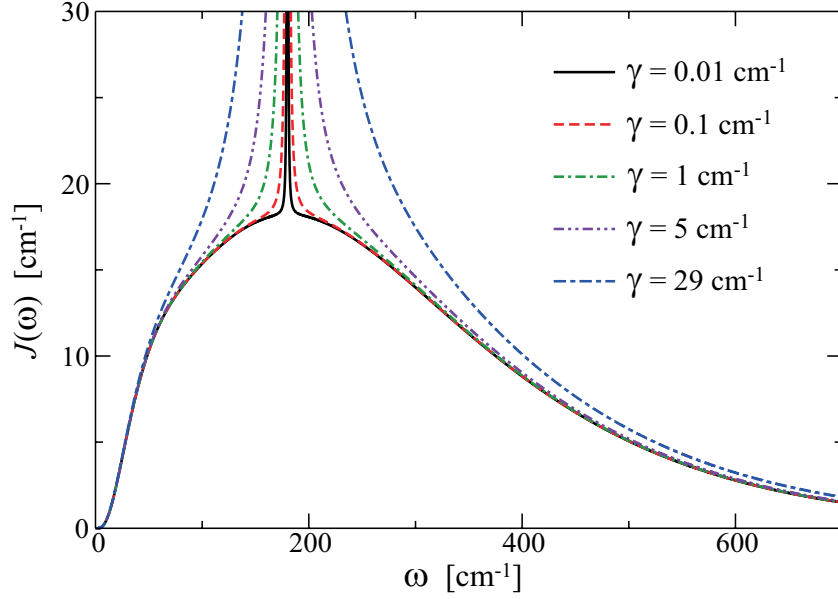


Figure 7.1: Spectral density function of Adolphs and Renger [Eq. (7.2.1)] for different Lorentzian peak widths γ centered at $\omega_H = 180 \text{ cm}^{-1}$.

Exc.	BChl 1	BChl 2	BChl 3	BChl 4	BChl 5	BChl 6	BChl 7	Energy
1	0.00	(-)0.01	0.83	0.15	0.01	0.00	0.00	0.0
2	0.01	0.00	(-)0.14	0.59	0.11	(-)0.01	0.14	123.7
3	0.69	0.27	0.01	0.00	(-)0.01	0.00	0.00	209.9
4	0.00	(-)0.01	0.00	(-)0.03	(-)0.26	0.00	0.70	286.1
5	0.00	0.01	0.01	(-)0.20	0.43	(-)0.22	0.12	301.6
6	0.29	(-)0.67	0.00	(-)0.01	0.02	0.00	0.00	400.7
7	0.01	(-)0.01	0.00	0.02	(-)0.16	(-)0.76	(-)0.03	512.6

Table 7.2: Square of the eigenvector elements $|b_{r,j}|^2$ of the FMO Hamiltonian [Eq. (7.1.1)] in the exciton representation with exciton numeration in ascending energy order. Energy is given in units of cm^{-1} . The negative sign (-) indicates that the corresponding eigenvector element is negative and the bold numbers indicate the dominant site contribution to the excitonic state.

If the ω_H value of the Lorentzian peak in Eq. (7.2.2) is equal to the energy difference between an exciton pair, it corresponds to the effective single vibrational mode being resonant with the transition energy between the involved excitons. When $\omega_H = 190.8 \text{ cm}^{-1}$ or when $\omega_H = 211.0 \text{ cm}^{-1}$, the effective vibrational mode is in resonance with the energy difference between excitons 3 and 6 and between excitons

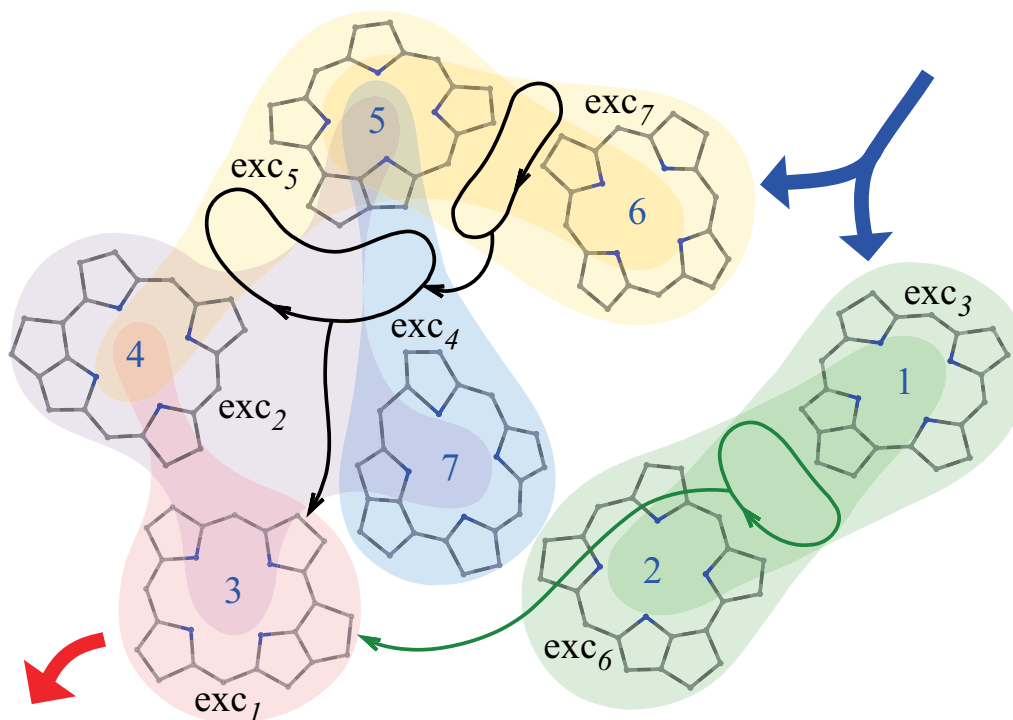


Figure 7.2: Structural arrangement of the seven BChl molecules (blue numbers) in the FMO complex of *Chl. tepidum* [193] superposed with a schematic representation of the delocalization patterns of the different excitons $|\Phi_r\rangle$ (colored shading, italic black numbers). The exciton numeration is in ascending energy order. The two main excitation transfer routes are indicated by the green and black thin arrows. Entrance and exit sites are indicated by blue and red thick arrows, respectively.

5 and 7, respectively. The resulting spectral density functions are shown in Fig. 7.3, together with the case where no localized vibration exist. The excitation energy transfer dynamics of the FMO complex for all these cases is examined in Chap. 8.

7.3 Spectral density of Kreisbeck and Kramer

The vibronic component of the experimentally determined fluctuational spectrum of the FMO complex [162] was parametrized by Kreisbeck and Kramer [214, 215] using the Meier-Tannor decomposition [217]. The latter represents a general spectral density function as a sum of shifted Drude-Lorentz peaks. The resulting environmental

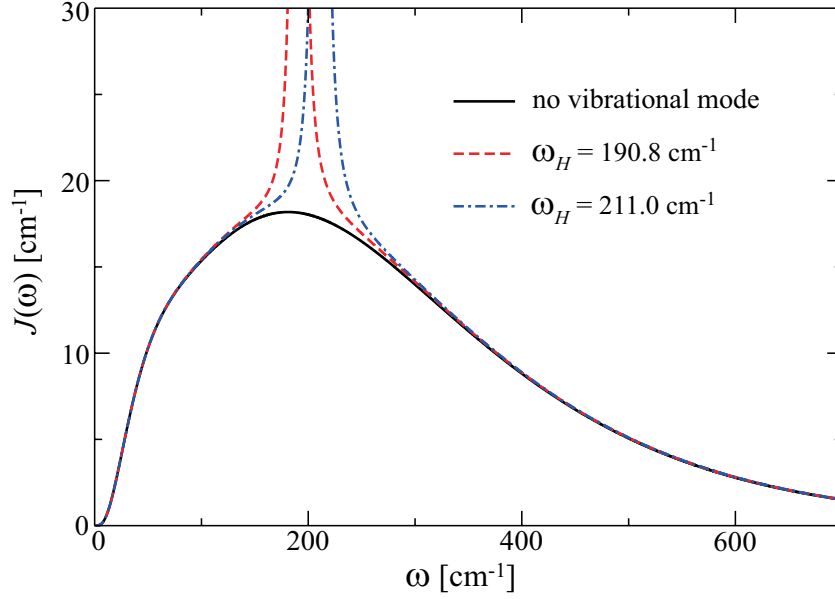


Figure 7.3: Spectral density function of Adolphs and Renger [Eq. (7.2.1)] with no localized vibrational mode (solid black line) and for ω_H in resonance with excitonic energy differences: $\omega_H = 190.8 \text{ cm}^{-1}$ (dashed red line) and $\omega_H = 211.0 \text{ cm}^{-1}$ (dash-dotted blue line). $\gamma = 1 \text{ cm}^{-1}$ in both cases.

spectral density for the FMO complex has the form

$$J_n(\omega) = \sum_{k=1}^n \left[\frac{\nu_k \lambda_k \omega}{\nu_k^2 + (\omega + \Omega_k)^2} + \frac{\nu_k \lambda_k \omega}{\nu_k^2 + (\omega - \Omega_k)^2} \right]. \quad (7.3.1)$$

Figure 7.4 shows the spectral density function in Eq. (7.3.1) with the corresponding parameters listed in Table 7.3. The experimental spectral density is well approximated by the sum of 11 shifted Drude-Lorentz peaks [$n = 11$ in Eq. (7.3.1)], reproducing the low-frequency portion and taking into account all the strongly coupled vibronic modes. They are visible as peaks in the spectral density function. An alternative parametrization with only three peaks [$n = 3$ in Eq. (7.3.1)] is also given.

7.4 Spectral density of Aghtar *et al.*

The spectral density function for the FMO complex has been calculated from molecular dynamics simulations by Aghtar *et al.* [165]. Their procedure [218], which has been also used to calculate the spectral density function of the light-harvesting II

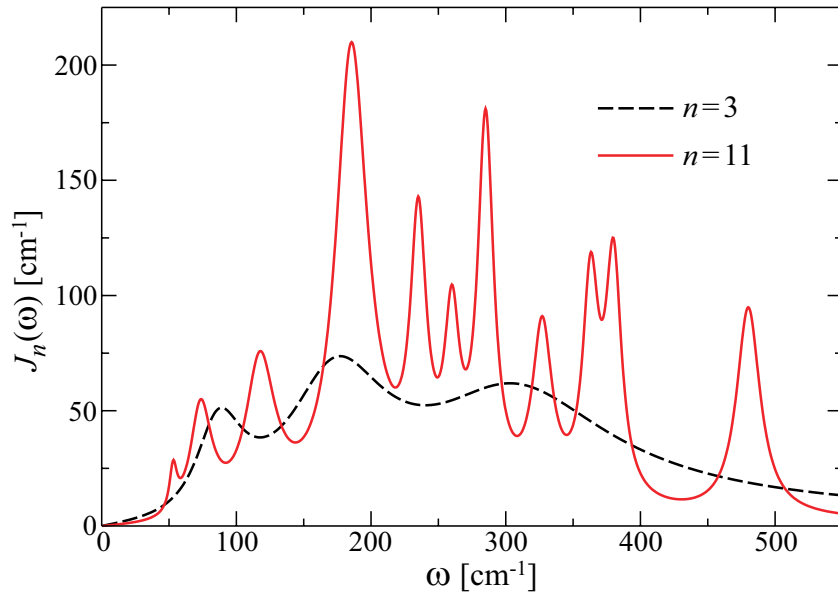


Figure 7.4: Spectral density function of Kreisbeck and Kramer for the FMO complex in form of a sum of shifted Drude-Lorentz peaks [Eq. (7.3.1)] with the parameters listed in Table 7.3.

3-peaks	Ω_k	85	170	300								
	ν_k^{-1}	250	120	65								
	λ_k	10	15	13								
11-peaks	Ω_k	53	73	117	185	235	260	285	327	363	380	480
	ν_k^{-1}	1600	550	400	370	750	800	750	600	750	750	500
	λ_k	1.2	6.4	7.4	15.6	3.4	1.8	4	2	1.8	1.9	2

Table 7.3: Parameters of the spectral density function [Eq. (7.3.1)] derived by Kreisbeck and Kramer [214]. Ω_k and λ_k are given in units of cm^{-1} and ν_k^{-1} is given in units of femtoseconds.

complex [164], consists in ground state energy minimizations at different temperatures and normal pressure, i.e., molecular dynamics simulations. The effects of thermal fluctuations on the energy transfer dynamics and optical properties are accounted for by quantum chemistry calculations of the excitation energies and the electronic couplings along the molecular dynamics trajectories. For this, they use Zerner’s intermediate neglect of differential overlap method with parameters for spectroscopic properties together with the configuration interaction scheme using single excitations only (ZINDO/S-CIS) [219]. Specifically, as the nuclear degrees

of freedom of the bath [modeled as the classical coordinates $q_k^{\text{cl}}(t)$] fluctuate about their equilibrium configuration, the energy gap between the BChl i ground and first excited state fluctuates about its average value (i.e., its site energy E_i) as the function $E_i + \sum_k c_k^{(i)} q_{i,k}^{\text{cl}}(t)$, with $c_k^{(i)}$ being the strength of the system-bath coupling in Eq. (2.2.1). The correlation function $C_i(t)$ of the BChl i energy gap fluctuations about its equilibrium average at temperature T is then [5]

$$C_i(t) = \sum_k |c_k^{(i)}|^2 \langle q_{i,k}^{\text{cl}}(t) q_{i,k}^{\text{cl}}(0) \rangle_{k_B T}, \quad (7.4.1)$$

which is related to the real part of the bath autocorrelation function in Eq. (2.2.11) as $C_i(t) = \text{Re } L_i(t)$ [212]. This allows one to obtain the spectral density function $J_i(\omega)$ of site i through

$$J_i(\omega) = \frac{2}{\pi \hbar} \tanh\left(\frac{\hbar \omega}{2k_B T}\right) \int_0^\infty dt C_i(t) \cos(\omega t). \quad (7.4.2)$$

It describes the frequency-dependent coupling of BChl i to the thermal environment [165]. Molecular dynamics simulations allow one to include the microscopic description of the solvent environment used in the experimental measurements of the FMO complex [179, 181]. Here, two specific cases are considered: water as a solvent at 300 K and a glycerol:water 65:35 mixture as a solvent at 310 K. The resulting site-dependent spectral density functions $J_i(\omega)$ are shown in Fig. 7.5.

7.5 Discussion

In spite of the specific details of the different spectral densities in Eqs. (7.2.1), (7.3.1), and (7.4.2), all of them include peaks associated with particular vibrational modes of the pigment-protein-solvent environment. The spectral density functions derived by Adolphs and Renger [207] (Sec. 7.2) and by Kreisbeck and Kramer (Sec. 7.3) are based on experimental data and can be considered as more accurate. However, they differ in how the vibrational modes are treated and therefore obtain different functions. The most simplified fluctuational spectrum is that obtained by Adolphs and Renger because they construct a single effective vibrational mode carrying all spectral weight, as specified by the large Huang-Rhys factor associated with the effective mode. In contrast, experimental results indicate that the spectral weight is spread over many channels (see Table 7.1). Kreisbeck and Kramer on the other hand, use the experimentally determined vibronic component but the resulting spectral density function is parametrized as a sum of shifted Drude-Lorentz peaks. Note that in both cases, the fluctuations at different BChl sites are assumed to be

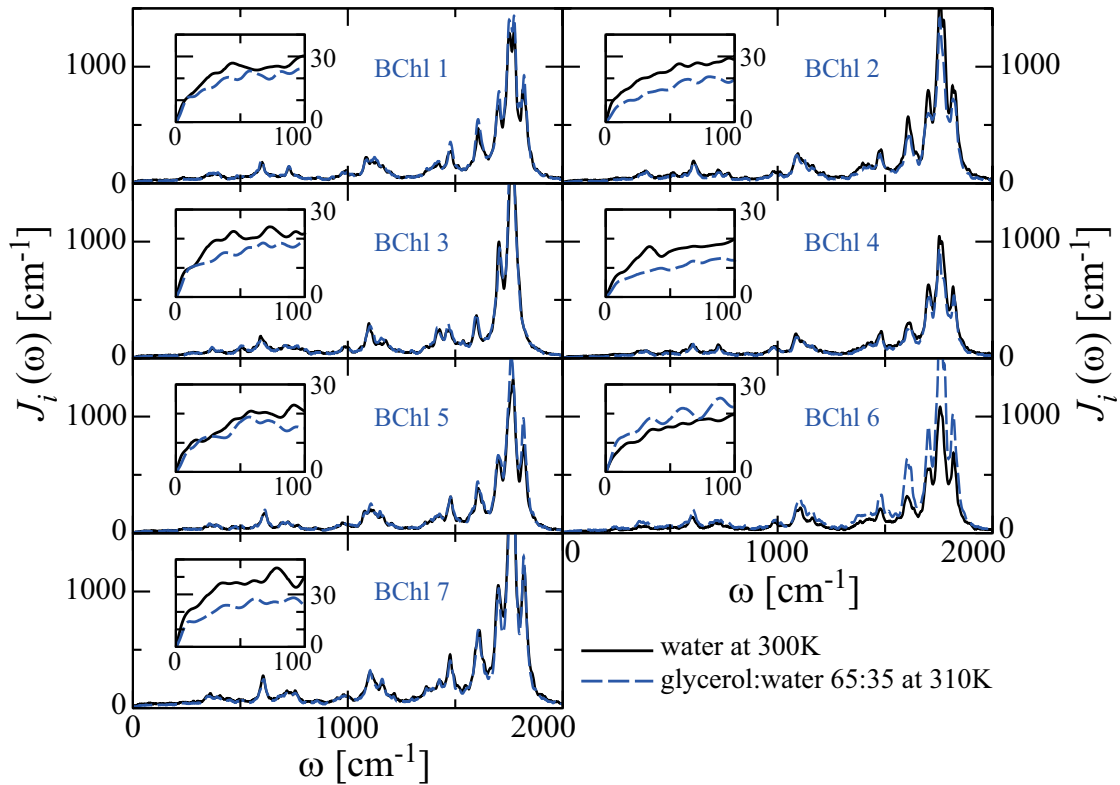


Figure 7.5: Site-dependent spectral density functions $J_i(\omega)$ of Aghtar *et al.* for the FMO complex as determined from molecular dynamics simulations [165] with water as a solvent at 300 K (solid black line) and with a glycerol:water 65:35 mixture as a solvent at 310 K (dashed blue line). The low-frequency region is shown in the insets.

identical in their characteristics and specific details of the environment surrounding a particular BChl site are neglected. These details, as well as those of the polar solvent, are included in the fluctuational spectrum derived by Aghtar *et al.* (Sec. 7.4), which makes it more realistic. However, the amount of atoms involved requires the use of ground-state molecular dynamics that includes approximations due to the underlying force field [218].

In summary, the spectral density functions derived by Adolphs and Renger and by Kreisbeck and Kramer allow one to evaluate the effect of a single and several localized vibrational modes on the excitation energy transfer dynamics of the FMO complex. The site-dependent spectral density functions derived by Aghtar *et al.* allow one to evaluate the effect of the specific microscopic details of the polar environment. The resulting dynamics generated by all these models is presented in Chap. 8. The fluctuational spectrum derived by Adolphs and Renger will be used

in Chap. 9 to evaluate the influence of an underdamped vibrational mode on the quantum coherent beatings and on the energy transfer speed through the FMO complex.

Dynamics in presence of equilibrium vibrations

All spectral density functions of the FMO complex presented in Chap. 7 exhibit a nontrivial structure with several peaks attributed to vibrational modes of the pigment-protein complex. The fluctuational spectra derived by Adolphs and Renger [207] [Eq. (7.2.1) and Figs. 7.1 and 7.3] and by Kreisbeck and Kramer [214] [Eq. (7.3.1) and Fig. 7.4] include, respectively, a single and several localized vibrational modes. On the other hand, the site-dependent fluctuational spectra derived by Aghtar *et al.* [165] [Eq. (7.4.2) and Fig. 7.5] include the specific microscopic details of the polar environment. All of them are compared in Fig. 8.1 for BChl 1. It is clear that the fluctuational spectra derived by Aghtar *et al.* exhibit the largest spectral weight at low frequencies, while the opposite applies for the fluctuational spectra derived by Kreisbeck and Kramer. This indicates that the dynamics in the Aghtar *et al.* model exhibits the shortest coherence times (Sec. 8.3), while the dynamics in the Kreisbeck and Kramer model shows the longest coherence times (see Sec. 8.2). The dynamics generated by the spectral density of Adolphs and Renger (see Sec. 8.1) exhibits coherence times that are in between these extreme cases.

In this chapter, the vibrational modes of the pigment-protein complex are explicitly included as part of the environment. It is important to note that, within the open system approach used here, the environment is assumed to be in thermal equilibrium, thus allowing to investigate the influence of quantum and thermal equi-

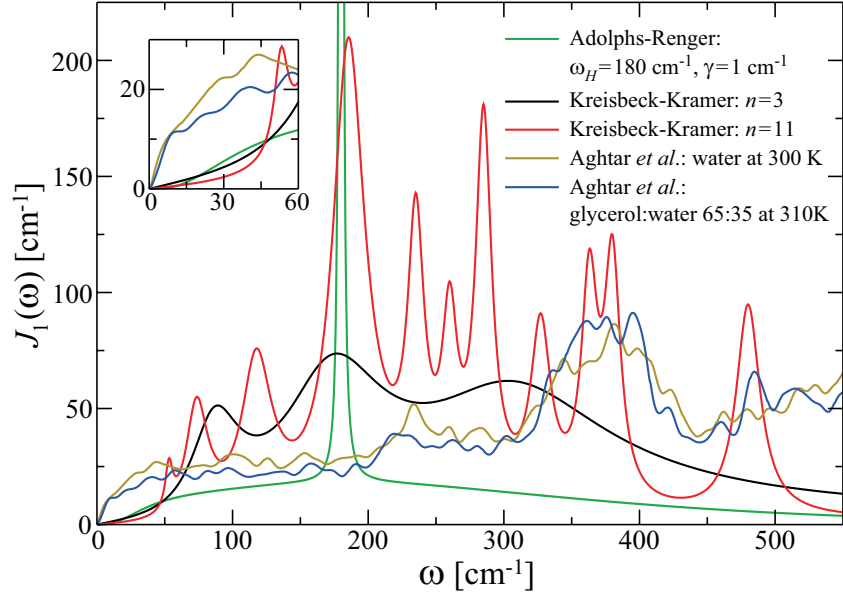


Figure 8.1: Spectral density functions $J_1(\omega)$ in Eqs. (7.2.1), (7.3.1), and (7.4.2) for BChl 1. The inset shows the low-frequency region.

librium fluctuations on the system. By including specific vibrational modes with a substantial coupling to the system into the environmental spectrum one assumes, consequently, that the thermalization time scale of these modes is much shorter than any system time scale. This does not exclude non-Markovian dynamics of the system but only nonequilibrium fluctuations of the vibrational modes.

The real-time excitation energy transfer dynamics of the FMO complex for the different models presented in Chap. 7 is examined by using the iterative QUAPI scheme presented in Sec. 2.2.1. Here, the extended scheme [37], in which each BChl site interacts with a separate environment, is used (see Sec. 2.2.2). Two typical experimental values for the temperature T are considered: cryogenic temperature (77 K) and physiological temperature (300 K). The two initial preparations $\rho_{11}(0) = 1$ and $\rho_{66}(0) = 1$, corresponding to the initially excited BChls 1 and 6, are evaluated. Considering these initial conditions and the coupling among BChls given in Eq. (7.1.1), as well as the delocalization of the exciton wavefunctions indicated in Table 7.2, two main excitation energy transfer routes emerge [178], which in site representation are $1 \rightarrow 2 \rightarrow 3$ and $6 \rightarrow (5/7) \rightarrow 4 \rightarrow 3$. They are schematically indicated in Fig. 7.2 by the green and black thin arrows, respectively. The resulting dynamics is reported in terms of the time-dependent site occupation probabilities $\rho_{jj}(t) = \langle j | \rho(t) | j \rangle$, where coherent oscillations in the population of the chromophores are signatures of coherent energy transfer.

8.1 Population dynamics in the Adolphs-Renger model

Here, the exciton dynamics in the FMO complex for the spectral density function derived by Adolphs and Renger [207] [Eq. (7.2.1)] is simulated. A Huang-Rhys factor of $S_H = 0.22$ is considered, i.e., results are presented for the strong exciton–vibrational coupling regime. In this regime, coherence times are expected to be shorter, and therefore represent a lower bound. The influence of the spectral position ω_H and width γ of the Lorentzian peak in Eq. (7.2.2) on the quantum coherent dynamics is evaluated systematically.

The time-dependent pigment occupation probabilities $\rho_{jj}(t)$ when the localized vibrational mode is centered at $\omega_H = 180 \text{ cm}^{-1}$ with width $\gamma = 1 \text{ cm}^{-1}$ are shown in Fig. 8.2. Identical results have been obtained for smaller (up to 0.01 cm^{-1})

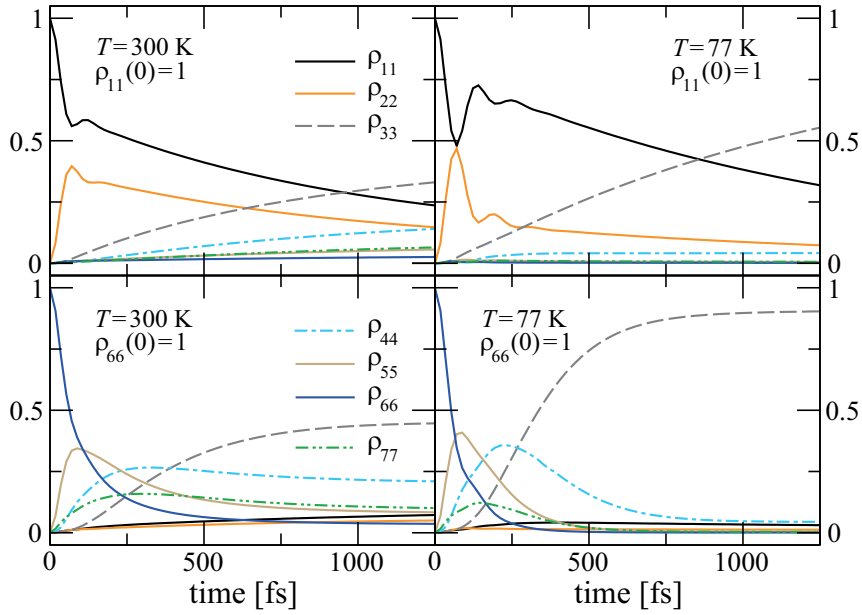


Figure 8.2: Time-dependent occupation probabilities of all seven FMO sites for $T = 300$ (left) and 77 K (right) with $\rho_{11}(0) = 1$ (top) and $\rho_{66}(0) = 1$ (bottom) for the spectral density function derived by Adolphs and Renger [Eq. (7.2.1)] with $\omega_H = 180 \text{ cm}^{-1}$ and $\gamma = 1 \text{ cm}^{-1}$.

and for larger (up to 30 cm^{-1}) peak widths, as exemplified in Fig. 8.3 for BChl 1, which indicates almost no dependence on the width of the Lorentzian peak. This can be explained by observing that in the present case, the continuous background spectrum $g_0(\omega)$ is rather large (see Figs. 7.1 and 7.3), which broadens the exciton

transitions leading to a weak dependence on the width γ of the Lorentzian peak.

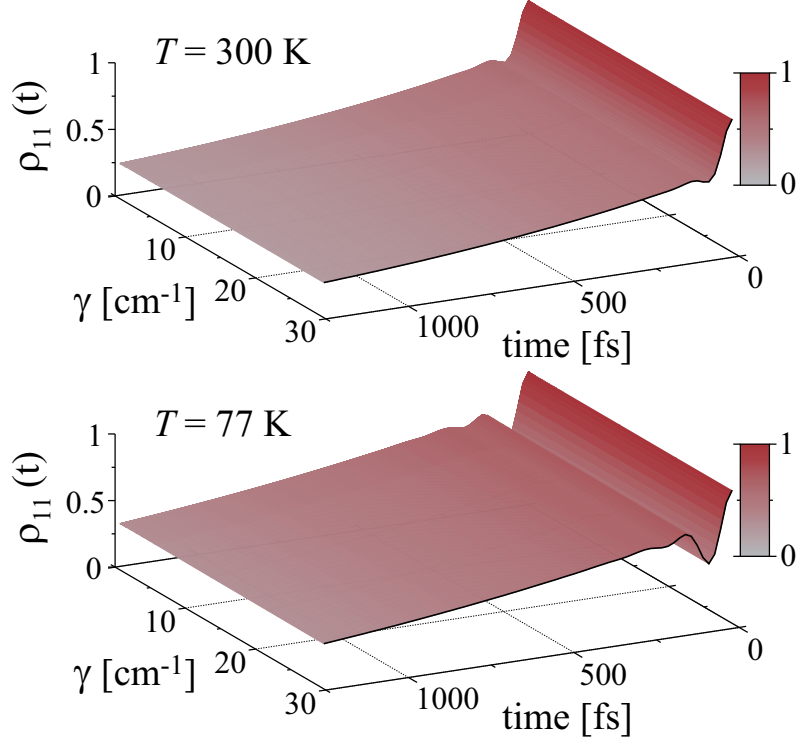


Figure 8.3: Peak width dependence of the population of BChl 1 for $\rho_{11}(0) = 1$ at 300 K (top) and at 77 K (bottom) for the spectral density function derived by Adolphs and Renger [Eq. (7.2.1)] with $\omega_H = 180 \text{ cm}^{-1}$.

The results show that for $\rho_{66}(0) = 1$, coherent oscillations are suppressed even at cryogenic temperature, while for $\rho_{11}(0) = 1$ they survive for up to 250 fs at room temperature and for up to about 500 fs at cryogenic temperature. As expected, coherent oscillations are supported longer for $\rho_{11}(0) = 1$ due to the strong electronic coupling between sites 1 and 2 as compared to that between sites 5 and 6 or 6 and 7 when $\rho_{66}(0) = 1$. It is interesting to note in Fig. 8.2 that the population of BChl 3 grows faster for $\rho_{66}(0) = 1$ than for $\rho_{11}(0) = 1$. Because this site is connected to the reaction center (RC), an increased population of this site means a higher transfer efficiency toward the RC and therefore an overall enhanced efficiency in the excitation energy transfer of the FMO complex. The results indicate that the faster energy transfer route is $6 \rightarrow (5/7) \rightarrow 4 \rightarrow 3$. This route has been indentified by Adolphs and Renger [207] as the fast subpicosecond transfer branch as compared to the relatively slow picosecond transfer branch of excitons, which involves BChls 1 and 2. This faster energy transfer route however, does not necessarily lead to

sustained coherent oscillations in the population dynamics.

Recently, it has been shown that the 180 cm^{-1} mode drives strong long-lasting coherent oscillations in an effective (two sites) FMO model [187]. There, a multi-frequency beating and a revival dynamics in the coherences $\rho_{ij}(t)$ have been observed and interpreted as an indicator of mode-driven coherence. In Fig. 8.4 are shown the time-dependent pigment coherences $\rho_{ij}(t)$ of the FMO complex with the localized vibrational mode centered at $\omega_H = 180 \text{ cm}^{-1}$ with width $\gamma = 1 \text{ cm}^{-1}$. These coherences are evaluated along the two main excitation energy transfer pathways indicated in Fig. 7.2. Similar to the site populations, the coherences decay faster at higher temperatures. Identical results for the coherences have been obtained for a wide range of γ values (not shown). In any case, sustained coherent oscillations are not observed in this full FMO model, neither in the real part nor in the imaginary part of the coherences. Rather, their decay times are similar to those of the populations and therefore, the same observations made before about the coherence times remain valid. These results indicate that the width of the localized vibrational mode at 180 cm^{-1} at thermal equilibrium does not modify substantially the dynamics of the FMO complex.

In order to evaluate the effect of the localized vibrational mode in resonance with exciton energy differences, in Fig. 8.5 are shown the populations and coherences of the FMO complex when $\omega_H = 190.8$ and $\gamma = 0.01 \text{ cm}^{-1}$ and when $\omega_H = 211.0 \text{ cm}^{-1}$ and $\gamma = 29 \text{ cm}^{-1}$. The width of 29 cm^{-1} has been found for the lowest energy peak of protein vibrations in the the light-harvesting II complex [164]. The evaluated ω_H values correspond to the localized vibrational mode exactly in resonance with the energy difference between excitons 3 and 6 (190.8 cm^{-1}) and between excitons 5 and 7 (211.0 cm^{-1}). It is observed that the behavior of the populations and the coherences is similar for these two ω_H values, and also similar to that obtained when the vibrational mode is centered at $\omega_H = 180 \text{ cm}^{-1}$ (compare with Figs. 8.2 and 8.4). Identical results are obtained for a wide range of γ values, as shown in Fig. 8.6 for the population of BChl 1, with only minor changes in the transient behavior of the populations (with respect to those in Fig. 8.3) and coherences due to the different spectral weight of the Lorentzian peak for different peak widths (see Fig. 7.1). These results confirm that the width of the vibrational mode at thermal equilibrium does not have any noticeable influence on the populations or the coherences of the FMO complex, even when it is in resonance with exciton transitions.

Results for the pigment occupation probabilities $\rho_{jj}(t)$ and coherences $\rho_{ij}(t)$ in the absence of any localized vibrational mode are shown in Figs. 8.7 and 8.8, respectively. Here, qualitative and quantitative differences are observed. In particular, the absence of the localized mode leads to a lower weight of the spectral density func-

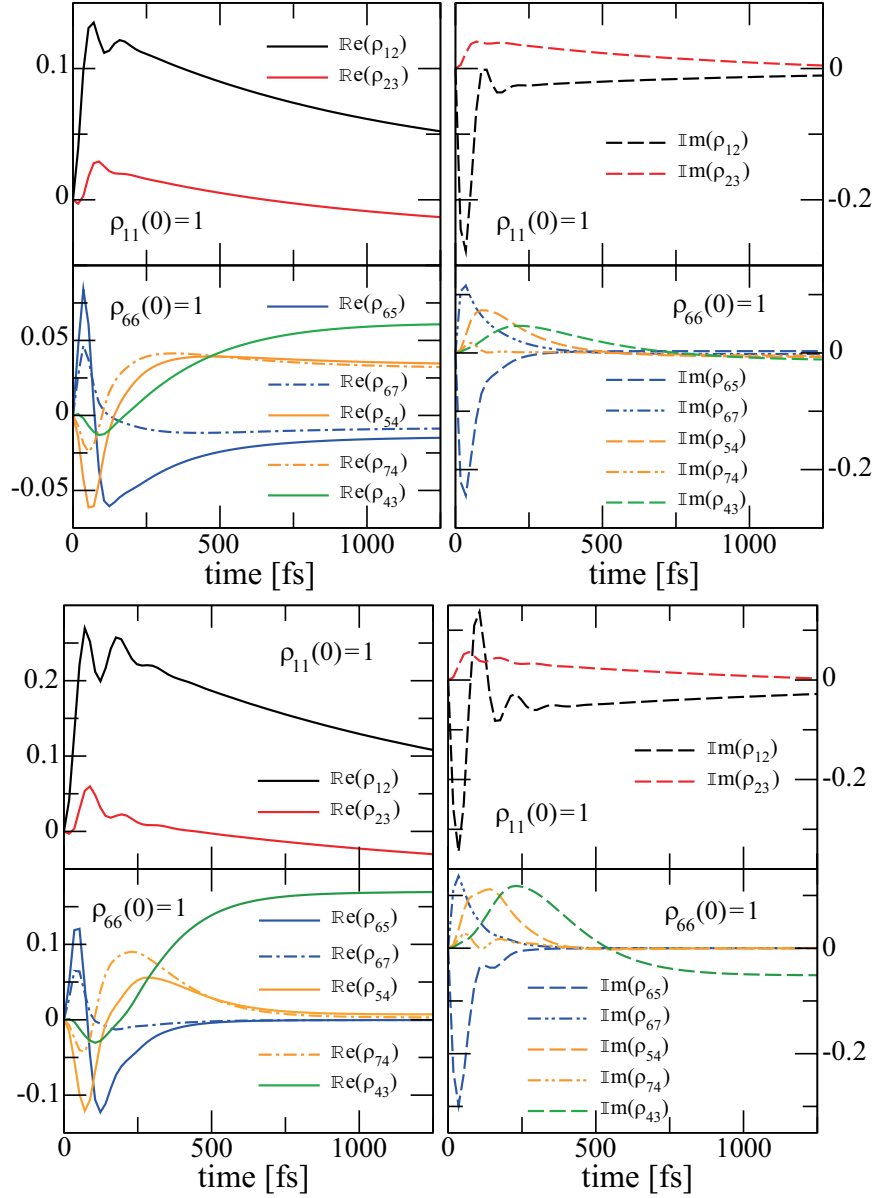


Figure 8.4: Coherences (real part in the left column and imaginary part in the right column) between FMO sites at 300 K (top set) and at 77 K (bottom set) with $\rho_{11}(0) = 1$ (upper row) and $\rho_{66}(0) = 1$ (lower row) for the spectral density function derived by Adolphs and Renger [Eq. (7.2.1)] with $\omega_H = 180 \text{ cm}^{-1}$ and $\gamma = 1 \text{ cm}^{-1}$.

tion (black solid line in Fig. 7.3) and therefore sustained coherent oscillations result. These survive for up to 400 fs at room temperature and for up to about 700 fs at cryogenic temperature for $\rho_{11}(0) = 1$. For the initial preparation $\rho_{66}(0) = 1$, coherent oscillations survive for up to 500 fs at cryogenic temperature, but are still

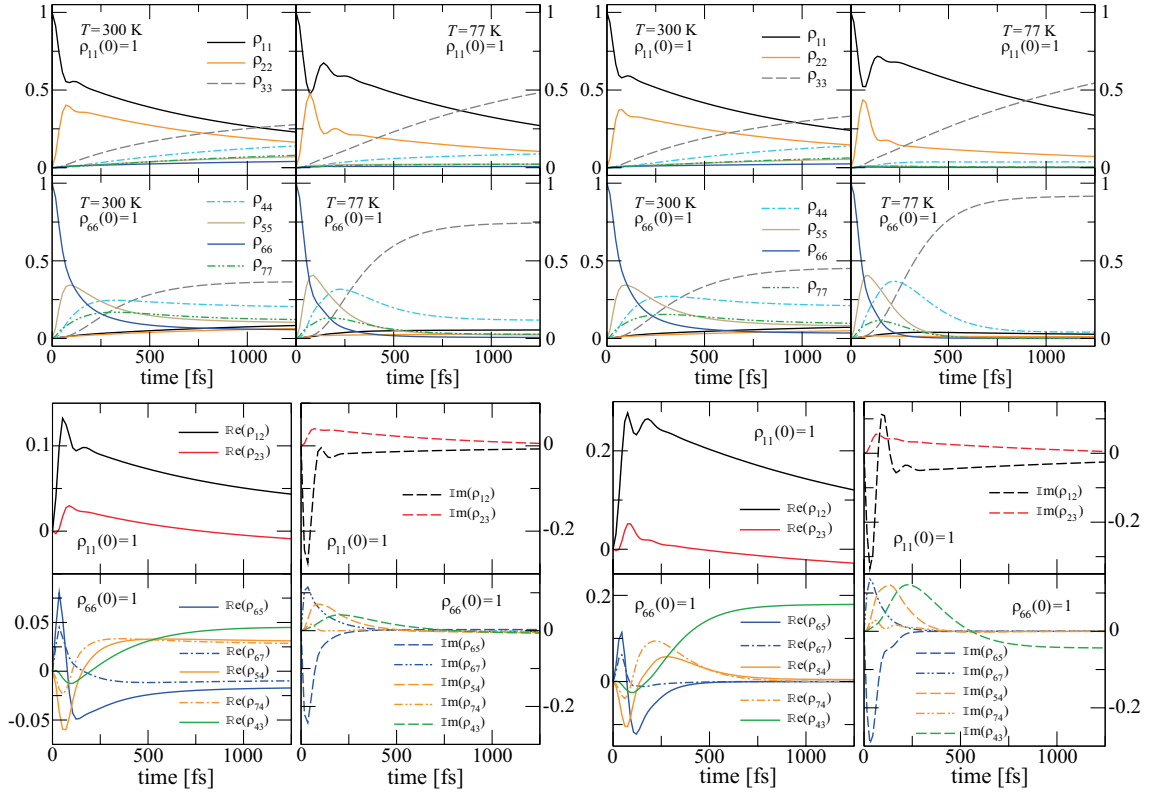


Figure 8.5: Time-dependent occupation probabilities (top sets) and coherences (bottom sets) for the spectral density function derived by Adolphs and Renger [Eq. (7.2.1)] with $\omega_H = 190.8 \text{ cm}^{-1}$ and $\gamma = 0.01 \text{ cm}^{-1}$ (left set) and with $\omega_H = 211.0 \text{ cm}^{-1}$ and $\gamma = 29 \text{ cm}^{-1}$ (right set). Coherences are shown at 300 K when $\omega_H = 190.8 \text{ cm}^{-1}$ (lower set left) and at 77 K when $\omega_H = 211.0 \text{ cm}^{-1}$ (lower set right).

suppressed at room temperature. The most important effect due to the lack of the localized mode is the overall reduced efficiency in the excitation energy transfer of the FMO complex, regardless of the sustained coherent oscillations in the populations. This can be understood by observing the smaller final population of BChl 3 in Fig. 8.7, as compared, for example, to Fig. 8.2. The reduced population of this site means a lower transfer efficiency toward the reaction center.

The effect on the site populations of the smaller Huang-Rhys factor $S_H = 0.027$, corresponding to an intermediate exciton-vibrational coupling regime, is presented in Fig. 8.9 for $\omega_H = 180 \text{ cm}^{-1}$ and $\gamma = 1 \text{ cm}^{-1}$. As expected, longer coherence times are observed as compared to the results in Fig. 8.2, in particular for cryogenic temperature. This sustained coherence results from the smaller exciton-vibrational coupling, i.e., the weaker coupling with the environmental mode, which therefore,

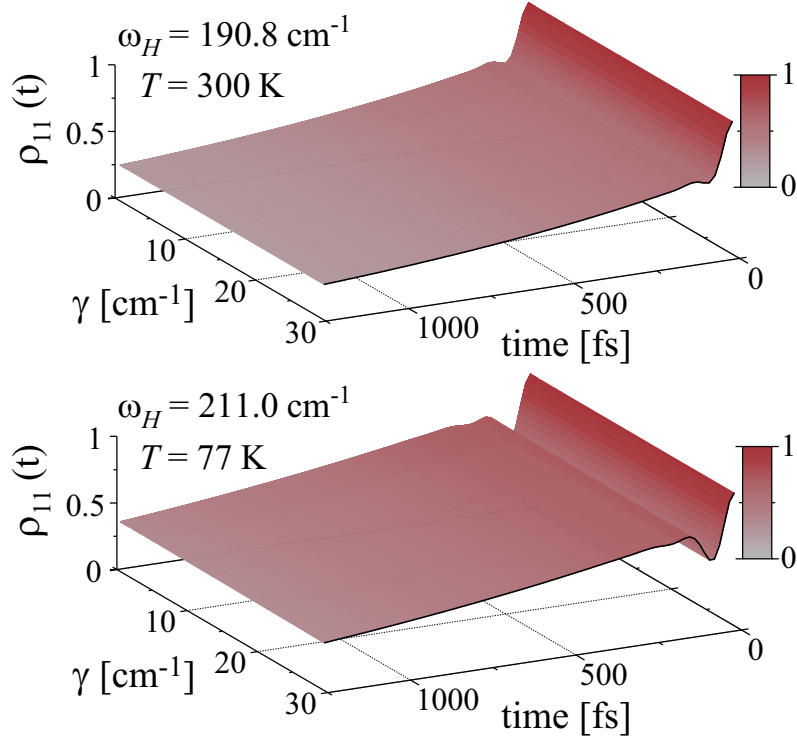


Figure 8.6: Time-dependent occupation probability of BChl 1 when $\omega_H = 190.8 \text{ cm}^{-1}$ at 300 K (top) and when $\omega_H = 211.0 \text{ cm}^{-1}$ at 77 K (bottom) for $\rho_{11}(0) = 1$.

causes weaker dissipation. Again, longer coherence times do not necessarily lead to higher transfer efficiency, as concluded from comparing the final population of BChl 3 in Figs. 8.2 and 8.9.

In order to evaluate the effect of the spectral weight of the continuous background spectrum $g_0(\omega)$ on the transfer dynamics, the localized vibrational mode in the spectral density in Eq. (7.2.1) is neglected. The resulting spectral function is written as $\tilde{J}(\omega) = \zeta\omega^2 S_0 g_0(\omega)$, with a prefactor ζ in front of $g_0(\omega)$. The resulting time-dependent occupation probability of the BChl 1 molecular site is shown in Fig. 8.10. The sustained coherence at smaller ζ values confirms that the large continuous background spectrum $g_0(\omega)$ is responsible for the negligible dependence on the width γ of the Lorentzian peak observed in Figs. 8.3 and 8.6.

The importance of the results in this section relies on the fact that the characteristics of a localized vibrational mode, i.e., its width and spectral position, does not influence substantially the coherence times. However, its presence seems to enhance the exciton transfer efficiency toward the RC. This effect is quantified in Chap. 9 when considering the explicit nonequilibrium dynamics of the localized modes.

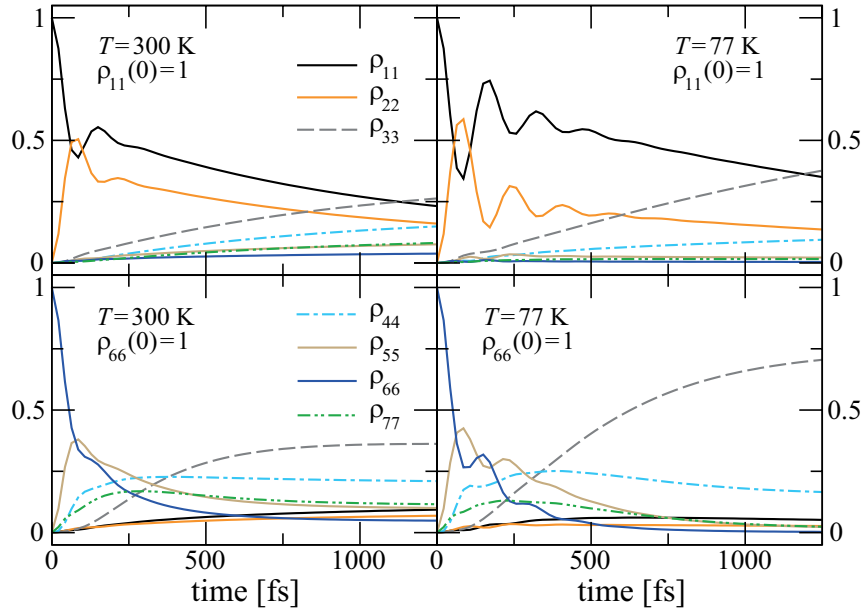


Figure 8.7: Same as Fig. 8.2 in the absence of any localized vibrational mode.

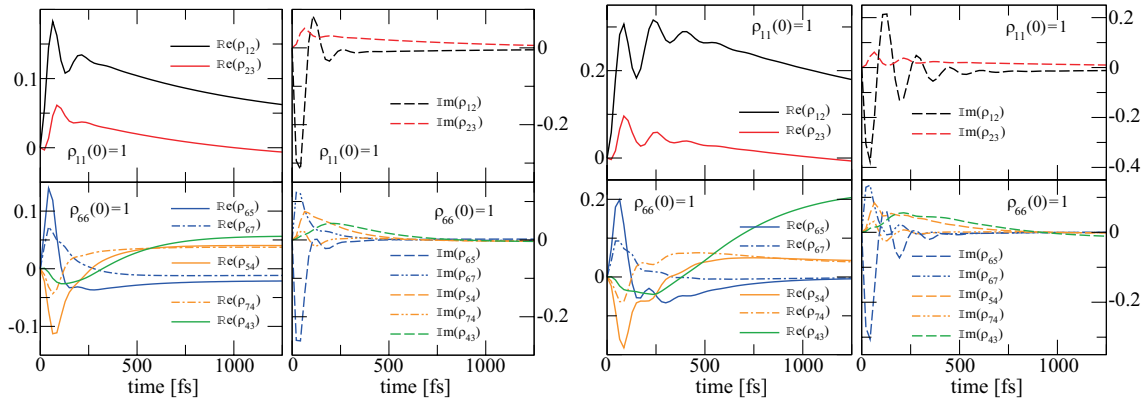


Figure 8.8: Same as Fig. 8.4 in the absence of any localized vibrational mode. Data for $T = 300$ K are shown in the left set and for $T = 77$ K in the right set.

8.2 Population dynamics in the Kreisbeck-Kramer model

The site occupation probabilities $\rho_{jj}(t)$ of the FMO complex are presented in Fig. 8.11 for the spectral density function derived by Kreisbeck and Kramer [214]. These correspond to the two parametrizations including $n = 3$ and $n = 11$ shifted Drude-Lorentz peaks in Eq. (7.3.1) (see Fig. 7.4). In this model, both parametrizations

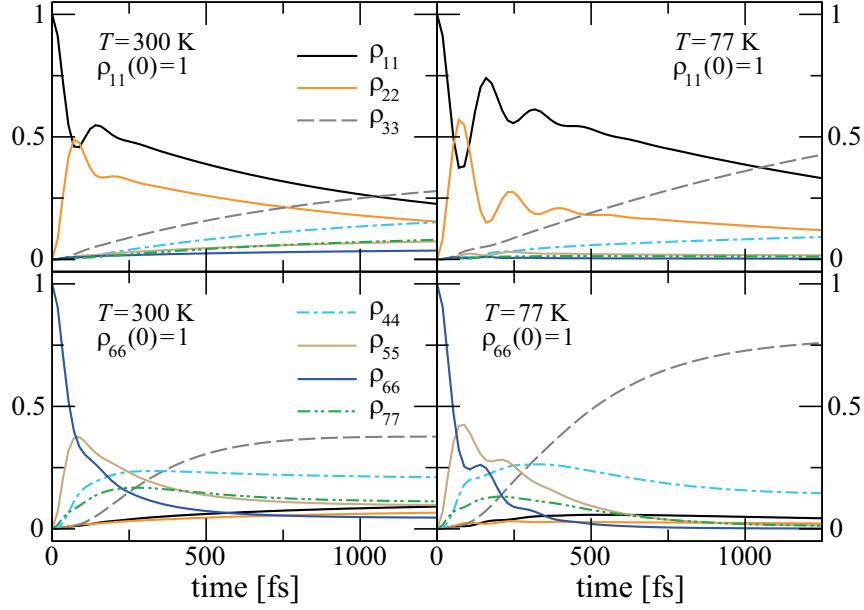


Figure 8.9: Same as Fig. 8.2 in the intermediate exciton–vibrational coupling regime for which $S_H = 0.027$.

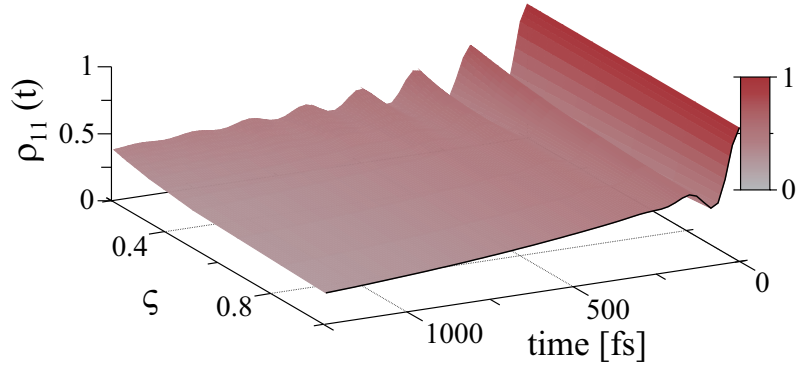


Figure 8.10: Population of the BChl 1 at $T = 300$ K in the absence of any localized vibrational mode as a function of the prefactor ζ in the continuous background spectrum $g_0(\omega)$ of the spectral density derived by Adolphs and Renger.

exhibit longer coherence times, as compared to those obtained using the Adolphs–Renger model (Sec. 8.1), due to the lower spectral weight at low frequencies (see Fig. 8.1). For $n = 3$ and for the initial preparation $\rho_{11}(0) = 1$, sustained coherent oscillations up to 300 fs at 300 K and up to 800 fs at 77 K are observed. Rather shorter coherence times are obtained for $\rho_{66}(0) = 1$. The even shorter coherence times for $n = 11$ can be attributed to the faster increase of the spectral weight at

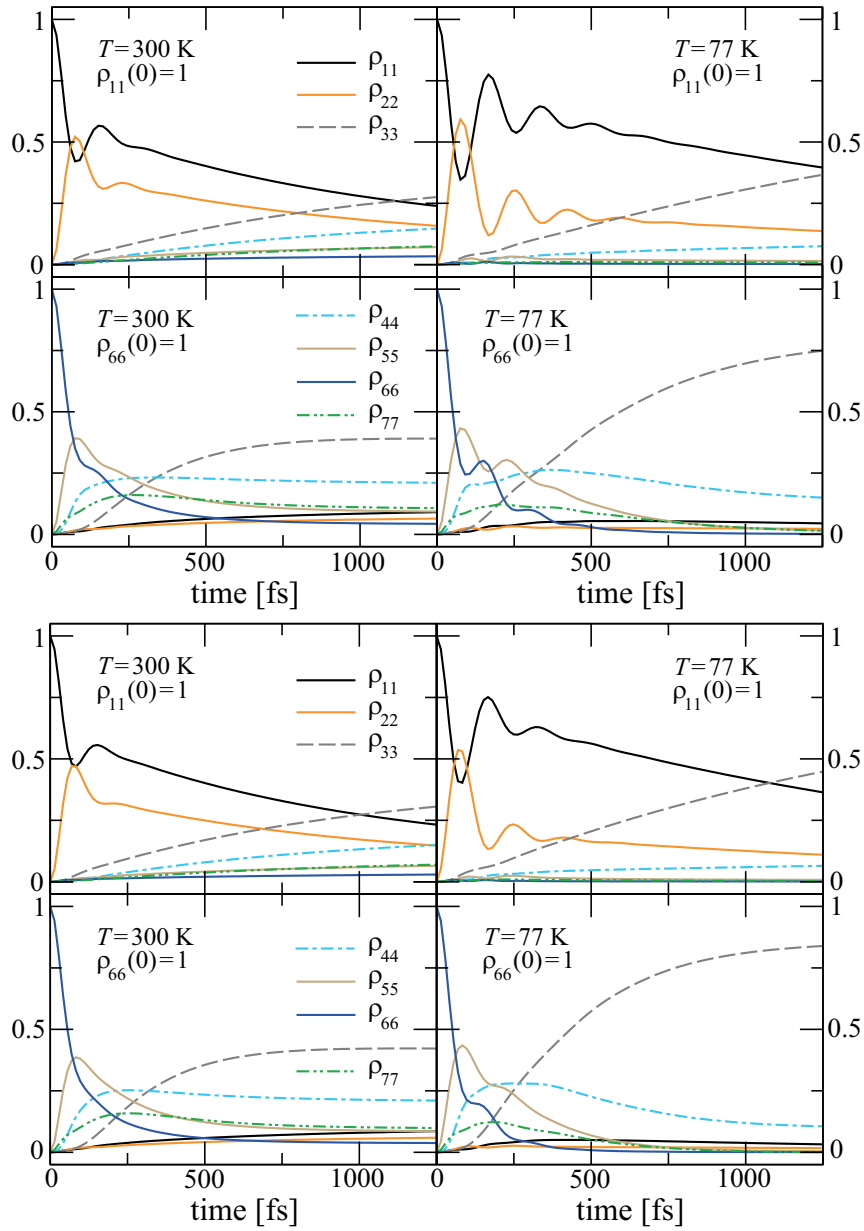


Figure 8.11: Same as Fig. 8.2 for the spectral density function derived by Kreisbeck and Kramer [Eq. (7.3.1)] with $n = 3$ (upper set) and with $n = 11$ (lower set).

low frequencies as compared with the case when $n = 3$ (see Fig. 7.4). For both parametrizations, the coherences $\rho_{ij}(t)$ shown in Fig. 8.12 do not exhibit any long time sustained oscillations.

The most important result is the enhanced exciton transfer efficiency toward the RC due to the explicit inclusion of vibronic modes. This is evidenced by the larger final population of BChl 3 when $n = 11$ (lower set in Fig. 8.11), as compared to

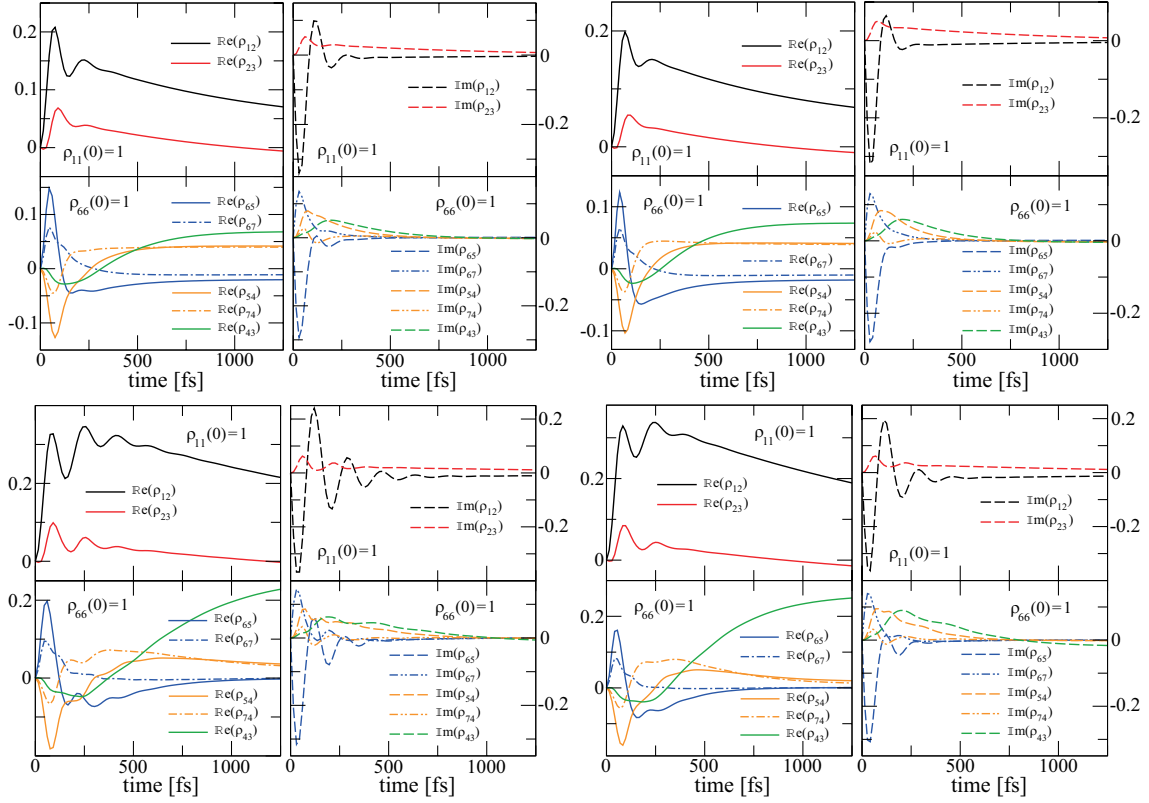


Figure 8.12: Site coherences at 300 K (upper set) and at 77 K (lower set) for the spectral density function derived by Kreisbeck and Kramer [Eq. (7.3.1)] with $n = 3$ (left set) and with $n = 11$ (right set).

that when $n = 3$ (upper set). By comparing these two parametrizations, one can also observe that a higher transfer efficiency does not necessarily lead to sustained coherent oscillations in the population dynamics, as found in the previous section. These results allow one to conclude that the presence of localized vibrational modes might have a relevant physiological role in maximizing the exciton transfer efficiency toward the RC. Sustained coherent oscillations, however, seem to play no role at all.

8.3 Population dynamics in the Aghtar *et al.* model

The site populations and coherences of the FMO complex are presented in Figs. 8.13 and 8.14. These correspond to the exciton dynamics resulting from the site-dependent spectral density functions derived by Aghtar *et al.* [165] [Eq. (7.4.2)]

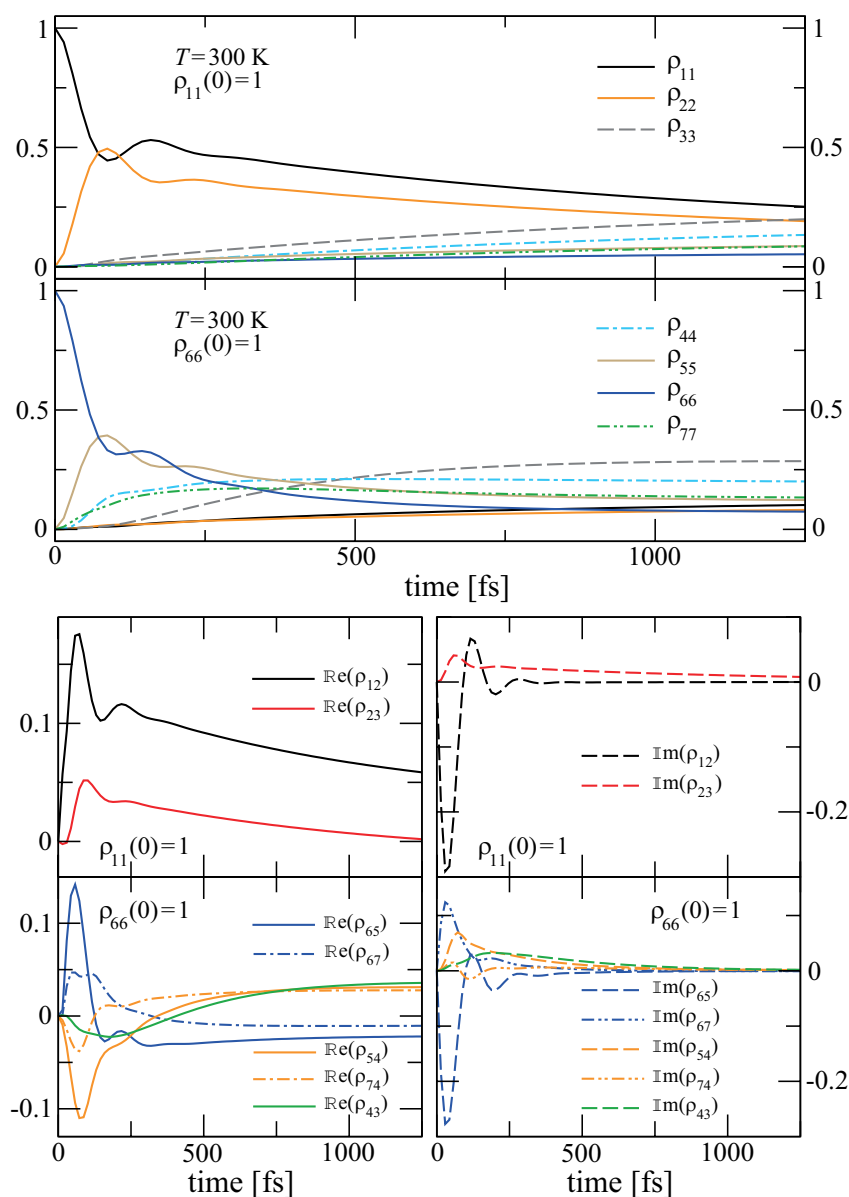


Figure 8.13: Site populations (upper set) and coherences (lower set) for the spectral density function derived by Aghtar *et al.* [Eq. (7.4.2)] with water as a solvent at 300 K.

considering water as a solvent at 300 K and a glycerol:water 65:35 mixture as a solvent at 310 K, respectively.

The results exhibit a quite overdamped dynamics as compared with those obtained using the previous models (Secs. 8.1 and 8.2). This is due to the larger spectral weight at low frequencies (see Fig. 8.1), which leads to shorter coherence times. These are on the order of 400 fs for both cases. In spite of the different mi-

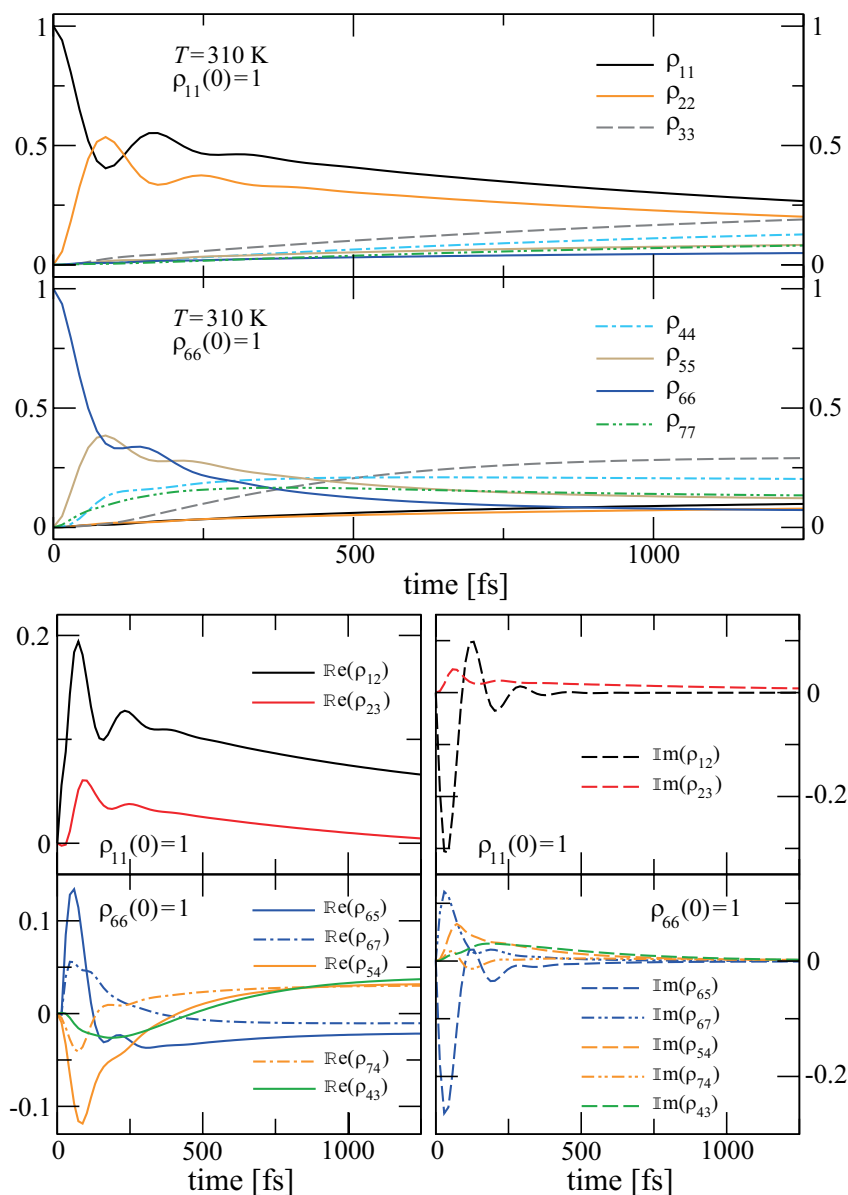


Figure 8.14: Same as Fig. 8.13 with a glycerol:water 65:35 mixture as a solvent at 310 K.

Microscopic details of both solvents, they generate a polar environment that induces a rather similar dynamical behavior of the FMO complex. This allows one to conclude that the microscopic details of the polar environment do not have any appreciable effect on the coherence times, neither on the exciton transfer efficiency toward the reaction center.

8.4 Concluding remarks

In this chapter, the excitation energy transfer dynamics of the FMO complex has been investigated by using the numerically exact QUAPI scheme. The BChl system is described according to experimental results and the fluctuating pigment-protein-solvent environment is described by known spectral functions, which are obtained either from experimental data or from molecular dynamics simulations (see Chap. 7). All spectral density functions exhibit a nontrivial structure with peaks attributed to vibrational modes of the pigment-protein complex. They are explicitly included as part of the environment and therefore, it is assumed that their thermalization time scale is much shorter than any system time scale. The spectral density functions derived by Adolphs and Renger [207], Eq. (7.2.1), and by Kreisbeck and Kramer [214], Eq. (7.3.1), include, respectively, a single and several localized vibrational modes. On the other hand, the site-dependent spectral density functions derived by Aghtar *et al.* [165], Eq. (7.4.2), include the specific microscopic details of the polar environment. The influence that these localized vibrational modes have on the dynamics has been examined in detail. Results for possible non-Markovian effects arising during the dynamical evolution generated by these models are presented in Sec. 10.1.

The localized vibrational modes included in the spectral density functions derived by Adolphs and Renger (Sec. 8.1) and by Kreisbeck and Kramer (Sec. 8.2) generate qualitative and quantitative differences on the coherence times of the site populations. More importantly, these two models indicate that the presence of these vibrational modes enhance the final population of BChl 3, suggesting that they might have a relevant physiological role in maximizing the exciton transfer efficiency toward the reaction center. A higher transfer efficiency, however, does not necessarily lead to sustained coherent oscillations in the population dynamics, i.e., long-lasting coherences do not have a relevant physiological role. It was also found that the faster energy transfer route is $6 \rightarrow (5/7) \rightarrow 4 \rightarrow 3$ as indicated by the larger final population of BChl 3 when $\rho_{66}(0) = 1$, as compared to the case when $\rho_{11}(0) = 1$. This route involves BChl 5, which is the best connected pigment as evidenced by its significant contribution to four excitonic states (see bold numbers in Table 7.2). These results are in agreement with those reported by Adolphs and Renger [207], who have also identified this energy transfer route as the fast (sub-picosecond) transfer branch. On the other hand, the specific microscopic details of the polar environment, as specified in the site-dependent spectral density functions derived by Aghtar *et al.* (Sec. 8.3), do not generate any appreciable effect on the coherence times, neither on the exciton transfer efficiency.

Dynamics in presence of non-equilibrium vibrations

The results in the previous chapter indicate that a higher transfer efficiency does not necessarily lead to or has to rely on sustained coherent quantum oscillations in the population dynamics. In all simulations there, the vibrational modes of the pigment-protein complex were explicitly included as part of the environment. This is assumed to be always in thermal equilibrium within the employed system-bath approach. Thus, it is implicitly assumed that the time scale of thermalization of the vibrational mode is much shorter than any system time scale. Alternatively, its specific heat must be infinite, so that energy exchange with the system cannot drive it out of equilibrium. Then, the discrete mode only provides thermal equilibrium fluctuations around its thermal state. Those however, might be in general correlated over time. Recent analyses [185, 187, 188, 189, 203] indicate that the observed long-lasting coherent signals in the two-dimensional optical spectra of the FMO complex [179, 181] result from a coupled exciton–vibrational mode system, with the modes being underdamped, strongly coupled to the electronic transitions, and close to resonance to energy differences between excitonic transitions. In this scenario, the full nonadiabatic quantum dynamics of the vibrational mode has to be considered and not only its thermal equilibrium fluctuations. Therefore, in this chapter the vibrational modes are explicitly included as part of the *system* Hamiltonian and thus their nonequilibrium quantum dynamics is described on an equal footing as

the excitonic states. This allows one to address the fundamental questions of how long the quantum coherent beatings survive and how they profit from an interaction with underdamped vibrations in a realistic setting.

Because the vibrational modes are included as part of the system Hamiltonian, only the spectral density function derived by Adolphs and Renger without any peak is considered, i.e., only the first term in the right-hand-side of Eq. (7.2.1), plotted as a black solid line in Fig. 7.3. Separating the mode from the environment to treat it as part of the system results in a total Hamiltonian $H = H_{\text{FMO,vib}} + H'_{\text{SB}}$ with

$$H_{\text{FMO,vib}} = H_{\text{FMO}} + \sum_{j=1}^7 \left[|j\rangle\langle j| \kappa_H^{(j)} q_{j,H} + \frac{1}{2} (p_{j,H}^2 + \omega_{j,H}^2 q_{j,H}^2) \right], \quad (9.0.1)$$

where H'_{SB} is the system-bath part excluding the localized vibrational mode from the environmental spectrum in Eq. (7.2.1). Notice that the summation in Eq. (9.0.1) implies that one vibrational mode at each chromophore is considered, and therefore, a total of seven vibrational modes is assumed. In order to obtain a numerically tractable model, the Hilbert space of the seven vibrational modes is restricted to include only a finite number of vibrational excitations, i.e., an effective system Hamiltonian

$$\begin{aligned} H_{\text{FMO,vib}} &= H_{\text{FMO}} + \sum_{j=1}^7 \sum_{v_j=0}^{v_{j,\max}} v_j \hbar \omega_H |v_j\rangle\langle v_j| \\ &+ \sum_{j=1}^7 |j\rangle\langle j| \sum_{v_j=1}^{v_{j,\max}} \lambda_{v_j} (|v_j - 1\rangle\langle v_j| + |v_j\rangle\langle v_j - 1|), \end{aligned} \quad (9.0.2)$$

with $\lambda_{v_j} = \sqrt{v_j} \hbar \omega_H S_H$. The requirement of a finite number of vibrational excitations, specified by $v_{j,\max}$, is due to the exponential growth of needed computer power for QUAPI with increasing system size (as discussed in Sec. 2.2.1). The enlarged basis set of the effective system Hamiltonian in Eq. (9.0.2) resulting from the inclusion of vibrational excited states is written as $|j, v_j\rangle = |j\rangle \otimes |v_j\rangle$. Here, the j -th site is in its *electronic* excited state $|j\rangle$ (with all other sites in their electronic ground states, see Sec. 7.1) and in the *vibrational* state $|v_j\rangle$. This vibrational state can be the ground state $|v_j\rangle = |g\rangle$, the first excited state $|v_j\rangle = |e_1\rangle$, and so on. States where the exciton is at a different site than the vibrational excitation are omitted, thus, only states $|j, v_j, v_{i \neq j} = 0\rangle$ are taken into account. In order to still allow energy transfer between the different chromophore sites, dipolar couplings $V_{(j,v_j),(i,v_i)} = V_{j,i}$ are assumed. Qualitatively similar results are obtained for $V_{(j,v_j),(i,v_i)} = 0$ but not further discussed.

In this chapter, the influence of the nonequilibrium vibrational modes on the speed and thus efficiency of excitation energy transfer (EET) through the FMO

complex toward the reaction center (RC) is quantitatively investigated. The RC is modeled as an energy sink which is connected solely to BChl 3. Thus, another state $|RC\rangle$ is included into the description. The transfer toward the RC is then treated as a population decay on a purely phenomenological level by a constant decay rate $\Gamma_{\text{RC}} = 1 \text{ ps}^{-1}$ since the explicit details of the dumping process are not of interest. Backtransfer from the RC to the FMO complex is then excluded. In turn, the rise time of the population growth of the RC is taken as a measure for the efficiency of the energy transfer through the complex.

Explicitly, the dynamics is treated within an effective master equation for the total statistical operator $\hat{\rho}$ for the FMO complex and its environment and the occupation of the reaction center $\rho_{\text{RC}} = |RC\rangle\langle RC|$ according to

$$\partial_t \hat{\rho} = -\frac{i}{\hbar} [H, \hat{\rho}] - \Gamma_{\text{RC}} \sum_{v_3} |3, v_3\rangle\langle 3, v_3| \quad (9.0.3)$$

$$\partial_t \rho_{\text{RC}} = \Gamma_{\text{RC}} \sum_{v_3} |3, v_3\rangle\langle 3, v_3|. \quad (9.0.4)$$

As in the previous chapter, simulations are carried out using the iterative QUAPI scheme (Sec. 2.2.1) in its extended version [37] in which each BChl site interacts with a separate environment (Sec. 2.2.2). These are assumed to be identical in their characteristics, but spatially uncorrelated [43], and therefore, using the influence functional in Eq. (2.2.33). Results are presented for cryogenic (77 K) and physiological (300 K) temperatures, as well as for the initial preparations $\rho_{11}(0) = 1$ and $\rho_{66}(0) = 1$ with the corresponding vibrational mode in the ground state. The resulting exciton transfer dynamics in absence of any vibrational mode is provided in Fig. 9.1 as a reference. These results correspond to the site populations in their respective vibrational ground states $|j, g\rangle$ labeled as ρ_{jj} . It is observed that apart from few oscillations of selected site populations at very short times, no long-lasting coherent oscillations in the populations are found. The population of the RC ρ_{RC} increases in a monotonous manner.

9.1 Effect of intermediate-frequency vibrational modes

The numerically exact results for the quantum dynamics of the FMO complex in presence of equilibrium vibrational modes presented in Chap. 8 and in Ref. [43] indicate that the coherence times are considerably shorter than the experimentally observed ones. Very strong underdamped high-frequency ($> 750 \text{ cm}^{-1}$) vibrations

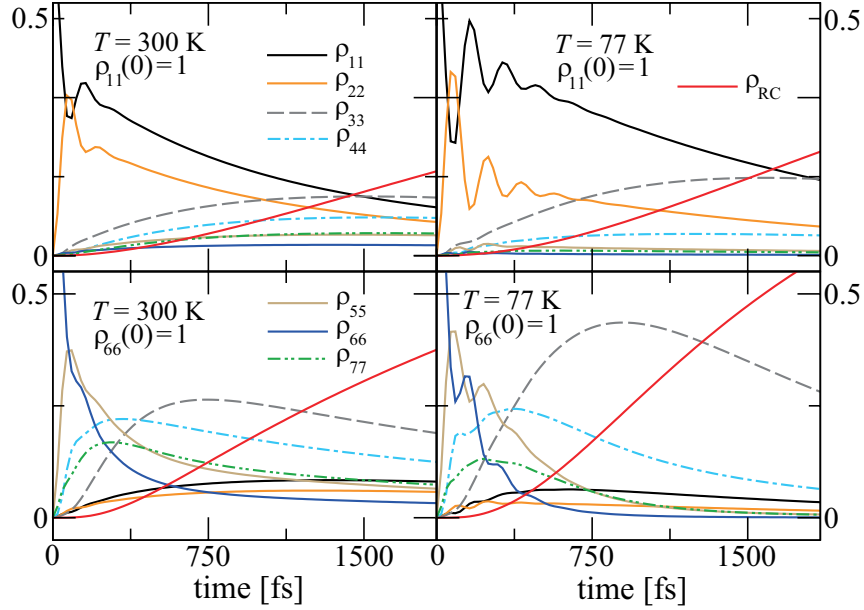


Figure 9.1: Time evolution of the FMO site populations and RC in absence of any vibrational mode at $T = 300$ K (left column) and $T = 77$ K (right column) for the initial preparations $\rho_{11}(0) = 1$ (upper row) and $\rho_{66}(0) = 1$ (lower row).

can also be ruled out as a possible origin of the experimentally observed long-lived coherent beatings [44]. Recently, by explicitly including the vibrational mode at 180 cm^{-1} into the system's nonadiabatic quantum dynamics, Christensson *et al.* [188] found coherence times in line with experimental findings employing a Redfield approach to treat the environmental fluctuations. Chin *et al.* [187] observed the same results employing a numerically exact treatment of an effective FMO model with only two pigments. In this section, the vibrational mode at 180 cm^{-1} is explicitly included as part of the full (seven sites FMO) system Hamiltonian.

9.1.1 EET dynamics in the intermediate coupling regime

Taking the results in Fig. 9.1 as a reference, the exciton dynamics when every individual FMO site is coupled to its own vibrational mode is considered next. All of them are assumed to have equal characteristics and a Huang-Rhys factor of $S_H = 0.027$ is chosen in this section, i.e., an intermediate exciton-vibrational mode coupling regime. Because of the computational limitations imposed by the implementation of the QUAPI method, only vibrational states resulting in diagonal entries in $H_{\text{FMO,vib}}$ up to 450 cm^{-1} above the energy of site 3 are included. This leaves sites 2, 5 and 6 without any vibrational excited state due to their high frequency,

but includes the ground and first (and second for site 3) vibrational excited states for the other sites, resulting in $M = 12$. Explicitly, the included states $|j, v_j\rangle$ are $\{|1, 0\rangle, |2, 0\rangle, |3, 0\rangle, |4, 0\rangle, |5, 0\rangle, |6, 0\rangle, |7, 0\rangle, |1, 1\rangle, |3, 1\rangle, |3, 2\rangle, |4, 1\rangle, |7, 1\rangle\}$.

Because the relevant vibrational modes which influence the system dynamics are those with energies comparable to the energy difference between the exciton states [44], the relevant FMO excitonic energy ranges (see Table 7.2) are covered by the included vibrational states and therefore, the technical restriction of truncated number vibrational excited states has no severe implications. The results are shown in Fig. 9.2, where ρ_{vib_j} ($\rho_{2\text{vib}_j}$) denote the population of the electronically excited site j in its first $|j, e_1\rangle$ (second $|j, e_2\rangle$) vibrational excited state. When compared with

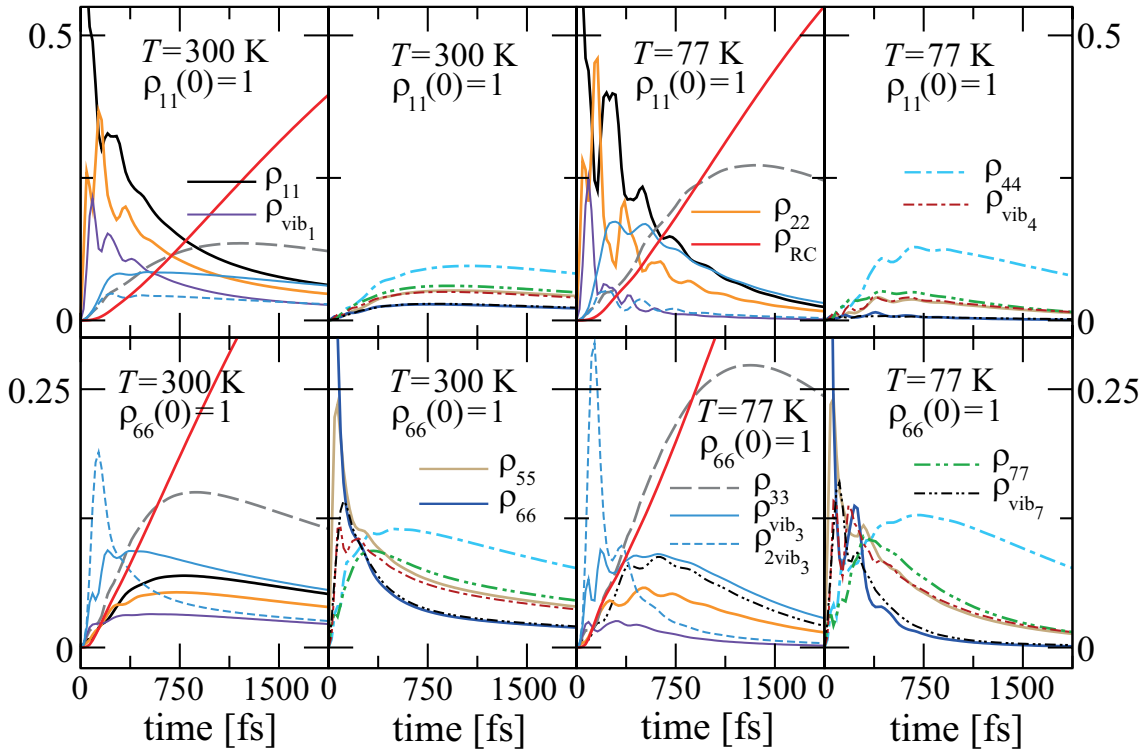


Figure 9.2: Same as in Fig. 9.1 but in presence of a vibrational mode at each individual molecular site. Vibrational excited states with energies up to 450 cm^{-1} above the energy of site 3 are included. Results at $T = 300 \text{ K}$ are shown in the first and second columns while those at $T = 77 \text{ K}$ are shown in the third and fourth columns. Upper and lower rows show results for the initial preparations $\rho_{11}(0) = 1$ and $\rho_{66}(0) = 1$, respectively.

those in Fig. 9.1, they exhibit both prolonged oscillatory population dynamics with increased coherence times *and* an increased transfer efficiency, as indicated by the

faster rise of the population of the RC. The sustained coherences arise from a population exchange between the vibrational ground state at site j and its corresponding vibrational excited state(s). The dynamics of ρ_{RC} at 300 K is compared in Fig. 9.3 (left column) for the cases when vibrational excited states with energies up to 450 cm^{-1} are included (red thick line) and when there is no vibrational mode present (black thick line).

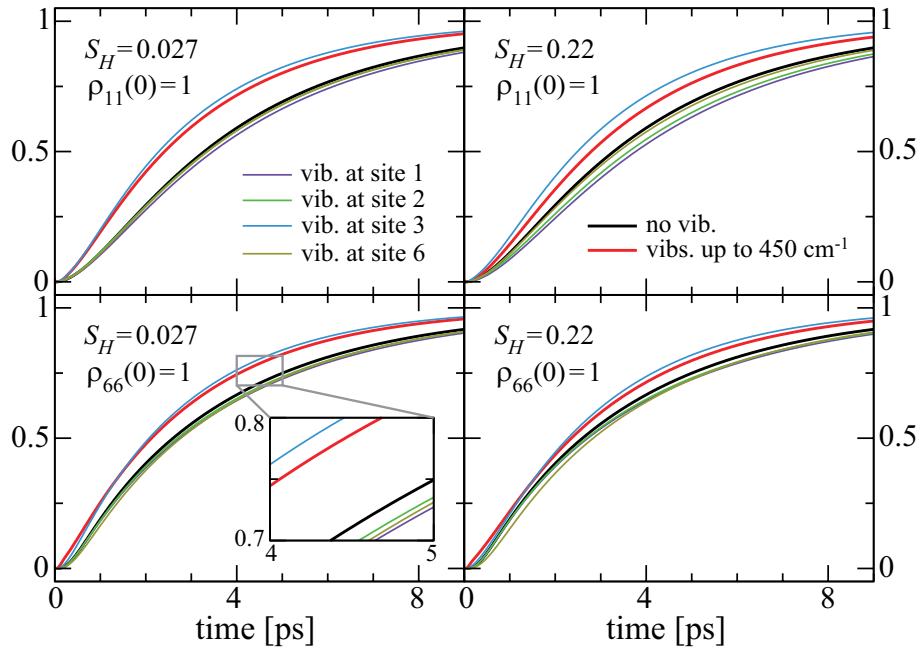


Figure 9.3: RC population ρ_{RC} at 300 K for several number of vibrational excited states. Left column: dynamics in the intermediate exciton–vibrational mode coupling regime. Right column: dynamics in the strong coupling regime. See text for details.

The increased transfer efficiency can be quantified in terms of the time which is required for the transfer of excitation energy through the FMO complex. A measure for this is the rise time of the exponential growth of the RC population, henceforth referred as ‘transfer time’. Adjusting the population of the RC to the expression $\rho_{RC}(t) = 1 - \exp(-t/\tau_{EET})$, allows one to extract the transfer time τ_{EET} . The results are summarized in Table 9.1. It is found that, when vibrational modes are coupled to all individual sites separately, the transfer times decreases by about 25%. The EET speed-up is slightly larger when the initial excitation starts at site 1 as compared to the case when it starts at site 6, because the former case, which induces EET through the slower route (green thin arrows in Fig. 7.2), is prone to exhibit dynamical effects more strongly.

Localized vibrational mode coupled to	Initial FMO excitation at site	Transfer time [ps]	Change by
NO vibration	1	3.84	–
	6	3.39	–
all sites (up to 450 cm ⁻¹)	1	2.87	-25.3 %
	6	2.80	-17.4 %
site 1	1	4.12	+ 7.3 %
	6	3.62	+ 6.8 %
site 2	1	3.97	+ 3.4 %
	6	3.53	+ 4.1 %
site 3	1	2.68	-30.2 %
	6	2.60	-23.3 %
site 6	1	3.95	+ 2.9 %
	6	3.51	+ 3.5 %

Table 9.1: Excitation energy transfer times at 300 K without and with coupled nonequilibrium vibrational modes. A negative change in the transfer time indicates a EET speed-up, while a positive sign indicates a slower transfer as compared to the case without vibrational states. Results are given for the Huang-Rhys factor $S_H = 0.027$.

To further elucidate by which more detailed mechanism the vibrations enhance the coherence times and the transfer efficiency, the excitonic dynamics is evaluated next when a single localized vibrational mode ($v_{j,\max} = 1$) is included only at selected sites separately. In particular, three cases are considered, (i) when the vibrational mode is coupled to the entrance sites 1 or 6, (ii) when it is coupled to the intermediate site 2, and (iii) when it is coupled to the exit site 3. The corresponding results are presented in Figs. 9.4, 9.5, and 9.6, respectively. The population of the RC at 300 K for all cases are compared in Fig. 9.3 (left column) and the resulting energy transfer times are given in Table 9.1.

When coupling a single vibrational mode to the entrance site 1, an enlarged time window with oscillatory dynamics of the populations is observed in Fig. 9.4 (upper set) for both values of the temperature, as compared to the results without any vibrational mode in Fig. 9.1. At longer times, they continue by an incoherent decay. This effect is more pronounced when the site 1 is initially excited (upper set upper row) as compared to an initial preparation in site 6 (upper set lower row). In particular, the energy coherently oscillates between the sites 1 and 2 over several

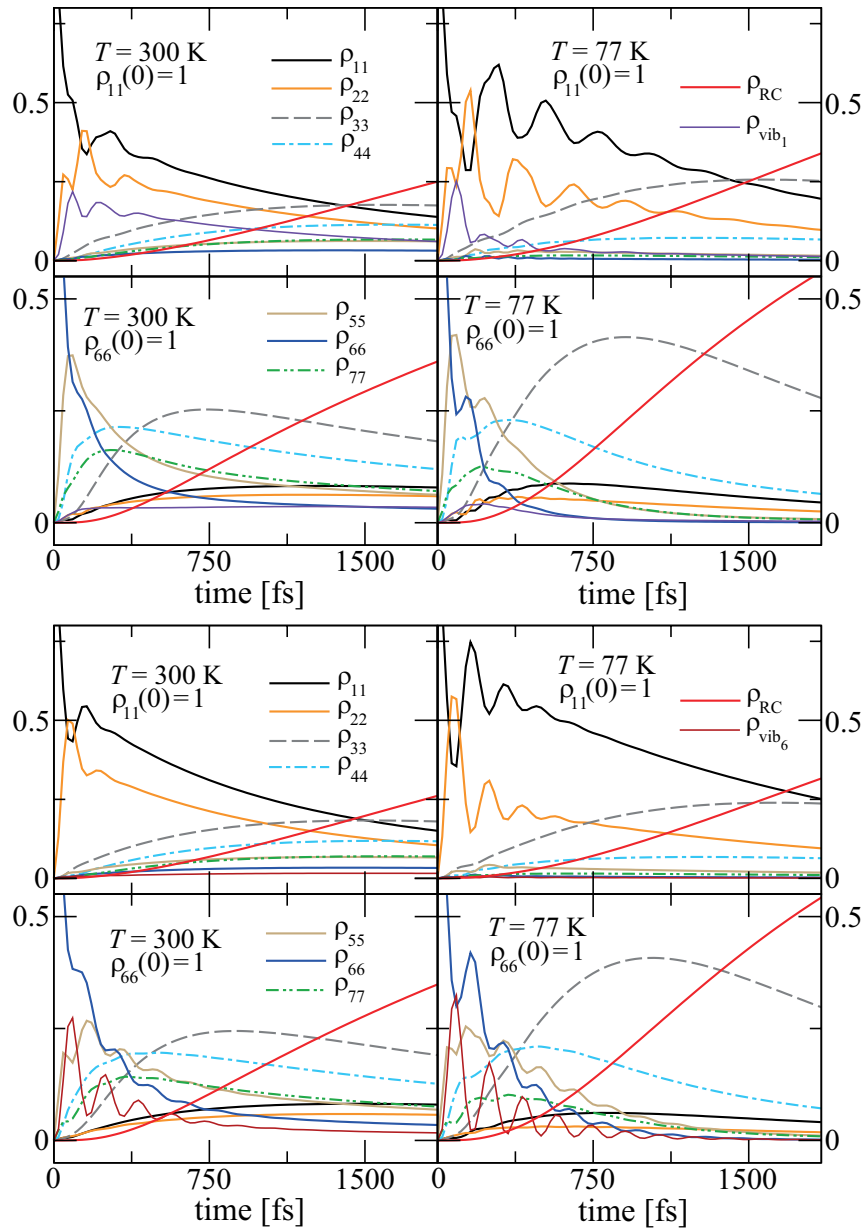


Figure 9.4: Time evolution of the populations of the FMO sites, the RC, and the single vibrational mode coupled solely to the entrance site 1 (upper set) or to the entrance site 6 (lower set).

hundreds of femtoseconds. A closer inspection of the dynamics reveals that the oscillations in the populations indeed go back to coherent transitions between the vibrational ground state (ρ_{11}) and the vibrational first excited state ρ_{vib_1} at site 1. Coherence times of over 1000 fs for $T = 77$ K and of about 400 fs for $T = 300$ K are extracted, which agree with those reported in the experiments [179, 181]. However,

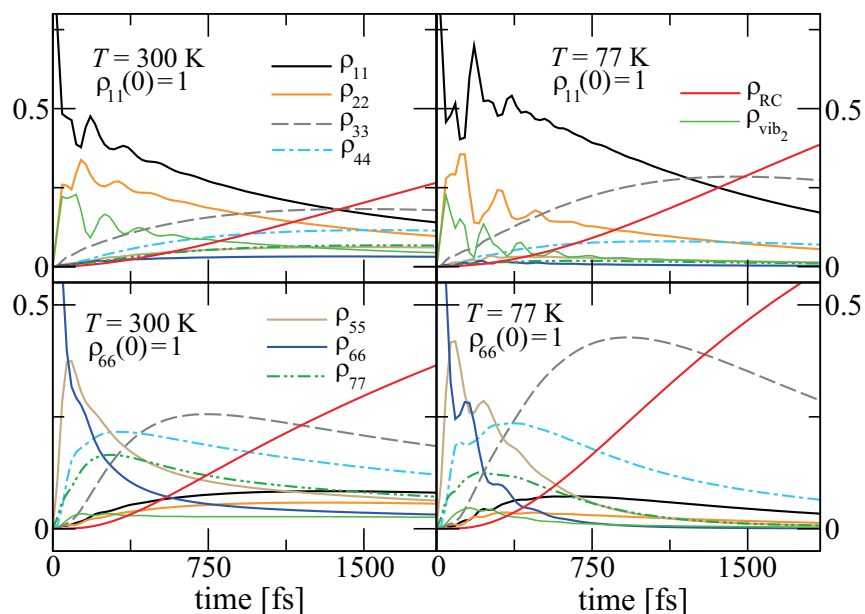


Figure 9.5: Same as in Fig. 9.4, but with the single vibrational mode coupled solely to the intermediate site 2.

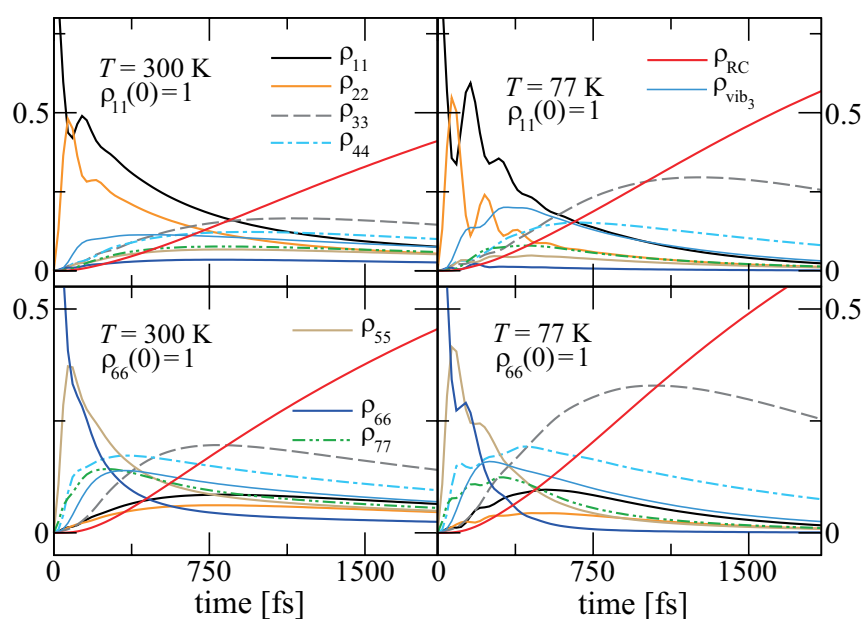


Figure 9.6: Same as in Fig. 9.4, but with the single vibrational mode coupled solely to the exit site 3.

it is important to note that the associated energy transfer times have *increased* in comparison with the case when vibrational modes are excluded, which is reflected

by the positive change in the transfer time shown in Table 9.1.

Analogous observations apply when the vibrational mode is coupled to the entrance site 6 (lower set in Fig. 9.4). In this case coherent oscillations are sustained longer when the site 6 is initially excited. From these results coherence times of 1000 fs for $T = 77$ K and of about 700 fs for $T = 300$ K are extracted. However, despite the enhanced coherence times, the transfer efficiency decreases as seen in Table 9.1. The increase in the transfer times when the vibrational mode is coupled to the entrance site 6 is nevertheless, smaller than in the case when the mode is coupled to the entrance site 1 (in particular when $\rho_{11}(0) = 1$). This is due to the fact that the initial conditions $\rho_{11}(0) = 1$ and $\rho_{66}(0) = 1$ induce exciton transfer dynamics through the slow $1 \rightarrow 2 \rightarrow 3$ and fast $6 \rightarrow (5/7) \rightarrow 4 \rightarrow 3$ routes [178, 207], respectively. Therefore, the mode coupled to site 6 will have reduced impact in the transfer dynamics through the already faster route. These results prove that the coupling of a nonequilibrium vibrational mode to an entrance site enhances coherence times, but decreases the overall transfer efficiency.

The same observations apply when the vibrational mode is coupled to the intermediate site 2 (see Fig. 9.5). In this case also, oscillations in the populations between the vibrational ground state and the vibrational first excited state at site 2 are observed. By this, the population is intermittently trapped in this site, and therefore, the overall transfer efficiency is reduced, as shown in Table 9.1.

On the other hand, when the vibrational mode is coupled to the *exit* site 3 (see Fig. 9.6), the coherence times are not enhanced as compared to the case without any vibrational mode (Fig. 9.1). Instead, the site populations decay quickly. However, the population of the RC grows faster in this situation and, consequently, the transfer efficiency is increased, as evidenced by the shorter transfer times in Table 9.1. This speed-up of the transfer efficiency can be directly rationalized in terms of an additional transfer channel which is provided by the excited vibrational state at site 3. This excited vibrational state is nearly resonant with neighbouring electronic transitions and thus decreases the energy gap with the entrance sites. By this, it adds an additional efficient pathway in form of a vibrational decay channel into the RC. Accordingly, more states connected to the RC are available to become populated during the exciton transfer in the complex and, consequently, more states can dump their energy into the RC in parallel. The population of the RC can then grow faster, resulting in an overall increased transfer efficiency.

Altogether, the underdamped mode at 180 cm^{-1} enhances the efficiency of the quantum excitation energy transfer and at the same time sustains prolonged quantum coherent oscillations. Both are a result of the modes being underdamped, such that they cannot thermalize on faster time scales compared to the electronic energy

transfer dynamics. Beyond that, the speed-up of the energy transfer is rather insensitive to the actual coherence lifetimes. To illustrate this, the FMO dynamics with twice the spectral weight in the continuous background spectrum $g_0(\omega)$, such that the spectral density is written as $\tilde{J}(\omega) = 2\omega^2 S_0 g_0(\omega)$, is shown in Fig. 9.7 for the cases when no vibrational mode is included and when all vibrational excited states with energies up to 450 cm^{-1} above the energy of site 3 are included. In both cases the coherence times are reduced, with the transfer times at $T = 300 \text{ K}$ in absence of any vibrational mode being 3.89 and 3.46 ps for the initially excited sites 1 and 6, respectively. The corresponding transfer times when all vibrational excited states with energies up to 450 cm^{-1} are included are 2.96 and 2.85 ps for the initial preparations $\rho_{11}(0) = 1$ and $\rho_{66}(0) = 1$, respectively. They correspond to a change in the transfer time by -23.9 % and -17.6 %, respectively, which only differ by a few percent from those reported in Table 9.1 for the same conditions. This indicates the robustness of the EET mechanism to the actual coherence lifetime of the populations.

9.1.2 EET dynamics in the strong coupling regime

Here, the transfer efficiency for the case of the larger Huang-Rhys factor $S_H = 0.22$ is determined, i.e., for the case of a strong exciton–vibrational mode coupling. The excitonic dynamics in absence of any vibrational mode shown in Fig. 9.1 is taken as the reference. Results for five cases with a different number of vibrational modes are shown. (i) Figure 9.8 illustrates the dynamics including all vibrational excited states with energies up to 450 cm^{-1} above the energy of site 3. (ii-v) Figure 9.9 shows results when only a single vibrational mode ($v_{j,\text{max}} = 1$) is included. This mode is coupled to (ii) the entrance site 1, (iii) the intermediate site 2, (iv) the exit site 3, and (v) to the entrance site 6. These results should be compared to those in the intermediate coupling regime shown in Fig. 9.2 for the case (i), in Fig. 9.4 for the cases (ii) and (v), in Fig. 9.5 for the case (iii), and in Fig. 9.6 for the case (iv). The dynamics of the RC is compared in Fig. 9.3 (right column) for all cases at 300 K and the corresponding transfer times are given in Table 9.2.

The same physical picture given in the previous section for the intermediate coupling regime applies for this strong coupling regime, but small quantitative differences arise. In particular, the overall efficiency is reduced, i.e., the speed-up of the energy transfer is smaller as in the case of intermediate coupling when including all vibrational excited states with energies up to 450 cm^{-1} and when including a single vibrational mode coupled to the exit site 3. The opposite line of reasoning holds when a single vibrational mode is coupled to the entrance sites 1 or 6 or to the

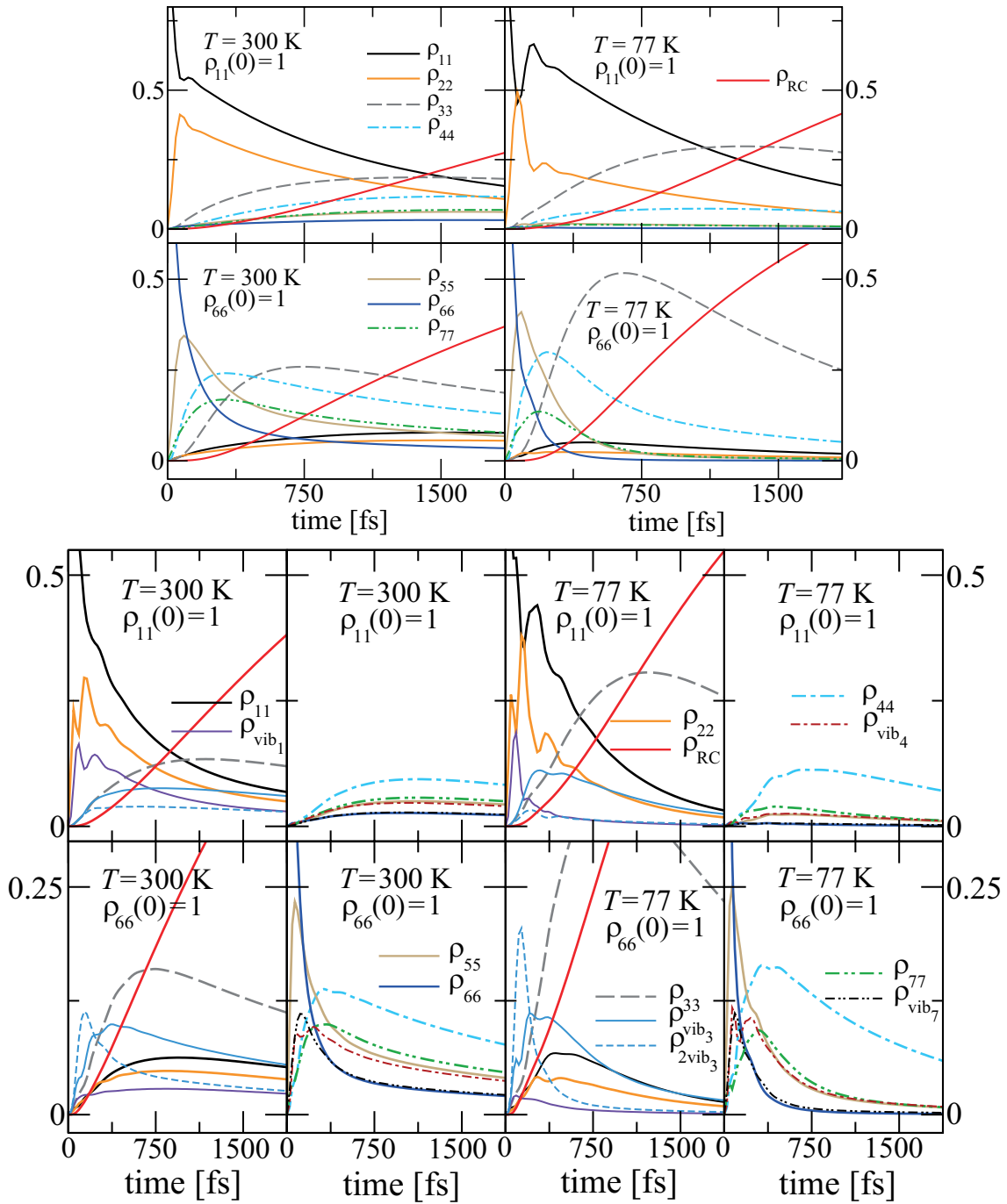


Figure 9.7: FMO dynamics when no vibrational mode is included (left set) and when all vibrational excited states with energies up to 450 cm^{-1} above the energy of site 3 are included (right set). In both cases, a spectral density function with twice the spectral weight in the continuous background spectrum $g_0(\omega)$ is used.

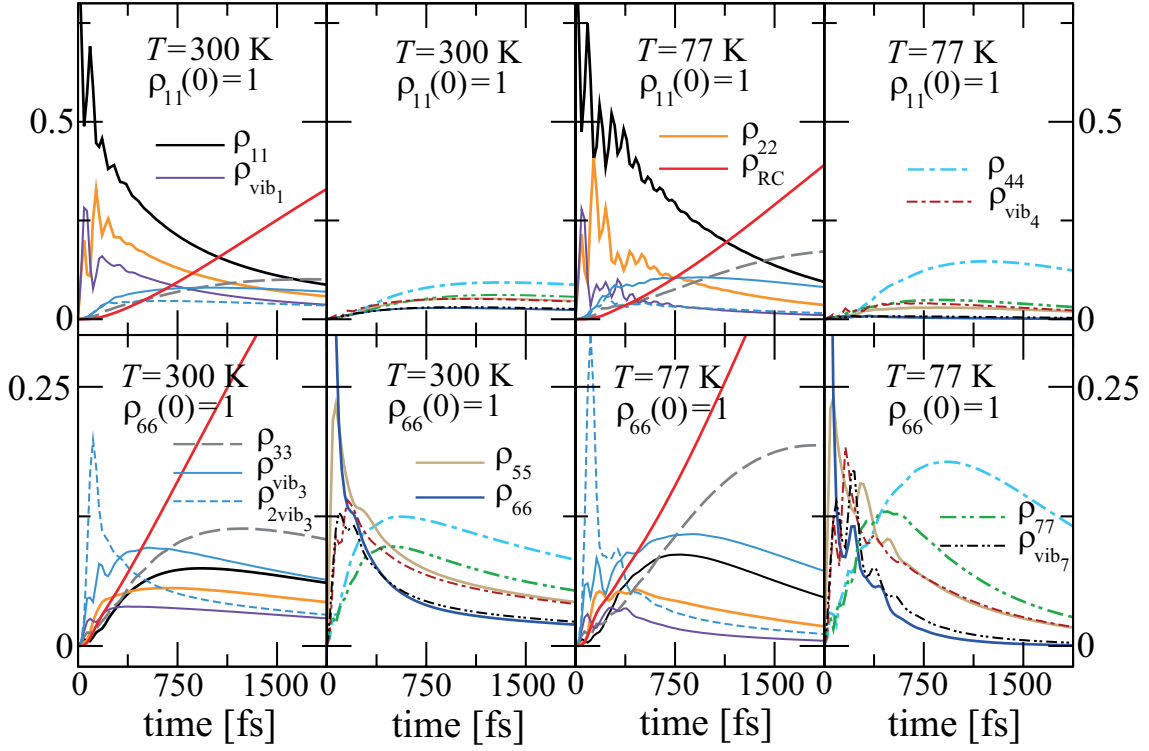


Figure 9.8: Same as in Fig. 9.2 but with the Huang-Rhys factor $S_H = 0.22$.

intermediate site 2, i.e., the transfer times are increased. This is due to the fact that a stronger exciton–mode coupling leads to stronger intrasite beatings in the population, i.e., longer coherent oscillations between the vibrational ground state and the vibrational excited state(s). This localizes the population on the site coupled to the vibrational mode for longer times and therefore, the overall efficiency is reduced. The change in the transfer times, however, is only a few percent when comparing the results in Table 9.2 with those in Table 9.1, even when the Huang-Rhys factors in both regimes differ by one order of magnitude.

The localization of the population can be illustrated by considering a single vibrational mode coupled to the entrance site 1. This site is strongly coupled electronically to site 2 and the transient dynamics of the populations depends on the exciton–mode coupling regime. In the intermediate regime, intersite (site 1 vs site 2) coupling is stronger than the intrasite (ground vs first excited vibrational states at site 1) coupling, and therefore the population $\rho_{22}(t)$ rises faster than the population of $\rho_{\text{vib}_1}(t)$ (see upper set in Fig. 9.4). Conversely, in the strong coupling regime, the increase in the population of $\rho_{\text{vib}_1}(t)$ is faster than $\rho_{22}(t)$ (see top row in Fig. 9.9). The same competing behavior is observed between $\rho_{55}(t)$ and $\rho_{\text{vib}_6}(t)$ when the

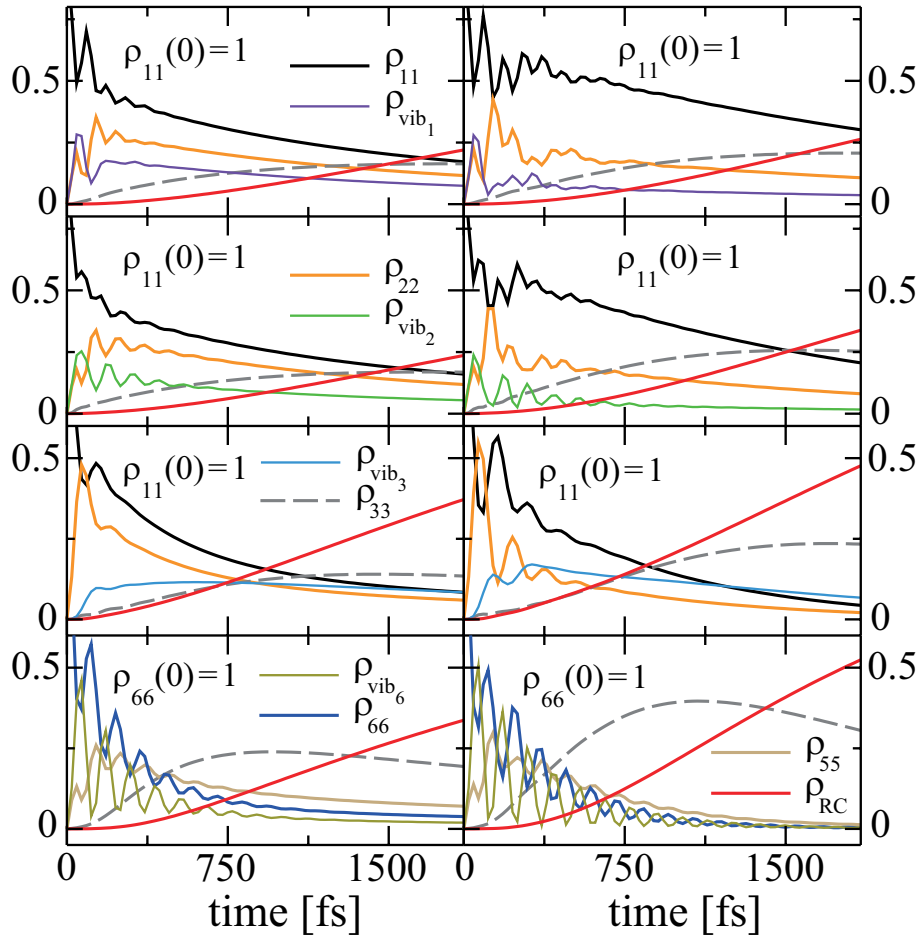


Figure 9.9: Time evolution of the populations of the FMO sites, the RC, and the single vibrational mode coupled to the entrance site 1 (first row), the intermediate site 2 (second row), the exit site 3 (third row), and to the entrance site 6 (last row). Results at $T = 300$ K are shown in left column and at $T = 77$ K in the right column.

vibrational mode is coupled to the entrance site 6.

These results validate the conclusions drawn in the last section: an additional underdamped vibrational mode at the exit site increases the transfer efficiency since it provides additional channels for the parallel decay of the energy into the RC. In contrast, additional underdamped vibrational states at other sites tend to decrease the transfer efficiency since they provide additional states in which the energy is intermittently stored and eventually dissipated via the vibrational channel. Hence, only an efficiently connected exit site helps to improve the global transfer, while additional states at the intermediate sites only lead to an inefficient spreading-out of the energy into too many channels.

Localized vibrational mode coupled to	Initial FMO excitation at site	Transfer time [ps]	Change by
NO vibration	1	3.84	–
	6	3.39	–
all sites (up to 450 cm ⁻¹)	1	3.18	-17.2 %
	6	2.98	-12.1 %
site 1	1	4.46	+16.1 %
	6	3.64	+ 7.4 %
site 2	1	4.28	+11.5 %
	6	3.58	+ 5.6 %
site 3	1	2.83	-26.3 %
	6	2.73	-19.5 %
site 6	1	4.00	+ 4.2 %
	6	3.53	+ 4.1 %

Table 9.2: Same as in Table 9.1 with the dynamics calculated in the strong exciton–mode coupling regime ($S_H = 0.22$). Transfer times in absence of any vibrational mode are included for comparison purposes.

9.1.3 EET dynamics including an equilibrium vibrational mode

In order to further illustrate the robustness of the EET mechanism, in this section, the FMO dynamics is evaluated by keeping the Lorentzian peak in the environmental spectral density, i.e., the full spectral density function given in Eq. (7.2.1) with $\omega_H = 180 \text{ cm}^{-1}$ and $\gamma = 29 \text{ cm}^{-1}$ is used (blue dash-dotted line in Fig. 7.1). The resulting population dynamics of the RC at $T = 300 \text{ K}$ is shown in Fig. 9.10 and the corresponding energy transfer times are given in Table 9.3. Results for smaller values of γ are similar (not shown).

In general, it is found that though the absolute transfer times are different, the overall transfer efficiencies change only by a few percent when compared with the results in Tables 9.1 and 9.2. This clearly corroborates that the position or width of an equilibrium vibrational mode has a negligible effect on the exciton transfer dynamics, which for the FMO complex is already dominated by the large continuous background, as discussed in Sec. 8.1.

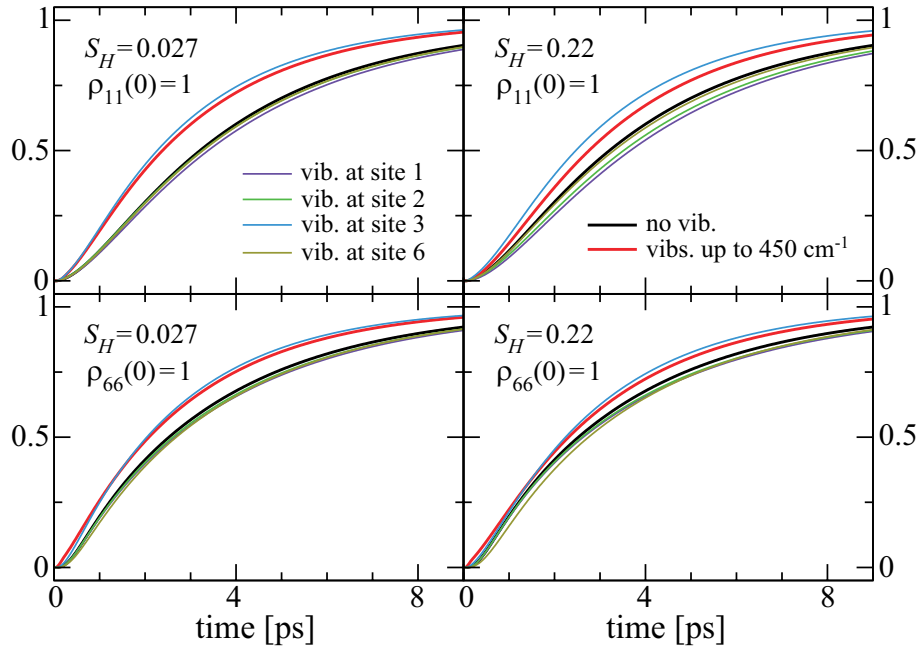


Figure 9.10: Same as in Fig. 9.3 but considering the full spectral density function in Eq. (7.2.1) with $\omega_H = 180 \text{ cm}^{-1}$ and $\gamma = 29 \text{ cm}^{-1}$.

9.2 Effect of low-frequency vibrational modes

The experimental vibrational frequencies determined by Wendling *et al.* [162] from temperature-dependent fluorescence line-narrowing measurements indicate two dominant low frequency modes at 36 and 70 cm^{-1} with large Huang-Rhys factors (italic numbers in Table 7.1). In this section, these two modes are explicitly included as part of the *system* Hamiltonian. Special emphasis is put on the effect of the number N of vibrational excited states on the EET dynamics. The spectral density function derived by Adolphs and Renger without any peak is used, i.e., $J(\omega) = \omega^2 S_0 g_0(\omega)$. Results in Fig. 9.1 are taken as a reference.

9.2.1 Dynamics in presence of the 36 cm^{-1} vibrational mode

For the vibrational mode at 36 cm^{-1} with Huang-Rhys factor of 0.01 (see Table 7.1), the resulting exciton-vibrational mode coupling strength is $\kappa^{(j)} = \omega_H \sqrt{S_H} = 3.6 \text{ cm}^{-1}$.

Considering first a single vibrational mode coupled to the entrance site 1, the effect of an increasing number N (from 1 to 3) of vibrational excited states is illustrated in Fig. 9.11. For simplicity, instead of showing the population of every vibrational

Localized mode coupled to	FMO site initially excited	intermediate coupling ($S_H = 0.027$)		strong coupling ($S_H = 0.22$)	
		Transfer time [ps]	Change by	Transfer time [ps]	Change by
NO vibration	1	3.73	–	3.73	–
	6	3.30	–	3.30	–
all sites (up to 450 cm^{-1})	1	2.82	-24.4 %	3.11	-16.6 %
	6	2.74	-17.0 %	2.90	-12.1 %
site 1	1	3.99	+ 7.0 %	4.31	+15.5 %
	6	3.51	+ 6.4 %	3.53	+ 7.0 %
site 2	1	3.85	+ 3.2 %	4.15	+11.3 %
	6	3.43	+ 3.9 %	3.47	+ 5.2 %
site 3	1	2.64	-29.2 %	2.79	-25.2 %
	6	2.56	-22.4 %	2.68	-18.8 %
site 6	1	3.83	+ 2.7 %	3.88	+ 4.0 %
	6	3.41	+ 3.3 %	3.42	+ 3.6 %

Table 9.3: Comparison of energy transfer times at 300 K with and without nonequilibrium vibrational modes but including an additional equilibrium vibrational mode with width $\gamma = 29 \text{ cm}^{-1}$. Results in the intermediate coupling regime are shown in columns 3 and 4, while those in the strong coupling regime are shown in columns 5 and 6. A negative change in the transfer time indicates a speed-up, while a positive sign indicates a slow-down.

excited state, the total population of the vibrational excited states at site 1 is shown as a violet thin line, i.e., it corresponds to $\rho_{\Sigma \text{vib}_1}(t) = \sum_{v_1 \neq g} \langle 1, v_1 | \rho(t) | 1, v_1 \rangle$. The total population at site 1 is also shown as a green thick line, i.e., it is the population of site 1 after tracing out the vibrational states $\tilde{\rho}_{11}(t) = \sum_{v_1} \langle 1, v_1 | \rho(t) | 1, v_1 \rangle$. The results in Fig. 9.11 indicate that a larger number N of vibrational excited states leads to long-lasting intrasite beatings in the population, i.e., longer coherent oscillations between the vibrational ground state and the vibrational excited states. This results in a slower decay of the population of the site coupled to the vibrational mode due to intrasite population trapping, which causes a slower increase of the RC population and therefore a reduced EET efficiency. Similar results are obtained when the vibrational mode is coupled to the entrance site 6 (not shown).

Results when the vibrational mode is coupled to the exit site 3 are presented in Fig. 9.12. In this case, including a larger number N of vibrational excited states

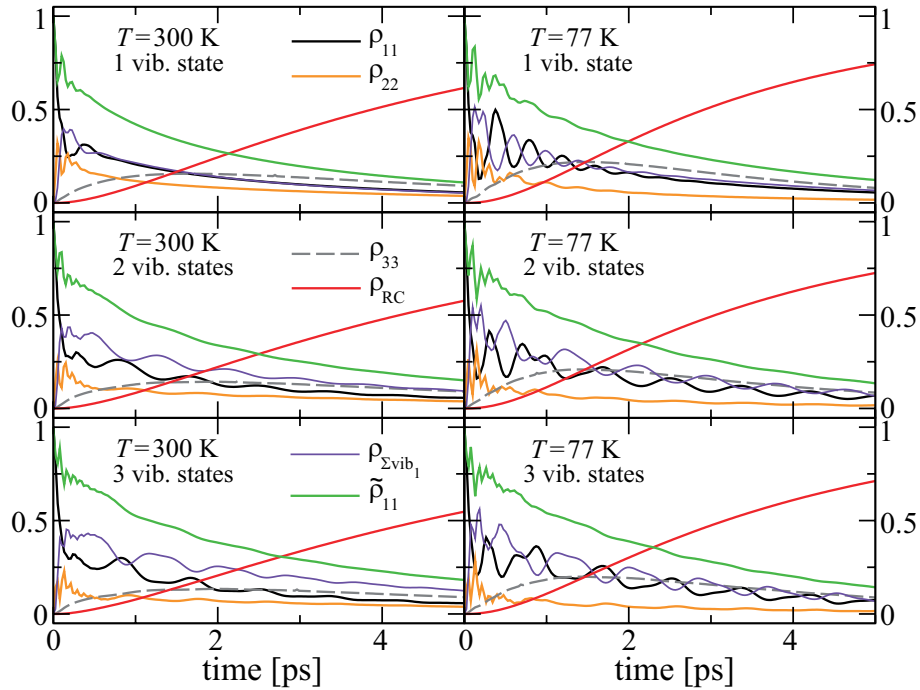


Figure 9.11: Time evolution of selected populations when a single vibrational mode at 36 cm^{-1} is coupled to the entrance site 1 and one ($v_{1,\text{max}} = 1$, top row), two ($v_{1,\text{max}} = 2$, middle row), or three ($v_{1,\text{max}} = 3$, bottom row) vibrational excited states are included. $\rho_{\Sigma vib_1}(t)$ (violet thin line) corresponds to the total population of the vibrational excited states, meanwhile $\tilde{\rho}_{11}(t)$ (green thick line) corresponds to the total population of site 1 regardless of its vibrational state. Results at $T = 300 \text{ K}$ are shown in the left column and at $T = 77 \text{ K}$ in the right column.

provides additional transfer channels, which are available to become populated and can then dump their energy into the RC in parallel, improving the overall EET efficiency. The population ρ_{RC} of the RC is compared for these two situations in Fig. 9.13 and the energy transfer times at $T = 300 \text{ K}$ are given in Table 9.4 for all cases. Observe that increasing the number N of vibrational excited states at the exit site improves the transfer efficiency, while it is deteriorated if the mode is coupled to entrance sites. This is evident, in particular, when the mode is coupled to the entrance site 6 and the initial preparation is $\rho_{66}(0) = 1$. The reason for this is the intrasite population trapping along the already fast EET branch. The opposite reasoning explains the largest improvement in transfer times along the slow EET branch when the site 1 is initially excited and the vibration is coupled to the exit site 3.

Figure 9.14 shows the results when all vibrational excited states with energies

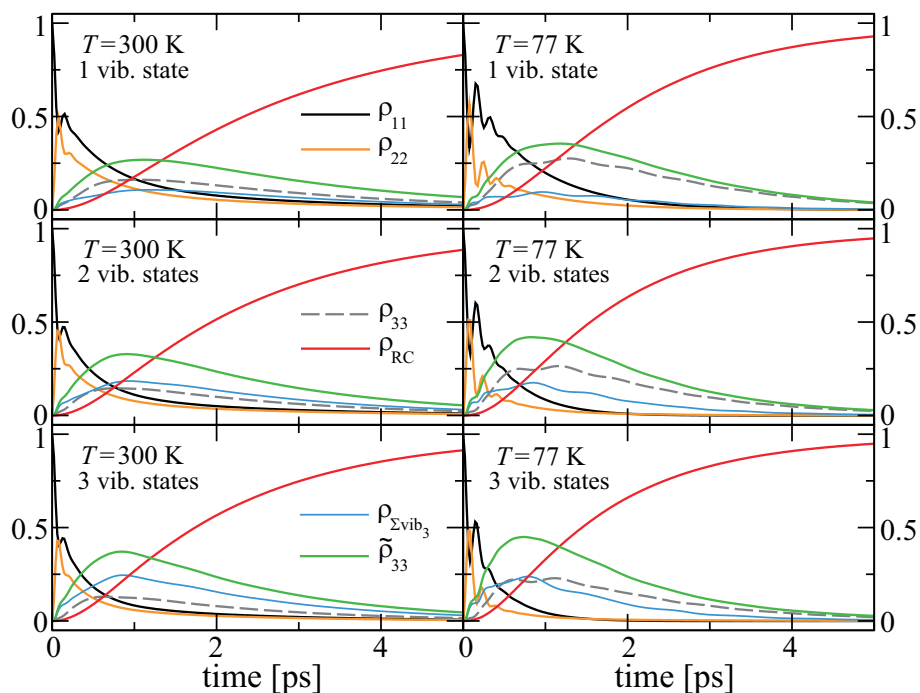


Figure 9.12: Same as in Fig. 9.11 but with the vibrational mode at 36 cm^{-1} coupled to the exit site 3.

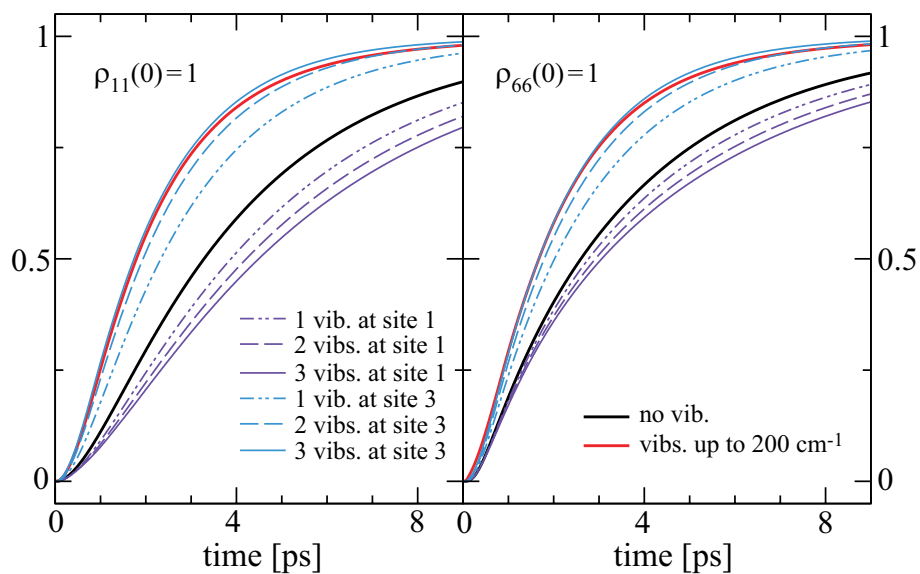


Figure 9.13: RC population ρ_{RC} at 300 K for a different number of vibrational excited states of the mode at 36 cm^{-1} . Results are shown for the initial preparations $\rho_{11}(0) = 1$ (left) and $\rho_{66}(0) = 1$ (right).

Localized mode coupled to	Initial excitation at	Number N of vibrational states		
		$N = 1$	$N = 2$	$N = 3$
site 1	site 1	4.69 (+22.1%)	5.22 (+35.9%)	5.64 (+46.9%)
	site 6	3.73 (+10.0%)	4.03 (+18.9%)	4.29 (+26.5%)
site 3	site 1	2.58 (-32.8%)	2.11 (-45.1%)	1.88 (-51.0%)
	site 6	2.43 (-28.3%)	2.05 (-39.5%)	1.86 (-45.1%)
site 6	site 1	3.96 (+ 3.1%)	4.06 (+ 5.7%)	4.16 (+ 8.3%)
	site 6	4.27 (+26.0%)	4.88 (+44.0%)	5.49 (+61.9%)

Table 9.4: Energy transfer times (in [ps]) and relative change with respect to the case without any vibrational mode (in parenthesis as %) at 300 K for an increasing number N of vibrational excited states of the mode at 36 cm^{-1} . A negative change in the transfer time indicates a speed-up, while a positive sign indicates a slow-down.

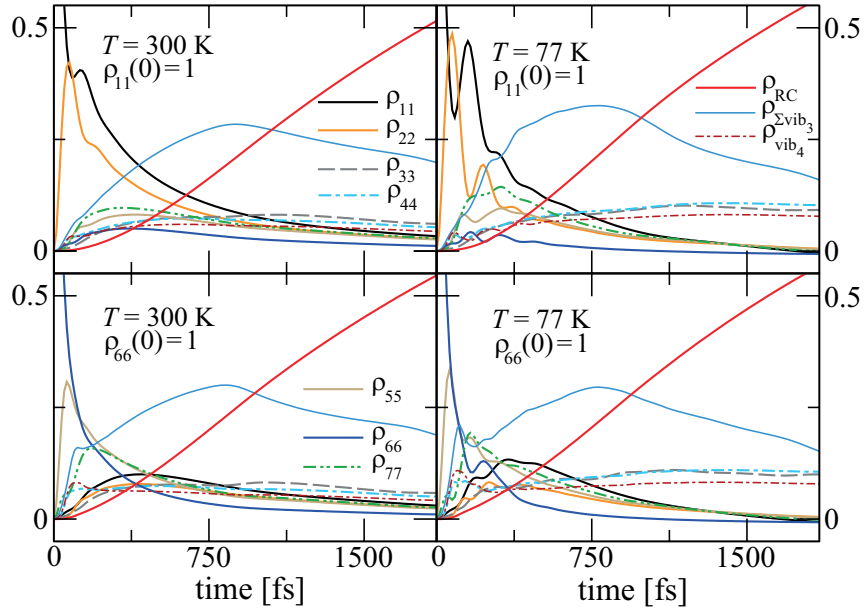


Figure 9.14: FMO populations including all vibrational excited states with energies up to 200 cm^{-1} above the energy of site 3 of the vibrational mode at 36 cm^{-1} .

up to 200 cm^{-1} above the energy of site 3 are included. The smaller cut-off energy results from the low frequency of the considered vibrational mode. It includes, however, five vibrationally excited states at site 3 and a single vibrationally excited state at site 4, which results in a system Hilbert space dimension at the edge of the capabilities for the QUAPI method ($M \simeq 13$). The dynamics of ρ_{RC} at $T = 300$

K is shown in Fig. 9.13 as a red thick line. Transfer times of 1.96 and 1.93 ps are found for the initially excited sites 1 and 6, respectively. They correspond to a change in the transfer time by -49.0 % and -43.1 %, respectively. It is expected that by including five vibrationally excited states at site 3, the transfer time would be highly reduced, much more than when including three excited states. However, the population trapping at site 4 resulting from the inclusion of a single excited state reduces the overall efficiency, counteracting the effect of the large number of decay channels available at site 3.

The results of this section indicate that an adequately connected vibrational mode can improve the transfer efficiency considerably. The improvement depends on how many additional transfer channels are available.

9.2.2 Dynamics in presence of the 70 cm^{-1} vibrational mode

An exciton–vibrational mode coupling strength of 7.0 cm^{-1} results for the vibrational mode at 70 cm^{-1} with a Huang-Rhys factor of 0.01 (see Table 7.1).

The transfer times as a function of an increasing number N (from 1 to 3) of vibrational excited states of a single vibrational mode coupled to the entrance sites 1 or 6 or to the exit site 3 are given in Table 9.5. The improved or decreased transfer efficiency can be explained by the same underlying physics drawn in last section, with intrasite population trapping deteriorating the efficiency and additional decay channels at site 3 improving it.

Localized mode coupled to	Initial excitation at	Number N of vibrational states		
		$N = 1$	$N = 2$	$N = 3$
site 1	site 1	4.22 (+ 9.9%)	4.47 (+16.4%)	4.65 (+21.1%)
	site 6	3.73 (+10.0%)	3.99 (+17.7%)	4.17 (+23.0%)
site 3	site 1	2.47 (-35.7%)	2.07 (-46.1%)	1.89 (-50.8%)
	site 6	2.37 (-30.1%)	2.03 (-40.1%)	1.87 (-44.8%)
site 6	site 1	3.96 (+ 3.1%)	4.07 (+ 6.0%)	4.16 (+ 8.3%)
	site 6	3.64 (+ 7.4%)	3.86 (+13.9%)	4.08 (+20.4%)

Table 9.5: Same as in Table 9.4 for the mode at 70 cm^{-1} .

Results for different number of vibrationally excited states at sites 3 and 4 are shown in Fig. 9.15. In this case, including all vibrational excited states with energies up to 250 cm^{-1} (upper set) or up to 300 cm^{-1} (upper set) above the energy of site 3, includes three and one ($M = 11$) or four and two ($M = 13$) excited states at sites 3 and 4, respectively. This compares then the effect of including an additional decay

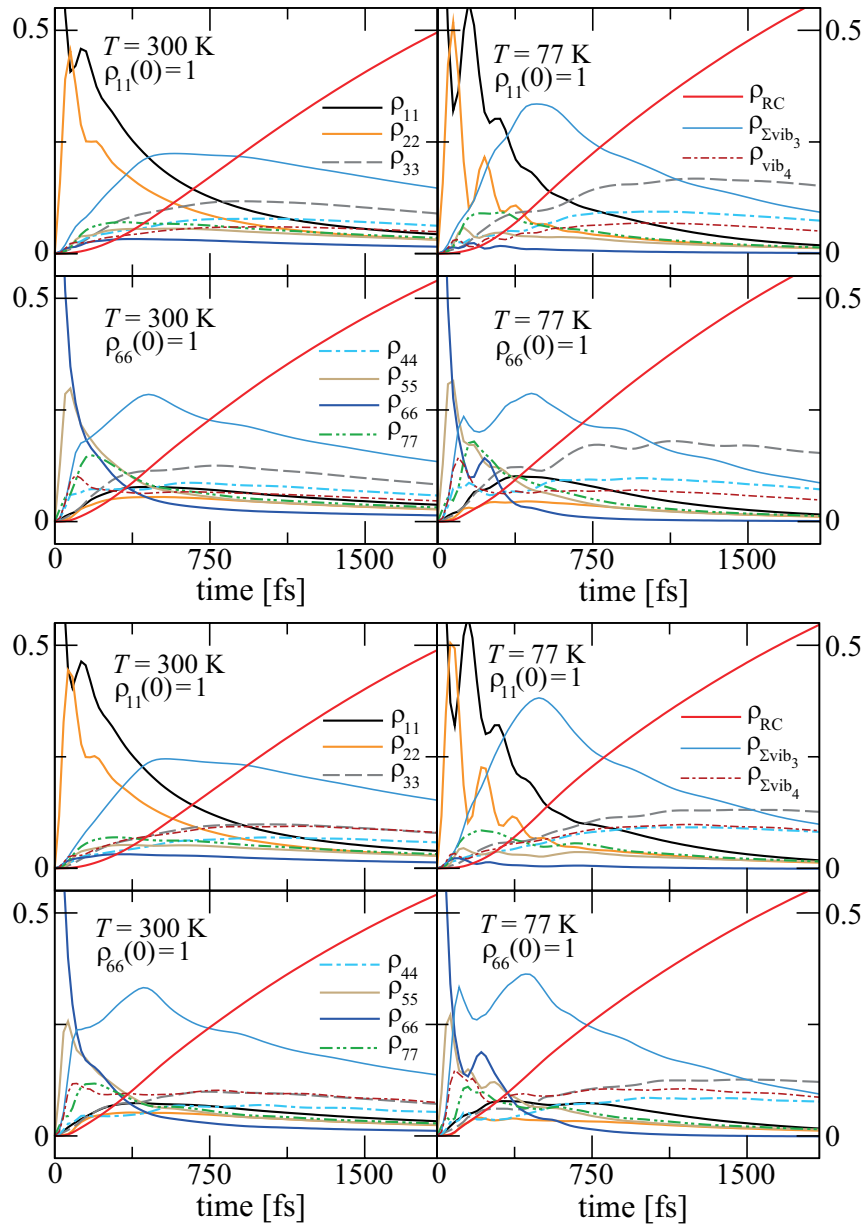


Figure 9.15: FMO populations in presence of a vibrational mode at 70 cm^{-1} including all vibrational excited states with energies up to 250 cm^{-1} (upper set) and up to 300 cm^{-1} (lower set) above the energy of site 3.

channel to the site 3 and simultaneously an additional trapping state at site 4. The energy transfer times at $T = 300 \text{ K}$ for these two cases are given in Table 9.6. The dynamics of ρ_{RC} for all cases is shown in Fig. 9.16. Results in Table 9.6 clearly illustrate that any additional state in a site not connected to the RC counteracts any additional decay channel at the exit site, leading to population trapping and,

Number of vibrational excited states at		Initial FMO excitation at site	Transfer time [ps]	Change by
site 3	site 4			
3	1	1	2.15	-44.0 %
(up to 250 cm ⁻¹)		6	2.12	-37.5 %
4	2	1	2.23	-41.9 %
(up to 300 cm ⁻¹)		6	2.20	-35.1 %

Table 9.6: Comparison of energy transfer times at 300 K including a different number of vibrational excited states of the mode at 70 cm⁻¹ coupled to sites 3 and 4. A negative change in the transfer time indicates a speed-up, while a positive sign indicates a slow-down.

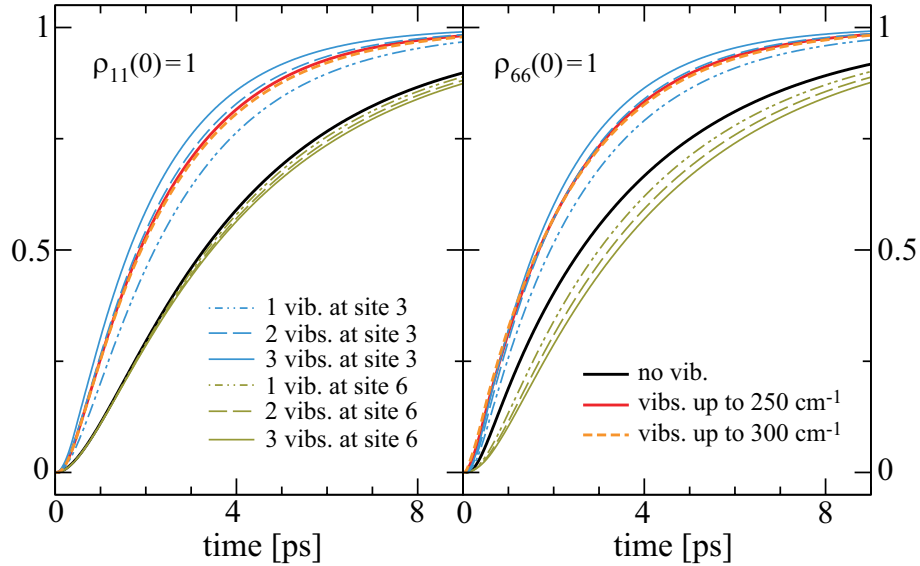


Figure 9.16: RC population ρ_{RC} at 300 K for a different number of vibrational excited states of the 70 cm⁻¹ mode. Results are given for the initial excitation at site 1 (left) and 6 (right).

therefore, to an overall reduced efficiency. It is observed that the transfer efficiency will be always reduced by adding a single trapping state, even if two additional decay channels at the exit site are considered, as found in the previous section when comparing the change in the transfer times by including three excited states connected to site 3 (-51.0%) with the change by including excited states up to 200 cm⁻¹ (-49.0 %).

The results of this section complement those presented in the previous section,

additional underdamped vibrational states at any other sites tend to decrease the transfer efficiency since they provide additional states in which the energy is intermittently stored and eventually dissipated via the vibrational channel. Hence, only an efficiently connected exit site helps to improve the global transfer, while additional states at the intermediate sites only lead to an inefficient spreading-out of the energy into too many channels. The observed long-lasting coherence in the FMO complex results from the coupling of the vibrational modes to particular entrance and exit sites, but it is not functionally necessary for the speed-up of energy transfer which thus is a rather robust mechanism.

The fact that the presented results for the exciton dynamics in presence of nonequilibrium vibrational modes agree with the experimental ones indicate a breakdown of the Franck-Condon (or, equivalently, the Born-Oppenheimer) approximation. Put differently, strongly coupled vibrational modes evolve on a similar time scale as the excitation transfer and therefore, they should be described on an equal footing as the excitonic states. This coupled exciton–vibrational mode system is particularly relevant when calculating the two-dimensional electronic spectrum of the FMO complex.

These results offer a benchmark principle that can be used, for example, for optimizing artificial light-harvesting systems. Their global quantum transfer efficiency can be significantly increased by engineering the distribution of vibrational modes, thereby maintaining the number of absorbing photoactive sites constant.

Quantification of non-Markovian effects in the exciton dynamics

The many prominent vibrational peaks in the spectral density functions of the FMO complex presented in Chap. 7 induce a complicated pattern of temporal bath correlations with long life time [see discussion following Eq. (2.2.11)]. Then, it is a priori not clear whether simple Redfield-like quantum master equations are an appropriate tool to describe the transfer dynamics. This is because such an approach is by construction based on a weak-coupling assumption which goes along with a Markovian approximation [7]. Such an assumption is valid only for a pure and structureless Ohmic spectral distribution of the bath fluctuations. In order to describe the dynamics of an open quantum system beyond the Markovian approximation, few numerically exact approaches are available, with the drawback that these all need substantial computer power [169].

Results presented in chapters 8 and 9 were calculated using the iterative QUAPI scheme, which is a deterministic summation of the path integral and thus does not suffer from any sign problem as being present in quantum Monte Carlo schemes. Besides, it allows one to treat arbitrary spectral functions at finite temperatures without invoking any approximation, and therefore the results are numerically exact. Other studies on the FMO complex, however, have used Markovian master equations (see, for example, Refs. [188, 204, 205]), although it has been shown that a weak-coupling Markovian approach fails [7, 220, 221], the reason being that multiphonon

processes are neglected [7]. In this chapter, the question of whether or not the quantum dynamics of the FMO complex is Markovian is investigated. In the case that the dynamics is Markovian, a weak-coupling lowest-order Born approximation can still not be used to determine the Redfield rate tensor [7, 220, 221]. However, importantly, a Markovian quantum master equation could still be used to discuss the dynamics if the rate tensor is either treated as an effective fit parameter or obtained from some more advanced theory.

Here, the non-Markovianity measure of Ref. [49] is used to quantify non-Markovian effects during the excitation energy transfer dynamics of the FMO complex in the presence of discrete vibrational modes. It is based on the physical features of the system-bath interaction in terms of information backflow from the environment to the system. The resulting non-Markovianity quantifier is given by Eq. (2.3.4). In the case of the FMO complex, the two initial states $\rho_1(0) = \rho_{11}$ and $\rho_2(0) = \rho_{66}$ are considered, which correspond to the initially excited BChls 1 and 6 sites, respectively. Results in Sec. 10.1 correspond to the dynamics due to equilibrium vibrations as presented in Chap. 8, meanwhile, those in Sec. 10.2 correspond to the dynamics due to nonequilibrium vibrations as presented in Chap. 9.

10.1 Non-Markovian effects in presence of equilibrium vibrations

Results in Chap. 8 include any vibrational mode as part of the environmental spectrum. It is then assumed that the thermalization time scale of the mode(s) is much shorter than any system time scale. This does not exclude non-Markovian dynamics of the system but only nonequilibrium fluctuations of the vibrational modes. In this section, any possible non-Markovian effects are evaluated.

10.1.1 Non-Markovianity in the Adolphs-Renger model

The evolution of the trace distance [Eq. (2.3.1)] for the spectral density function derived by Adolphs and Renger [Eq. (7.2.1)] as a function of the position ω_H and width γ of the Lorentzian peak is presented in Fig. 10.1. It is observed that the trace distance decays faster at higher temperatures and this decay is monotonic, indicating a unidirectional flow of information from the system to the environment, rendering the dynamics Markovian. The same kind of dynamics is observed when no localized vibrational mode is included in Eq. (7.2.1), as shown in Fig. 10.2.

Because there is no time interval over which the trace distance increases, $\mathcal{N} = 0$

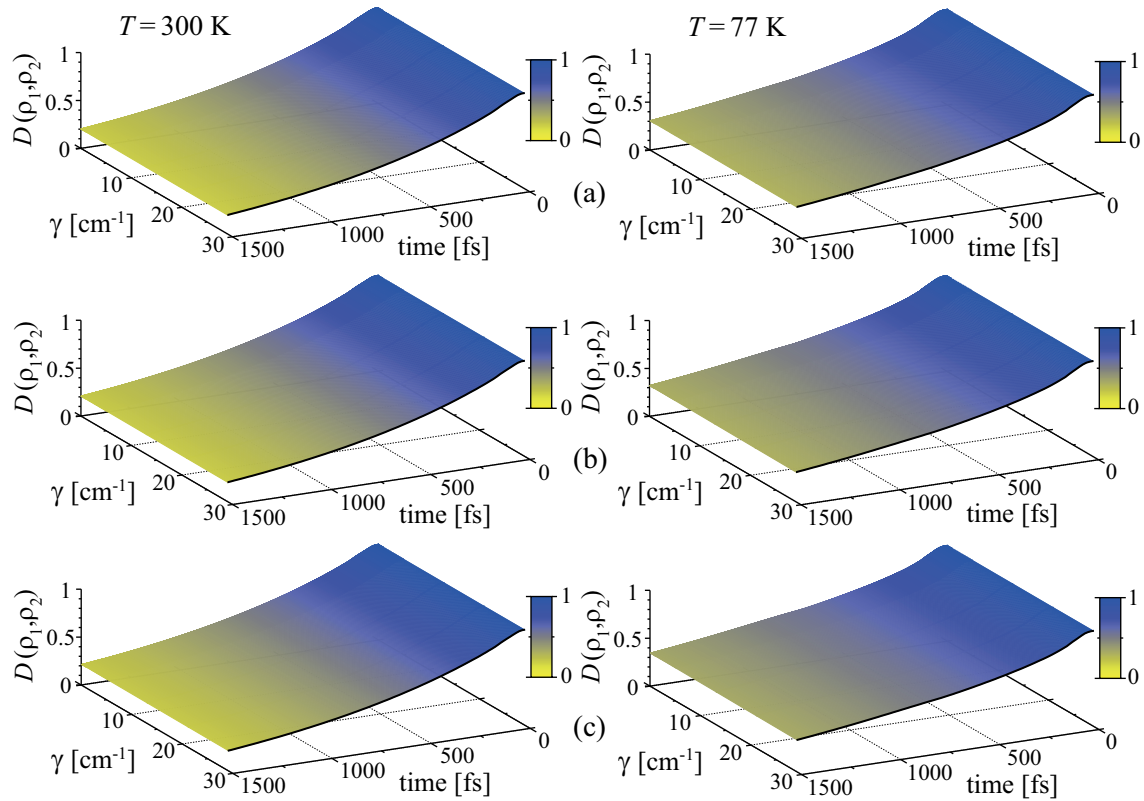


Figure 10.1: Time evolution of the trace distance [Eq. (2.3.1)] for the spectral density function derived by Adolphs and Renger [Eq. (7.2.1)] as a function of the width γ of the Lorentzian peak centered at (a) 180, (b) 190.8, and (c) 211.0 cm^{-1} . Left and right columns correspond to temperatures of $T = 300$ and $T = 77$ K, respectively.

results for all cases shown in Figs. 10.1 and 10.2. These results indicate that the presence of a single localized vibrational mode in the bath spectral density does not induce any non-Markovian effect in the exciton dynamics of the FMO complex, even in the case when its frequency is exactly in resonance with exciton energy differences. The broadening of this vibrational mode over a wide range of γ values does not induce any non-Markovian effect either.

The negligible effect of the Lorentzian peak on the dynamics can be understood by the rather large continuous background spectrum $g_0(\omega)$ in Eq. (7.2.1), which results in line widths for the exciton transitions already exceeding the width of the Lorentzian peak. In such a case, the Lorentzian peak becomes effectively *smeared out* and detailed results depend only weakly on its width γ and position ω_H (see also Figs. 8.3 and 8.6). This, in turn, would suppress any non-Markovian behavior

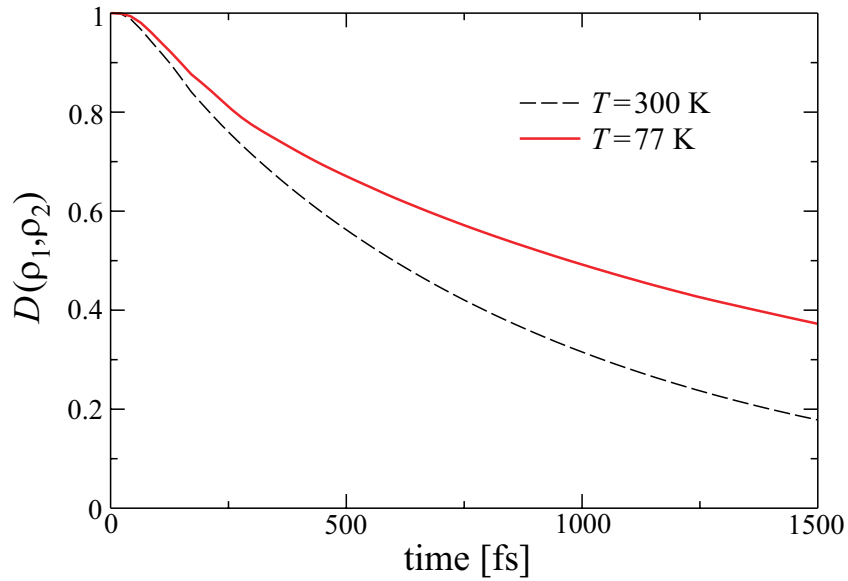


Figure 10.2: Same as in Fig. 10.1 in the absence of any localized vibrational mode.

too, as observed in Fig. 10.1.

10.1.2 Non-Markovianity in the Kreisbeck-Kramer model

Figure 10.3 shows the time-dependent trace distance [Eq. (2.3.1)] for the spectral density derived by Kreisbeck and Kramer [Eq. (7.3.1)] with $n = 3$ and $n = 11$. As before, the monotonic decay of the trace distance at room temperature is faster as compared to the decay at cryogenic temperature. This decay is faster for $n = 11$ than for $n = 3$ due to the faster increase of the spectral weight at low frequencies in the former case (see Fig. 7.4). $\mathcal{N} = 0$ is then obtained for all the examined cases. These results allow one to conclude that in spite of the role played by localized vibrational modes in the coherence times (see Sec. 8.2), they do not induce any non-Markovian effects in the exciton dynamics of the FMO complex.

10.1.3 Non-Markovianity in the Aghtar *et al.* model

The trace distance evolution for the site-dependent spectral density function derived by Aghtar *et al.* [165] [Eq. (7.4.2)] is shown in Fig. 10.4. In both cases, a similar monotonic decay of the trace distance is observed, which again indicates a Markovian dynamics ($\mathcal{N} = 0$). The fact that the trace distance at 300 K decays faster than the case at 310 K is because the spectral weight at low frequencies for water as a solvent is larger than for the glycerol:water 65:35 mixture as a solvent (see Fig.

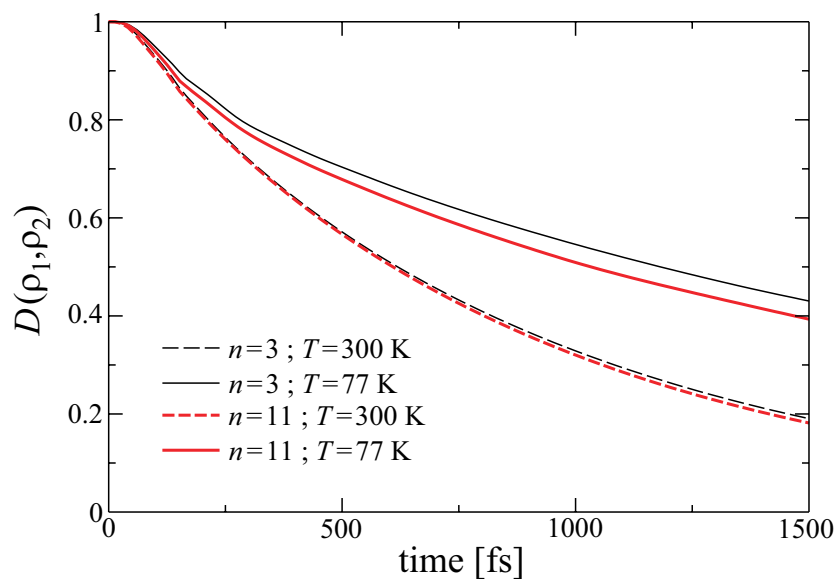


Figure 10.3: Time-dependent trace distance [Eq. (2.3.1)] for the spectral density derived by Kreisbeck and Kramer [Eq. (7.3.1)] with $n = 3$ (thin black lines) and $n = 11$ (thick red lines) at 77 K (solid lines) and 300 K (dashed lines).

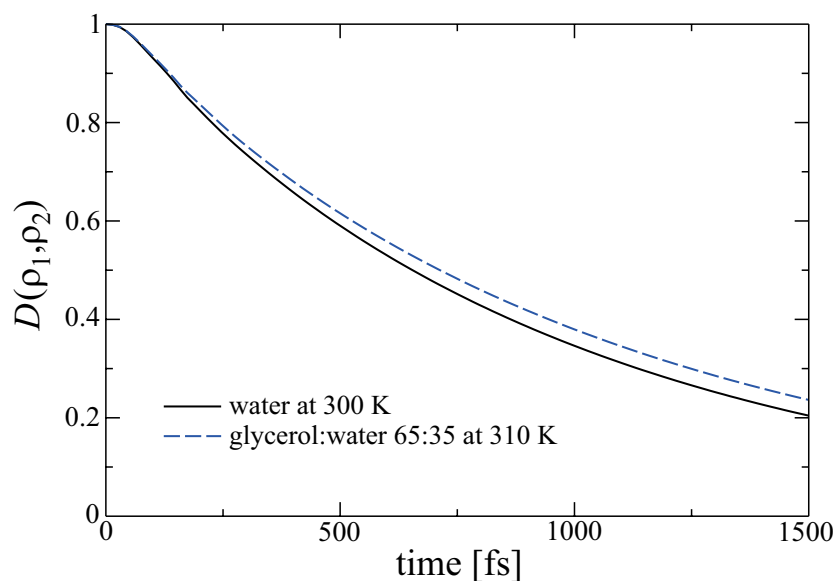


Figure 10.4: Time evolution of the trace distance [Eq. (2.3.1)] for the spectral density derived by Aghtar *et al.* [Eq. (7.4.2)] with water as a solvent at 300 K (solid black line) and with a glycerol:water 65:35 mixture as a solvent at 310 K (dashed blue line).

7.5). This allows one to rule out the possibility of non-Markovian effects arising from microscopic details of the polar environment.

10.2 Non-Markovian effects in presence of non-equilibrium vibrations

The results shown in Chap. 9 include vibrational modes as part of the system Hamiltonian and thus, their nonequilibrium quantum dynamics is described on an equal footing as the excitonic states. The dynamics presented in Fig. 9.1, where no vibrational mode is considered, is taken as a reference and the corresponding evolution of the trace distance is shown in Fig. 10.5. Similar to the results in Fig.

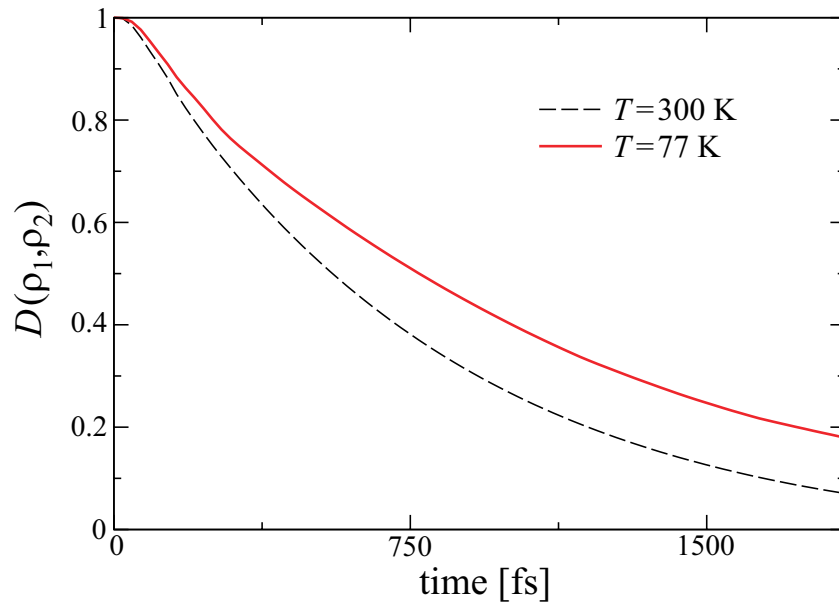


Figure 10.5: Time evolution of the trace distance for the dynamics presented in Fig. 9.1 in the absence of any localized vibrational mode but including the RC into the description.

10.2, there is a monotonic decay of the trace distance, which is faster at higher temperatures. However, a faster decay is observed in this case due to the explicit inclusion of the RC into the transfer dynamics. This monotonic decay indicates a unidirectional flow of information from the system to the environment, rendering the dynamics Markovian, i.e., $\mathcal{N} = 0$.

10.2.1 Non-Markovianity in presence of the 180 cm^{-1} mode

The evolution of the trace distance for all cases evaluated in Sec. 9.1 is presented in Fig. 10.6. The dynamics corresponds (from top to bottom) to the cases when

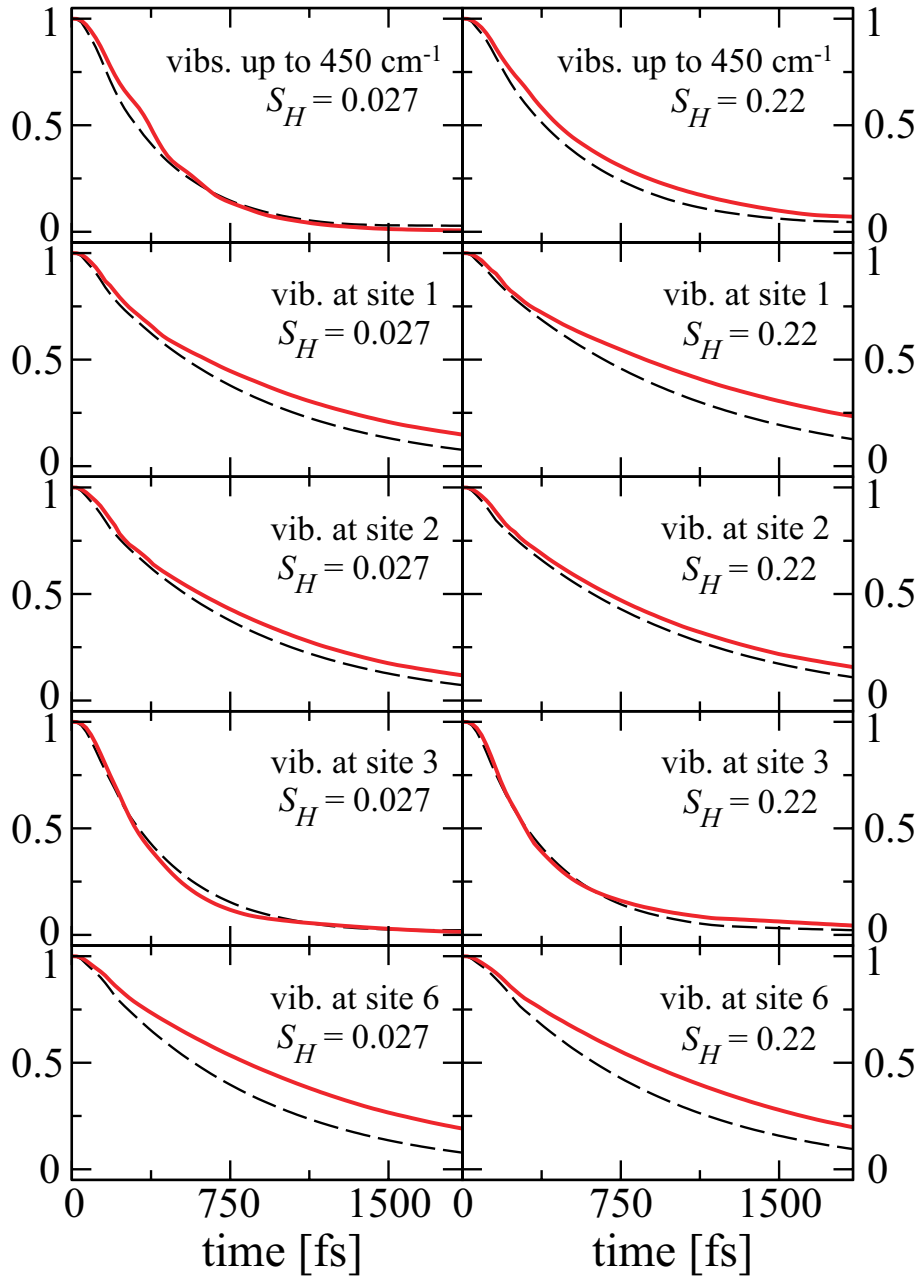


Figure 10.6: Time evolution of the trace distance in Eq. (2.3.1) considering the 180 cm^{-1} vibrational mode coupled to several BChl sites. Results at 77 K are shown as solid red lines and at 300 K as dashed black lines.

a vibrational mode at each individual molecular site is included, and when a single vibrational mode is coupled to the entrance site 1, to the intermediate site 2, to the exit site 3, and to the entrance site 6, respectively. In all cases, the resulting dynamics in the intermediate and in the strong exciton–vibrational mode coupling regimes is presented in the left and right columns, respectively. It is found that $\mathcal{N} = 0$ for all evaluated cases. In general, the decay of the trace distance is slower in the strong coupling regime. This is because the resulting intrasite population trapping, that reduces the transfer efficiency, leads to a slower dissipation and therefore a slower flow of information from the system to the environment. The dissipation, and also the information flow, is faster when the vibrational mode is coupled to the exit site 3. This is not surprising since site 3 is coupled to the RC acting as an incoherent energy sink.

The results indicate that even when the full nonadiabatic quantum dynamics of a single vibrational mode is considered, it does not induce any non-Markovian effects in the exciton transfer dynamics of the FMO complex. The same results are obtained when several vibrational modes are considered.

10.2.2 Non-Markovianity in presence of the 36 and 70 cm^{-1} modes

Figure 10.7 shows the time evolution of the trace distance when a different number N of vibrational excited states of the low frequency modes in Sec. 9.2 are included. As in the previous section, the decay of the trace distance is faster when the vibrational mode is coupled to the exit site 3, with the decay being faster for larger N . Put differently, the larger the number of states connected to the incoherent energy sink, the faster is the flow of information from the system to the environment. Conversely, when the vibrational mode is coupled to the entrance sites, the intrasite population trapping is stronger and therefore the decay of the trace distance is slightly slower. However, independently of which site the vibrational mode is coupled to and how many vibrational excited states are considered, there is no time interval over which the trace distance increases. The same results are obtained by including vibrational modes coupled to different BChl sites, as shown Fig. 10.8. In this case, a different number of vibrational excited states above the energy of site 3 are included: those with energies up to 200 cm^{-1} of the 36 cm^{-1} mode (top), those with energies up to 250 cm^{-1} (middle) and up to 300 cm^{-1} (bottom) of the 70 cm^{-1} mode. It is obtained $\mathcal{N} = 0$ for all cases.

The results indicate that the excitation energy transfer of the FMO complex follows a Markovian dynamics.

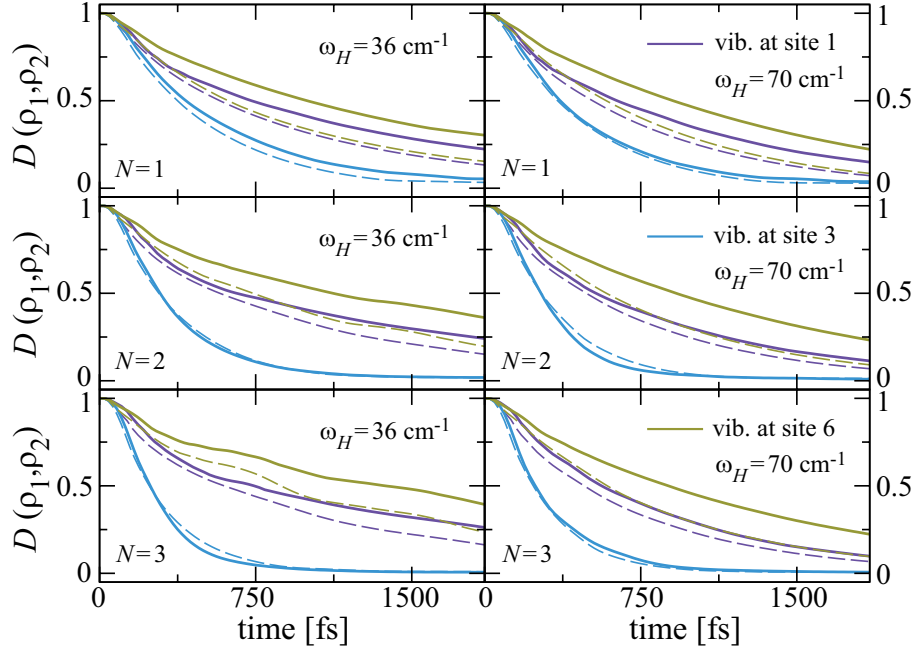


Figure 10.7: Time-dependent trace distance including a different number N of vibrational excited states of the mode at 36 cm^{-1} (left column) and of the mode at 70 cm^{-1} (right column). Results at 77 K are shown as solid thick lines and at 300 K as dashed thin lines.

10.3 Concluding remarks

In this chapter, non-Markovian effects during the excitation transfer dynamics in the FMO complex are quantified by means of a non-Markovianity measure based on the trace distance of two quantum states (Sec. 2.3). The time evolution of the trace distance indicates that the presence of localized vibrational modes, either as part of the environmental spectrum or as part of the system Hamiltonian, does not induce any non-Markovian effects in the exciton dynamics of the FMO complex.

When considering equilibrium vibrational modes, neither the position of a single mode nor its width induce any non-Markovian exciton dynamics (Sec. 10.1.1), even in the case when its frequency is exactly in resonance with exciton energy differences. These effects do not arise when several localized vibrational modes are included (Sec. 10.1.2) nor from the microscopic details of the polar environment (Sec. 10.1.3). When considering nonequilibrium vibrational modes (Sec. 10.2), neither the frequency of the mode nor the number of vibrational excited states considered induce any non-Markovian exciton dynamics. It is found, however, that when the vibrational mode is coupled to the exit site 3, the decay of the trace

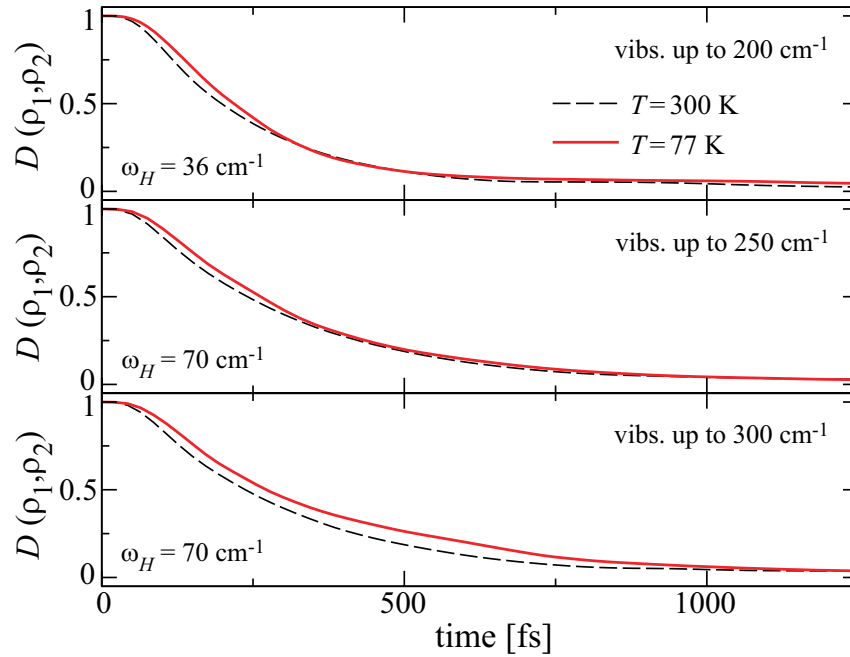


Figure 10.8: Time-dependent trace distance including a different number of vibrational excited states of the 36 cm^{-1} mode and of the 70 cm^{-1} mode.

distance is the fastest due to quickly unidirectional flow of information from the system to the environment through the incoherent energy sink.

The results of this chapter show that the transfer of excitation energy in the FMO complex follows a Markovian dynamics. Similarly, it has been shown that the excitation energy transfer efficiency does not depend on the presence of non-Markovian effects [222]. The discrete vibrational modes within the environmental fluctuation spectra do not render the dynamics non-Markovian since the continuous phonon contribution of the fluctuation spectra results already in large linewidths for the exciton transitions. Hence, each exciton transition overlaps with the spectral peak of the vibrational mode, thus suppressing non-Markovian effects.

The resulting Markovian dynamics is still not describable by weak system-bath coupling approaches, the reason being that multiphonon processes are neglected [7]. However, these results show that Markovian quantum master equations could be used to discuss the dynamics, or the transfer efficiency, if the rate tensor is either treated as an effective fitting parameter or obtained from some more involved theory approach. These results therefore will help to considerably simplify the numerical effort in future investigations and, thus, larger light-harvesting complexes will be treatable in an accurate and reliable manner.

Part III

Biomolecular systems: The PE545 complex

The PE545 complex

Photosynthesis occurs mainly in higher (green) plants, algae and certain bacteria, like the green sulfur bacteria in Chap. 6. Algae are plants lacking roots, stems, and leaves and are found mainly in aquatic environments [156]. Cryptophytes (genus *Cryptomonas*) are single celled photosynthetic algae, 6-20 μm in size. They are important primary producers in the food chain in both marine and freshwater environments, where they live at the bottom of shallow water. They propel themselves with two unequal flagella and can survive in low light conditions [223, 224, 225]. Its photosynthetic apparatus is illustrated in Fig. 11.1.

There are approximately 200 known species of cryptophyte algae [156, 223]. They have two different light-harvesting complexes, a chlorophyll *a/c2* complex together with the carotenoid alloxanthin on the outside of the thylakoid membranes and a phycobiliprotein complex that, peculiarly, accumulates as dense material in the thylakoid lumina [see Fig. 11.1(c)-(d)]. Each species has a single phycobiliprotein antenna complex of two possible, phycoerythrin (three types, leading to red coloured organisms) or phycocyanin (five types, leading to blue coloured organisms) [156, 223, 224]. All cryptophyte phycobiliproteins are structurally similar in that they are based on an $\alpha\alpha'\beta_2$ tetramer complex (arranged as a dimer of $\alpha\beta$ monomers). They contain eight bilin chromophores, which are characterized by a linear tetrapyrrole structure and are covalently linked to the protein scaffold through a thioether linkage with a cysteine [226].

One of the best characterized phycoerythrin proteins is the PE545 [see Fig.

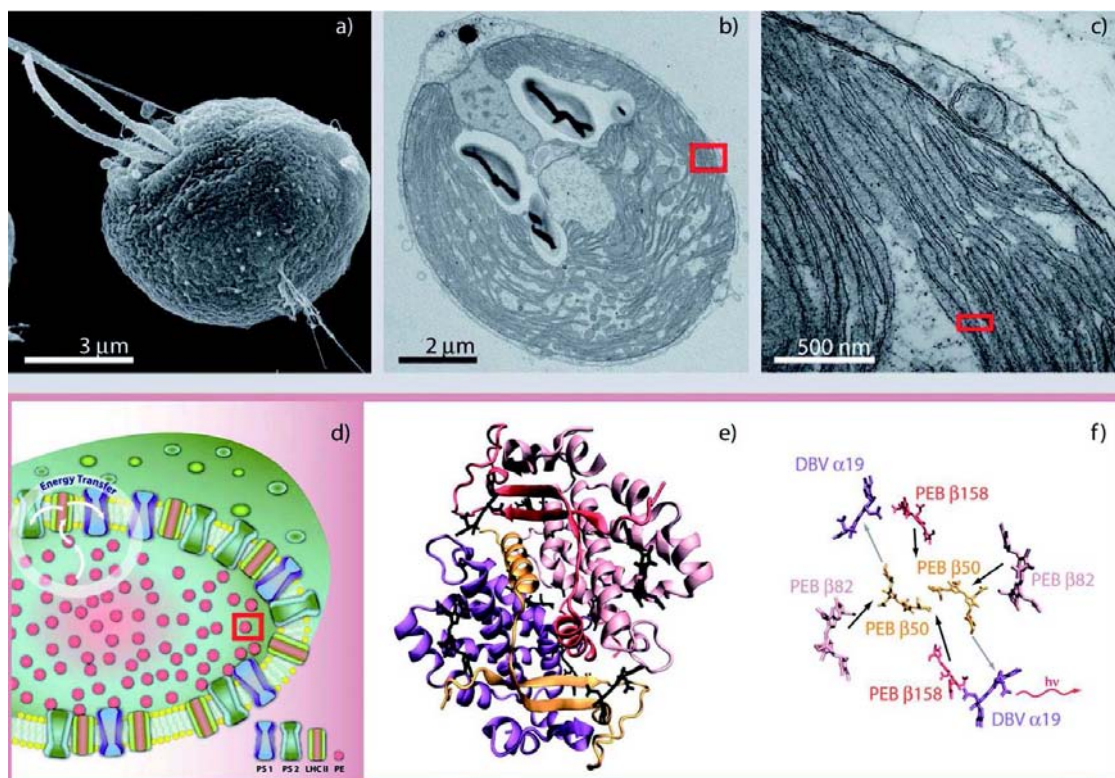


Figure 11.1: Antenna complex of a cryptophyte algae. (a) Scanning electron microscope micrograph of the flagellated cryptophyte alga *Proteomonas sulcata*. (b)-(c) Transmission electron micrographs, with the red rectangles in (b)-(d) representing areas being zoomed-in in subsequent figure panels. The light-harvesting phyco-biliproteins appear in (c) as the dark, electron-rich regions located in the intrathylakoid space. They transfer the excitation to other membrane-bound antenna systems and to the photosystems I or II (d). Structural model of PE545 with bilin chromophores shown in black (e), and in (f) without the enveloping apoprotein. Arrows in (f) indicate the energy flow in PE545. Reproduced from Ref. [156] with permission from The Royal Society of Chemistry.

11.1(e)], that is the principal light-harvesting antenna of the cryptomonad *Rhodomonas* sp. strain CS24. Its crystal structure has been determined at 0.97 Å resolution [227]. Phycoerythrin PE545 is the antenna pigment involved in the initial energy-capture step, from which the excitation is funneled to membrane-bound antenna systems and then to the core of photosystem I or II, as schematically shown in Fig. 11.1(d) [156].

In PE545 each α chain (A and B) contains a 15,16-dihydrobiliverdin (DBV), whereas each β polypeptide chain (C or D) is linked to three phycoerythrobilins

(PEB). The corresponding chromophores are labeled as DBV_{19A}, DBV_{19B}, PEB_{158C}, PEB_{158D}, PEB_{50/61C}, PEB_{50/61D}, PEB_{82C}, and PEB_{82D}. The subscript denotes the cysteine residue linked to the chromophore and the protein subunit, respectively. The central PEB_{50/61} pigments, shown as yellow molecules in Fig. 11.1(f), are linked to the protein by two cysteine residues. The overall PE545 structure (and the chromophores) displays a pseudosymmetry about the 2-fold axis relating the $\alpha_1\beta$ and $\alpha_2\beta$ monomers, as illustrated in Fig. 11.1(e)-(f) [226].

Chromophores in cryptophyte light-harvesting antenna proteins have large energy gaps and are separated by an average distance of 20 Å. This is about twice the average pigment distance in the major light-harvesting proteins of plants [182, 228]. PE545 is unusual in that it contains a deep, water-filled slot between the monomers [224, 229]. Because of the structural flexibility of the linear tetrapyrrole molecules, energy tuning in PE545 is mostly achieved by constraining the conformational space available to the bilin pigments in the protein scaffold, rather than by specific pigment-protein interactions, as in chlorophyll-based photosynthetic complexes like the FMO complex [230]. Additional tuning is achieved by assembling two different bilin types (DBV and PEB) in the antenna [226].

The light-harvesting mechanism is based on a model where the four highest-energy pigments (PEB₈₂ and PEB₁₅₈) direct their excitation energy first to the central PEB_{50/61} pair, as shown in Fig. 11.1(f). Subsequent steps involve the transfer of that excitation to the two lowest-energy pigments DBV₁₉, from which excitation energy is transferred to other proteins [156]. Interestingly, in PE545 only two bilin types cover the same part of the spectrum, which in other organisms, like cyanobacteria and red algae, is covered by multiple proteins and bilins. The central dimer in PE545 expands spectral coverage, ensures more efficient trapping of energy, and mediates the ensuing transfer of this excitation to the red-shifted DBV bilins [224]. The low energy of the DBVs is a consequence of their more extended π -conjugated system as compared to PEBs, thus making them the obvious candidates for the energy trapping site in the complex [224, 226].

Experimental results using two-dimensional electronic spectroscopy in the phycoerythrin PE545 (from *Rhodomonas* CS24) and in the phycocyanin PC645 (from *Chroomonas* CCMP270) proteins have also revealed long-lived oscillatory components at ambient temperature [182, 183]. In particular, coherent oscillations lasting longer than 200 fs are observed in the signal associated to the central PEB_{50/61} dimer in PE545. It is assumed that this long-lived coherence results from the covalent attachment of the chromophores to their protein environment. This may support correlated motions between chromophores and protein and thus be an important factor in slowing down decoherence in cryptophyte antenna proteins, even

at physiological temperature [182, 230].

In this part, the excitation energy transfer dynamics of the PE545 complex is calculated by means of the iterative QUAPI scheme (Sec. 2.2.1) in its extended version (Sec. 2.2.2). In Sec. 11.1, it is shown how the PE545 complex is modeled and the environmental fluctuation spectral function, extracted from molecular dynamics simulations, is explicitly shown. The resulting energy transfer dynamics is calculated in Chap. 12, where non-Markovian effects are also quantified.

11.1 PE545 Model

As in the FMO complex (see Sec. 7.1), the system Hamiltonian for the eight bilins is formulated within the single excitation subspace as $H_{\text{PE545}} = \sum_{j=1}^8 E_j |j\rangle\langle j| + \sum_{j \neq i} V_{ji} (|j\rangle\langle i| + |i\rangle\langle j|)$. Analogously, the basis states $|j\rangle$ indicate that the j -th site is in its electronic excited state and all other sites are in their electronic ground states. E_j denotes the energy of the j -th site and V_{ji} denotes the electronic coupling between sites j and i . Site energies and electronic couplings of all eight bilins in PE545 have been determined by structure-based calculations relying on a mixed quantum mechanics/molecular mechanics scheme [226]. The chromophores are described at the quantum mechanical level whereas the protein-solvent environment is described through a classical polarizable force field, combined with a quantitative modeling of the spectra and the energy transfer dynamics. The resulting Hamiltonian in the site representation (corresponding to the bilins DBV_{19A}, DBV_{19B}, PEB_{158C}, PEB_{158D}, PEB_{50/61C}, PEB_{50/61D}, PEB_{82C}, and PEB_{82D}) is [226]

$$H_{\text{PE545}} = \begin{pmatrix} 0 & -4.3 & -27.3 & 3.5 & 2.2 & -39.3 & -11.4 & 34.3 \\ & 0 & -3.7 & 26.3 & -42.6 & 1.4 & -36.1 & 11.6 \\ & & 800 & -6.1 & -21.5 & -15.2 & 7.3 & 6.4 \\ & & & 650 & 24.5 & 19.1 & 6.8 & 8.2 \\ & & & & 1450 & 71.7 & 34.0 & 12.1 \\ & & & & & 1050 & -16.0 & -35.6 \\ & & & & & & 550 & 4.0 \\ & & & & & & & 50 \end{pmatrix} \text{cm}^{-1}. \quad (11.1.1)$$

Due to the large bilin separations, the site energy differences $|E_j - E_i|$ are very large in comparison to inter-site electronic interaction V_{ji} [228]. This also leads to a high localization of the excitonic eigenstate $|j\rangle$ in the site j , as compared to the case of the FMO complex.

The lowest energy chromophores are the pair of DBV₁₉ bilins. The PEB_{50/61} dimer

is positioned in the middle of the DBV dimer, while the PEB bilins are positioned in an open arrangement on the outside of the protein [see Fig. 11.1(f)]. This arrangement of chromophores funnels the energy out of the DBV traps [231]. For the PE545 complex, it is assumed that the initially populated site is the PEB_{50/61C} or the PEB_{50/61D}. This is concordant with a laser pulse shifted well into the blue end of the spectrum, such that it only excites the highest excitonic eigenstate [228, 229].

The full pigment-protein-solvent system is modeled by employing an open system approach [1, 29], as in the case of the FMO complex, in terms of the total Hamiltonian

$$H = H_{\text{PE545}} + \sum_{j=1}^8 |j\rangle\langle j| \sum_k \kappa_k^{(j)} q_{j,k} + \sum_{j=1}^8 \frac{1}{2} \sum_k (p_{j,k}^2 + \omega_{j,k}^2 q_{j,k}^2), \quad (11.1.2)$$

with $p_{j,k}$, $q_{j,k}$, $\omega_{j,k}$, and $\kappa_k^{(j)}$ being the momenta, displacements, frequencies, and couplings of the environmental vibrations at site j , respectively.

The environmental influence on the system dynamics is fully characterized by the spectral density function $J(\omega) = \sum_{j,k} (|\kappa_k^{(j)}|^2 / 2\omega_{j,k}) \delta(\omega - \omega_{j,k})$. In the case of the PE545 complex, $J(\omega)$ has been determined in Ref. [232], assuming water as a solvent at 300 K, by means of molecular dynamics simulations using the same procedure in Sec. 7.4. In this case, however, they use the high-temperature limit of Eq. (7.4.2) such that the spectral density function $J_j(\omega)$ of site j is given by

$$J_j(\omega) = \frac{\omega}{\pi k_B T} \int_0^\infty dt C_j(t) \cos(\omega t). \quad (11.1.3)$$

This change in the prefactor mainly influences the high-frequency regime of the spectral density [232]. The resulting site-dependent fluctuational spectra $J_j(\omega)$ are shown in Fig. 11.2. As compared with the results in Fig. 7.5 for the FMO complex, a more pronounced vibrational structure is observed for the PE545 complex. This is expected due to the more flexible linear tetrapyrrole structure of the bilins in the PE545 complex as compared with the rigid tetrapyrrole ring of the BChls in the FMO complex. In particular, the low frequency part of the spectral density of the PE545 complex is mainly given by internal modes of the flexible bilins, while for the FMO complex it is entirely due to environmental fluctuations [232]. In Fig. 11.2, it is also observed that the vibrational structure of the PEB and DBV chromophores is quite different, in particular, in the low-to-medium frequency region, which is consistent with the different chemical structure of both chromophores, leading to different vibrational modes. In spite of the chemical structure of all PEB chromophores being the same, the central PEB_{50/61} dimer exhibits a quite different vibrational structure at high frequencies as compared to the other PEBs. This can be attributed to the

double linking to the protein scaffold, which also leads to the smallest fluctuations [232].

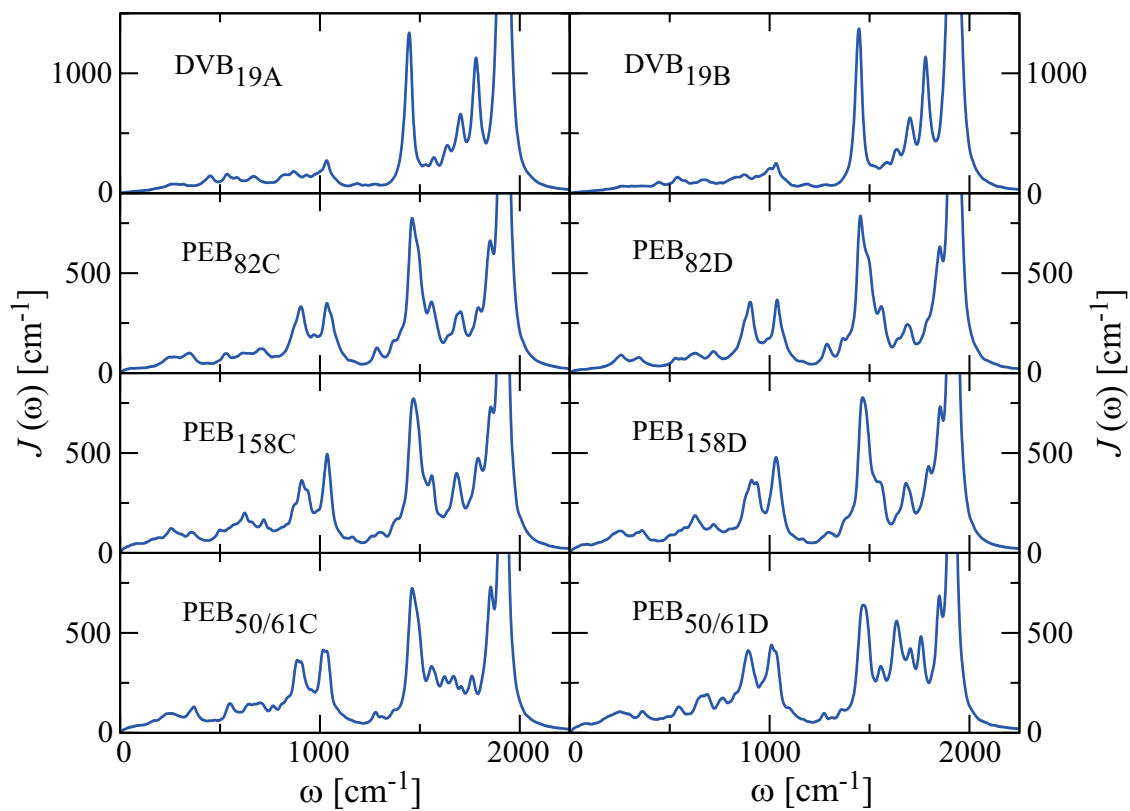


Figure 11.2: Site-dependent spectral density functions $J_j(\omega)$ for the PE545 complex as determined from molecular dynamics simulations [232] with water as a solvent at 300 K.

Dynamics of the PE545 complex

In this chapter, the real-time excitation energy transfer dynamics of the PE545 complex is examined by using the iterative QUAPI scheme in its extended version [37]. Each bilin interacts with its own environment (see Sec. 2.2.2), defined by the site-dependent spectral density functions in Fig. 11.2. It is then assumed that the complex is embedded in water at 300 K.

The central $\text{PEB}_{50/61}$ bilins are considered as the initially populated sites. This leads to three initial preparations, $\rho(0) = \text{PEB}_{50/61\text{C}}$, $\rho(0) = \text{PEB}_{50/61\text{D}}$, and to a linear combination of both, such that $\rho(0) = \alpha\text{PEB}_{50/61\text{C}} + \beta\text{PEB}_{50/61\text{D}}$, with $\alpha^2 + \beta^2 = 1$.

The time-dependent occupation probabilities of the individual bilins and of all bilins within a protein subunit are shown in Fig. 12.1. The dynamics in the lowest row corresponds to the initial preparation $\rho(0) = 1/\sqrt{2}(\text{PEB}_{50/61\text{C}} + \text{PEB}_{50/61\text{D}})$. Due to the large site energy differences, no coherent oscillations are observed in the site populations of the PE545 complex, except for the $\text{PEB}_{50/61}$ pair, which are the most strongly coupled bilins in Eq. (11.1.1), in the superposed initial state. The population of both DBV_{19} bilins increases monotonically in a similar fashion, which is consistent with these sites being responsible for passing the excitation energy to membrane-bound chlorophylls [224].

A similar overdamped dynamics has been obtained for the PE545 complex using a spectral density based on experimental information [228]. As in Eq. (7.2.1), it also contains a super-Ohmic continuous part and several Lorentzian peaks originated

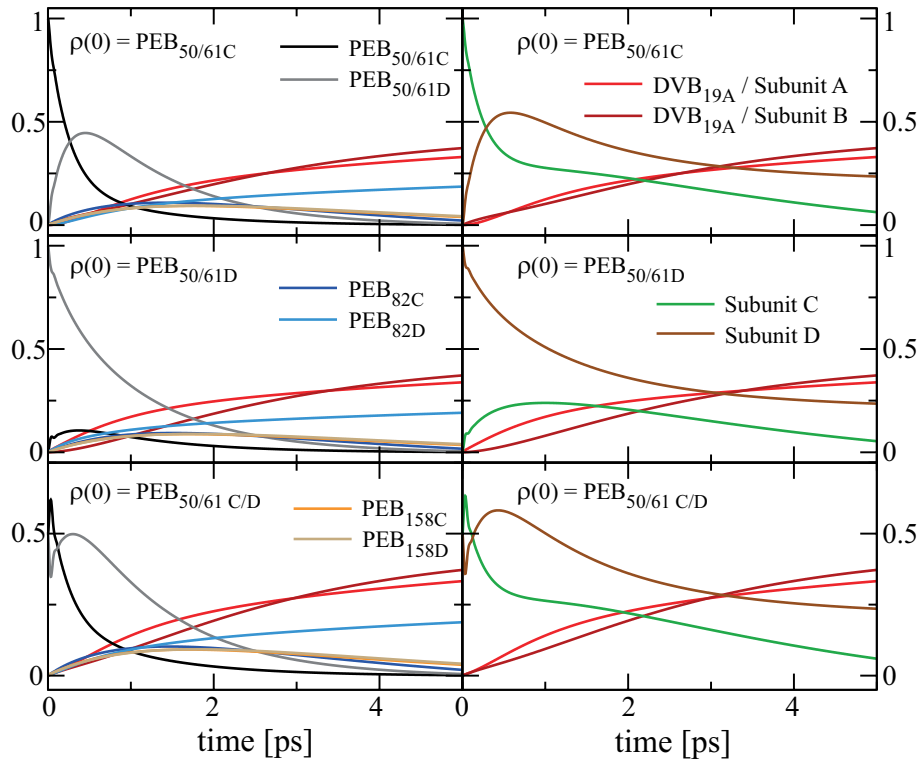


Figure 12.1: Time-dependent occupation probabilities of all bilins (left column) and of every subunit (right column) of the PE545 complex for the different initial preparations at $T = 300$ K.

from molecular vibrations. The results in Fig. 12.1 and those reported in Ref. [228] indicate that equilibrium vibrational modes cannot explain the experimentally observed long-lasting coherences in the PE545 complex in Refs. [182, 183]. It may be speculated that only underdamped modes could explain the experimental observations, as was found for the FMO complex in Chap. 9.

The time evolution of the trace distance in Eq. (2.3.1) is presented in Fig. 12.2 for the cases when the initial states are $\rho_1(0) = \text{PEB}_{50/61C}$ and $\rho_2(0) = \alpha\text{PEB}_{50/61C} + \beta\text{PEB}_{50/61D}$ (left plot), and when they are $\rho_1(0) = \text{PEB}_{50/61D}$ and $\rho_2(0) = \alpha\text{PEB}_{50/61C} + \beta\text{PEB}_{50/61D}$ (right plot). It is found that the trace distance decays monotonically in both cases, indicating a unidirectional flow of information from the system to the environment, rendering the dynamics Markovian. Observe that increasing the contribution of the ρ_1 state relative to the ρ_2 state leads to a reduction of the initial value of the trace distance from 1, because the distinguishability of both states decrease.

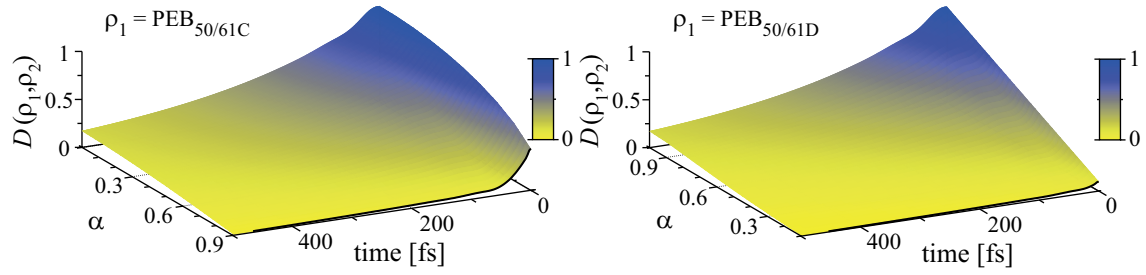


Figure 12.2: Time evolution of the trace distance [Eq. (2.3.1)] as a function of α in the state $\rho_2 = \alpha \text{PEB}_{50/61C} + (\sqrt{1 - \alpha^2}) \text{PEB}_{50/61D}$ at $T = 300$ K. See text for details.

12.1 Concluding remarks

The calculated real-time excitation energy transfer dynamics of the PE545 complex resulting from the site-dependent spectral density functions in Fig. 11.2 exhibits an overdamped dynamics. These findings are in contrast to the long-lasting coherences in the PE545 observed experimentally [182, 183]. Similar results have been reported in Ref. [228]. In both cases the vibrational peaks are explicitly included as part of the environment, such that the thermalization time scale of these modes is much shorter than any system time scale. It is concluded then, that the explicit nonequilibrium vibrational dynamics has to be considered in order to possibly explain the experimental results, as was found for the FMO complex in Chap. 9. The monotonic decay of the trace distance also indicates that the transfer of excitation energy in the PE545 complex follows a Markovian dynamics.

Summary

In this work, the real-time quantum dissipative dynamics of electronic and excitonic states in three different molecular systems has been determined by means of the iterative QUAPI scheme. In the first part, molecular heterostructures in the form of multi-block copolymers are designed by using the organic π -conjugated oligomers PDA and *l*-PPP. Due to the alignment of their frontier MOs, a heterostructure in the form A/B/A/B/A results in a molecular double quantum dot, with oligomers of PDA defining the wells B and oligomers of *l*-PPP defining the barriers A for charge carriers within the conduction band. By modifying the lengths of the oligomers, it is possible to restrict the number of confined MOs within the conduction band to only two, namely, the LUMO and LUMO+1. The energy difference between these MOs defines the electronic energy splitting $\hbar\Delta$, which characterizes any particular heterostructure. A polymeric radical anion is formed when the molecule is single negatively doped. If only the two possible dominant locations of the single excess charge carrier are considered and spin effects are neglected, a molecular charge qubit results. Because the electronic degrees of freedom of these systems are restricted to the two confined states defining the charge qubit, their description is given in terms of the spin-boson model [1, 8], in which the molecular vibrations are formalized as the bosonic bath. The parameters characterizing the system and the vibrational bath are extracted from electronic structure calculations on the doped systems by using semiempirical methods. The spectral density function is directly obtained from the vibrational spectrum. It is given as a sum of Lorentzian peaks centered

at the molecular vibrational frequencies, with heights related to the mode intensity and widths related to the coupling strength between the qubit and the vibrational modes. A characteristic value of $\hbar\Delta$, associated with a specific number of vibrational modes at lower energies, is obtained by systematically modifying the length of the oligomers, which allows one to *chemically* engineer not only the electronic energy splitting of the charge qubit but also its damping behavior. The time-dependent population difference of these systems exhibits coherent oscillations. The resulting coherence times and quality factors spread over about two orders of magnitude, with exact values that depend on the specific damping strength considered. By evaluating the time-dependent trace distance, it is found that non-Markovian effects are present. They contribute to sustain coherences by a non-Markovian flow of information from the vibrational degrees of freedom back to the electronic degrees of freedom. Transitions between the left/right states of the charge qubit, analogous to single qubit gates, can be controlled by means of an external classical field. A more efficient control of the dynamics of the oscillating electronic charge can be achieved by using quantum optimal control theory [138, 143]. Spectroscopic techniques can be implemented to read-out the charge qubit state as has been demonstrated for single negatively charged self-assembled InAs quantum dots [150]. Scalability in the designed molecular systems can be achieved, for example, by the use of molecular clamps. This would allow one to hold two or more charge qubits together and therefore, to implement multiqubit control gates. The same physics should be valid if a radical cation is used instead of a radical anion. This requires, however, the use of a different combination of parent polymers. The systems presented in this part, constitute then a novel implementation for quantum computation hardware able, in principle, to operate at room temperature. Other uses, for example, as very sensitive charge meters are also envisaged.

The second and third parts present the excitation energy transfer dynamics of two biomolecular light-harvesting complexes, for which excitonic coherences lasting several hundreds of fs at ambient temperature have been found experimentally [181, 182]. Then, instead of engineer these systems to exhibit even longer coherences as in the first part, these parts elucidate the origin of such a sustained quantum coherence and its significance in the speed and efficiency of the energy transfer dynamics. In both cases, the system is described by the electronic degrees of freedom within the single excitation subspace of the pigments involved in the energy transfer, while the vibrational pigment-protein-solvent environment induces thermal fluctuations on the excitation transfer dynamics. In the second part, the BChl-containing FMO complex is investigated. Its excitonic energies are obtained from calculations of the electrochromic shifts and a simultaneous fit of optical spectra. On the other

hand, several structured environmental spectral density functions, determined from experimental results or from molecular dynamics simulations, are available. These include a single or several localized vibrational modes, and the specific microscopic details of the polar environment. The influence of these localized modes is determined by evaluating whether a breakdown of the Franck-Condon (or, equivalently, the Born-Oppenheimer) approximation occurs. Put differently, the exciton dynamics is determined for two cases: (i) considering that the modes are in equilibrium, for which they are included as part of the fluctuational spectrum, and (ii) considering the nonequilibrium dynamics of the vibrations, for which, they are explicitly included as part of the system Hamiltonian and described on an equal footing as the excitonic states. These two cases imply, respectively, that the mentioned approximation does or does not hold during the energy transfer dynamics. It is found that the long-lived oscillatory components observed in the two-dimensional optical spectra cannot be explained by equilibrium fluctuations coming from a continuous frequency distribution of the pigment-protein-solvent environment. Instead, the explicit nonequilibrium dynamics of the discrete vibrational modes of the molecular backbone may yield increased coherence times depending on which molecular site the vibration couples to, influencing also the energy transfer times. These results demonstrate that only an efficiently connected exit site helps to improve the transfer efficiency since it provides additional channels for the parallel decay of the energy into the reaction center. Additional states at the entrance or intermediate sites only lead to an inefficient spreading-out of the energy into too many channels since they provide additional states in which the energy is intermittently stored, with the concomitant long-lasting coherences, and eventually dissipated via the vibrational channel. Thus, this constitutes a very general mechanism in which sustained coherence is not functionally necessary for the speed-up of energy transfer. This mechanism can be used to optimize the global quantum transfer efficiency in artificial light-harvesting systems by engineering the distribution of vibrational modes while maintaining the number of absorbing photoactive sites constant. The agreement between the coherence times in the presented results and the experimental ones indicate a breakdown of the Franck-Condon approximation. This can be further tested by comparing the experimental two-dimensional electronic spectrum of the FMO complex with one calculated assuming nonequilibrium vibrational modes. The results also indicate that the transfer of excitation energy in the FMO complex follows a Markovian dynamics. When considering equilibrium vibrational modes, neither the position of a single mode nor its width induce any non-Markovian exciton dynamics, even in the case when its frequency is exactly in resonance with exciton energy differences. These effects do not arise when several localized vibrational modes are

included nor from the microscopic details of the polar environment. When considering nonequilibrium vibrational modes, neither the frequency of the mode nor the number of vibrational excited states considered induce any non-Markovian exciton dynamics. The resulting Markovian dynamics, however, is still not describable by weak system-bath coupling approaches since multiphonon processes are not taken into account [7].

The third part investigates the biomolecular light-harvesting PE545 complex. Its excitonic energies are determined by structure-based calculations employing a mixed quantum mechanics/molecular mechanics scheme, while only the site-dependent spectral density functions extracted from molecular dynamics simulations are considered. An overdamped dynamics is found, in contrast to the long-lasting coherences in the PE545 claimed experimentally [182, 183]. The monotonic decay of the trace distance also indicates that the transfer of excitation energy in the PE545 complex follows a Markovian dynamics. Results are obtained for the vibrational modes assumed to be in equilibrium. As for the FMO complex, probably, only by considering the explicit nonequilibrium vibrational dynamics would be possible to explain the experimental results.

Appendix

Here, the quantum chemistry methods used to calculate the electronic properties of the molecular systems in Chap. 4 are presented. Appendix A illustrates how the electronic spin is treated in these methods. The concept of potential energy surface resulting from the Born-Oppenheimer approximation is introduced in Appendix B. There, it is also shown how these methods look for stationary points on the potential energy surface and how the vibrational modes are determined once a stationary point is found. The extended Hückel method, used for single-point electronic-structure calculations, is presented in Appendix C. The explicit form of the first molecular orbitals within the conduction band of the Δ_N systems in Table 4.1 are shown in Appendix D. The parameters determining the spectral density function in Eq. (4.3.4) for all Δ_N systems are given in Appendix E. There, it is also shown the resulting bath autocorrelation function in Eq. (2.2.11). Finally, Appendix F presents the real-time dynamics of the Δ_4 system determined using the QUAPI scheme.

A Spin in electronic structure methods

The full wave function of an electron in a molecule is given by the product of a spin wave function and a spatial wave function, i.e., $\tilde{\Psi}(\mathbf{r}, \sigma) = S(\sigma) \otimes \Psi(\mathbf{r})$. The spin wave function is either α or β , which corresponds to electronic spin “up” or “down”, respectively.

In closed shell systems, i.e., with an *even* number of electrons, they are divided into pairs of opposite spin that are forced to occupy the same spatial orbital. In other words, it is assumed that both α - and β -electrons are described by the same spatial wave function, and therefore, it is calculated only once. On the other hand, open shell systems have an *odd* number of electrons. Therefore, the spatial wave function should be calculated separately for α - and β -electrons. Molecules with an odd number of electrons, excited states, and processes involving bond breaking and/or formation should be described as open shell systems [233].

All electronic structure calculations in Chap. 4 are carried out by considering the doped molecular heterostructures as open shell systems.

B About geometry optimizations and vibrational analysis

The full wave function of a molecular system $\Psi(\mathbf{R}, \mathbf{r})$ depends on the nuclear coordinates \mathbf{R} and on the electronic coordinates \mathbf{r} . However, due to the different masses of nuclei and electrons, the nuclei may be assumed as stationary from the electronic point of view, and the Born-Oppenheimer approximation can be applied. It neglects the coupling between the nuclear and electronic dynamics, giving effectively a separate motion of the electrons from the motion of the nuclei. This allows one to write the full wave function as

$$\Psi(\mathbf{R}, \mathbf{r}) = \Phi(\mathbf{R})\psi(\mathbf{r}|\mathbf{R}),$$

where the electronic wave function $\psi(\mathbf{r}|\mathbf{R})$ depends parametrically on the nuclear coordinates, since it only depends on the position \mathbf{R} of the nuclei, not on their momentum [234]. $\psi(\mathbf{r}|\mathbf{R})$ is obtained by solving the electronic structure problem for a set of fixed nuclear positions. Because this can be repeated for any set of nuclear positions, a potential energy surface (PES) results. A PES describes how the energy of the molecule in a particular (electronic) state varies as a function of the structure of the molecule [235]. A molecule with M atoms requires $3M$ nuclear coordinates that define the geometry, and therefore the PES is $3M$ -dimensional. However, only $3M - 6$ independent coordinates are required to describe the internal movement of the nuclei ($3M - 5$ in the case of linear molecules), i.e., the three translations and three (two) rotations of the center of mass are excluded.

B1 Geometry optimizations

In a geometry optimization, the geometry of the molecule will be adjusted until a stationary point on the PES is found [236]. This stationary point may correspond to a local or global minimum on the PES, i.e., the equilibrium geometry, or to a transition structure [233]. The default algorithm used in [116] for both minimizations (optimizations to a local minimum) and optimizations to transition states and higher-order saddle points is the Bernaly algorithm using GEDIIS (geometry optimization method using an energy-represented direct inversion in the iterative subspace algorithm) [237] in redundant internal coordinates [236].

Geometry optimization methods can be roughly divided into first-order methods, that use only analytic first derivatives to search for stationary points, and second-order methods, that use analytic first and second derivatives [237]. The first set of methods include the steepest descent and the conjugate gradient methods. They

exploit the fact that the gradient vector points in the direction where the energy increases most. Then, the energy value can always be lowered by stepping in the opposite direction [234]. However, due to its nature, they are only able to locate minima, but are very cheap computationally, requiring storage of one or two gradient vectors. Second-order methods assume a quadratic model for the PES and a Newton-Raphson step for the search of the minima.

A local quadratic approximation to the PES is given by a second-order Taylor expansion of the energy around the current point \mathbf{R}_0

$$E(\mathbf{R}) = E(\mathbf{R}_0) + \mathbf{g}_0^T \Delta \mathbf{R} + \frac{1}{2} \Delta \mathbf{R}^T \mathbf{H}_0 \Delta \mathbf{R}, \quad (\text{B1})$$

where \mathbf{g}_0 is the gradient ($dE/d\mathbf{R}$) at \mathbf{R}_0 , \mathbf{H}_0 is the Hessian or matrix of second derivatives of the energy ($d^2E/d\mathbf{R}^2$) at \mathbf{R}_0 (also known as the force constant matrix), and $\Delta \mathbf{R} = \mathbf{R} - \mathbf{R}_0$. The gradient \mathbf{g}_0 and the Hessian \mathbf{H}_0 are used to confirm the character of the stationary point. The gradient at any stationary point is zero. There, the forces are also zero, because the negative of the gradient is the vector of forces on the atoms in the molecule. All of the eigenvalues of the Hessian in a stationary point corresponding to a minimum must be positive (by definition). On the other hand, in a stationary point corresponding to a transition structure, the Hessian has one (and only one) negative eigenvalue, as expected from a first-order saddle point [235].

Requiring the gradient of the second-order approximation in Eq. (B1) to be zero, $\mathbf{g}(\mathbf{R}) = \mathbf{g}_0 + \mathbf{H}_0 \Delta \mathbf{R} = 0$, the displacement to the minimum or Newton-Raphson step is obtained by

$$\Delta \mathbf{R} = -\mathbf{H}_0^{-1} \mathbf{g}_0. \quad (\text{B2})$$

Observe that the step direction is opposite to the gradient direction (like in first-order methods), as it should be. Sufficiently close to the stationary point, the gradient is reduced quadratically [234], which reduces the number of steps required to reach convergence in second-order optimization schemes as compared to first-order methods. However, these approaches can quickly become very expensive with increasing system size because the explicit computation of the Hessian scales as $\mathcal{O}(M^4) - \mathcal{O}(M^5)$ [237]. For each step in the Newton method, the Hessian in Eq. (B2) is calculated at the current point. For quasi-Newton methods, an initial estimate of the Hessian is obtained by some inexpensive method, and subsequently, the Hessian in Eq. (B2) is updated at each step of the optimization using the first derivatives and displacements [235]. This makes quasi-Newton methods intermediate between pure first- and second-order approaches, with a computational cost comparable to first-order methods and convergence speed comparable to second-order methods [237].

A drawback is that the Newton-Raphson step in Eq. (B2) can give excessively large step sizes in the wrong direction if the PES is far away from a quadratic region. Therefore, step control techniques are required. These guarantee that the step direction is correct and control the total length of the step, such that it does not exceed the region in which the second-order Taylor expansion [Eq. (B1)] is valid [234]. This is specified by a trust radius τ_r . Among step control techniques, two are widely used. In the trust radius model, the energy is minimized under the constraint that the step is not larger than τ_r . On the other hand, in the rational function optimization, the quadratic approximation of the energy in Eq. (B1) is replaced by a rational function approximation, in which the energy is minimized with respect to the step $\Delta\mathbf{R}$. This step will always be shorter than the pure Newton-Raphson step in Eq. (B2), but, because there is no guarantee that it will be within the trust radius, it may be scaled down by a multiplicative factor [234, 235, 237].

To reduce the number of iterations required to reach convergence, the direct inversion in the iterative subspace (DIIS) scheme is used. The goal is to construct a new geometry \mathbf{R}^* as a linear combination of previous geometries, i.e., $\mathbf{R}^* = \sum_i k_i \mathbf{R}_i$ with $\sum_i k_i = 1$. In GEDIIS, \mathbf{R}_i are geometries and k_i minimizes an energy function. Therefore, the resulting geometry \mathbf{R}^* is associated with the optimal energy within the search space. Additional details can be found in [237]. In the final stages of a minimization, GEDIIS sometimes converges faster than quasi-Newton methods, and therefore, a hybrid of quasi-Newton and GEDIIS methods is used [235].

In principle, a geometry optimization can be done in any coordinate system, e.g., Cartesian coordinates. However, they are not well suited for geometry optimization because they do not reflect the “chemical structure” and bonding of a molecule. On the other hand, internal coordinates, like Z-matrices, are more descriptive of the molecular structure and are more useful for geometry optimizations [235]. The reason is that they require to define $M - 1$ distances, $M - 2$ angles, and $M - 3$ torsional (dihedral) angles, i.e., only $3M - 6$ coordinates. This means that the six translational and rotational modes are automatically removed. In contrast, the Hessian matrix in Cartesian coordinates have six eigenvalues, corresponding to the six translational and rotational modes, identical to zero, which should be projected out prior to formation of the optimization step in Eq. (B2) [234].

In order to avoid a premature identification of a minimum, four convergence criteria are used in Ref. [116]. These require that the forces and the root-mean-square of the forces be smaller than 10^{-4} atomic units, while the calculated displacement $\Delta\mathbf{R}$ for the next step and its root-mean-square should be smaller than 10^{-3} atomic units [233].

B2 Vibrational analysis

The eigenvectors of the Hessian in mass-weighted coordinates correspond to the vibrational normal modes (plus five or six modes for translation and rotation of the center of mass). The vibrational frequencies are proportional to the square root of the eigenvalues of the mass-weighted Hessian [235]. In the equilibrium geometry, i.e., at the minimum on the PES, all of the eigenvalues of the Hessian are positive, then, all vibrational frequencies are real. The single negative eigenvalue of the Hessian in a transition structure gives an imaginary vibrational frequency. The vibrational mode corresponding to this imaginary frequency is also known as the transition vector, which is tangent to the reaction path in mass-weighted coordinates [235].

In order to calculate the vibrational normal modes and frequencies, the Hessian is transformed from Cartesian nuclear coordinates to mass-weighted coordinates. This transformation is only valid at a stationary point [238]. Then, frequency calculations must be performed on optimized structures, and the calculation of the frequencies *must* use the same theoretical model (and basis set, if any) used to calculate the optimized geometry. Frequencies computed with a different theoretical model or basis set have no validity [233].

The vibrational analysis in Ref. [116] works as follows [239]: first, the Hessian matrix is converted to mass-weighted cartesian coordinates \mathbf{H}_{MWC} . The next step is to translate the center of mass to the origin, and to determine the moments and products of inertia, with the goal of finding the matrix that diagonalizes the moment of inertia tensor. With this matrix, it is possible to find the vectors corresponding to the rotations and translations. Once these vectors are known, the rest of the normal modes are internal vibrations. Schmidt orthogonalization is used to generate the $3M - 6$ (or $3M - 5$) remaining vectors, which are orthogonal to the five or six rotational and translational vectors. The result is a transformation matrix \mathbf{D} which transforms from mass-weighted cartesian coordinates \mathbf{q}_{MWC} to internal coordinates $\mathbf{S}_{\text{INT}} = \mathbf{D}\mathbf{q}_{\text{MWC}}$. Here, rotations and translations have been separated out, i.e., coordinates in the rotating and translating frame. The Hessian is also transformed into these new coordinates through $\mathbf{H}_{\text{INT}} = \mathbf{D}^\dagger \mathbf{H}_{\text{MWC}} \mathbf{D}$, and diagonalized to $\mathbf{L}^\dagger \mathbf{H}_{\text{INT}} \mathbf{L} = \mathbf{\Lambda}$, with $\mathbf{\Lambda}$ being a diagonal matrix that contains the frequencies and the column vectors of \mathbf{L} contain the normal modes. These are printed in the output given by Ref. [116] as Cartesian displacement vectors normalized to unit distance [239], which, in order to obtain the real Cartesian coordinates, requires the multiplication of the resulting values by the inverse square root of the pertinent reduced mass. This is particularly important when displacing each atom in its normal mode direction, as in Sec. 4.3.2, because heavy nuclei tend to move shorter distances than

light nuclei. Additional details can be found in Ref. [239].

In general, the calculated vibrational frequencies must be multiplied by a scale factor (in the range of 0.8 to 1.0) to better match experimental vibrational frequencies [240]. This scaling compensates approximations made when considering the PES as harmonic (in order to locate the minimum) and in the electronic structure calculation. Therefore, they are specific to the used theoretical model (and basis set, if any). The scaling factor χ is obtained from the experimentally observed ν_i and the calculated ω_i vibrational frequencies as [240]

$$\chi = \sum_i \frac{\nu_i \omega_i}{\omega_i^2}. \quad (\text{B3})$$

In the case of AM1 calculations the scaling factor is 0.954 [120].

C The extended Hückel method

The extended Hückel method (EHM) [117] is an improvement over the original Hückel method [241] and is analogous to the tight-binding method widely used in solid state physics [242]. It is based on a σ - π energy separation of the full electronic system [243]. This separation works very well in conjugated (particularly planar) systems due to the fact that the inner electrons are localized into the σ chemical bonds forming the molecular backbone, while the valence electrons are delocalized in π orbitals above and below the molecular plane (see Fig. 3.1). The total electronic Hamiltonian is written as

$$H_e = H_{\text{core}} + H_{\text{valence}}, \quad (\text{C1})$$

with the valence Hamiltonian being written as a sum of monoelectronic effective Hamiltonians, which do not need to be explicitly specified, in the form

$$H_{\text{valence}} = \sum_i H^{\text{eff}}(i). \quad (\text{C2})$$

The molecular orbitals (MOs) are written as a linear combination of valence atomic orbitals (AOs)

$$|\psi_i\rangle = \sum_r c_r^{(i)} |\phi_r\rangle, \quad (\text{C3})$$

with $|c_r^{(i)}|^2$ being the contribution of the r -th AO to the i -th MO. In the original Hückel method, a single AO (the $2p_\pi$) is considered for each carbon atom and the contribution of the hydrogen AO is neglected, whereas in the EHM four carbon AOs (one $2s$ and three $2p$) and the $1s$ hydrogen AO are considered. Slater-type AOs are used [244].

For the Hamiltonian in Eq. (C2), the problem is reduced to a set of monoelectronic Schrödinger equations

$$H^{\text{eff}}(i)|\psi_i\rangle = E_i|\psi_i\rangle. \quad (\text{C4})$$

When the variational theorem is applied on Eq. (C4), it yields the secular equation

$$\sum_{r,s}^{4n+m} [(H_{rs}^{\text{eff}} - E_i S_{rs}) c_s^i] = 0, \quad (\text{C5})$$

where n is the number of carbon atoms and m is the number of hydrogen atoms. Equation (C5) has a non-trivial solution only if

$$\det(H_{rs}^{\text{eff}} - E_i S_{rs}) = 0. \quad (\text{C6})$$

This equation is similar to that obtained in the original Hückel method [241]. However, it approximates the overlap integrals $S_{rs} = \langle \phi_r | \phi_s \rangle$ as Kronecker's deltas δ_{rs} , as well as the resonance integrals $H_{rs}^{\text{eff}} = \langle \phi_r | H^{\text{eff}} | \phi_s \rangle$. In the EHM all the overlap integrals S_{rs} are explicitly evaluated using the chosen forms for the AOs and the internuclear distances. The diagonal elements H_{rr}^{eff} (the Coulomb or site integrals) in Eq. (C6) are set equal to the valence orbital ionization potentials taken from experimental data.

The non-diagonal terms H_{rs}^{eff} (the resonance or hopping integrals) are parameterized by the Wolfsberg-Helmholz formula [245]

$$H_{rs}^{\text{eff}} = \frac{1}{2} \bar{K} (H_{rr}^{\text{eff}} + H_{ss}^{\text{eff}}) S_{rs}, \quad (\text{C7})$$

where \bar{K} is an empirical parameter that can be constant [245], weighted [246] or be given by a distance-dependent formula [247]. Other parametrizations of H_{rs}^{eff} are in terms of the geometric mean of H_{rr}^{eff} and H_{ss}^{eff} [248]. Hoffmann [117] used Eq. (C7) with $\bar{K} = 1.75$, which was chosen such that the calculated rotational barrier from ethane matches the experimental value. However, it has been suggested that this parameter can take a value between 1.0 and 3.0 [244].

In this work, Eq. (C7) with $\bar{K} = 2.43$ is used. This value has been shown to reproduce the experimental optical gap in several one- and quasi-one-dimensional π -conjugated polymers [81, 249]. This larger \bar{K} value is reasonable when considering that the electronic delocalization along conjugated molecules implies a larger contribution from the resonance and overlap integrals to the total energy.

D MOs of the Δ_N molecular heterostructures

Here, the first MOs within the conduction band of the Δ_N systems in Table 4.1 are shown. In all cases, only MOs corresponding to α -electrons are depicted. It has been verified, however, that the resulting spatial wave function for α - and β -electrons is the same.

It is also shown the spin density, which indicates the total electron density difference between α - and β -electrons, i.e., the spatial distribution of the unpaired electron or excess spin. The negative doping of the molecular heterostructures leads to a singly occupied LUMO¹. Because this orbital “carries” the excess electron, the spatial distribution of the LUMO should be exactly the same as that of the spin density (see below).

In all cases, the depicted MO and spin density isosurfaces correspond to an electron density of 2×10^{-2} and $4 \times 10^{-4} e/\text{\AA}^3$, respectively.

Alternatively, the information about the *shape* of a MO along the longitudinal direction of the molecule is described in terms of the localization parameter on the j -th atom defined as [250]

$$L_j^{(i)} = \sum_r |c_{rj}^{(i)}|^2, \quad (\text{D1})$$

where r labels the AOs centered on the j -th atom contributing to the i -th Hückel MO as defined in Eq. (C3). The contributions of the $1s$ AOs centered at the hydrogen nuclei are not taken into account. The set j of atomic indexes can be interpreted as a discretization of the position coordinate along the chain and therefore, the parameter $L_j^{(i)}$ provides a measure of the probability density associated with the i -th MO at the j -th site of the molecule. Additional details can be found in Refs. [81, 149, 249].

¹Typically, a singly occupied MO is called SOMO, however, by the use of “singly occupied LUMO” it is specified that the additional electron occupies the first (otherwise empty) state within the conduction band.

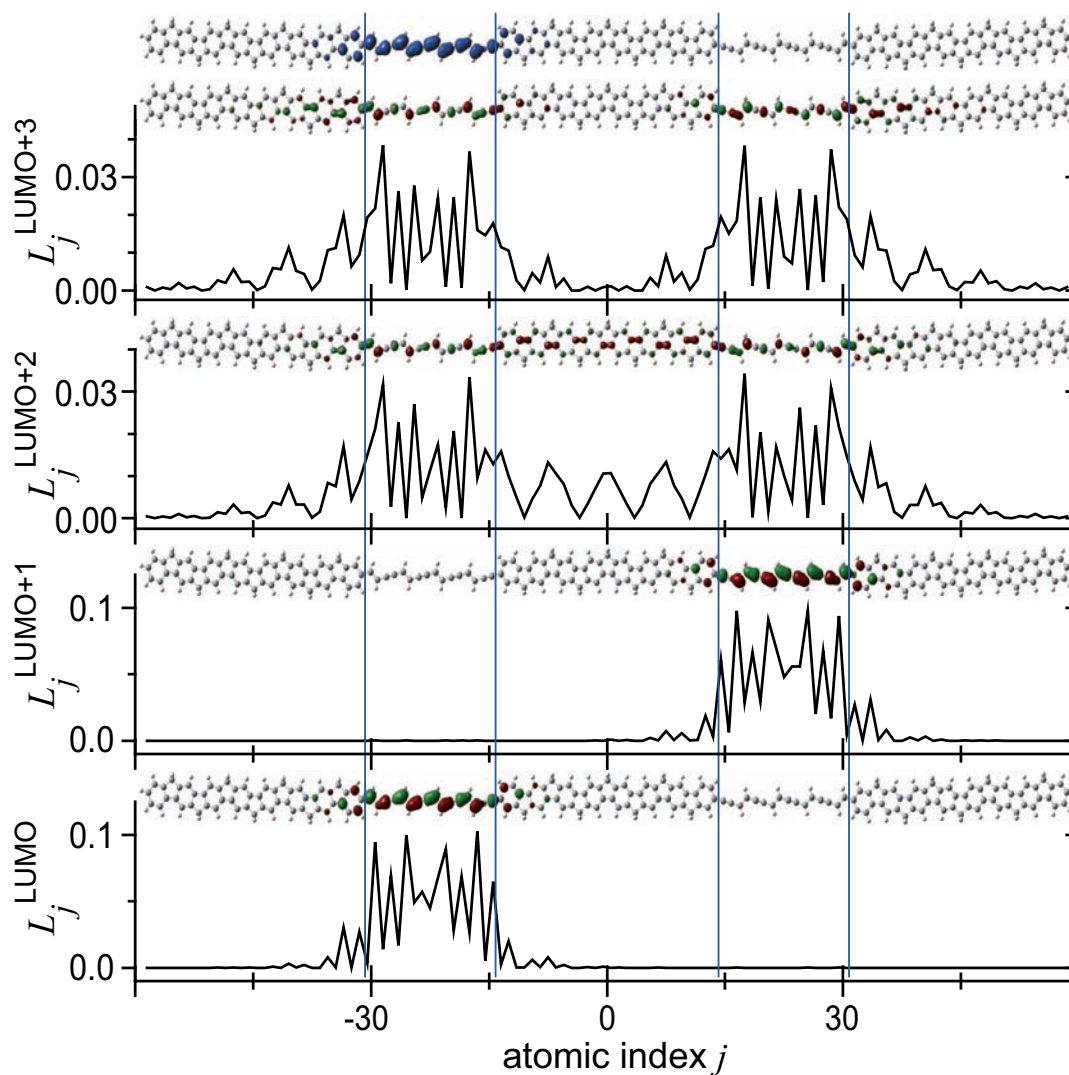
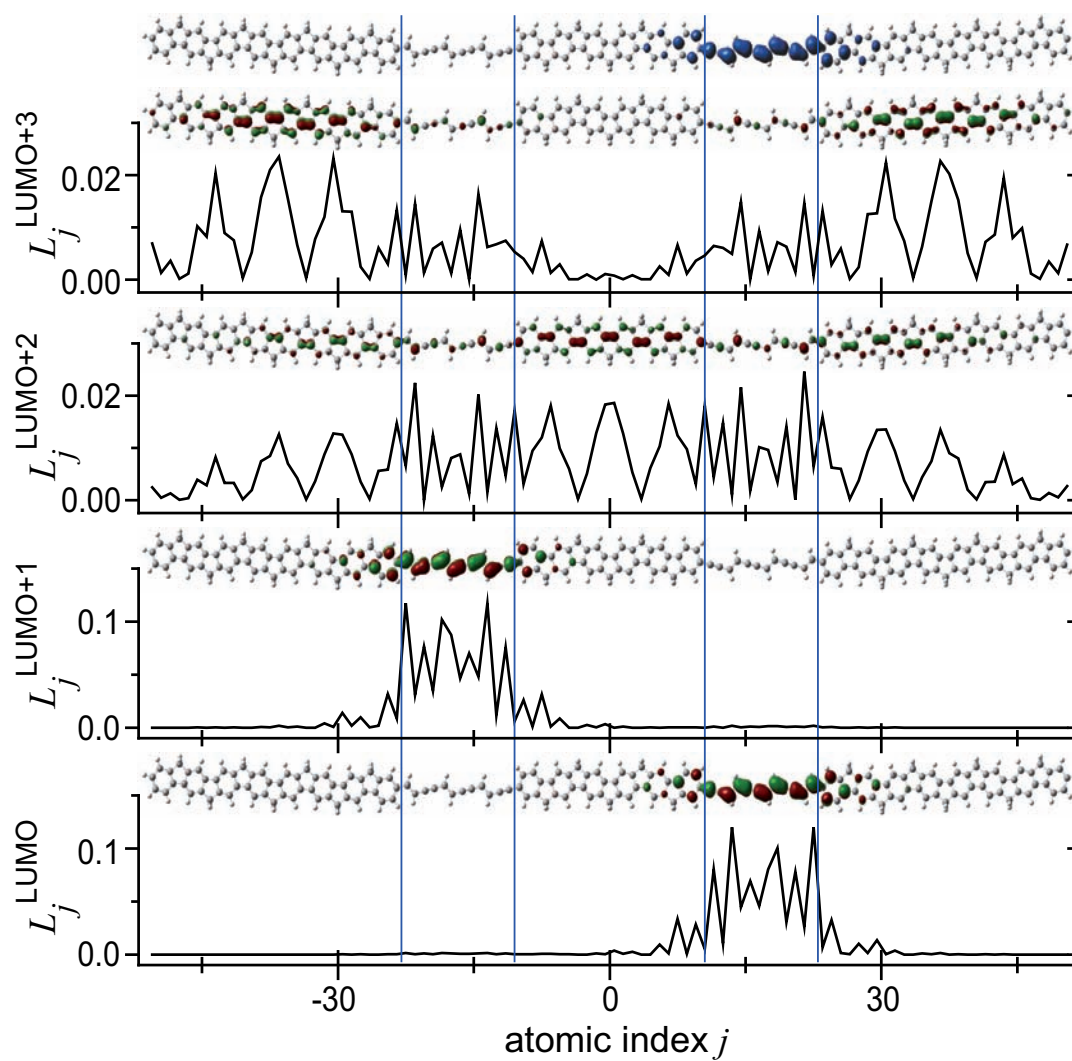


Figure D1: Localization parameter $L_j^{(i)}$ in Eq. (D1) (lower plot) and MO isosurface (upper plot) of LUMO, LUMO+1, LUMO+2, and LUMO+3 MOs (from bottom to top) for the Δ_0 system. Top most plot: spin density isosurface. Thin blue lines indicate the heterojunctions.

Figure D2: Same as in Fig. D1 for the Δ_1 system.

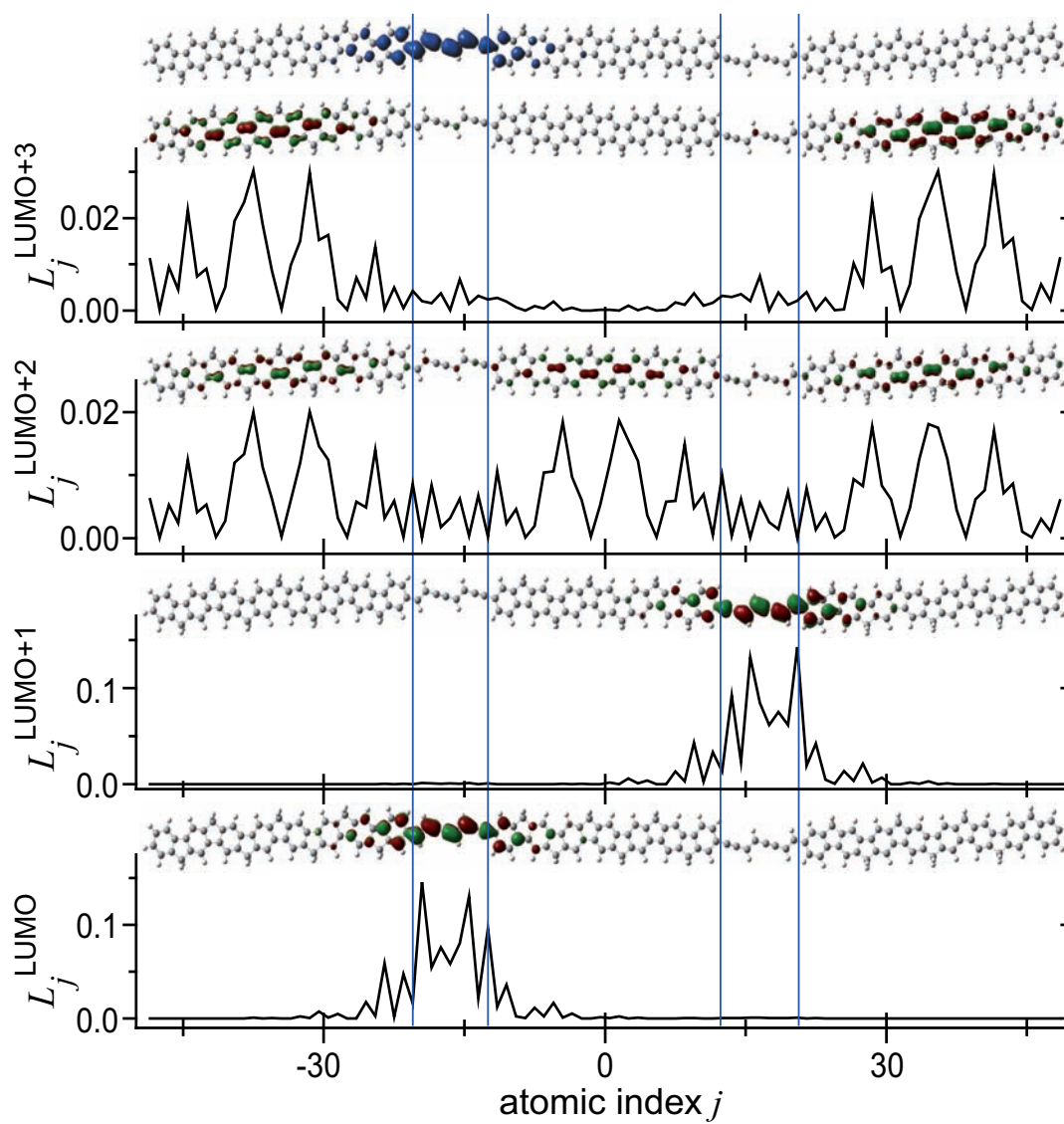
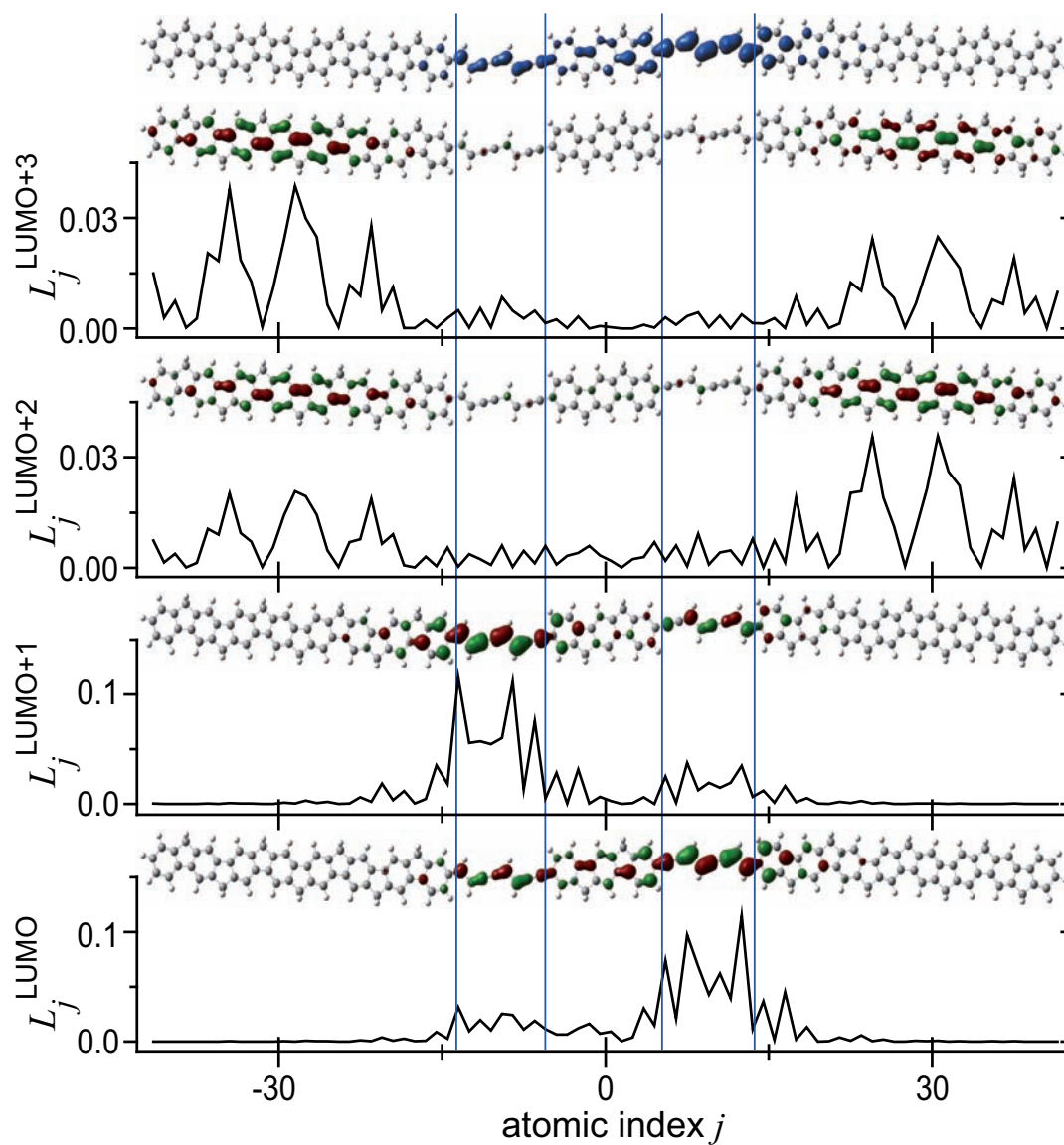


Figure D3: Same as in Fig. D1 for the Δ_2 system.

Figure D4: Same as in Fig. D1 for the Δ_3 system.

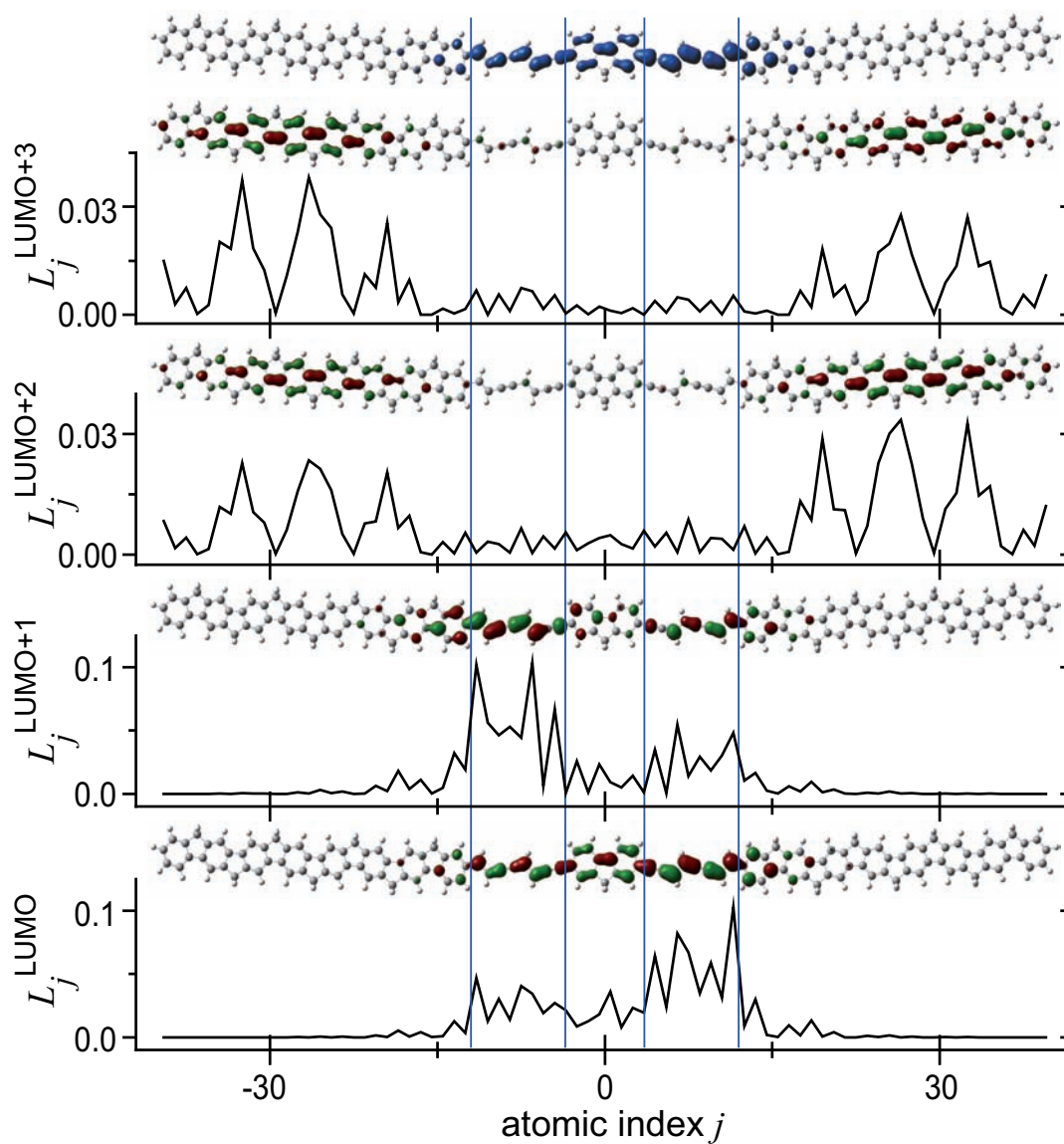


Figure D5: Same as in Fig. D1 for the Δ_4 system.

E $J(\omega)$ and $L(t)$ of the Δ_N molecular heterostructures

The spectral density function for the Δ_N systems in Table 4.1 is given by

$$J(\omega) = \omega \sum_i \frac{\eta_i \gamma^2}{(\omega - \omega_i)^2 + \gamma^2}.$$

The parameters ω_i and η_i are given in Tables E1-E5 for $N = 0-4$, respectively. The effect of increasing the width γ of the Lorentzian peaks in $J(\omega)$ is shown in Figs. E1, E3, E5, E7, and E9, respectively. It is observed that due to the large number of peaks around 1500 cm^{-1} , a significant spectral overlap occurs in all cases, resulting in an effective broad single mode with a large spectral weight.

The temporal correlation properties of the fluctuations are given by the bath autocorrelation function

$$L(t) = \frac{\hbar}{\pi} \int_0^\infty d\omega J(\omega) \left[\coth \left(\frac{\hbar\omega}{2k_B T} \right) \cos(\omega t) - i \sin(\omega t) \right] = L_r(t) + L_i(t).$$

Thus, the fluctuations are composed of harmonic modes with frequency ω at temperature T , and each mode contributes with a spectral weight given by $J(\omega)$. The resulting autocorrelation functions for different values of γ are shown in Figs. E2, E4, E6, E8, and E10 for $N = 0-4$, respectively. A vibrational mode centered at frequency ω_i with finite linewidth γ leads to oscillatory correlations that decay exponentially with time according to $L(t) \propto e^{-i\omega_i t - \gamma t}$ [31]. Then, larger linewidths result in faster decaying correlations as observed in the corresponding figures. The large number of peaks at frequencies $\omega_i < \Delta_4$ generates very long-lived correlations for the Δ_4 system as compared with the other systems.

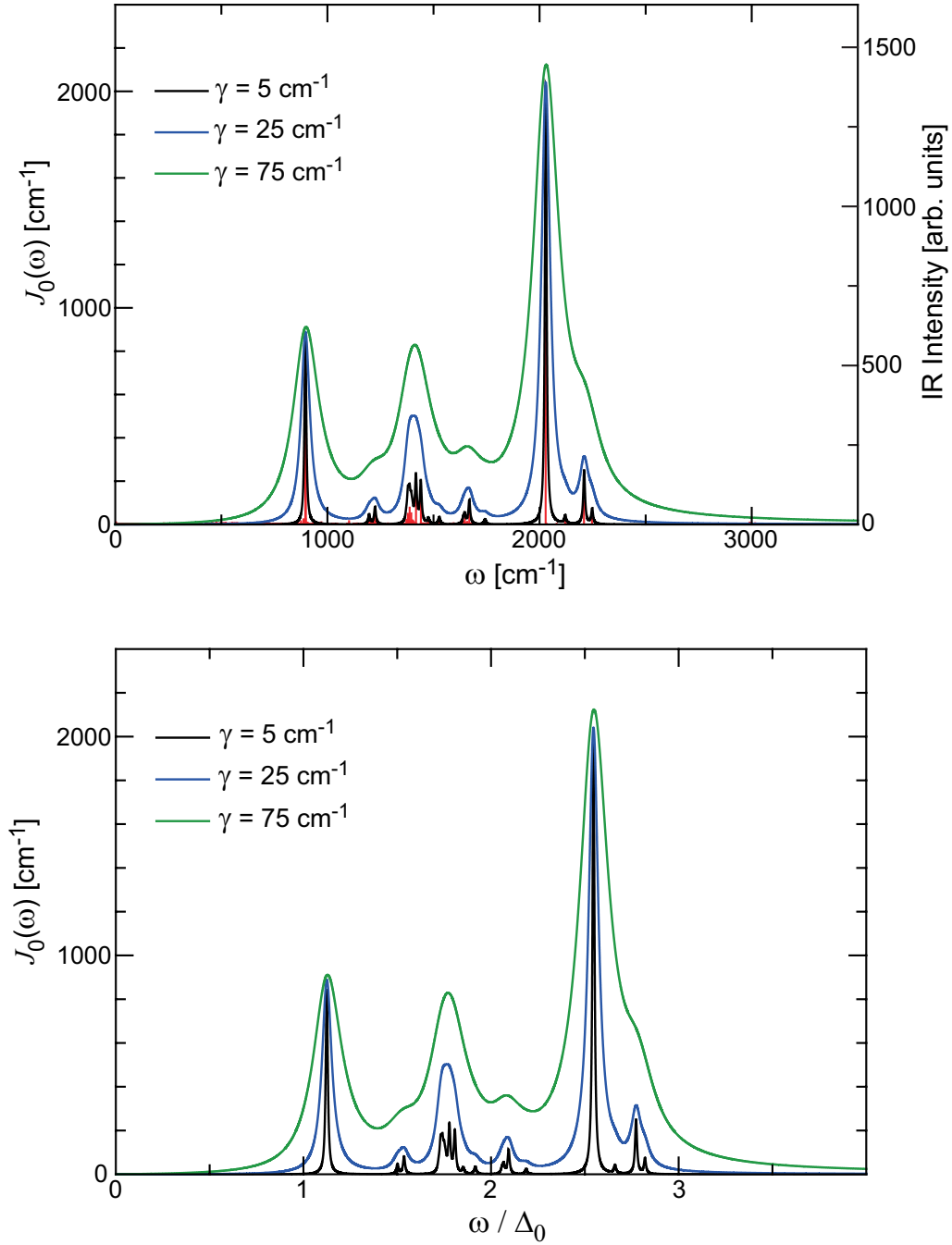


Figure E1: Spectral density in Eq. (4.3.4) for the system Δ_0 with the parameters listed in Table E1. Top: comparison with the IR spectrum (shown as vertical red lines). Bottom: the frequency ω has been scaled with respect to Δ_0 .

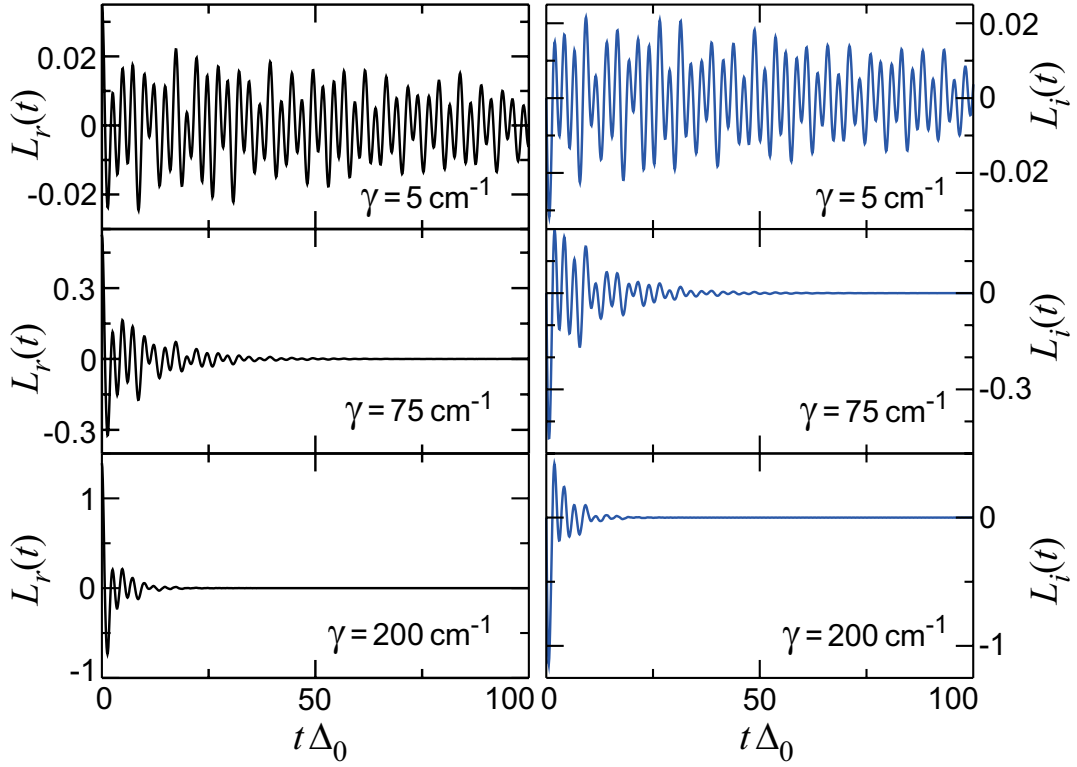


Figure E2: Bath autocorrelation function in Eq. (2.2.11) for the system Δ_0 . The real part $L_r(t)$ is shown in the left column, while the imaginary part $L_i(t)$ is shown in the right column.

ω_i [cm^{-1}]	η_i	ω_i [cm^{-1}]	η_i	ω_i [cm^{-1}]	η_i
894.721	0.40451	1387.116	0.08016	1647.429	0.02628
896.317	0.02330	1394.587	0.05200	1668.743	0.06586
896.992	0.56346	1399.680	0.01713	1742.873	0.01341
1196.354	0.03760	1401.092	0.01471	2029.095	1.00000
1224.083	0.03945	1417.037	0.15143	2120.524	0.01754
1224.913	0.02623	1440.097	0.13262	2209.949	0.11188
1371.448	0.01900	1476.080	0.01747	2247.822	0.03100
1378.602	0.04964	1526.981	0.02176		
1380.610	0.04205	1640.040	0.01261		

Table E1: Parameters ω_i and η_i for the spectral density of the Δ_0 system.

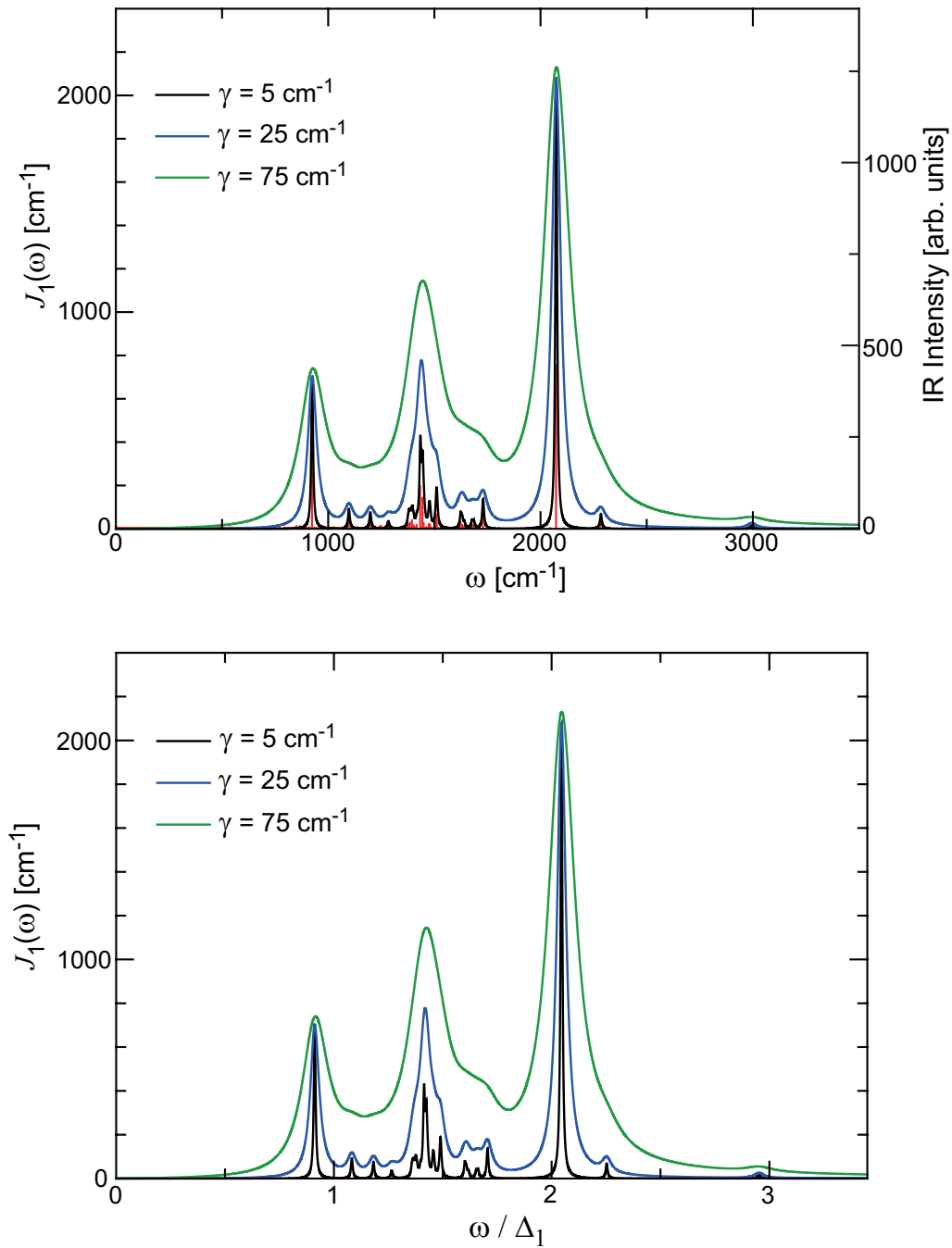
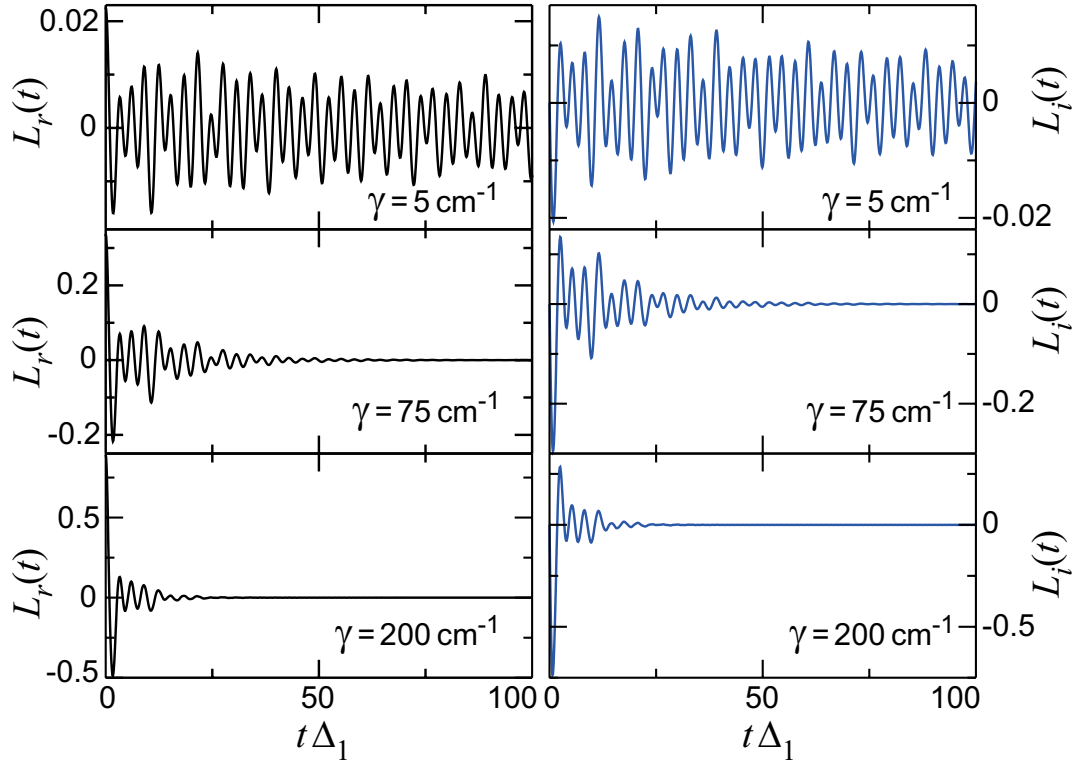


Figure E3: Same as in Fig. E1 for the Δ_1 system with the parameters listed in Table E2.

Figure E4: Same as in Fig. E2 for the Δ_1 system.

ω_i [cm^{-1}]	η_i	ω_i [cm^{-1}]	η_i	ω_i [cm^{-1}]	η_i
924.621	0.75596	1434.032	0.25790	1631.351	0.02117
1097.607	0.08313	1444.806	0.18627	1641.230	0.01388
1198.301	0.06255	1450.638	0.03122	1677.504	0.01853
1283.421	0.02644	1475.318	0.02263	1685.615	0.01787
1377.072	0.02419	1476.021	0.02643	1729.551	0.07833
1381.279	0.02177	1479.673	0.02088	2074.106	1.00000
1386.237	0.03389	1479.980	0.01659	2284.401	0.02923
1395.702	0.04914	1509.545	0.08482	2994.687	0.00757
1401.446	0.01836	1512.527	0.04614		
1417.221	0.02052	1624.030	0.03944		

Table E2: Parameters ω_i and η_i for the spectral density of the Δ_1 system.

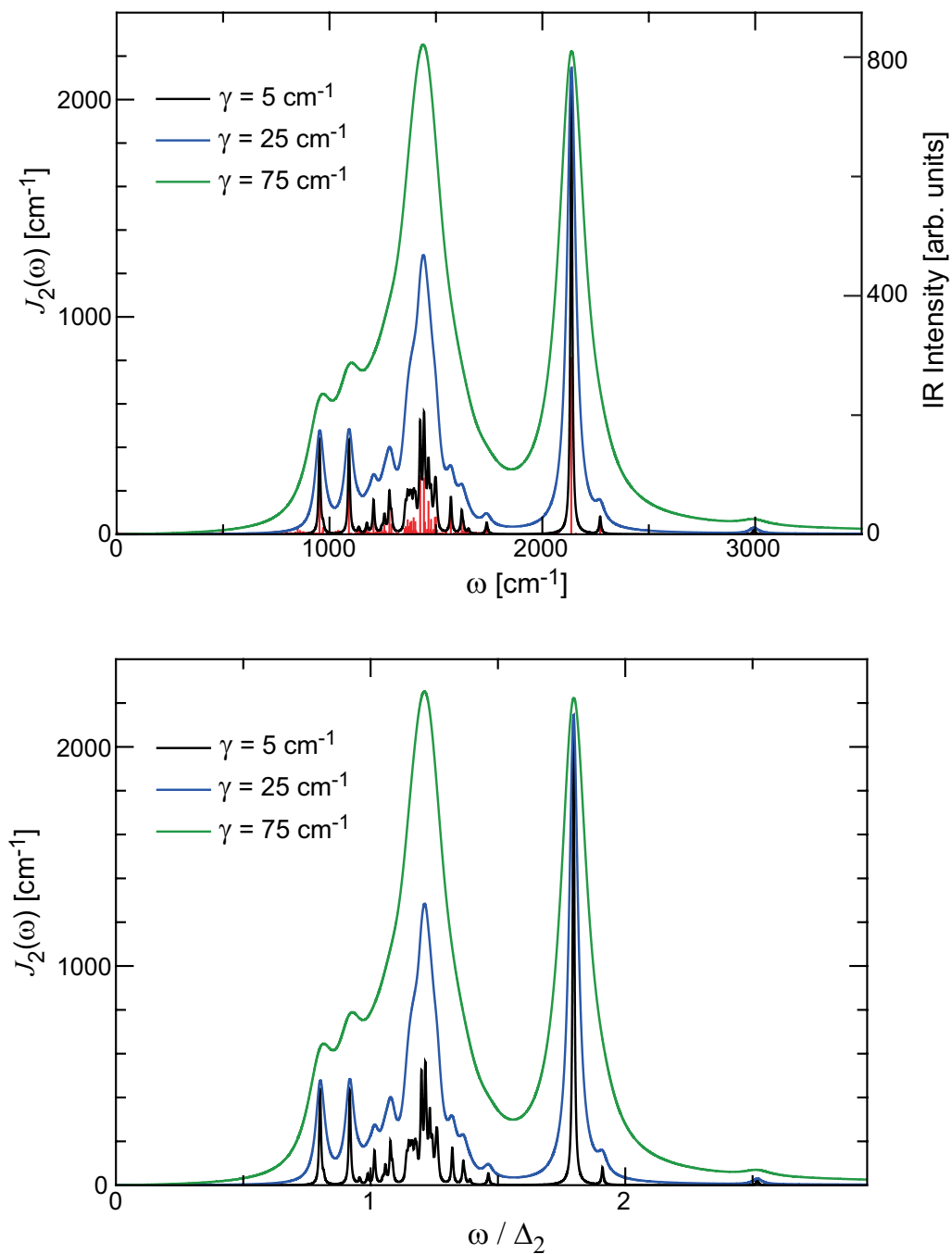
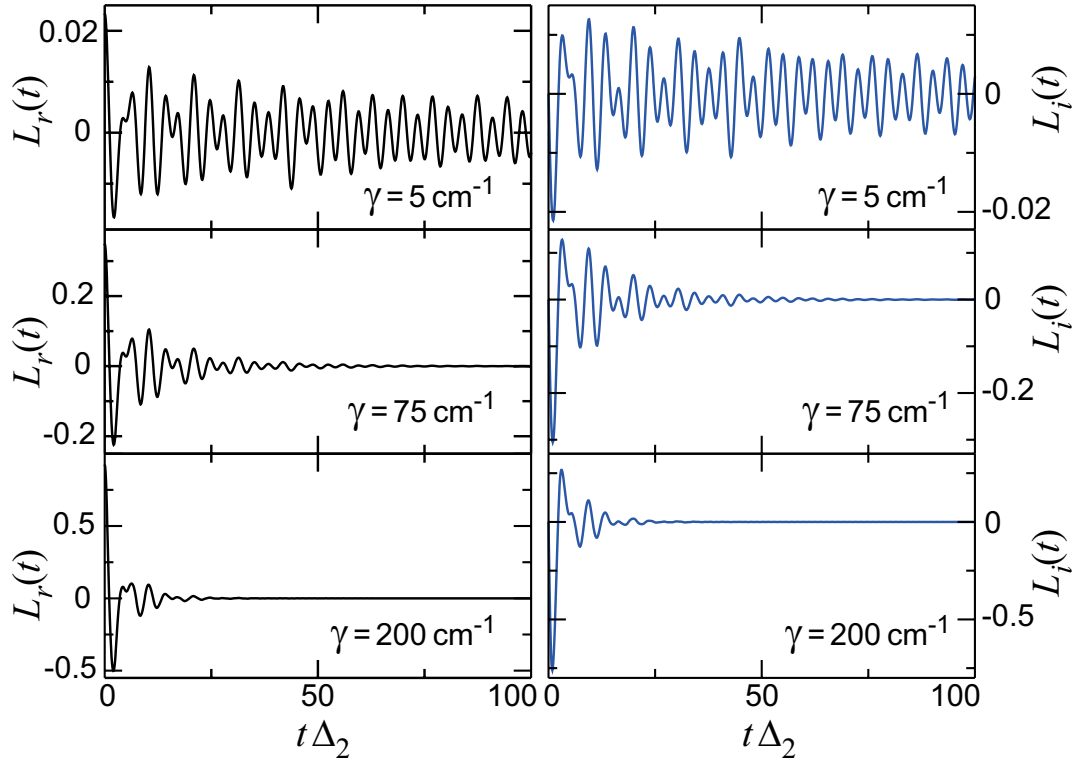


Figure E5: Same as in Fig. E1 for the Δ_2 system with the parameters listed in Table E3.

Figure E6: Same as in Fig. E2 for the Δ_2 system.

ω_i [cm^{-1}]	η_i	ω_i [cm^{-1}]	η_i	ω_i [cm^{-1}]	η_i
953.148	0.45713	1365.141	0.02864	1477.189	0.07808
970.135	0.03208	1367.923	0.07584	1489.465	0.02090
1091.566	0.39745	1374.991	0.03784	1495.682	0.09020
1137.814	0.02413	1379.740	0.06068	1500.379	0.09176
1175.606	0.03867	1385.386	0.06757	1506.312	0.01842
1207.210	0.12678	1395.776	0.08758	1570.352	0.10501
1245.988	0.01780	1403.406	0.06543	1621.516	0.06173
1257.454	0.04460	1405.144	0.01674	1628.919	0.01411
1259.287	0.01942	1426.216	0.32719	1652.808	0.01301
1281.463	0.14037	1444.037	0.31282	1738.695	0.03018
1291.292	0.05185	1448.900	0.06284	2136.274	1.00000
1353.280	0.02612	1458.629	0.02131	2271.540	0.03444
1357.218	0.02420	1465.305	0.18154	2994.326	0.00859
1358.446	0.03741	1475.112	0.02150		

Table E3: Parameters ω_i and η_i for the spectral density of the Δ_2 system.

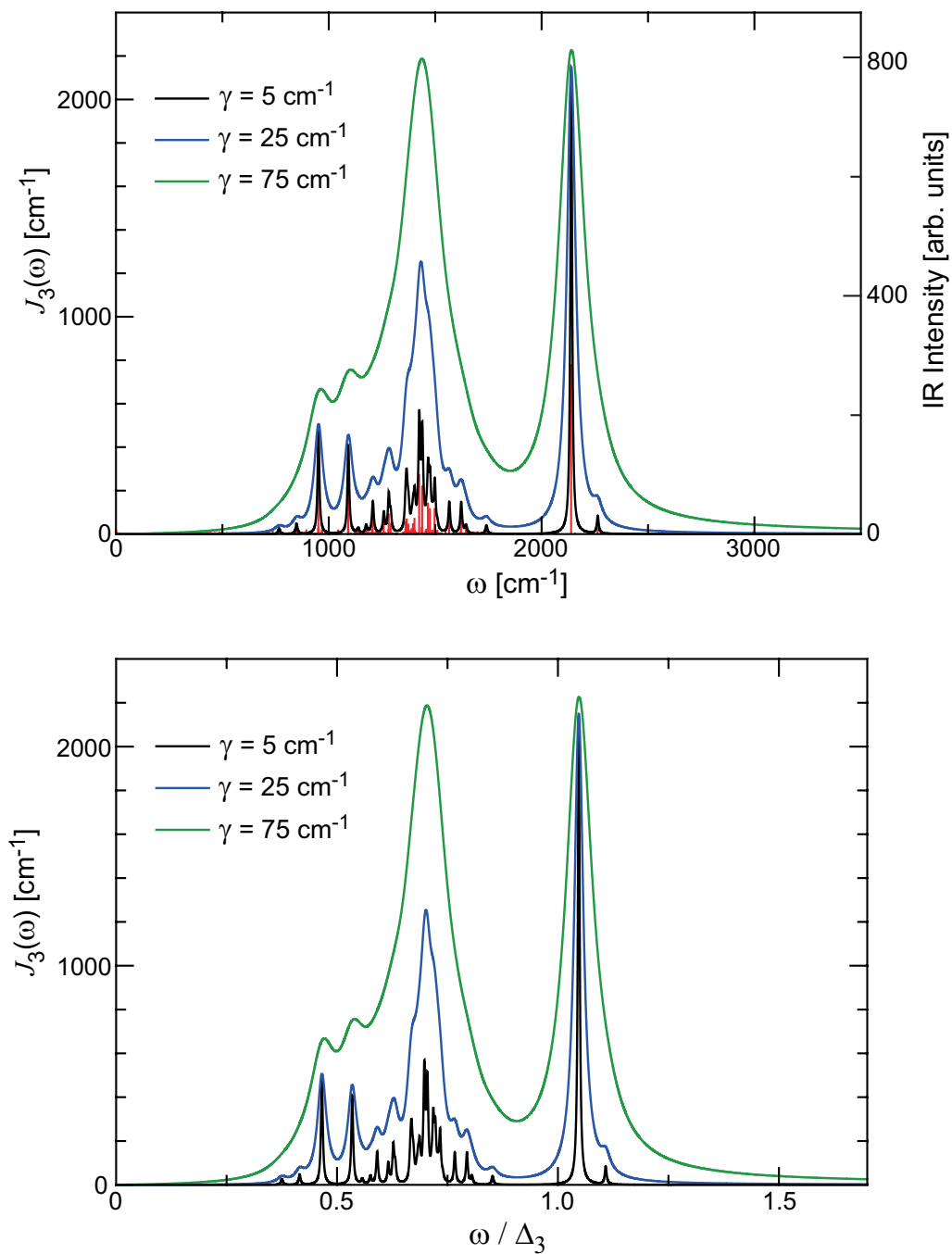
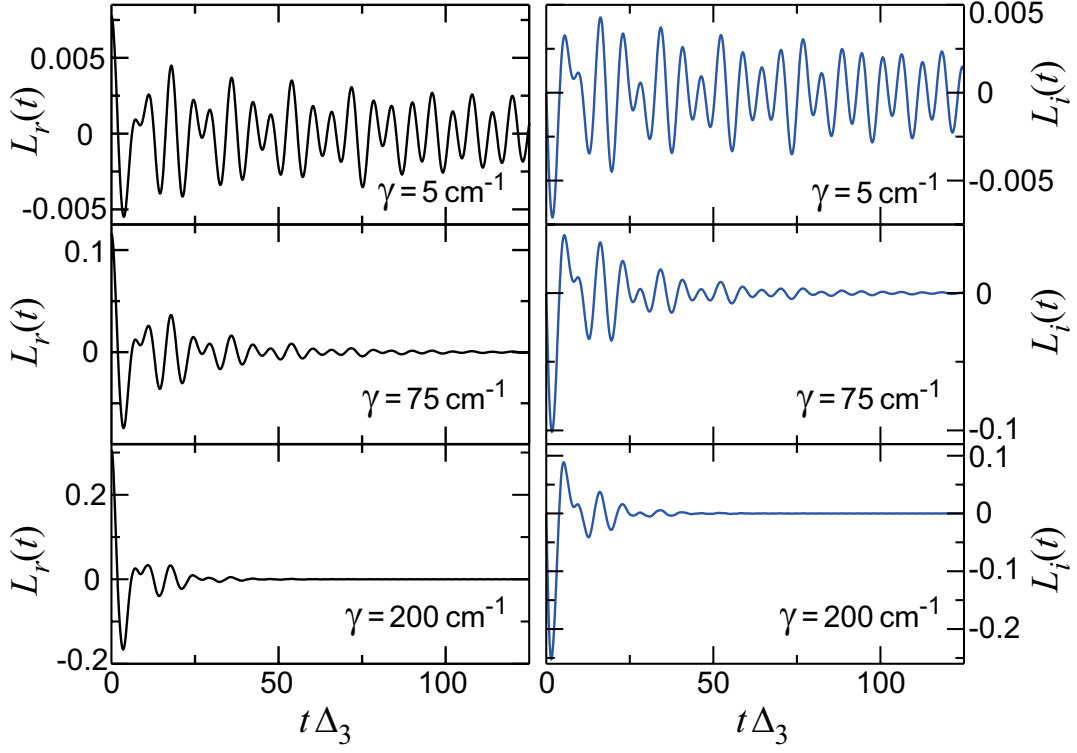


Figure E7: Same as in Fig. E1 for the Δ_3 system with the parameters listed in Table E4.

Figure E8: Same as in Fig. E2 for the Δ_3 system.

ω_i [cm^{-1}]	η_i	ω_i [cm^{-1}]	η_i	ω_i [cm^{-1}]	η_i
766.757	0.03358	1364.413	0.08089	1476.013	0.14449
848.597	0.05537	1366.994	0.08336	1486.124	0.01678
951.549	0.47964	1372.342	0.02991	1489.103	0.01759
1091.798	0.31361	1375.277	0.05300	1498.098	0.14660
1137.896	0.02044	1389.740	0.02626	1510.608	0.01670
1175.820	0.03120	1396.322	0.05578	1566.185	0.09121
1205.089	0.02028	1403.172	0.08758	1622.186	0.08802
1207.375	0.10488	1404.892	0.01817	1644.891	0.02184
1258.557	0.07299	1425.199	0.34798	1740.846	0.02218
1280.627	0.02052	1436.555	0.03286	2139.289	1.00000
1282.197	0.11293	1439.528	0.27928	2263.826	0.03584
1291.219	0.05732	1458.436	0.02276		
1360.758	0.06634	1466.608	0.17776		

Table E4: Parameters ω_i and η_i for the spectral density of the Δ_3 system.

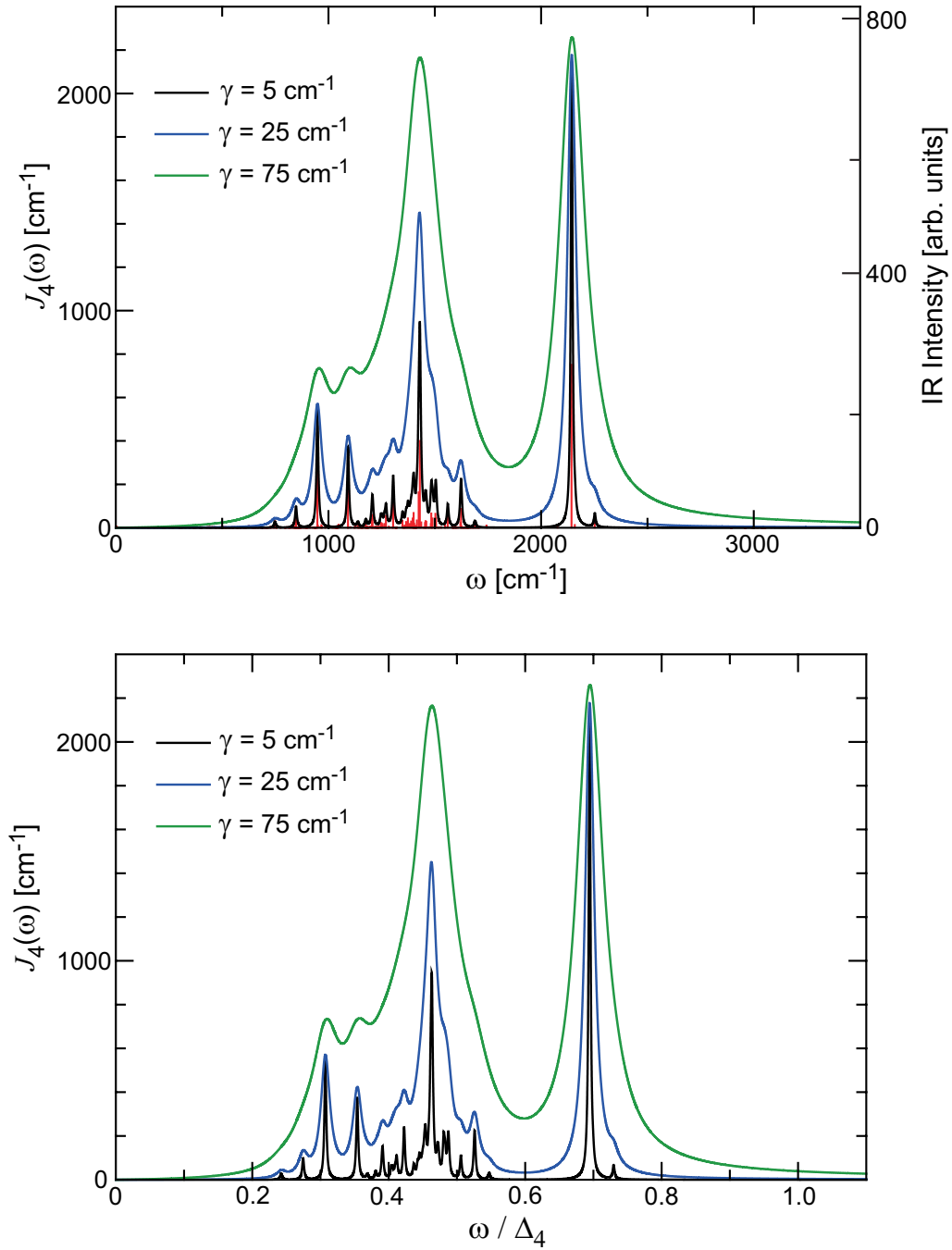
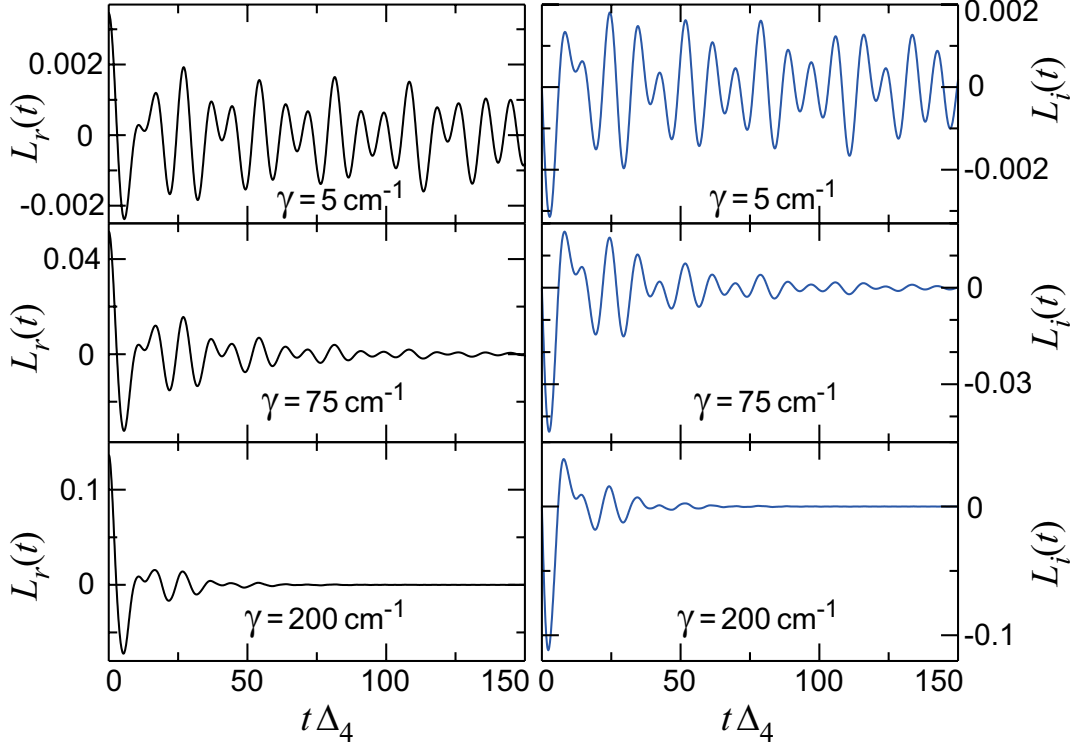


Figure E9: Same as in Fig. E1 for the Δ_4 system with the parameters listed in Table E5.

Figure E10: Same as in Fig. E2 for the Δ_4 system.

ω_i [cm^{-1}]	η_i	ω_i [cm^{-1}]	η_i	ω_i [cm^{-1}]	η_i
748.447	0.03826	1365.514	0.03368	1481.888	0.02142
847.369	0.11420	1374.033	0.05589	1483.887	0.08621
948.017	0.57614	1383.189	0.02133	1489.917	0.05559
1092.285	0.34105	1389.275	0.03650	1503.522	0.08403
1137.995	0.01948	1396.270	0.05532	1506.586	0.05574
1175.884	0.02815	1400.786	0.08908	1561.183	0.06573
1205.199	0.05222	1403.331	0.02398	1621.124	0.02861
1207.556	0.07702	1416.374	0.04338	1623.920	0.11413
1246.264	0.02895	1424.550	0.21579	1689.129	0.01762
1251.469	0.02423	1430.046	0.53203	2143.687	1.00000
1263.489	0.02157	1436.681	0.03141	2159.138	0.01508
1270.574	0.07160	1454.442	0.02755	2252.472	0.02775
1304.371	0.17739	1456.946	0.03904		
1348.344	0.04144	1460.572	0.03515		

Table E5: Parameters ω_i and η_i for the spectral density of the Δ_4 system.

F Dissipative dynamics of the Δ_4 system

This appendix presents the real-time dynamics of the Δ_4 system, given in terms of the population difference $P(t)$, determined using the QUAPI scheme. Results are determined by choosing a compromise between a large enough memory time (given by a large K) and a small enough Trotter error (given by a small δt step). For this particular system, an *optimal* parameter combination is difficult to find due to the long-lived oscillatory correlations resulting from the large number of peaks at frequencies $\omega_i < \Delta_4$. The results in this appendix illustrate the effect of $N = 4$ main IR modes at energies below $\hbar\Delta_N$ and should be compared with those in Chap. 5 for $N = 0, 1, 2$, and 3.

The population difference $P(t)$ is shown in Fig. F1 as a function of the damping strength γ and for a fixed value $\gamma = 250 \text{ cm}^{-1}$. These results should be compared with those in Figs. 5.1 and 5.2, respectively. In this case, sustained coherent oscillations of the population difference result from the vibrational modes below $\hbar\Delta_N$. The resulting values for $T_{1,4}$ and for Q_4 as a function of the damping strength γ

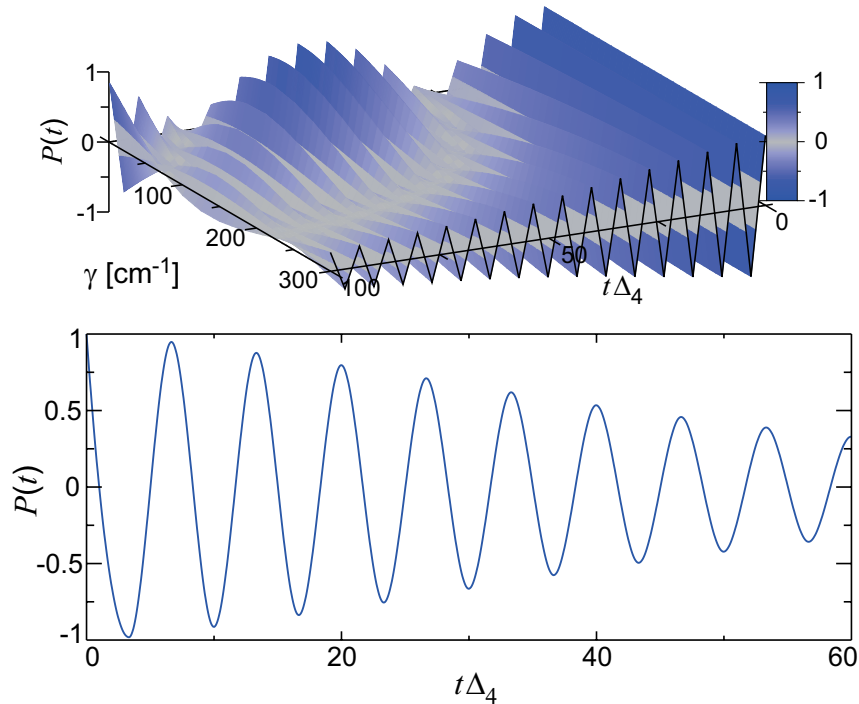


Figure F1: Time-dependent population difference $P(t)$ for the Δ_4 system as a function of the damping strength γ (top) and for a fixed value $\gamma = 250 \text{ cm}^{-1}$ of the electron–vibration coupling (bottom).

are shown in Fig. F2. Complementing the results in Table 5.1, it is obtained that $T_{1,4} = 4321, 1201, 575, 226,$ and 114 ns and $Q_4 = 2510, 696, 332, 118,$ and 63 for $\gamma = 5, 20, 45, 100,$ and 250 cm^{-1} , respectively. These values indicate the coherence times decrease with increasing coupling but for a fixed γ , the coherence times increase with Δ_N .

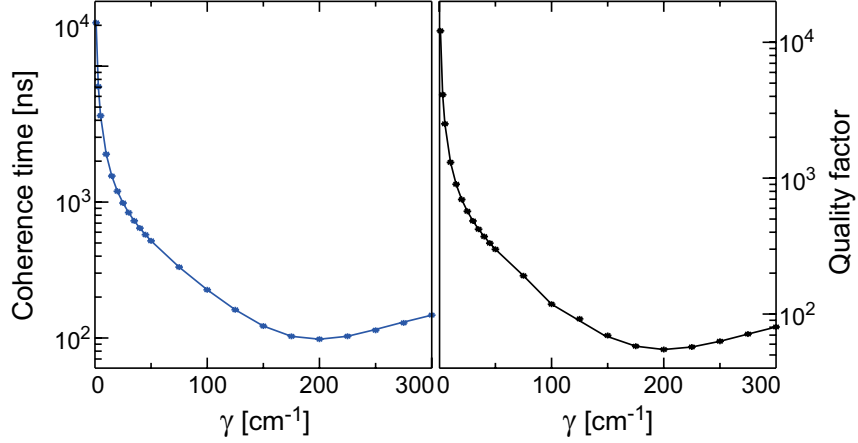


Figure F2: Coherence times $T_{1,4}$ (left) and quality factors Q_4 (right) as a function of the damping strength γ .

The evolution of the trace distance $D(\rho_1, \rho_2)$ is shown in Fig. F1 as a function of the damping strength γ and for specific values of γ . These results should be compared with those in Figs. 5.4 and 5.5, respectively. In spite no oscillations are seen in the trace distance for large γ values, its decay is the slowest due to the slow dynamics of the vibrational bath resulting from the modes at frequencies $\omega_j < \Delta_4$. The resulting non-Markovianity measure \mathcal{N} is shown in Fig. F4 as a function of γ .

The population difference $P(t)$ under the same weak field parameters as in Fig. 5.8 for $N = 0-3$, is shown in Fig. F5 for $N = 4$ and a fixed value $\gamma = 200$ cm^{-1} of the electron-vibration coupling. Square-wave oscillations in $P(t)$ due to population trapping are attained by the combination of large amplitude with slow driving frequency, as illustrated in Fig. F6. The driving strength of $\mu A = 10\hbar\Delta_4$, results in an electric field of 212.1×10^7 V/m, and a driving frequency of 9.3 THz. The corresponding field intensity is 1194 GW/cm^2 . These values of the laser field, though larger than those required for the other systems, are still achievable with quantum cascade lasers. However, competing processes such as bond breaking or ionization may occur at the required field for this system. The resulting non-Markovianity measure \mathcal{N} is shown in Fig. F7 as a function of γ for increasing driving strength A .

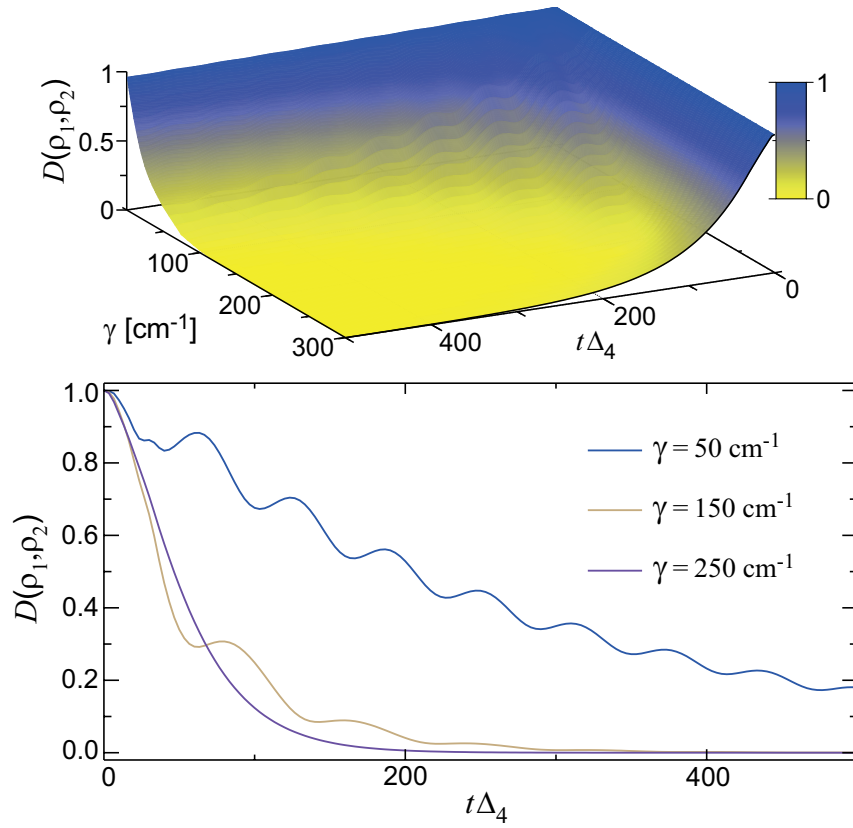


Figure F3: Time-dependent trace distance $D(\rho_1, \rho_2)$ for the Δ_4 system as a function of the damping strength γ (top) and for specific values of the electron–vibration coupling as indicated (bottom).

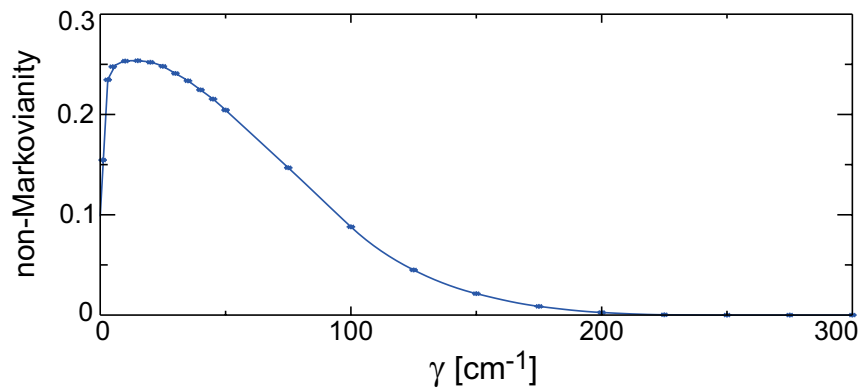


Figure F4: Non-Markovianity \mathcal{N} as a function of the damping strength γ for the Δ_4 system.

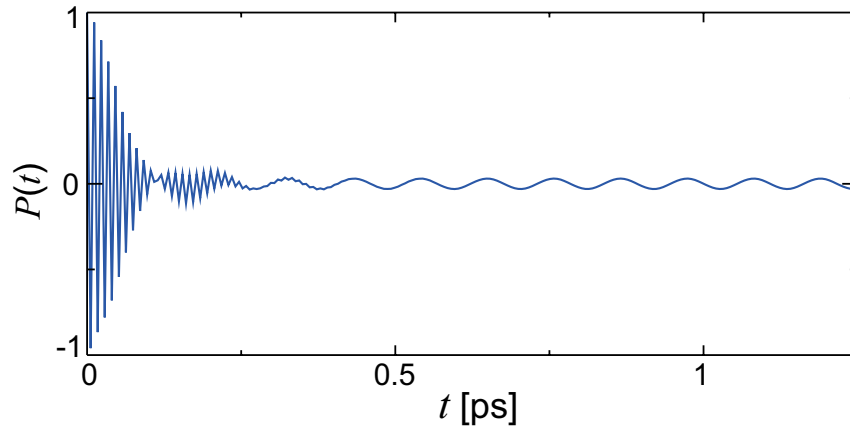


Figure F5: Time-dependent population difference $P(t)$ at fixed $\gamma = 200 \text{ cm}^{-1}$ for the Δ_4 system with field parameters $A = 0.1\Delta_4$ and $\Omega = 0.1\Delta_4$.

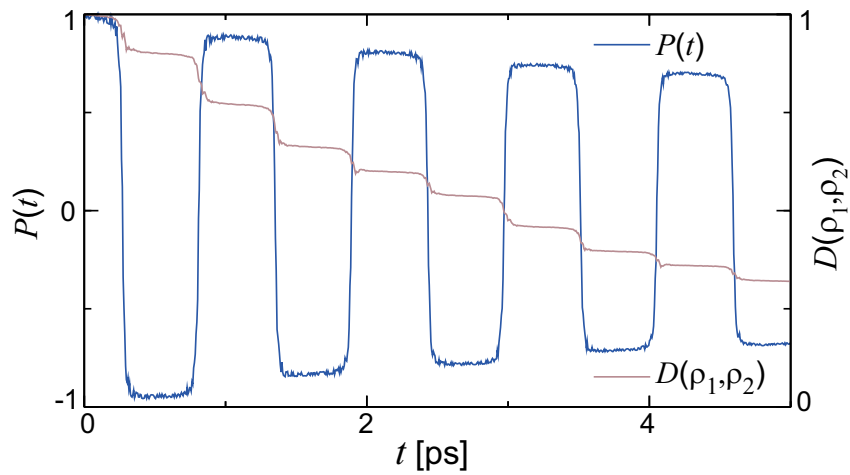


Figure F6: Evolution of $P(t)$ and $D(\rho_1, \rho_2)$ for the Δ_4 system at fixed $\gamma = 5 \text{ cm}^{-1}$ and field parameters $A = 10\Delta_4$ and $\Omega = 0.1\Delta_4$.

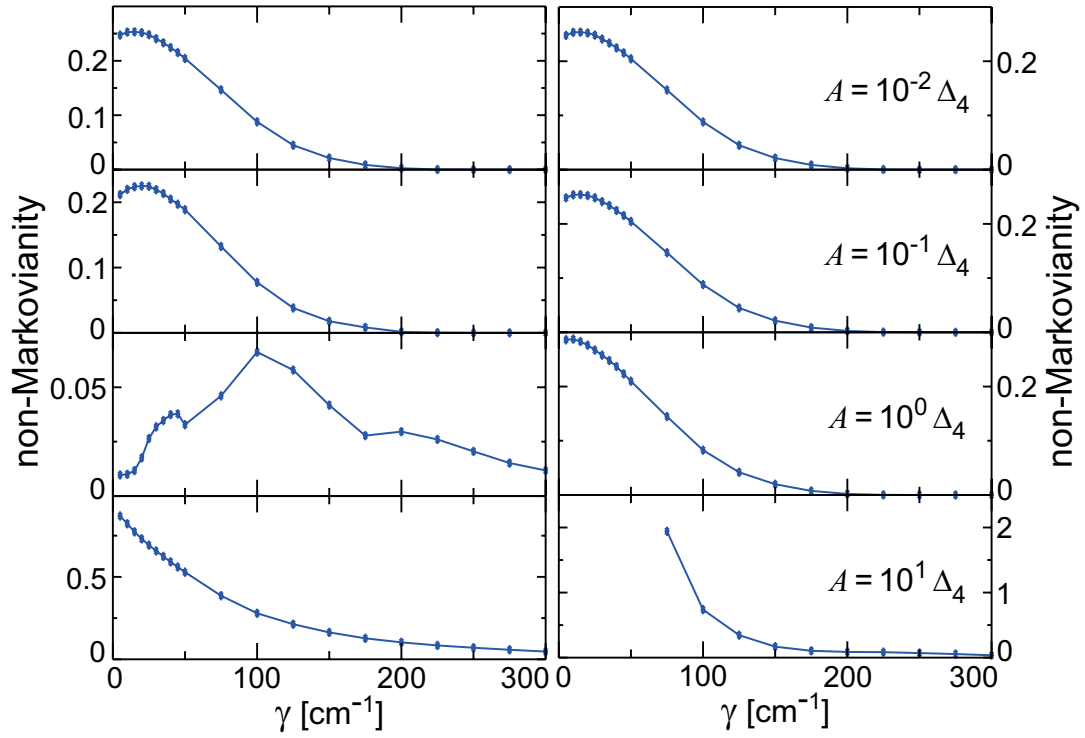


Figure F7: Non-Markovianity \mathcal{N} as a function of the damping strength γ for different values of the driving strength A for the Δ_4 system at fixed driving frequencies $\Omega = 0.1\Delta_4$ (left) and $\Omega = 10\Delta_4$ (right).

Bibliography

- [1] U. Weiss, *Quantum Dissipative Systems* (World Scientific, Singapore, 2008), 3rd ed.
- [2] T. D. Ladd, F. Jelezko, R. Laflamme, Y. Nakamura, C. Monroe, and J. L. O'Brien, *Quantum computers*. *Nature* (London) **464**, 45 (2010).
- [3] M. A. Nielsen and I. L. Chuang, *Quantum Computation and Quantum Information* (Cambridge University Press, Cambridge, 2010), 10th anniversary ed.
- [4] Focus issue on 'Materials issues for quantum computation', J. N. Eckstein and J. Levy, Eds. *MRS Bulletin* **38**, Issue 10 (2013).
- [5] N. Makri, *Quantum dissipative dynamics: A numerically exact methodology*. *J. Phys. Chem. A* **102**, 4414 (1998).
- [6] N. Makri, *Time-dependent quantum methods for large systems*. *Annu. Rev. Phys. Chem.* **50**, 167 (1999).
- [7] P. Nalbach and M. Thorwart, *Multiphonon transitions in the biomolecular energy transfer dynamics*. *J. Chem. Phys.* **132**, 194111 (2010).
- [8] A. J. Leggett, S. Chakravarty, A. T. Dorsey, M. P. A. Fisher, A. Garg, and W. Zwerger, *Dynamics of the dissipative two-state system*. *Rev. Mod. Phys.* **59**, 1 (1987); *ibid.* **67**, 725 (1995).
- [9] M. Grifoni and P. Hänggi, *Driven quantum tunneling*. *Phys. Rep.* **304**, 229 (1998).

- [10] M. Grifoni, E. Paladino, and U. Weiss, *Dissipation, decoherence and preparation effects in the spin-boson system*. Eur. Phys. J. B **10**, 719 (1999).
- [11] F. Grossmann, T. Dittrich, P. Jung, and P. Hänggi, *Coherent destruction of tunneling*. Phys. Rev. Lett. **67**, 516 (1991).
- [12] S. Florens, D. Venturelli, and R. Narayanan, *Quantum phase transition in the spin boson model*, in *Quantum Quenching, Annealing and Computation*, A. K. Chandra, A. Das, and B. K. Chakrabarti, Eds. (Springer, Berlin, 2010), pp. 145-162.
- [13] J. A. Jones, *Quantum computing with NMR*. Prog. Nucl. Magn. Reson. Spectrosc. **59**, 91 (2011).
- [14] A. E. P. Da Silva and G. M. E. Silva, *Polyacetylene as a qubit system*. Int. J. Quantum Chem. **95**, 224 (2003).
- [15] D. Stepanenko, M. Trif, and D. Loss, *Quantum computing with molecular magnets*. Inorg. Chim. Acta **361**, 3740 (2008).
- [16] P. C. E. Stamp and A. Gaita-Ariño, *Spin-based quantum computers made by chemistry: Hows and whys*. J. Mater. Chem. **19**, 1718 (2009).
- [17] G. Aromí, D. Aguilà, P. Gamez, F. Luis, and O. Roubeau, *Design of magnetic coordination complexes for quantum computing*. Chem. Soc. Rev. **41**, 537 (2012).
- [18] R. de Vivie-Riedle and U. Troppmann, *Femtosecond lasers for quantum information technology*. Chem. Rev. **107**, 5082 (2007).
- [19] E. Berrios, M. Gruebele, D. Shyshlov, L. Wang, and D. Babikov, *High fidelity quantum gates with vibrational qubits*. J. Phys. Chem. A **116**, 11347 (2012).
- [20] K. Mishima, K. Tokumo, and K. Yamashita, *Quantum computing using molecular electronic and vibrational states*. Chem. Phys. **343**, 61 (2008).
- [21] A. Ishizaki and G. R. Fleming, *Quantum coherence in photosynthetic light harvesting*. Annu. Rev. Condens. Matter Phys. **3**, 333 (2012).
- [22] N. Makri, *Numerical path integral techniques for long time dynamics of quantum dissipative systems*. J. Math. Phys. **36**, 2430 (1995).

- [23] N. Makri and D. E. Makarov, *Tensor propagator for iterative quantum time evolution of reduced density matrices. I. Theory*. J. Chem. Phys. **102**, 4600 (1995); *Tensor propagator for iterative quantum time evolution of reduced density matrices. II. Numerical methodology*. *ibid.* **102**, 4611 (1995).
- [24] C. Cohen-Tannoudji, B. Diu, and F. Laloë, *Quantum Mechanics* (Hermann, Paris, 1977), Vol. 1, Chap. 3.
- [25] G.-L. Ingold, *Path integrals and their application to dissipative quantum systems*, in *Coherent Evolution in Noisy Environments*, A. Buchleitner and K. Hornberger, Eds. (Springer, Berlin, 2002), pp. 1-53.
- [26] R. P. Feynman, *Space-time approach to non-relativistic quantum mechanics*. Rev. Mod. Phys. **20**, 367 (1948).
- [27] D. Derbes, *Feynman's derivation of the Schrödinger equation*. Am. J. Phys. **64**, 881 (1996).
- [28] M. Thorwart, *Tunneling and vibrational relaxation in driven multilevel systems*, Dissertation, Universität Augsburg (2000).
- [29] V. May and O. Kühn, *Charge and Energy Transfer Dynamics in Molecular Systems* (Wiley-VCH, Weinheim, 2011), 3rd ed.
- [30] J. Eckel, J. H. Reina, and M. Thorwart, *Coherent control of an effective two-level system in a non-Markovian biomolecular environment*. New J. Phys. **11**, 085001 (2009).
- [31] M. Thorwart, E. Paladino, and M. Grifoni, *Dynamics of the spin-boson model with a structured environment*. Chem. Phys. **296**, 333 (2004).
- [32] W. H. Press, S. A. Teukolsky, W. T. Vetterling, and B. P. Flannery, *Numerical Recipes in Fortran* (Cambridge University Press, Cambridge, 1992).
- [33] R. P. Feynman and F. L. Vernon Jr., *The theory of a general quantum system interacting with a linear dissipative system*. Ann. Phys. **24**, 118 (1963).
- [34] M. Thorwart, P. Reimann, P. Jung, and R. Fox, *Quantum hysteresis and resonant tunneling in bistable systems*. Chem. Phys. **235**, 61 (1998).
- [35] M. Thorwart, P. Reimann, and P. Hänggi, *Iterative algorithm versus analytic solutions of the parametrically driven dissipative quantum harmonic oscillator*. Phys. Rev. E **62**, 5808 (2000).

- [36] A. A. Golosov, R. A. Friesner, and P. Pechukas, *Efficient memory equation algorithm for reduced dynamics in spin-boson models*. J. Chem. Phys. **110**, 138 (1999).
- [37] P. Nalbach, J. Eckel, and M. Thorwart, *Quantum coherent biomolecular energy transfer with spatially correlated fluctuations*. New J. Phys. **12**, 065043 (2010).
- [38] M. Thorwart, J. Eckel, and E. R. Mucciolo, *Non-Markovian dynamics of double quantum dot charge qubits due to acoustic phonons*. Phys. Rev. B **72**, 235320 (2005).
- [39] J. Eckel, S. Weiss, and M. Thorwart, *Phonon-induced decoherence and dissipation in donor-based charge qubits*. Eur. Phys. J. B **53**, 91 (2006).
- [40] M. Thorwart, J. Eckel, J. H. Reina, P. Nalbach, and S. Weiss, *Enhanced quantum entanglement in the non-Markovian dynamics of biomolecular excitons*. Chem. Phys. Lett. **478**, 234 (2009).
- [41] P. Nalbach and M. Thorwart, *Landau-Zener transitions in a dissipative environment: Numerically exact results*. Phys. Rev. Lett. **103**, 220401 (2009).
- [42] C. A. Mujica-Martinez, P. Nalbach, and M. Thorwart, *Organic π -conjugated copolymers as molecular charge qubits*. Phys. Rev. Lett. **111**, 016802 (2013); *ibid.* **113**, 139903 (2014).
- [43] P. Nalbach, D. Braun, and M. Thorwart, *Exciton transfer dynamics and quantumness of energy transfer in the Fenna-Matthews-Olson complex*. Phys. Rev. E **84**, 041926 (2011).
- [44] P. Nalbach and M. Thorwart, *The role of discrete molecular modes in the coherent exciton dynamics in FMO*. J. Phys. B: At. Mol. Opt. Phys. **45**, 154009 (2012).
- [45] C. A. Mujica-Martinez, P. Nalbach, and M. Thorwart, *Quantification of non-Markovian effects in the Fenna-Matthews-Olson complex*. Phys. Rev. E **88**, 062719 (2013).
- [46] H.-P. Breuer, *Foundations and measures of quantum non-Markovianity*. J. Phys. B: At. Mol. Opt. Phys. **45**, 154001 (2012).
- [47] A. Rivas, S. F. Huelga, and M. B. Plenio, *Entanglement and non-Markovianity of quantum evolutions*. Phys. Rev. Lett. **105**, 050403 (2010).

-
- [48] M. M. Wolf, J. Eisert, T. S. Cubitt, and J. I. Cirac, *Assessing non-Markovian quantum dynamics*. Phys. Rev. Lett. **101**, 150402 (2008).
- [49] H.-P. Breuer, E.-M. Laine, and J. Piilo, *Measure for the degree of non-Markovian behavior of quantum processes in open systems*. Phys. Rev. Lett. **103**, 210401 (2009).
- [50] B.-H. Liu, L. Li, Y.-F. Huang, C.-F. Li, G.-C. Guo, E.-M. Laine, H.-P. Breuer, and J. Piilo, *Experimental control of the transition from Markovian to non-Markovian dynamics of open quantum systems*. Nat. Phys. **7**, 931 (2011).
- [51] J.-S. Tang, C.-F. Li, Y.-L. Li, X.-B. Zou, G.-C. Guo, H.-P. Breuer, E.-M. Laine, and J. Piilo, *Measuring non-Markovianity of processes with controllable system-environment interaction*. Europhys. Lett. **97**, 10002 (2012).
- [52] R. Horodecki, P. Horodecki, M. Horodecki, and K. Horodecki, *Quantum entanglement*. Rev. Mod. Phys. **81**, 865 (2009).
- [53] P. Haikka, J. D. Cresser, and S. Maniscalco, *Comparing different non-Markovianity measures in a driven qubit system*. Phys. Rev. A **83**, 012112 (2011).
- [54] H.-S. Zeng, N. Tang, Y.-P. Zheng, and G.-Y. Wang, *Equivalence of the measures of non-Markovianity for open two-level systems*. Phys. Rev. A **84**, 032118 (2011).
- [55] D. Chruściński, A. Kossakowski, and Á. Rivas, *Measures of non-Markovianity: Divisibility versus backflow of information*. Phys. Rev. A **83**, 052128 (2011).
- [56] B. Vacchini, A. Smirne, E.-M. Laine, J. Piilo, and H.-P. Breuer, *Markovianity and non-Markovianity in quantum and classical systems*. New J. Phys. **13**, 093004 (2011).
- [57] H. Zeng, N. Tang, Y. Zheng, and T. Xu, *Non-Markovian dynamics for an open two-level system without rotating wave approximation: Indivisibility versus backflow of information*. Eur. Phys. J. D **66**, 255 (2012).
- [58] E.-M. Laine, J. Piilo, and H.-P. Breuer, *Measure for the non-Markovianity of quantum processes*. Phys. Rev. A **81**, 062115 (2010).
- [59] G. Clos and H.-P. Breuer, *Quantification of memory effects in the spin-boson model*. Phys. Rev. A **86**, 012115 (2012).

- [60] P. Reberntrost and A. Aspuru-Guzik, *Communication: Exciton–phonon information flow in the energy transfer process of photosynthetic complexes*. J. Chem. Phys. **134**, 101103 (2011).
- [61] A. Smirne, H.-P. Breuer, J. Piilo, and B. Vacchini, *Initial correlations in open-systems dynamics: The Jaynes-Cummings model*. Phys. Rev. A **82**, 062114 (2010).
- [62] E.-M. Laine, J. Piilo, and H.-P. Breuer, *Witness for initial system–environment correlations in open-system dynamics*. Europhys. Lett. **92**, 60010 (2010).
- [63] T. J. G. Apollaro, C. Di Franco, F. Plastina, and M. Paternostro, *Memory-keeping effects and forgetfulness in the dynamics of a qubit coupled to a spin chain*. Phys. Rev. A **83**, 032103 (2011).
- [64] J.-G. Li, J. Zou, and B. Shao, *Non-Markovianity of the damped Jaynes-Cummings model with detuning*. Phys. Rev. A **81**, 062124 (2010).
- [65] L. Mazzola, E.-M. Laine, H.-P. Breuer, S. Maniscalco, and J. Piilo, *Phenomenological memory-kernel master equations and time-dependent Markovian processes*. Phys. Rev. A **81**, 062120 (2010).
- [66] P. Haikka, S. McEndoo, G. De Chiara, G. M. Palma, and S. Maniscalco, *Quantifying, characterizing, and controlling information flow in ultracold atomic gases*. Phys. Rev. A **84**, 031602 (2011).
- [67] E.-M. Laine, H.-P. Breuer, J. Piilo, C.-F. Li, and G.-C. Guo, *Nonlocal memory effects in the dynamics of open quantum systems*. Phys. Rev. Lett. **108**, 210402 (2012).
- [68] D. P. DiVincenzo and D. Loss, *Quantum information is physical*. Superlattices Microstruct. **23**, 419 (1998).
- [69] D. DiVincenzo, Ed. *Quantum Information Processing: Lecture Notes of the 44th IFF Spring School 2013* (Forschungszentrum Jülich, Jülich, 2013).
- [70] D. P. DiVincenzo, *The physical implementation of quantum computation*. Fortschr. Phys. **48**, 771 (2000).
- [71] A. Zrenner, E. Beham, S. Stuffer, F. Findeis, M. Bichler, and G. Abstreiter, *Coherent properties of a two-level system based on a quantum-dot photodiode*. Nature (London) **418**, 612 (2002).

- [72] D. Loss and D. P. DiVincenzo, *Quantum computation with quantum dots*. Phys. Rev. A **57**, 120 (1998).
- [73] B. E. Kane, *A silicon-based nuclear spin quantum computer*. Nature (London) **393**, 133 (1998).
- [74] R. Hanson and D. D. Awschalom, *Coherent manipulation of single spins in semiconductors*. Nature (London) **453**, 1043 (2008).
- [75] S. Simmons, R. M. Brown, H. Riemann, N. V. Abrosimov, P. Becker, H.-J. Pohl, M. L. W. Thewalt, K. M. Itoh, and J. J. L. Morton, *Entanglement in a solid-state spin ensemble*. Nature (London) **470**, 69 (2011).
- [76] G. D. Fuchs, G. Burkard, P. V. Klimov, and D. D. Awschalom, *A quantum memory intrinsic to single nitrogen-vacancy centres in diamond*. Nat. Phys. **7**, 789 (2011).
- [77] K. D. Petersson, J. R. Petta, H. Lu, and A. C. Gossard, *Quantum coherence in a one-electron semiconductor charge qubit*. Phys. Rev. Lett. **105**, 246804 (2010).
- [78] D. Harbusch, S. Manus, H. P. Tranitz, W. Wegscheider, and S. Ludwig, *Radio frequency pulsed-gate charge spectroscopy on coupled quantum dots*. Phys. Rev. B **82**, 195310 (2010).
- [79] J. H. Davies, *The Physics of Low-dimensional Semiconductors* (Cambridge University Press, Cambridge, 1998).
- [80] P. Harrison, *Quantum Wells, Wires and Dots: Theoretical and Computational Physics of Semiconductor Nanostructures* (Wiley, Chichester, 2005), 2nd ed.
- [81] J. C. Arce, A. Perdomo-Ortiz, M. L. Zambrano, and C. A. Mujica-Martinez, *Envelope molecular-orbital theory of extended systems. I. Electronic states of organic quasilinear nanoheterostructures*. J. Chem. Phys. **134**, 104103 (2011).
- [82] H. Shirakawa, E. J. Louis, A. G. MacDiarmid, C. K. Chiang, and A. J. Heeger, *Synthesis of electrically conducting organic polymers: Halogen derivatives of polyacetylene, (CH)_x*. J. Chem. Soc., Chem. Commun. (16), 578 (1977).
- [83] C. K. Chiang, C. R. Fincher, Y. W. Park, A. J. Heeger, H. Shirakawa, E. J. Louis, S. C. Gau, and A. G. MacDiarmid, *Electrical conductivity in doped polyacetylene*. Phys. Rev. Lett. **39**, 1098 (1977); *ibid.* **40**, 1472 (1977).

- [84] C. K. Chiang, M. A. Druy, S. C. Gau, A. J. Heeger, E. J. Louis, A. G. MacDiarmid, Y. W. Park, and H. Shirakawa, *Synthesis of highly conducting films of derivatives of polyacetylene*, $(\text{CH})_x$. J. Am. Chem. Soc. **100**, 1013 (1978).
- [85] A. J. Heeger, *Nobel Lecture: Semiconducting and metallic polymers: The fourth generation of polymeric materials*. Rev. Mod. Phys. **73**, 681 (2001); A. G. MacDiarmid, *Nobel Lecture: "Synthetic metals": A novel role for organic polymers*. *ibid.* **73**, 701 (2001); H. Shirakawa, *Nobel Lecture: The discovery of polyacetylene film—The dawning of an era of conducting polymers*. *ibid.* **73**, 713 (2001).
- [86] N. Hall, *Twenty-five years of conducting polymers*. Chem. Commun. (1), 1 (2003).
- [87] A. Moliton and R. C. Hiorns, *Review of electronic and optical properties of semiconducting π -conjugated polymers: Applications in optoelectronics*. Polym. Int. **53**, 1397 (2004).
- [88] M. Kertesz, C. H. Choi, and S. Yang, *Conjugated polymers and aromaticity*. Chem. Rev. **105**, 3448 (2005).
- [89] I. Hwang and G. D. Scholes, *Electronic energy transfer and quantum-coherence in π -conjugated polymers*. Chem. Mater. **23**, 610 (2011).
- [90] T. A. Skotheim and J. R. Reynolds, Eds. *Handbook of Conducting Polymers: Theory, Synthesis, Properties and Characterization* (CRC Press, Boca Raton, 2007), Vol. 1.
- [91] H. S. Nalwa, Ed. *Handbook of Advanced Electronic and Photonic Materials and Devices: Conducting Polymers* (Academic Press, San Diego, 2001), Vol. 8.
- [92] T. A. Skotheim and J. R. Reynolds, Eds. *Handbook of Conducting Polymers: Processing and Applications* (CRC Press, Boca Raton, 2007), Vol. 2.
- [93] J. L. Brédas and A. J. Heeger, *Influence of donor and acceptor substituents on the electronic characteristics of poly(paraphenylene vinylene) and poly(paraphenylene)*. Chem. Phys. Lett. **217**, 507 (1994).
- [94] U. Scherf, *Conjugated ladder-type structures*, in *Handbook of Conducting Polymers*, T. A. Skotheim, R. L. Elsenbaumer, and J. R. Reynolds, Eds. (Marcel Dekker, New York, 1998), 2nd ed., Chap. 14.

- [95] D. L. Smith and C. Mailhot, *Theory of semiconductor superlattice electronic structure*. Rev. Mod. Phys. **62**, 173 (1990).
- [96] J. M. Tour, *Conjugated macromolecules of precise length and constitution. Organic synthesis for the construction of nanoarchitectures*. Chem. Rev. **96**, 537 (1996).
- [97] L. Akcelrud, *Electroluminescent polymers*. Prog. Polym. Sci. **28**, 875 (2003).
- [98] Y.-J. Cheng, S.-H. Yang, and C.-S. Hsu, *Synthesis of conjugated polymers for organic solar cell applications*. Chem. Rev. **109**, 5868 (2009).
- [99] H. Sakaguchi, H. Matsumura, and H. Gong, *Electrochemical epitaxial polymerization of single-molecular wires*. Nat. Mater. **3**, 551 (2004).
- [100] H. Sakaguchi, H. Matsumura, H. Gong, and A. M. Abouelwafa, *Direct visualization of the formation of single-molecule conjugated copolymers*. Science **310**, 1002 (2005).
- [101] Y. Okawa and M. Aono, *Nanoscale control of chain polymerization*. Nature (London) **409**, 683 (2001).
- [102] Y. Okawa, M. Akai-Kasaya, Y. Kuwahara, S. K. Mandal, and M. Aono, *Controlled chain polymerisation and chemical soldering for single-molecule electronics*. Nanoscale **4**, 3013 (2012).
- [103] F. Dubin, R. Melet, T. Barisien, R. Grousson, L. Legrand, M. Schott, and V. Voliotis, *Macroscopic coherence of a single exciton state in an organic quantum wire*. Nat. Phys. **2**, 32 (2006).
- [104] E. Collini and G. D. Scholes, *Coherent intrachain energy migration in a conjugated polymer at room temperature*. Science **323**, 369 (2009).
- [105] E. Collini and G. D. Scholes, *Electronic and vibrational coherences in resonance energy transfer along MEH-PPV chains at room temperature*. J. Phys. Chem. A **113**, 4223 (2009).
- [106] J. L. Brédas and R. Silbey, *Excitons surf along conjugated polymer chains*. Science **323**, 348 (2009).
- [107] U. Scherf, *Ladder-type materials*. J. Mater. Chem. **9**, 1853 (1999).

- [108] J. G. Müller, M. Anni, U. Scherf, J. M. Lupton, and J. Feldmann, *Vibrational fluorescence spectroscopy of single conjugated polymer molecules*. Phys. Rev. B **70**, 035205 (2004).
- [109] Y. Okawa, S. K. Mandal, C. Hu, Y. Tateyama, S. Goedecker, S. Tsukamoto, T. Hasegawa, J. K. Gimzewski, and M. Aono, *Chemical wiring and soldering toward all-molecule electronic circuitry*. J. Am. Chem. Soc. **133**, 8227 (2011).
- [110] S. Liu, D. Schmitz, S.-S. Jester, N. J. Borys, S. Höger, and J. M. Lupton, *Coherent and incoherent interactions between cofacial Π -conjugated oligomer dimers in macrocycle templates*. J. Phys. Chem. B **117**, 4197 (2013).
- [111] W. J. Baker, T. L. Keevers, J. M. Lupton, D. R. McCamey, and C. Boehme, *Slow hopping and spin dephasing of coulombically bound polaron pairs in an organic semiconductor at room temperature*. Phys. Rev. Lett. **108**, 267601 (2012).
- [112] D. R. McCamey, H. A. Seipel, S.-Y. Paik, M. J. Walter, N. J. Borys, J. M. Lupton, and C. Boehme, *Spin Rabi flopping in the photocurrent of a polymer light-emitting diode*. Nat. Mater. **7**, 723 (2008).
- [113] G. Gandhi and A. K. Bakhshi, *Theoretical designing of the electronic structures and conduction properties of copolymers of donor–acceptor polymers: Effect of multi-neighbour interaction*. Chem. Phys. **309**, 143 (2005).
- [114] M. A. Eriksson, S. N. Coppersmith, and M. G. Lagally, *Semiconductor quantum dot qubits*. MRS Bulletin **38**, 794 (2013).
- [115] M. J. S. Dewar, E. G. Zoebisch, E. F. Healy, and J. J. P. Stewart, *Development and use of quantum mechanical molecular models. 76. AM1: A new general purpose quantum mechanical molecular model*. J. Am. Chem. Soc. **107**, 3902 (1985).
- [116] Gaussian 09, Revision D.01, M. J. Frisch, et al., Gaussian, Inc., Wallingford CT, 2009.
- [117] R. Hoffmann, *An extended Hückel theory. I. Hydrocarbons*. J. Chem. Phys. **39**, 1397 (1963).
- [118] HyperChem(TM) Professional 8.0.3, Hypercube, Inc., 1115 NW 4th Street, Gainesville, Florida 32601, USA.

- [119] C. A. Mujica-Martinez and J. C. Arce, *Mini-bandstructure tailoring in π -conjugated periodic block copolymers using the envelope crystalline-orbital method*. Int. J. Quantum Chem. **110**, 2532 (2010).
- [120] NIST Standard Reference Database 101 (Computational Chemistry Comparison and Benchmark DataBase), Precomputed Vibrational Scaling Factors, <http://cccbdb.nist.gov/vibscalejust.asp>.
- [121] I. B. Bersuker, *Pseudo-Jahn-Teller-effect—A two-state paradigm in formation, deformation, and transformation of molecular systems and solids*. Chem. Rev. **113**, 1351 (2013).
- [122] H. Hwang and P. J. Rossky, *Electronic decoherence induced by intramolecular vibrational motions in a Betaine dye molecule*. J. Phys. Chem. B **108**, 6723 (2004).
- [123] J. L. McHale, *Molecular Spectroscopy* (Prentice-Hall, New York, 1999).
- [124] S. Palese, S. Mukamel, R. J. D. Miller, and W. T. Lotshaw, *Interrogation of vibrational structure and line broadening of liquid water by Raman-induced Kerr effect measurements within the multimode Brownian oscillator model*. J. Phys. Chem. **100**, 10380 (1996).
- [125] J. J. Turmer, *Bandwidths*, in *Handbook of Vibrational Spectroscopy*, J. M. Chalmers and P. R. Griffiths, Eds. (Wiley, Chichester, 2006), Vol. 1, pp. 101-127.
- [126] F. Milota, J. Sperling, A. Tortschanoff, V. Szöcs, L. Kuna, and H. F. Kauffmann, *Probing phase relaxation by measuring fluorescence interference: Polarization beating and electron-phonon coupling in conjugated polymers*. J. Lumin. **108**, 205 (2004).
- [127] Y. J. Yan and S. Mukamel, *Molecular fluorescence and near resonance Raman yield as a probe for solvation dynamics*. J. Chem. Phys. **86**, 6085 (1987).
- [128] K. Shan, Y. J. Yan, and S. Mukamel, *Intramolecular dephasing and vibrational redistribution in the dispersed fluorescence of ultracold molecules: Application to anthracene*. J. Chem. Phys. **87**, 2021 (1987).
- [129] J. Repp, P. Liljeroth, and G. Meyer, *Coherent electron-nuclear coupling in oligothiophene molecular wires*. Nat. Phys. **6**, 975 (2010).

- [130] F. Reckermann, M. Leijnse, M. R. Wegewijs, and H. Schoeller, *Transport signature of pseudo Jahn-Teller dynamics in a single-molecule transistor*. *Europhys. Lett.* **83**, 58001 (2008).
- [131] Q. Q. Wang, A. Muller, P. Bianucci, C. K. Shih, and Q. K. Xue, *Quality factors of qubit rotations in single semiconductor quantum dots*. *Appl. Phys. Lett.* **87**, 031904 (2005).
- [132] C. J. Wedge, G. A. Timco, E. T. Spielberg, R. E. George, F. Tuna, S. Rigby, E. J. L. McInnes, R. E. P. Winpenny, S. J. Blundell, and A. Ardavan, *Chemical engineering of molecular qubits*. *Phys. Rev. Lett.* **108**, 107204 (2012).
- [133] C. J. Myatt, B. E. King, Q. A. Turchette, C. A. Sackett, D. Kielpinski, W. M. Itano, C. Monroe, and D. J. Wineland, *Decoherence of quantum superpositions through coupling to engineered reservoirs*. *Nature (London)* **403**, 269 (2000).
- [134] W. Wohlleben, T. Buckup, J. L. Herek, and M. Motzkus, *Coherent control for spectroscopy and manipulation of biological dynamics*. *ChemPhysChem* **6**, 850 (2005).
- [135] P. Nuernberger, G. Vogt, T. Brixner, and G. Gerber, *Femtosecond quantum control of molecular dynamics in the condensed phase*. *Phys. Chem. Chem. Phys.* **9**, 2470 (2007).
- [136] C. Brif, R. Chakrabarti, and H. Rabitz, *Control of quantum phenomena: Past, present and future*. *New J. Phys.* **12**, 075008 (2010).
- [137] T. Brixner and G. Gerber, *Femtosecond polarization pulse shaping*. *Opt. Lett.* **26**, 557 (2001).
- [138] J. Werschnik and E. K. U. Gross, *Quantum optimal control theory*. *J. Phys. B: At. Mol. Opt. Phys.* **40**, R175 (2007).
- [139] D. Goswami, *Optical pulse shaping approaches to coherent control*. *Phys. Rep.* **374**, 385 (2003).
- [140] B. S. Williams, *Terahertz quantum-cascade lasers*. *Nat. Photon.* **1**, 517 (2007).
- [141] Focus issue on ‘Terahertz Optics’, *Nat. Photon.* **7**, Issue 9 (2013).
- [142] M. Sato, T. Higuchi, N. Kanda, K. Konishi, K. Yoshioka, T. Suzuki, K. Misawa, and M. Kuwata-Gonokami, *Terahertz polarization pulse shaping with arbitrary field control*. *Nat. Photon.* **7**, 1749 (2013).

- [143] R. Roloff, M. Wenin, and W Pötz, *Optimal control for open quantum systems: Qubits and quantum gates*. J. Comput. Theor. Nanosci. **6**, 1837 (2009).
- [144] D. G. Evans, R. D. Coalson, H. J. Kim, and Yu. Dakhnovskii, *Inducing coherent oscillations in the electron transfer dynamics of a strongly dissipative system with pulsed monochromatic light*. Phys. Rev. Lett. **75**, 3649 (1995).
- [145] I. S. Ulusoy and M. Nest, *Correlated electron dynamics: How aromaticity can be controlled*. J. Am. Chem. Soc. **133**, 20230 (2011).
- [146] G. S. Agarwal and W. Harshawardhan, *Realization of trapping in a two-level system with frequency-modulated fields*. Phys. Rev. A **50**, R4465 (1994).
- [147] W. Harshawardhan and G. S. Agarwal, *Multiple Landau-Zener crossings and quantum interference in atoms driven by phase modulated fields*. Phys. Rev. A **55**, 2165 (1997).
- [148] M. W. Noel, W. M. Griffith, and T. F. Gallagher, *Frequency-modulated excitation of a two-level atom*. Phys. Rev. A **58**, 2265 (1998).
- [149] C. A. Mujica-Martinez, J. C. Arce, J. H. Reina, and M. Thorwart, *Molecular architectures based on π -conjugated block copolymers for global quantum computation*. J. Phys.: Conf. Ser. **167**, 012061 (2009).
- [150] E. D. Kim, K. Truex, Y. Wu, A. Amo, X. Xu, D. G. Steel, A. S. Bracker, D. Gammon, and L. J. Sham, *Picosecond optical spectroscopy of a single negatively charged self-assembled InAs quantum dot*. Appl. Phys. Lett. **97**, 113110 (2010).
- [151] S.-S. Jester, D. Schmitz, F. Eberhagen, and S. Höger, *Self-assembled monolayers of clamped oligo(phenylene-ethynylene-butadiynylene)s*. Chem. Commun. **47**, 8838 (2011).
- [152] L. M. K. Vandersypen, J. M. Elzerman, R. N. Schouten, L. H. Willems van Beveren, R. Hanson, and L. P. Kouwenhoven, *Real-time detection of single-electron tunneling using a quantum point contact*. Appl. Phys. Lett. **85**, 4394 (2004).
- [153] K. H. Nealson and P. G. Conrad, *Life: Past, present and future*. Phil. Trans. R. Soc. Lond. B **354**, 1923 (1999).
- [154] R. E. Blankenship, et al., *Comparing photosynthetic and photovoltaic efficiencies and recognizing the potential for improvement*. Science **332**, 805 (2011).

- [155] C. B. Field, M. J. Behrenfeld, J. T. Randerson, and P. Falkowski, *Primary production of the biosphere: Integrating terrestrial and oceanic components*. *Science* **281**, 237 (1998).
- [156] G. D. Scholes, T. Mirkovic, D. B. Turner, F. Fassioli, and A. Buchleitner, *Solar light harvesting by energy transfer: From ecology to coherence*. *Energy Environ. Sci.* **5**, 9374 (2012).
- [157] B. Ke, *Photosynthesis: Photobiochemistry and Photobiophysics* (Kluwer Academic Publishers, New York, 2003).
- [158] G. D. Scholes and G. Rumbles, *Excitons in nanoscale systems*. *Nat. Mater.* **5**, 683 (2006).
- [159] H. van Amerongen, L. Valkunas, and R. van Grondelle, *Photosynthetic Excitons* (World Scientific, Singapore, 2000).
- [160] F. Fassioli, R. Dinshaw, P. C. Arpin, and G. D. Scholes, *Photosynthetic light harvesting: Excitons and coherence*. *J. R. Soc. Interface* **11**, 20130901 (2014).
- [161] E. J. G. Peterman, T. Pullerits, R. van Grondelle, and H. van Amerongen, *Electron–phonon coupling and vibronic fine structure of light-harvesting complex II of green plants: Temperature dependent absorption and high-resolution fluorescence spectroscopy*. *J. Phys. Chem. B* **101**, 4448 (1997).
- [162] M. Wendling, T. Pullerits, M. A. Przyjalowski, S. I. E. Vulto, T. J. Aartsma, R. van Grondelle, and H. van Amerongen, *Electron–vibrational coupling in the Fenna-Matthews-Olson complex of *Prosthecochloris aestuarii* determined by temperature-dependent absorption and fluorescence line-narrowing measurements*. *J. Phys. Chem. B* **104**, 5825 (2000).
- [163] A. Nitzan, *Chemical Dynamics in Condensed Phases: Relaxation, Transfer and Reactions in Condensed Molecular Systems* (Oxford University Press, Oxford, 2006).
- [164] C. Olbrich and U. Kleinekathöfer, *Time-dependent atomistic view on the electronic relaxation in light-harvesting system II*. *J. Phys. Chem. B* **114**, 12427 (2010).
- [165] M. Aghtar, J. Strümpfer, C. Olbrich, K. Schulten, and U. Kleinekathöfer, *The FMO complex in a glycerol–water mixture*. *J. Phys. Chem. B* **117**, 7157 (2013).
- [166] BIPM, *The International System of Units* (Sèvres, 2006), 8th ed., Chap. 4.

- [167] G. D. Scholes, *Long-range resonance energy transfer in molecular systems*. Annu. Rev. Phys. Chem. **54**, 57 (2003).
- [168] D. Beljonne, C. Curutchet, G. D. Scholes, and R. J. Silbey, *Beyond Förster resonance energy transfer in biological and nanoscale systems*. J. Phys. Chem. B **113**, 6583 (2009).
- [169] P. Nalbach, A. Ishizaki, G. R. Fleming, and M. Thorwart, *Iterative path-integral algorithm versus cumulant time-nonlocal master equation approach for dissipative biomolecular exciton transport*. New J. Phys. **13**, 063040 (2011).
- [170] S. Mukamel, *Principles of Nonlinear Optics and Spectroscopy* (Oxford University Press, New York, 1995).
- [171] M. Cho, *Two-Dimensional Optical Spectroscopy* (CRC, Boca Raton, 2009).
- [172] S. T. Cundiff and S. Mukamel, *Optical multidimensional coherent spectroscopy*. Phys. Today **66**, 44 (2013).
- [173] A. M. Brańczyk, D. B. Turner, and G. D. Scholes, *Crossing disciplines - A view on two-dimensional optical spectroscopy*. Ann. Phys. (Berlin) **526**, 31 (2014).
- [174] Y.-C. Cheng and G. R. Fleming, *Dynamics of light harvesting in photosynthesis*. Annu. Rev. Phys. Chem. **60**, 241 (2009).
- [175] A. Ishizaki, T. R. Calhoun, G. S. Schlau-Cohen, and G. R. Fleming, *Quantum coherence and its interplay with protein environments in photosynthetic electronic energy transfer*. Phys. Chem. Chem. Phys. **12**, 7319 (2010).
- [176] K. L. M. Lewis and J. P. Ogilvie, *Probing photosynthetic energy and charge transfer with two-dimensional electronic spectroscopy*. J. Phys. Chem. Lett. **3**, 503 (2012).
- [177] N. Lambert, Y.-N. Chen, Y.-C. Cheng, C.-M. Li, G.-Y. Chen, and F. Nori, *Quantum biology*. Nat. Phys. **9**, 10 (2013).
- [178] T. Brixner, J. Stenger, H. M. Vaswani, M. Cho, R. E. Blankenship, and G. R. Fleming, *Two-dimensional spectroscopy of electronic couplings in photosynthesis*. Nature (London) **434**, 625 (2005).
- [179] G. S. Engel, T. R. Calhoun, E. L. Read, T.-K. Ahn, T. Mančal, Y.-C. Cheng, R. E. Blankenship, and G. R. Fleming, *Evidence for wavelike energy transfer through quantum coherence in photosynthetic systems*. Nature (London) **446**, 782 (2007).

- [180] S. Westenhoff, D. Paleček, P. Edlund, P. Smith, and D. Zigmantas, *Coherent picosecond exciton dynamics in a photosynthetic reaction center*. J. Am. Chem. Soc. **134**, 16484 (2012).
- [181] G. Panitchayangkoon, D. Hayes, K. A. Fransted, J. R. Caram, E. Harel, J. Wen, R. E. Blankenship, and G. S. Engel, *Long-lived quantum coherence in photosynthetic complexes at physiological temperature*. Proc. Natl. Acad. Sci. USA **107**, 12766 (2010).
- [182] E. Collini, C. Y. Wong, K. E. Wilk, P. M. G. Curmi, P. Brumer, and G. D. Scholes, *Coherently wired light-harvesting in photosynthetic marine algae at ambient temperature*. Nature (London) **463**, 644 (2010).
- [183] C. Y. Wong, R. M. Alvey, D. B. Turner, K. E. Wilk, D. A. Bryant, P. M. G. Curmi, R. J. Silbey, and G. D. Scholes, *Electronic coherence lineshapes reveal hidden excitonic correlations in photosynthetic light harvesting*. Nat. Chem. **4**, 396 (2012).
- [184] E. Harel and G. S. Engel, *Quantum coherence spectroscopy reveals complex dynamics in bacterial light-harvesting complex 2 (LH2)*. Proc. Natl. Acad. Sci. USA **109**, 706 (2012).
- [185] V. Tiwari, W. K. Peters, and D. M. Jonas, *Electronic resonance with anti-correlated pigment vibrations drives photosynthetic energy transfer outside the adiabatic framework*. Proc. Natl. Acad. Sci. USA **110**, 1203 (2013).
- [186] N. Christensson, F. Milota, J. Hauer, J. Sperling, O. Bixner, A. Nemeth, and H. F. Kauffmann, *High frequency vibrational modulations in two-dimensional electronic spectra and their resemblance to electronic coherence signatures*. J. Phys. Chem. B **115**, 5383 (2011).
- [187] A. W. Chin, J. Prior, R. Rosenbach, F. Caycedo-Soler, S. F. Huelga, and M. B. Plenio, *The role of non-equilibrium vibrational structures in electronic coherence and recoherence in pigment-protein complexes*. Nat. Phys. **9**, 113 (2013).
- [188] N. Christensson, H. F. Kauffmann, T. Pullerits, and T. Mančal, *Origin of long-lived coherences in light-harvesting complexes*. J. Phys. Chem. B **116**, 7449 (2012).
- [189] A. Chenu, N. Christensson, H. F. Kauffmann, and T. Mančal, *Enhancement of vibronic and ground-state vibrational coherences in 2D spectra of photosynthetic complexes*. Sci. Rep. **3**, 2029 (2013).

- [190] D. Hayes, and G. B. Griffin, and G. S. Engel, *Engineering coherence among excited states in synthetic heterodimer systems*. *Science* **340**, 1431 (2013).
- [191] A. Halpin, P. J. M. Johnson, R. Tempelaar, R. S. Murphy, J. Knoester, T. L. C. Jansen, and R. J. Dwayne Miller, *Two-dimensional spectroscopy of a molecular dimer unveils the effects of vibronic coupling on exciton coherences*. *Nat. Chem.* **6**, 196 (2014).
- [192] B. W. Matthews, R. E. Fenna, M. C. Bolognesi, M. F. Schmid, and J. M. Olson, *Structure of a Bacteriochlorophyll a-protein from the green photosynthetic bacterium Prosthecochloris aestuarii*. *J. Mol. Biol.* **131**, 259 (1979).
- [193] D. E. Tronrud, J. Wen, L. Gay, and R. E. Blankenship, *The structural basis for the difference in absorbance spectra for the FMO antenna protein from various green sulfur bacteria*. *Photosynth. Res.* **100**, 79 (2009); Protein Data Bank file 3ENI.
- [194] J. Overmann, *Green Sulfur Bacteria*, in *Encyclopedia of Life Sciences* (Wiley, Chichester, 2001).
- [195] J. M. Olson and R. E. Blankenship, *Thinking about the evolution of photosynthesis*. *Photosynth. Res.* **80**, 373 (2004).
- [196] H.-W. Rémigy, G. Hauska, S. A. Müller, and G. Tsiotis, *The reaction centre from green sulphur bacteria: Progress towards structural elucidation*. *Photosynth. Res.* **71**, 91 (2002).
- [197] M. T. W. Milder, B. Brüggemann, R. van Grondelle, and J. L. Herek, *Revisiting the optical properties of the FMO protein*. *Photosynth. Res.* **104**, 257 (2010).
- [198] J. A. Eisen, et al., *The complete genome sequence of Chlorobium tepidum TLS, a photosynthetic, anaerobic, green-sulfur bacterium*. *Proc. Natl. Acad. Sci. USA* **99**, 9509 (2002).
- [199] D. Hayes, J. Wen, G. Panitchayangkoon, R. E. Blankenship, and G. S. Engel, *Robustness of electronic coherence in the Fenna-Matthews-Olson complex to vibronic and structural modifications*. *Faraday Discuss.* **150**, 459 (2011).
- [200] Jmol: an open-source Java viewer for chemical structures in 3D. <http://www.jmol.org/>.

- [201] M. Schmidt am Busch, F. Müh, M. El-Amine Madjet, and T. Renger, *The eighth bacteriochlorophyll completes the excitation energy funnel in the FMO protein*. J. Phys. Chem. Lett. **2**, 93 (2011).
- [202] V. Tiwari, W. K. Peters, and D. M. Jonas, *Energy transfer: Vibronic coherence unveiled*. Nat. Chem. **6**, 173 (2014).
- [203] T. Mančal, N. Christensson, V. Lukeš, F. Milota, O. Bixner, H. F. Kauffmann, and J. Hauer, *System-dependent signatures of electronic and vibrational coherences in electronic two-dimensional spectra*. J. Phys. Chem. Lett. **3**, 1497 (2012).
- [204] M. Mohseni, P. Rebentrost, S. Lloyd, and A. Aspuru-Guzik, *Environment-assisted quantum walks in photosynthetic energy transfer*. J. Chem. Phys. **129**, 174106 (2008).
- [205] M. B. Plenio and S. F. Huelga, *Dephasing-assisted transport: Quantum networks and biomolecules*. New J. Phys. **10**, 113019 (2008).
- [206] F. Fassioli, A. Olaya-Castro, and G. D. Scholes, *Coherent energy transfer under incoherent light conditions*. J. Phys. Chem. Lett. **3**, 3136 (2012).
- [207] J. Adolphs and T. Renger, *How proteins trigger excitation energy transfer in the FMO complex of green sulfur bacteria*. Biophys. J. **91**, 2778 (2006).
- [208] J. Wen, H. Zhang, M. L. Gross, and R. E. Blankenship, *Membrane orientation of the FMO antenna protein from Chlorobaculum tepidum as determined by mass spectrometry-based footprinting*. Proc. Natl. Acad. Sci. USA **106**, 6134 (2009).
- [209] G. R. Fleming and M. Cho, *Chromophore-solvent dynamics*. Annu. Rev. Phys. Chem. **47**, 109 (1996).
- [210] S. A. Passino, Y. Nagasawa, and G. R. Fleming, *Three pulse stimulated photon echo experiments as a probe of polar solvation dynamics: Utility of harmonic bath models*. J. Chem. Phys. **107**, 6094 (1997).
- [211] G. R. Fleming, S. A. Passino, and Y. Nagasawa, *The interaction of solutes with their environments*. Phil. Trans. R. Soc. Lond. A **356**, 389 (1998).
- [212] A. Damjanović, I. Kosztin, U. Kleinekathöfer, and K. Schulten, *Excitons in a photosynthetic light-harvesting system: A combined molecular dynamics, quantum chemistry, and polaron model study*. Phys. Rev. E **65**, 031919 (2002).

- [213] T. Pullerits, R. Monshouwer, F. van Mourik, and R. van Grondelle, *Temperature dependence of electron–vibronic spectra of photosynthetic systems. Computer simulations and comparison with experiment*. Chem. Phys. **194**, 395 (1995).
- [214] C. Kreisbeck and T. Kramer, *Long-lived electronic coherence in dissipative exciton dynamics of light-harvesting complexes*. J. Phys. Chem. Lett. **3**, 2828 (2012).
- [215] C. Kreisbeck, T. Kramer, and A. Aspuru-Guzik, *Disentangling electronic and vibronic coherences in two-dimensional echo spectra*. J. Phys. Chem. B **117**, 9380 (2013).
- [216] T. Renger and R. A. Marcus, *On the relation of protein dynamics and exciton relaxation in pigment–protein complexes: An estimation of the spectral density and a theory for the calculation of optical spectra*. J. Chem. Phys. **116**, 9997 (2002).
- [217] C. Meier and D. J. Tannor, *Non-Markovian evolution of the density operator in the presence of strong laser fields*. J. Chem. Phys. **111**, 3365 (1999).
- [218] C. Olbrich, J. Strümpfer, K. Schulten, and U. Kleinekathöfer, *Theory and simulation of the environmental effects on FMO electronic transitions*. J. Phys. Chem. Lett. **2**, 1771 (2011).
- [219] J. Ridley and M. Zerner, *An intermediate neglect of differential overlap technique for spectroscopy: Pyrrole and the azines*. Theor. Chim. Acta **32**, 111 (1973).
- [220] A. Ishizaki and G. R. Fleming, *On the adequacy of the Redfield equation and related approaches to the study of quantum dynamics in electronic energy transfer*. J. Chem. Phys. **130**, 234110 (2009).
- [221] A. Ishizaki and G. R. Fleming, *Unified treatment of quantum coherent and incoherent hopping dynamics in electronic energy transfer: Reduced hierarchy equation approach*. J. Chem. Phys. **130**, 234111 (2009).
- [222] S. Jesenko and M. Žnidarič, *Excitation energy transfer efficiency: Equivalence of transient and stationary setting and the absence of non-Markovian effects*. J. Chem. Phys. **138**, 174103 (2013).
- [223] K. Hoef-Emden and J. M. Archibald, *Cryptomonads*, in The Tree of Life Web Project (2010).

- [224] A. B. Doust, K. E. Wilk, P. M. G. Curmi, and G. D. Scholes, *The photophysics of cryptophyte light-harvesting*. J. Photochem. Photobiol. A: Chem. **184**, 1 (2006).
- [225] C. Curutchet, J. Kongsted, A. Muñoz-Losa, H. Hossein-Nejad, G. D. Scholes, and B. Mennucci, *Photosynthetic light-harvesting is tuned by the heterogeneous polarizable environment of the protein*. J. Am. Chem. Soc. **133**, 3078 (2011).
- [226] C. Curutchet, V. I. Novoderezhkin, J. Kongsted, A. Muñoz-Losa, R. van Grondelle, G. D. Scholes, and B. Mennucci, *Energy flow in the cryptophyte PE545 antenna is directed by bilin pigment conformation*. J. Phys. Chem. B **117**, 4263 (2013).
- [227] A. B. Doust, C. N. J. Marai, S. J. Harrop, K. E. Wilk, P. M. G. Curmi, and G. D. Scholes, *Developing a structure–function model for the Cryptophyte Phycoerythrin 545 using ultrahigh resolution crystallography and ultrafast laser spectroscopy*. J. Mol. Biol. **344**, 135 (2004).
- [228] A. Kolli, E. J. O’Reilly, G. D. Scholes, and A. Olaya-Castro, *The fundamental role of quantized vibrations in coherent light harvesting by cryptophyte algae*. J. Chem. Phys. **137**, 174109 (2012).
- [229] V. I. Novoderezhkin, A. B. Doust, C. Curutchet, G. D. Scholes, and R. van Grondelle, *Excitation dynamics in Phycoerythrin 545: Modeling of steady-state spectra and transient absorption with modified redfield theory*. Biophys. J. **99**, 344 (2010).
- [230] L. Viani, C. Curutchet, and B. Mennucci, *Spatial and electronic correlations in the PE545 light-harvesting complex*. J. Phys. Chem. Lett. **4**, 372 (2013).
- [231] H. Hossein-Nejad, C. Curutchet, A. Kubica, and G. D. Scholes, *Delocalization-enhanced long-range energy transfer between Cryptophyte algae PE545 antenna proteins*. J. Phys. Chem. B **115**, 5243 (2011).
- [232] M. Aghtar, J. Strümpfer, C. Olbrich, K. Schulten, and U. Kleinekathöfer, *Different types of vibrations interacting with electronic excitations in Phycoerythrin 545 and Fenna-Matthews-Olson antenna systems*. J. Phys. Chem. Lett. **5**, 3131 (2014).
- [233] J. B. Foresman and Æ. Frisch, *Exploring Chemistry with Electronic Structure Methods* (Gaussian, Inc., Pittsburgh, 1996), 2nd ed.

- [234] F. Jensen, *Introduction to Computational Chemistry* (Wiley, Chichester, 2007), 2nd ed.
- [235] H. B. Schlegel, *Geometry optimization*. WIREs Comput. Mol. Sci. **1**, 790 (2011).
- [236] Gaussian, Inc. Gaussian 09 User's Reference: "Opt" Keyword, http://www.gaussian.com/g_tech/g_ur/k_opt.htm.
- [237] X. Li and M. J. Frisch, *Energy-represented direct inversion in the iterative subspace within a hybrid geometry optimization method*. J. Chem. Theory Comput. **2**, 835 (2006).
- [238] Gaussian, Inc. Gaussian 09 User's Reference: "Freq" Keyword, http://www.gaussian.com/g_tech/g_ur/k_freq.htm.
- [239] J. W. Ochterski, *Vibrational analysis in Gaussian* (1999), http://www.gaussian.com/g_whitepap/vib.htm.
- [240] NIST Standard Reference Database 101 (Computational Chemistry Comparison and Benchmark DataBase), Vibrational Scaling Factors, <http://cccbdb.nist.gov/vibnotes.asp>.
- [241] E. Heilbronner and H. Brock. *The HMO Model and its Applications: Basis and Manipulation* (Wiley, London, 1976).
- [242] N. W. Ashcroft and N. D. Mermin, *Solid State Physics* (Philadelphia, Holt-Saunders, 1976).
- [243] K. Jug, P. C. Hiberty, and S. Shaik, *σ - π energy separation in modern electronic theory for ground states of conjugated systems*. Chem. Rev. **101**, 1477 (2001).
- [244] I. N. Levine, *Quantum Chemistry* (Prentice-Hall, New Jersey, 2000), 5th ed.
- [245] M. Wolfsberg and L. Helmholz, *The spectra and electronic structure of the tetrahedral ions MnO_4^- , CrO_4^- , and ClO_4^-* . J. Chem. Phys. **20**, 837 (1952).
- [246] J. H. Ammeter, H. B. Buergi, J. C. Thibeault, and R. Hoffmann, *Counterintuitive orbital mixing in semiempirical and ab initio molecular orbital calculations*. J. Am. Chem. Soc. **100**, 3686 (1978).
- [247] G. Calzaferri, L. Forss, and I. Kamber, *Molecular geometries by the extended Hückel molecular orbital method*. J. Phys. Chem. **93**, 5366 (1989); S. Y. Hong

- and D. S. Marynick, *Modified extended Hückel band calculations on conjugated polymers*. *ibid.* **96**, 5497 (1992); G. Calzaferri and R. Rytz, *The band structure of diamond*. *ibid.* **100**, 11122 (1996).
- [248] C. J. Ballhausen and H. B. Gray, *The electronic structure of the Vanadyl ion*. *Inorg. Chem.* **1**, 111 (1962); L. L. Lohr Jr. and W. N. Lipscomb, *Molecular orbital theory of spectra of Cr³⁺ ions in crystals*. *J. Chem. Phys.* **38**, 1607 (1963); L. L. Lohr Jr., T. Jordan, H. Smith, and W. N. Lipscomb, *X-ray structure determination of (CH₃)₂NSO₂N(CH₃)₂ and LCAO-MO study of multiple bonding in Sulfones*. *J. Am. Chem. Soc.* **85**, 846 (1963).
- [249] C. A. Mujica-Martinez, *Teoría del orbital molecular de masa efectiva aplicada a poliácenos cuasi-unidimensionales y sus heteroestructuras*, Chemistry B.Sc. Thesis, Universidad del Valle (2006).
- [250] A. Piaggi, R. Tubino, and L. Colombo, *Electronic states in one-dimensional polymeric superlattices: A tight-binding approach*. *Phys. Rev. B* **51**, 1624 (1995).

Publications and participation in events

- C. A. Mujica-Martinez, P. Nalbach, and M. Thorwart, *Organic π -conjugated copolymers as molecular charge qubits*. Physical Review Letters **111**, 016802 (2013); *ibid.* **113**, 139903 (2014).
- C. A. Mujica-Martinez, P. Nalbach, and M. Thorwart, *Quantification of non-Markovian effects in the Fenna-Matthews-Olson complex*. Physical Review E **88**, 062719 (2013).
- C. A. Mujica-Martinez, P. Nalbach, and M. Thorwart. *Nonequilibrium quantum dynamics of biomolecular excitons*, in *Nonlinear Phenomena in Complex Systems: From Nano to Macro*, D. Matrasulov and E. Stanley, Eds. (Springer, Dordrecht, 2014), Chap. 5, pp. 61-78. Proceedings of the NATO Advanced Research Workshop on “New Challenges in Complex System Physics”. May 2013, Samarkand, Uzbekistan.
- P. Nalbach, C. A. Mujica-Martinez, and M. Thorwart. *Vibronic speed-up of the excitation energy transfer in the Fenna-Matthews-Olson complex*. arXiv:1311.6363 (2013).
- P. Nalbach, C. A. Mujica-Martinez, and M. Thorwart. *The effect of underdamped molecular vibrations on coherence and energy transfer times in light-harvesting complexes*. In preparation (2014).

Conferences

- Ultrafast X-ray Summer School 2011 (UXSS2011). June 2011, Deutsches Elektronen-Synchrotron (DESY), Hamburg.
- Second International Symposium on Electronic Properties of π -conjugated Materials II (π -2011). Poster: *Multiblock π -conjugated copolymer architectures as charge-qubits*. September 2011, Würzburg.
- XXVII Heidelberg Physics Graduate Days. October 2011, Heidelberg.
- 62nd Lindau Nobel Laureate Meeting dedicated to Physics. Participation by nomination. July 2012, Lindau.
- 2nd International Workshop on Exciton Dynamics and Spectroscopy. August 2012, Rostock.
- 44th IFF Spring School on Quantum Information Processing. February-March 2013, Jülich Forschungszentrum, Jülich.
- DPG-Frühjahrstagung der Sektion Kondensierte Materie: Regensburg 13. Oral presentation: *Organic π -conjugated copolymers as molecular charge-qubits*. March 2013, Regensburg.

Acknowledgements

Thanks to Prof. Dr. Michael Thorwart and to Priv. Doz. Dr. Peter Nalbach for their guidance and support during my studies. For the time used to evaluate the document, I would like to thank Prof. Dr. Carmen Herrmann and Prof. Dr. Ulrich Kleinekathöfer.

Financial support during my entire stay in Germany from the Deutscher Akademischer Austauschdienst (DAAD) under contract A0974132 is acknowledged, in special, the nomination and funding for my participation in the 62nd Lindau Nobel Laureate Meeting dedicated to Physics. Also to the Wilhelm und Else-Heraeus-Förderprogramm for partial financial support during my participation in the DPG-Tagung 2013 in Regensburg.

Lebenslauf

Cesar Augusto Mujica Martinez

Geburtsdatum und -ort: 18. Dezember 1984, Valencia, Venezuela

Schulische Ausbildung:

1990-2001 Colegio San Francisco de Asis, Cali, Kolumbien

Studium:

Aug. 2001-Okt. 2006 Chemie, Universidad del Valle, Cali, Kolumbien
Bachelorarbeit "Teoría del orbital molecular de masa efectiva aplicada a poliacenos cuasi-unidimensionales y sus heteroestructuras"

Aug. 2006-Dez. 2009 Master in Chemie, Universidad del Valle, Cali, Kolumbien
Masterarbeit "Electronic structure, dynamics, and applications to quantum computation of molecular architectures based on π -conjugated block copolymers"

Mai 2008-Nov. 2008 Forschungsaufenthalt an der Heinrich-Heine-Universität Düsseldorf

Okt. 2010-März 2014 Stipendiat des Deutschen Akademischen Austauschdiensts (DAAD)

Okt. 2010-heute Doktorand an der Universität Hamburg bei Prof. Dr. M. Thorwart

Erklärung

Die hier vorgelegte Dissertation habe ich eigenständig und ohne unerlaubte Hilfe angefertigt. Die Dissertation wurde in der vorgelegten oder in ähnlicher Form noch bei keiner anderen Institution eingereicht. Ich habe bisher keine erfolglosen Promotionversuche unternommen.

Cesar Augusto Mujica Martinez
Hamburg, den 31.07.2014